Modelling of the cooling and thermal treatment of bimetallic rolling mill rolls

PhD thesis by

Ingrid Neira Torres

Thesis developed in cotutelle for the degree of:

Doctor in Engineering Sciences (University of Liège)

Doctor in Materials Engineering and Science (University of Concepción)

November, 2015

A journey of a thousand miles

begins with a single step…

El viaje más largo

comienza con un solo paso…

Le plus long voyage commence

toujours par un premier pas…

JURY MEMBERS

Dr. Anne Marie HABRAKEN, supervisor
Research Director FNRS
ArGEnCo Department, University of Liège, Belgium
Anne.Habraken@ulg.ac.be

Dr. Paulo FLORES, co-supervisor
Professor PhD program
DIM Department, University of Concepción, Chile
pfloresv@udec.cl

Dr. Carlos CAMURRI
Director of PhD program
DIMAT Department, University of Concepción, Chile
ccamurri@udec.cl

Dr. Jacqueline Lecomte-Beckers
Professor
ArGEnCo Department, University of Liège, Belgium
Jacqueline.Lecomte@ulg.ac.be

Dr. David ROJAS
Professor PhD program
DIMAT Department, University of Concepción, Chile
davrojas@udec.cl

ACKNOWLEDGEMENTS

I would like to thank firstly to my tutors Dr. Anne Marie Habraken and Dr. Paulo Flores for their unmeasurable help through the whole research. They were a fundamental support patiently guiding the technical work but also encouraging me during the whole thesis development.

Thanks to Conicyt (National commission for scientific and technological research) Chile for their financial help that made possible the development of this work performed between Chile and Belgium.

I would like to express my gratitude to all my colleagues of the MSM and MMS teams from the University of Liège. In particular, thanks to Gaëtan Gilles, Olivier Millis and Jérôme Tchoufang Tchuindjang for their important technical support and for their always friendly disposition to help me.

I am infinitely grateful to my family for their unconditional and unmeasurable support and understanding during these years. Thanks to my parents being always there. Thanks to my husband for his great love, patience and help. Finally, thanks to my daughter, for her incredibly understanding at her shorts 10 years old and for being my principal motivation.

ABSTRACT

This work is focused on the modelling of post casting cooling and heat treatment stages, using a coupled thermo-mechanical metallurgical model in order to understand the behavior of bimetallic rolling mill rolls. The case of interest is a bimetallic rolling mill roll which materials and geometry present a risk of failure in industrial manufacturing. The analysis of residual stress fields together with a rough damage approach allows the understanding of the failure event and predicting trends when industrial conditions are modified.

Performed finite element modelling requires a complete set of materials parameters. Experimental and numerical methods are applied in order to obtain thermophysical, mechanical, metallurgical and coupled parameters.

Sensitivity analysis is performed in order to evaluate the effect of numerical predictions to different input data, modeling eventual modifications of materials or geometries.

Finally, conclusions and perspectives obtained from this research allow establishing some weakness of the implemented model, enhancing the importance of considering more advanced damage models. In addition, it is settled that the material characterization must be improved by considering materials pollution and complexity. However the work provides a convincing explanation of the observed phenomena of ruptures.

RESUMEN

Este trabajo se basa en la modelación de las etapas de enfriamiento y posterior tratamiento térmico usando un modelo termo-mecánico metalúrgico, con el objetivo de comprender el comportamiento de rodillos laminadores bimetálicos. El caso particular de interés en esta tesis es un rodillo laminador cuya geometría y materiales que lo conforman, representan un alto riesgo de falla en las condiciones de fabricación industrial. El análisis de campos de esfuerzos residuales junto con un modelo de daño aproximado, permite comprender los eventos de falla y predecir tendencias frente a diferentes condiciones industriales.

La modelación por elementos finitos requiere una completa serie de parámetros de los materiales involucrados. Por lo tanto, se aplican métodos experimentales y numéricos para obtener parámetros termo-físicos, mecánicos, metalúrgicos y acoplados.

Se realizan análisis de sensibilidad para evaluar el efecto en las predicciones, de diferentes parámetros de entrada que representan eventuales cambios de materiales o en la geometría del rodillo laminador.

Finalmente, de este trabajo se obtienen conclusiones y perspectivas que permiten establecer algunas debilidades del modelo implementado, resaltando la importancia de considerar un modelo de daño más avanzado. Además, se establece que la caracterización de los materiales debe ser mejorada considerando la contaminación entre ambos materiales y su complejidad. Sin embargo, esta tesis entrega una explicación concluyente del fenómeno de ruptura observado.

RESUMÉ

Ce travail se focalise sur la modélisation du refroidissement des cylindres de travail de laminoirs bimétalliques et de leur traitement thermique via des simulations thermomécaniques métallurgiques. L'étude est dédiée à des cylindres présentant des risques de fracture lors de leur procédé de fabrication.

L'analyse des champs de contraintes résiduelles ainsi qu'un modèle d'endommagement permettent de comprendre la genèse des bris et de prédire les tendances en cas de modification du procédé.

Le modèle éléments finis utilisé nécessite un jeu important de paramètres matériaux. Ces derniers sont obtenus de façon directe par expérience ou par méthode inverse qu'ils soient thermo physique, mécanique ou métallurgique.

La sensibilité des résultats prédits aux données d'entrée (géométrie, matériaux) a été investiguée.

En final, les conclusions et perspectives de cette recherche mettent en lumière certaines faiblesses du modèle et la nécessité d'une recherche approfondie dédiée à la rupture. Remarquons cependant que même si la complexité de la pollution des matériaux de cœur et d'enveloppe n'a pas pu être prise en compte, la thèse apporte des explications convaincantes des phénomènes observés.

TABLE OF CONTENTS

List of Figures

List of Tables

Chapter 1. Introduction

The studied bimetallic rolling mill rolls are composed of two different materials. A centrifugal casting process is applied to achieve this bimetallic structure. After the casting stage, the rolls are subjected to air cooling. Then, a tempering heat treatment is applied in order to homogenize the structure. During both thermal cycles, thermal gradients generate important effects on stress state and phase transformations. The level of stresses and strains can generate some failure cases during the tempering heat treatment of the rolls; however, internal cracks could already be present from the former cooling step. The Finite Element (FE) method might be an efficient tool for a complete understanding of the thermal, mechanical and metallurgical coupled phenomena and for the investigation of potential damage.

1.1 Motivation

Hot rolling process is one of the most used metalworking methods and it is performed above the recrystallization temperature of the material. In particular roughing stands of the hot strip mill require the employment of bimetallic rolling mill rolls since two imperative properties are required; a high toughness in the core and a high wear resistance and hardness in the shell.

The Belgian industry Marichal Ketin (MK) is dedicated to the manufacturing of rolling mill rolls since 1911, being one of the most important companies in this area [1]. Centrifugal casting is the method used by MK industry for the fabrication of bimetallic rolling mill rolls [2]. After the casting stage, rolls are subjected to air cooling called hereafter Post Casting Cooling (PCC) taking several days to reach room temperature depending of the roll size. Then, a Tempering

Heat Treatment (THT) is applied principally to reduce the fragility of martensite phase and to increase its toughness, but also for the structure homogenization and relaxation of the residual stress levels [3].

However despite of good results obtained by the MK products, a series of failure cases have been observed by MK industry for bimetallic rolls made of Spheroidal Graphite Iron (SGI) as core material and High Chromium Steel (HCS) as shell material, during heat treatment stage for diameters from 1200 mm, while for smaller diameters, no problems had been experienced. Failure cases (in a failure rate of 10%) generate a problem within the industry since the current tendency of the market for the application of roughing stands is the fabrication of bimetallic rolling mill rolls upper 1200 mm diameter. In addition, it is important to notice that these rolls have a weight of approximately 30 Ton and the associated cost is between 60.000 and 120.000 €/piece [4].

The mechanisms of crack initiation have not been identified with certainty. Observations after failure have not allowed establishing if the crack origin is located at the shell, core or at the interface between both materials. However, the cracks morphology shows that their origin is clearly associated to high levels of residual stresses. It is suspected that thermal gradients and phase transformations generate important strains; nevertheless a quantitative analysis is required for the understanding of the phenomenon and for the study of eventual modifications of the process that could reduce the crack events.

The problem presented here leads MK industry to demanding for numerical simulation of the industrial process. This thesis is the result of the cooperating work between MK industry and the University of Liège in MSM and MMS teams. The thesis of J. Tchoufang Tchuindjang (MMS team) [5] leads with the metallurgical aspects of the problem, while the numerical modeling and mechanical aspects are addressed in this thesis (MSM team). The research could rely on a part of former results from previous Waloon Region projects CENCYLAM and SOUBIRO where preliminary tests had been performed. The thesis was developed in cotutelle between the University of Liège and the University of Concepción.

1.2 Industrial process description

Different sizes of rolling mill rolls are manufactured by Marichal Ketin industry (MK). Since some cases of failure had been observed for this case, a bimetallic roll of 1200 mm diameter is studied in this thesis. A real specimen with corresponding dimensions is illustrated in Figure 1.1.

In rolling mills process, the roll is stressed in two different ways: the wear and roughing conditions in the surface and the high impacts resisted by the core. This is the reason why rolls for this application should be produced as compound or bimetallic rolls. Therefore, the core and necks must be made up with a ductile and tenacious core material, while the barrel must be made up with a hard and both wear and thermal resistant shell material. High Chromium Steel material (hereafter HCS) provides a high strength and wear resistance in the shell, and Spheroidal Graphite Iron (SGI) contributes with a significant toughness in the core of the roll [4].

The fabrication process by centrifugal casting, post casting cooling and subsequent heat treatment are described in this section. In addition, roll defects observed by the industry are also described.

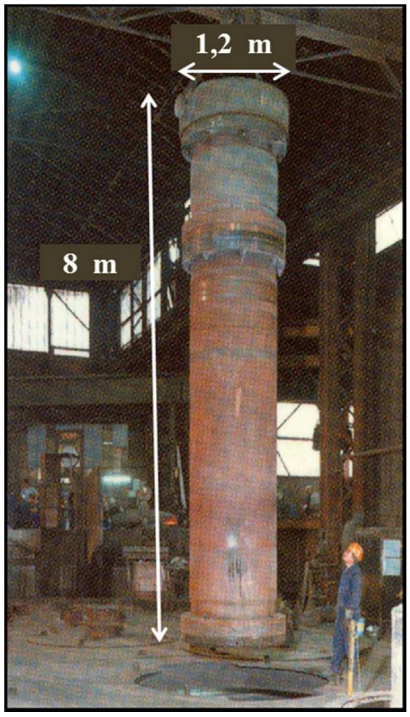

Figure 1.1. Bimetallic rolling mill roll 1200 mm diameter

1.2.1 Centrifugal casting

Centrifugal casting process is presented in Figure 1.2. First of all, the mold is prepared by molding necks using some sand pieces represented in yellow in Figure 1.2, shaping the roll according to the customer requirements, and then the mould is provided by a refractory coating. For centrifugal casting, the mould is placed in the spin caster; it provides rotation for the whole system by an electric motor reaching a rotating speed of approximately 600 rpm [2].

As a first part of the casting process the HCS shell material is poured into the mould in rotation, this first material is colored in red in Figure 1.2 and it goes filling directly the shell of the roll due to the centrifugal force field applied by the mould rotation. In order to prevent the oxidation of the inner surface of shell material, it is covered using a special flux, this step is essential for ensure the good bonding between shell and core materials. The temperature of the inner shell surface is monitored with the aim of determine the precise moment for the casting of core material. Then, the SGI core material (in blue in Figure 1.2) is poured into the mould in two stages; the first one to benefit the good bonding between both materials and the second one for the mold filling. The rotation speed is progressively reduced until finishing the casting process.

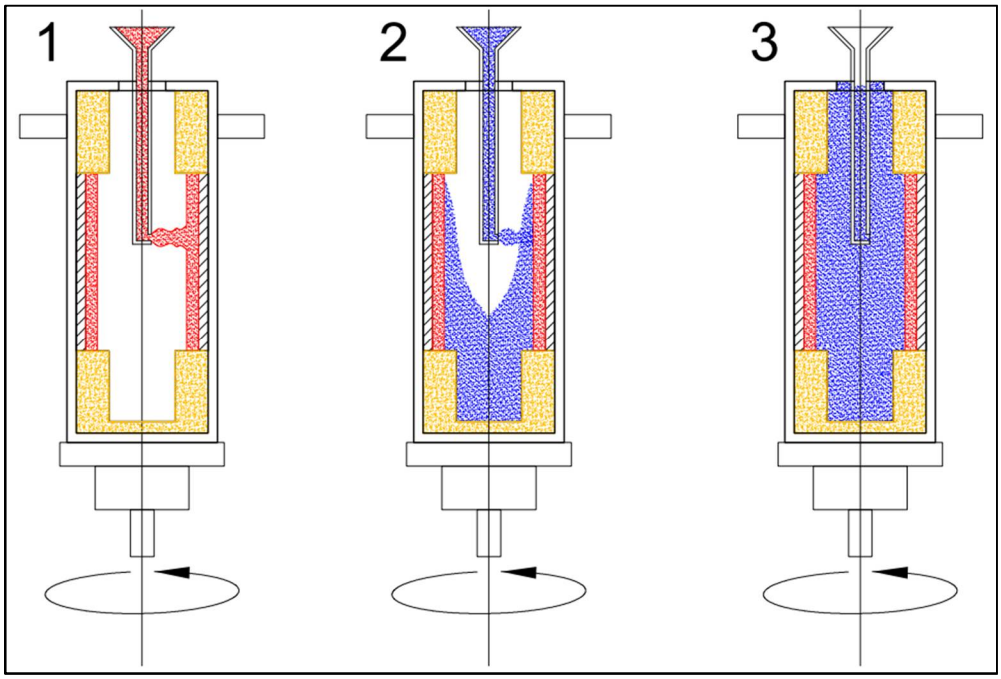

Figure 1.2. Centrifugal casting of bimetallic rolling mill rolls by MK industry

1.2.2 Post casting cooling and tempering heat treatment

After the casting process, the mould-roll system is removed from the spin caster and subjected to Post Casting Cooling (PCC). During PCC stage, the surface of a reference roll of 1200 mm diameter and 80 mm of shell thickness (**τ**), takes approximately 8 days (195 hrs) and 11 days (270 hrs) to reach temperatures below 100°C and room temperature respectively, as shown in Figure 1.3.

The next step is the application of a Tempering Heat Treatment (THT) at 500°C. The objective of this stage is to obtain heat treated martensite, to transform residual austenite into martensite phase within the shell material and to relax the residual stress generated. The THT stage takes approximately 6 days (150 hrs) (see Figure 1.3).

Consequently for a bimetallic mill roll of 1200 mm diameter, the total thermal cycle shown in Figure 1.3 is composed by the PCC and the THT stages and has a total duration of 17 days (420 hrs).

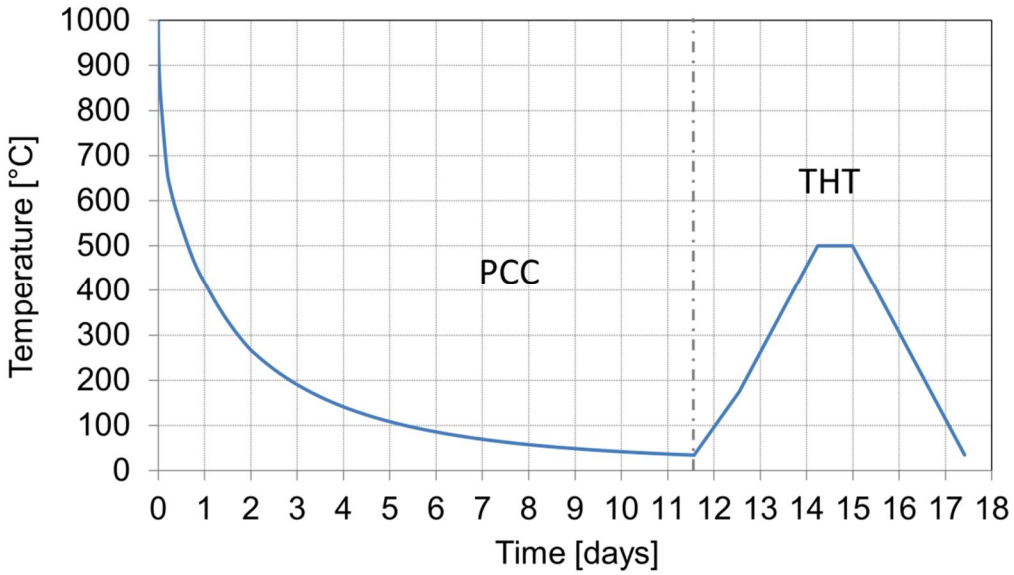

Figure 1.3. Surface temperature evolution during PCC and THT stages for a mill roll of 1200 mm/80 mm

1.2.3 Failure observations

For bimetallic rolls of 1200 mm diameter, a shell thickness of 80 mm is currently chosen. Smaller shell thicknesses were used in the past, generating fatigue failure during the work life of rolling mill rolls. Using an increased shell thickness, the stress peaks during work life of rolls, are applied within the shell and do nor reach the interface of both materials. However, even if fatigue resistance of rolls has been optimized, some failure cases can appear during the manufacturing process.

Two kinds of failure are observed by the MK industry:

- "Star" cracks are originated at the center of the roll and they propagate through the whole core material and until 2/3 of the shell material next to the interface. The 1/3 section close to the surface generally remains unbroken acting as a "crown" containing the roll. The schematization of broken rolls for these rupture cases is presented in Figure 1.4.

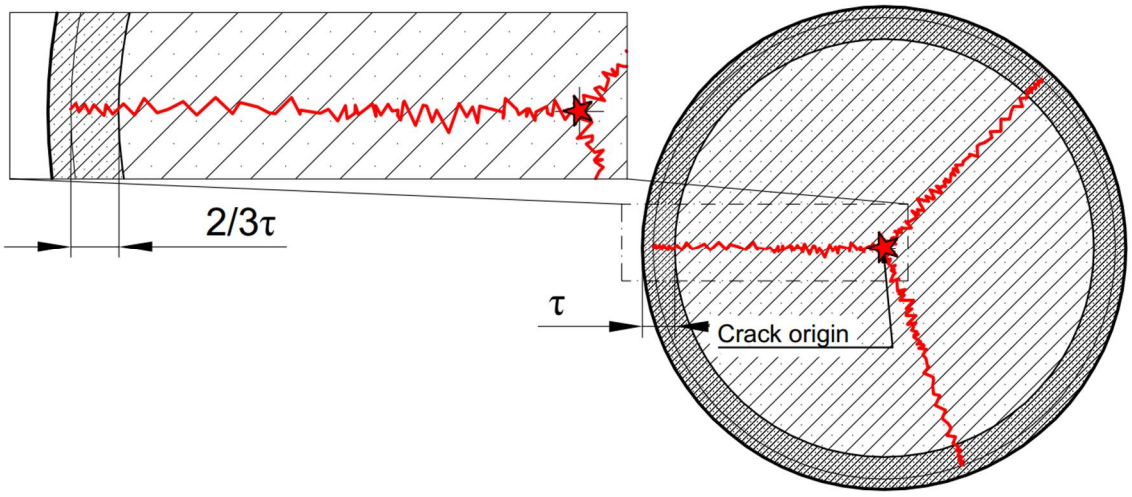

Figure 1.4. "Star" cracks

"Butterfly" cracks are originated within the shell material near the interface with core material. More precisely, in the internal 1/3 of the shell thickness. They propagate to the surface and can stay along a circumferential direction before breaking towards two directions, reaching the external surface. Observed cracks and the schematization of the broken roll for these cases are shown in Figure 1.5.

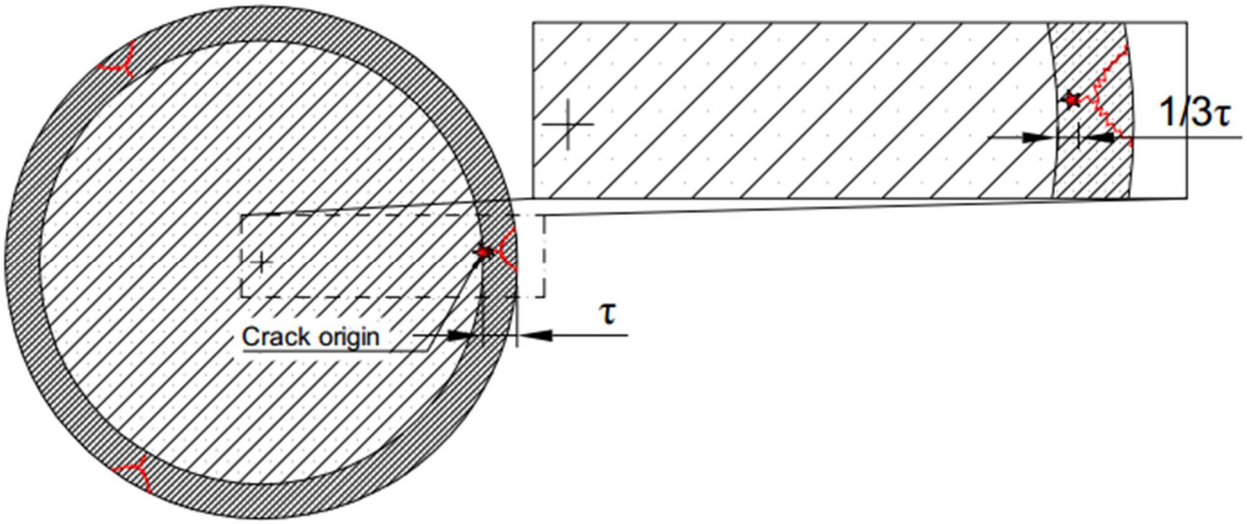

Figure 1.5. "Butterfly" cracks

Most part of failure cases are observed by the industry during tempering heat treatment stage. Both kinds of cracks are detected, however star cracks are the more frequent cases. In some cases, one could observe star cracks even after post casting cooling stage. If detected cracks did not reach the surface even during THT, a quick heat treatment is applied to break the roll and allow its recycling.

1.3 State of the art

This section presents a literature review about the modelling of rolling mill rolls and the existent phase transformations and damage prediction models. Numerous studies suggest numerical simulations for the analysis of coupled interactions and eventual cracks occurring in rolling mill rolls fabrication process [6, 7]. However, studies of modelling during cooling after casting or heat treatment and especially modelling of bimetallic rolls are quite limited. Furthermore, different methods exist for the phase transformation prediction. Phase Field Method [8, 9] and Fast Fourier Transform [10, 11] have been widely applied. However their application to the scale of work pieces is still limited. Regarding to damage analysis, different models have been proposed applied for fracture prediction and some works establish the importance of consider stress triaxiality and Lode angle dependence. A synthesis of these topics is provided hereafter.

1.3.1 Rolls modelling

As part of a previous project, Studer work [2] proposes a mathematical modelling of centrifugal casting based on bimetallic rolling mill rolls considering different materials from the ones studied here as core and shell materials, although they were similar. The numerical model combines both the fluid and the solidification aspects. The principle is to divide the time scale into sufficiently small intervals, for which the mass, momentum and energy conservation equations are solved simultaneously by two codes; one for the thermo-mechanical metallurgical aspects of the problem and the other ones for the flow dynamics aspects. As result, 2D flow mechanics model is established. However, the material parameters were lacking for further heat treatment simulations as well as experimental procedure for data acquiring. Numerous others authors have also modelled centrifugal casting process. For instance, Fu, Gao and Wu [12–14] investigate the effect during centrifugal casting of the manufacturing process parameters, microstructure heterogeneities and the nucleation-growth of microstructures respectively.

With the intention of improving the rolls lifetime, modeling of residual stresses at the surface during rolling mill process has been widely studied through a thermo-mechanical analysis. For example, wear and thermal fatigue simulations are proposed by Mercado in [15] to study the rolls fatigue failure at the rolls surface. Numerical results are compared with experimental measurements. In addition, the effect of the production parameters for the optimization of the rolls fatigue life have been studied by Domazet in [16] and by Corral in [17].

A few authors perform modelling of composed rolls during casting or heat treatment. Redkin [6] proposed an approach for rolls materials optimization by modeling centrifugal casting and heat treatment of composed rolls using a FE method that considered thermal and thermodynamic-kinetics analysis. In fact, CALPHAD (Calculation of Phase Diagrams) method is used for modelling of phase transformations and CFD (Computational Fluid Dynamics) model is used for incorporation of solidification and roll chemistry. Carbides precipitation phenomena are also predicted. Heat treatment is modelled for controlling residual stresses due to volumetric distortions and phase transformations. As result, an improvement in the roll development was achieved through the understanding of the roll behavior under mill conditions. Furthermore, Ziehenberger modelled bimetallic rolls in [7]. It studies the distribution of internal stresses to

determine the relationship between the residual compression stress in the surface and the consequent tensile stress in the core, with respect to the shell thickness and carbon content.

Even if several works focused on modelling of rolling mill rolls have been performed, the application of FE models is mostly directed to casting or rolling conditions models. The limited modelling of bimetallic rolling mill rolls is restricted to stress field prediction without damage analysis.

1.3.2 Phase transformations models

1.3.2.1 Phase field method

Phase Field Method (PFM) is a computational technique applied to the microstructure evolution of materials based on the diffuse interface description. It was originally developed by Van der Walls in [8] and by Cahn and Hilliard in [9]. PFM as an interesting alternative extensively used in several works. Even if it is mostly applied for martensitic transformations [10, 18–20], PFM is also applied for austenite decomposition to ferrite phase [21–23] and to pearlite phase [24, 25].

PFM is today widely developed and some authors couple it with strain gradient viscoplasticity [26] and interface stresses [20]. In addition, it is possible to find works where PFM is coupled with mechanical behavior of phase transformations [27–29]. Multi-Phase Field Method (MFPM) was developed by Steinbach in [30] as an extension of PFM for phase transformation involving more than two materials. MPFM is usually applied for steels modelling [23, 26].

New developments in PFM [10] model the phase transformation at the scale of the grains and provide an interesting input for the local investigation of a few grains studying the effect of carbon diffusion or TRansformation Induced Plasticity (TRIP). Determination of transformation induced plasticity, generated by mechanical metallurgical interaction, can rely on crystal plasticity and Fast Fourier Transform (FFT). Otsuka [11] developed a micromechanical model of crystal plasticity with phase transformation using FFT for periodic media. Lebensohn et al [32] presented a formulation based on FFT for the prediction of micromechanical fields in polycrystals deforming in the elasto-viscoplastic regime.

However, despite the wide applicability of PFM, MPFM and FFT methods, these type of models remains out of range for simulations that are related to cooling pieces of typical length within the meter range such as bimetallic rolling mill rolls of 8 m high and 1.2 m diameter. With the help of parallel computations, some teams apply multi scale simulations that link macroscopic behavior and crystal plasticity models [33, 34]. However, such simulations are not adapted for rolling mill rolls.

1.3.2.2 Classical method

The classical method for modeling thermo-mechanical-metallurgical interactions was developed in the 1980's. Its principal advantage is that it allows performing computations of phase transformations along realistic industrial large work pieces. Denis [35] provides an in depth study on the mechanical stresses during phase transformations based on TTT diagrams. FE model for calculating the internal stresses that are related to the stress state and phase evolution has been developed. Later, Assaker [36] studied the effect of thermo-mechanical metallurgical interactions during heat treatments based on CCT diagrams. A method for building a model and a numerical tool for the computation of stresses and strains was settled.

In 1992 Habraken and Bourdouxhe [37] describe a coupled thermo-mechanical metallurgical FE model, presenting an application on sheet piles while studying curvature changes during cooling. The coupled thermo-mechanical-metallurgical model is implemented into the LAGAMINE finite element code, which was developed at the University of Liège more than 20 years ago for rolling problems and other forming processes. LAGAMINE code has been applied and validated in several studies. For example, Lequesne [38], Pascon [39] and Schwartz [40] used the model for cracks prediction in continuous casting process. Moreover, Casotto [41] presented an application of the model for predicting geometrical distortions of rings after ring rolling operations. Denis [42] studied the evolution of internal stresses during the cooling of a steel cylinder. Geijselaers modeled laser hardening treatment through numerical simulations of solid state phase transformations through the classical method, and in [43] included the interactions between temperatures, stresses and phase transformations in constitutive models that used finite elements. Moreover, similar models have been used for a long time in different applications such as cryogenic treatment, steel carburization, hot-press forming and pipe weld [44–47]. In this thesis,

LAGAMINE code will be considered for modelling of cooling and heat treatment of bimetallic rolling mill rolls. Therefore, further description if this model will be provided in Chapter 2.

1.3.3 Damage model

Macroscopic damage model studied in this thesis is devoted to the loss of ductility of materials. The damage processes can be incorporated by continuously describing the local damage development on the stress-strain field. Different numerical models have been suggested to model fracture initiation and propagation and damage at variable temperatures has been widely studied [48–60].

Three groups can be distinguished: fracture criteria, micromechanical models and continuum damage models (CDM). In the first group, damage is defined by an external variable and does not modify plastic state variables. For instance, in the model of Johnson and Cook [48] the damage variable does not affect plastic properties of the materials and failure happens when damage reaches a critical value. In the second group macroscopic response is affected by the presence of voids which nucleate, grow and coalesce. Gurson established in [49] a micromechanically based model investigating approximate yield criteria and flow rules for ductile materials showing the role of hydrostatic stress in plastic yield and void growth. In the third group, defects are described in a phenomenological way. Rousselier and Lemaitre [50, 51] developed a model based on Continuum Damage Mechanics (CDM). Rousselier proposed stress-deformation constitutive relations in which fracture results from competition between hardening and damage while Lamaitre gave set of constitutive equations for elasticity, plasticity and visco-plasticity coupled with brittle, fatigue, ductile or creep damage.

Our focus will be on the first group of models. For instance, Cerri [52] propose the prediction of hot break through different rupture criteria identification using experimental and numerical methods. It is specifically devoted to casting process. At room temperature, a set of six rupture criteria to predict fracture have been studied by Clift [53] and Zhu [54]. This set is composed by Ghosh [55], McClintock [56], Freudenthal [57], Cockroft-Latham [58], Brozzo et al [59] and Oyane [60] criteria. In [53] Clift predicts fracture initiation in a range of simple metalforming processes using FE method according to experimental observations. In [54] Zhu presents a

coupled elastoplastic damage model to characterize damage and crack growth for ductile materials, he compares it to the previous set of six criteria.

The stress triaxiality is an important factor controlling initiation of ductile fracture. The relation of ductile fracture with triaxiality has been studied in several works for rupture prediction. For instance, Bao and Wierzbicki [61] have observed that the mechanism of fracture is different depending on the amount of triaxiality. They present a fracture locus depending on Lode angle and stress triaxiality. Their numerical model was identified and validated by experimental methods. Their well-known relation has been later used in different works [62, 63]. The fracture strain is defined as a surface in the third dimension over the plane of stress triaxiality and Lode angle parameter (the third deviatoric stress invariant). A new trend is to address the effect of the Lode angle dependence on ductile metal failure. It is considered by several authors for damage models [64–66] in the frame of continuum mechanics.

In this thesis, the set of six rupture criteria used by Clift and Zhu is extended to cumulative damage for non-isothermal cases. It has been implemented in LAGAMINE finite element code, and it has been applied for prediction of damage in bimetallic rolling mill rolls modelling.

1.4 Objectives and methods

The objective of the present thesis is to use a thermo-mechanical metallurgical model to perform numerical simulations of the post casting cooling and the subsequent tempering heat treatment of bimetallic rolling mill rolls in order to understand failure event observed by the manufacturing industry Marichal Ketin (MK).

Since the thermal history is the driving force that induce the geometric variations, stress loading and microstructure modifications of the rolls during the PCC and THT stages, a coupled model that consider all of the interactions is required. Numerical simulations of PCC and THT stages using FE LAGAMINE code are proposed. FE method is indeed an effective tool for addressing heterogeneous problems and can predict the residual stresses at the surface of the roll and also internally. The metallurgical model considers an additivity principle of phase transformation phenomena described by TTT diagrams. It was validated by the prediction of the transformation

history that is present in CCT diagrams [43, 67]. The Johnson-Mehl-Avrami and Koistinen-Marburger equations are used to predict the amount of each phase and the transformation kinetic. The TRansformation Induced Plasticity (TRIP) is among the difficult challenges that a thermo-mechanical metallurgical model must handle. However, no advanced methods are used but phenomenological relations. Inverse method is applied for the determination of the transformation plasticity coefficients. The model is validated through experimental results.

Accurate mechanical, thermal and also metallurgical parameters are required as input data for the numerical simulations. Mechanical parameters such as Young modulus, yield limit and hardening parameters are obtained by experimental compression tests performed at different temperatures. Each phase behavior has to be characterized. Fracture stresses and strains for each phase in SGI and HCS materials at different temperatures are determined by tensile tests. Thermophysical parameters; density, specific heat capacity and thermal diffusivity are measured using experimental methods such as dilatometry, Differential Scanning Calorimetry (DSC), and laser flash method respectively. Cryogenic cooling is used for determine start and finish temperature of martensitic transformation. Finally, inverse method is used for numerical determination of transformation plasticity coefficients, transformation strain and TTT diagrams.

Different rupture criteria are implemented and analyzed to predict the failure of the rolls. Potential damage is analyzed by performing a comparison of the predicted axial stress with rupture stresses. To consider stress triaxiality effect and tensorial stress effect, predictions of Ghosh, McClintock, Freudenthal, Cockroft-Latham, Brozzo and Oyane criteria are also analyzed. No extensive damage review is proposed as finally, most of the energy was devoted to parameters identification and the validation of the model prediction.

Several simulations are performed in order to analyze the sensitivity of the predictions to the input data allowing estimating the effect of different core and shell materials and of the material parameter accuracy. The effect of the geometry is also studied by modifying diameter of mill rolls and shell thickness. The aim of performed analysis is to better understand the process and identify the key factor yielding damage. This knowledge helps to find the way to avoid them and justifies the decrease of cracks of the current production.

1.5 Thesis contents

The introduction chapter presents the motivation of this thesis including a description of the industrial process. In addition, a summary of the state of the art including rolls modelling, phase transformations and damage models is provided.

In chapter 2, LAGAMINE code is described by presenting the most important equations and theory considered for modelling of bimetallic rolling mill rolls. Coupled thermo-mechanical metallurgical model together with the implemented damage model are described. This chapter also includes a summary of required input data parameters and a description of materials involved in fabrication of modelled bimetallic rolling mill rolls.

Chapter 3 widely describes the experimental campaign performed for thermophysical and mechanical parameters including further analyses performed to understand compression test results. Inverse methods applied for identification of unknown parameters are also described.

Finite element simulation of a reference rolling mill roll is presented in chapter 4. The thermal and mechanical fields computed are presented together with the damage approach. From obtained results, some rupture scenarios are discussed.

Chapter 5 presents results obtained for different simulations performed in order to analyze the sensitivity of predictions to modifications of the input data such as the core material TTT diagram, the martensite start temperature and the shift of martensitic transformation coefficients. Sensitivity to geometry parameters such as roll diameter and shell thickness is also analyzed.

Finally chapter 6 presents overall conclusions together with perspectives for future work established from performed research.

Chapter 2. Theoretical frame

Finite element modelling of rolling mill rolls can be performed using the coupled thermo-mechanical metallurgical code LAGAMINE. This code has been developed at the University of Liège since more than 20 years and it has been applied in several works [41, 42]. The code considers the classical method for modeling thermo-mechanical-metallurgical interactions. A complete description of the coupled model can be found in [68]. In this chapter, important theory and equations for rolling mill rolls modelling are presented as well as the implemented damage model. In addition, different required parameters for the input data are summarized. Finally, a brief description of modelled materials (SGI and HCS) is given.

2.1 Generalities

2.1.1 Coupled interactions

The implemented thermo-mechanical-metallurgical model into FE code LAGAMINE, takes into account all the interactions between the different fields reminded in Figure 2.1.

1. The thermal gradient is the driving force inducing phase transformations. TTT (Time, Transformation, Temperature) and CCT (Continuous, Cooling, Transformation) diagrams are used for the description of this phenomena.
2. Phase transformations taking place during cooling, release heat in a non-negligible amount that will affect the thermal history.

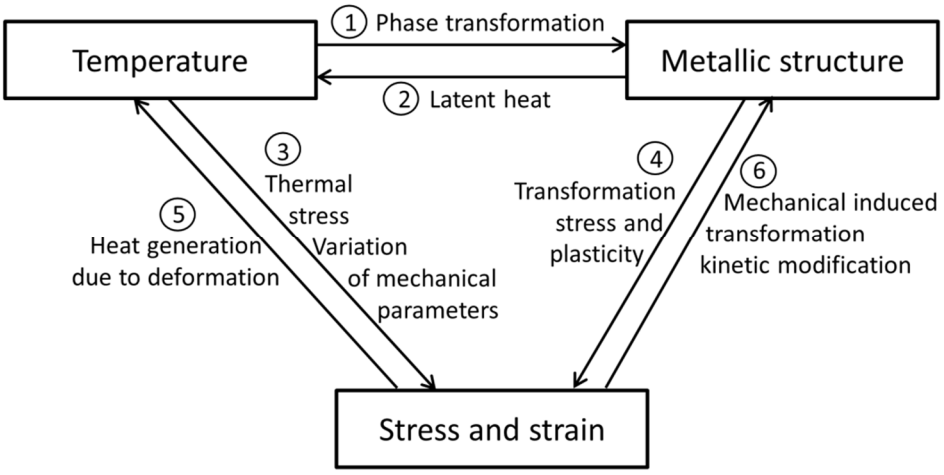

Figure 2.1. Interactions taken into account within the FE model

3. Thermal stresses and strains are generated from dilatation due to temperature history. In addition, mechanical parameters are significantly modified by the temperature.
4. Phase transformations induce stresses and strain since the density of each phase is different. Besides, when a phase transformation is carried out in a stressed material, "transformation induced plasticity" (TRIP) appears, even under low stress level. Two mechanisms are considered for explaining TRIP:
   - Greenwood–Johnson (1965) mechanism corresponds to the micromechanical plastic strain as consequence of the volume expansion coming from density differences.
   - Magee (1966) mechanism corresponds to the formation of selected martensitic variants resulting from the applied stress.
5. The temperature field can be affected by the dissipated energy when large plastic strain is generated. This effect takes importance in some forming process. However, for this thesis, this coupling will be neglected as in [36, 69, 70]. Indeed small plastic strains happen at low temperature so the heat generated is very low.
6. Two effects can be produced when a metallurgical phase is transformed under stress. The morphology of the transformed phase can be modified and phase transformation start can be delayed or accelerated.

2.1.2 Metallurgical phases

Steel is an iron (Fe) alloy with others elements principally carbon (C). Carbon can be present as graphite or as carbide Fe_3C. Different steel grades are widely used in different industrial and construction applications due to their wide range of properties generated by the presence of alloying elements in different amount. Metallurgical phases of steels are defined by the well-known Iron-Carbon equilibrium diagram presented in Figure 2.2.

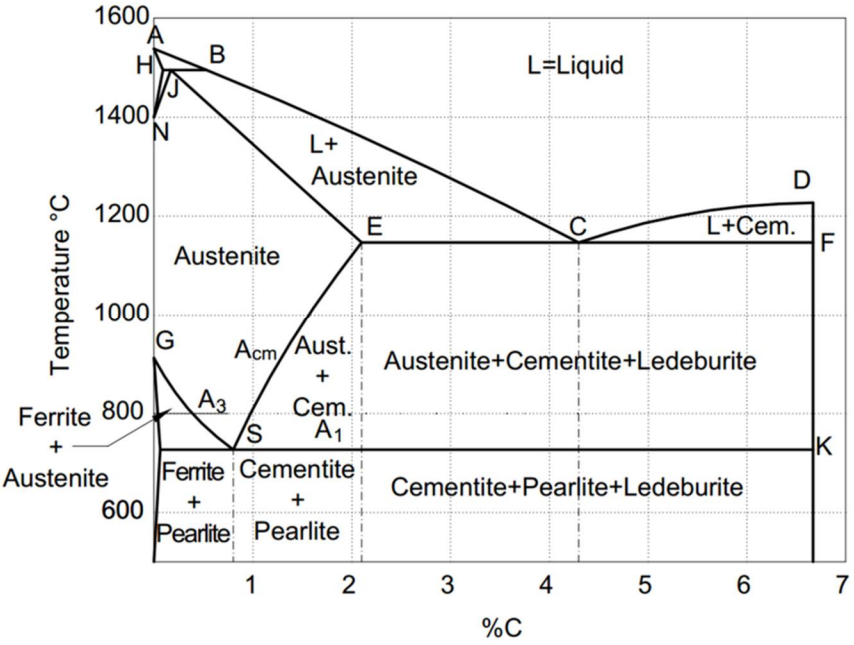

Figure 2.2. Equilibrium Iron – Carbon diagram

A brief description of different metallurgical phases that may be transformed within materials composing rolling mill rolls (SGI and HCS) is given below.

- Austenite (Au) is a solid solution of Fe-γ. Its structure is face centred cubic (FCC). It can contain up to 2.1% of C at 1142°C.
- Ferrite (Fe) is a solid solution of Fe-α. Its structure is body centred cubic (BCC). It can contain up to 0.02% of C at 723°C.
- Cementite (Fe_3C) is an iron carbide composed by 93.3%Fe - 6.67%C.
- Pearlite (Pe) is the eutectoid phase that appears at the point 0.76%C at 723°C. It is a lamellar structure composed of alternating layers of ferrite and cementite phases.

In practice, austenite decomposition is developed in conditions far from thermodynamic equilibrium. The TTT (Time, Temperature, Transformation) diagram (see Figure 2.3) describes isothermal phase transformations according to time and temperature variations. TTT curves usually gives the starting curve of each phase as well as curves corresponding to 10% and 90% of the transformed phase.

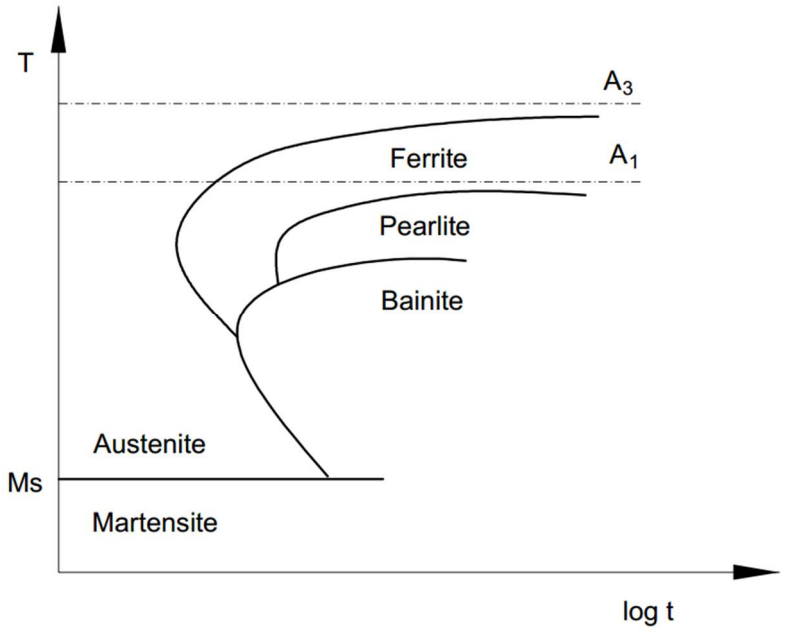

Figure 2.3. Schematic TTT diagram

Furthermore, in the industrial real conditions, phase transformations do not occur at a constant temperature. The CCT (Continuous Cooling Transformation) diagram (see Figure 2.4) describes phase transformations that occur during continuous cooling. The phase transformed amount depends on the cooling rate $\dot{T}$.

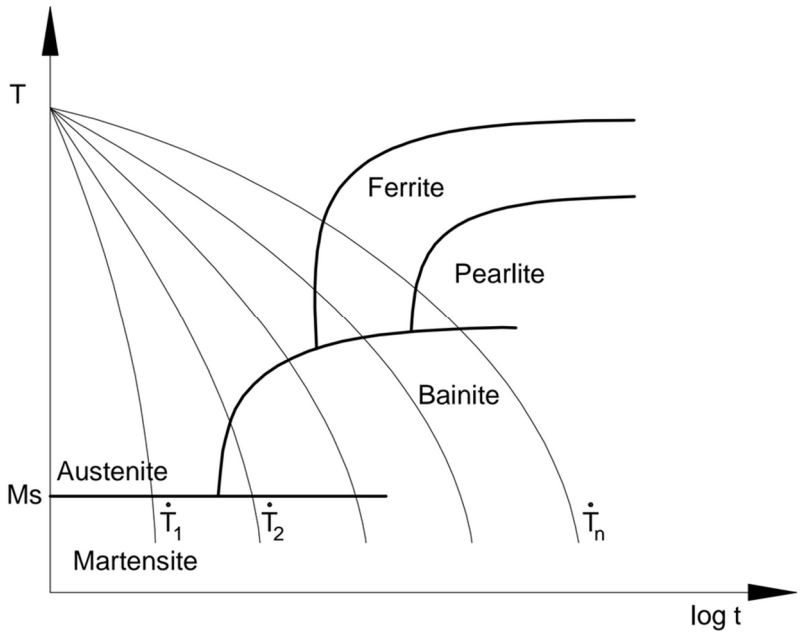

Figure 2.4. Schematic CCT diagram

Depending on the cooling rate, two additional phases can appear from austenite transformation:

- Bainite (Ba) is a mixed phase composed by ferrite and cementite. It is transformed when austenite is cooled relatively fast. Depending on temperature, upper or lower bainite might be formed.
- Martensite (Ma) is formed by a very rapid cooling (quench) of austenite, because carbon atoms do not have the time to form cementite. It is a solid solution of carbon inserted in a BCC structure similar to ferrite phase structure.

When a metallurgical phase is formed by migration of carbon atoms, it is referred to a diffusional transformation. This is the case of Ferrite, Cementite, Pearlite and Bainite. In contrast, martensite phase is very quickly formed without incubation time. No atom migration occurs; it is a sort of rapid rearrangement of atomic positions like twinning phenomena.

2.1.3 Mixture law

The existence of different phases in steels has an evident influence on different material properties. Any material property and its associated material parameter x_{eq} depends on the temperature and on the volume quantity of each phase. Therefore, it relies on a mixture law [54] based on the value of property x_k within the different phase volume fraction y_k at temperature T.

$$x_{eq}(T, y_k) = \sum_{k=1}^{5} y_k \, x_k(T) \qquad \textbf{2.1}$$

where ($k = 1$ austenite; $k = 2$ ferrite; $k = 3$ pearlite; $k = 4$ cementite $k = 5$ bainite; $k = 6$ martensite). This mixture law is a very basic assumption that can generate some inaccuracy. However most of the FE codes use it for the computation of mechanical and thermo-physical properties, due to its simplicity. More details on the drawbacks of mixture law can be found in [71].

2.2Thermo-metallurgical model

2.2.1 Thermal model

LAGAMINE code deals with non lineal thermal analysis. Bi and tri –dimensional solid finite elements as well as surface elements can be used for modelling thermal exchange by conduction, convection and radiation phenomena.

Thermal flow $\underline{q}$ is computed inside the roll and at the roll surface by eqs. 2.2 and 2.3 respectively. The model includes both internal conduction phenomenon and heat extraction from the roll to the environment being characterized by thermal conductivity k and heat transfer coefficient h_{tc}.

$$\underline{q} = -k\nabla T \qquad \textbf{2.2}$$

$$\underline{q} = h_{tc}(T_s - T_\infty)\underline{n} \quad \textbf{2.3}$$

where T_s and T_∞ are the surface and environment temperatures respectively. The differential equation describing heat balance is the classical Fourier law:

$$\rho c\dot{T} + \nabla\underline{\dot{q}} = \dot{Q} \quad \textbf{2.4}$$

where the dot symbol means rate value, ρ is the density, c the specific heat and Q the heat generation/extraction, in this case represented by enthalpy of phase transformation and heat exchange (at the surface of the roll). Material properties (k, ρ, c) are temperature and phase dependent, mixture law is applied (see eq. 2.1).

Heat transfer coefficients include both convection and radiation terms:

$$h_{tc} = h_{conv} + \varepsilon_r\sigma_{SB}(T_s + T_\infty)({T_s}^2 + T_\infty) \quad \textbf{2.5}$$

where h_{conv} is the convection term, ε the relative emissivity and σ_{SB} the Stefan-Boltzmann constant.

2.2.2 Diffusive transformations

Transformations happening by diffusion (ferrite, cementite, pearlite, bainite) are characterized by two phenomena: the germination of particles and their growth. The implemented model considers both steps separately. It is based on three concepts: the “additivity principle”, the computation of the germination time by Scheil’s sum and the computation of the growth according to Pumphey and Jones method.

In order to model phase transformation happening during continuous cooling, the “additivity principle” is used by extending the isothermal transformation model considering that the microstructure obtained at the end of a continuous cooling is the result of a succession of elementary isothermal transformations; each one is independent of the preceding thermal history.

When the Scheil’s sum reaches the unity, it is assumed that germination is achieved. The Scheil’s sum is defined by:

$$\int_0^{t_j} \frac{dt}{\prod(T)} \cong \sum_{t=1}^{j} \frac{\Delta t_i}{\prod(T_i)} = 1 \qquad \textbf{2.6}$$

with $\prod(T)$= the germination time for an isothermal transformation at temperature T, t_j= the germination time for continuous cooling and Δt_i=the length of successive isothermal steps T_i modelling the cooling curve.

For modelling of growth during an isothermal transformation Johnson-Mehl-Avrami's model [72] is considered:

$$y_k = 1 - \exp(-b_k t^{n_k}) \qquad \textbf{2.7}$$

where y_k is the fraction of the new phase k ($k = 1$ austenite; $k = 2$ ferrite; $k = 3$ pearlite; $k = 4$ cementite $k = 5$ bainite; $k = 6$ martensite) and t the time. b_k and n_k are temperature dependent material parameters describing the phase transformation kinematics.

Since previous formula assumes that the austenite is completely transformed into the phase k, the partial transformation must be taken into account by the fictitious fraction of phase k, $y_{k\,fic}$:

$$y_{k\,fic} = 1 - \exp(-b_k t^{n_k}) = \frac{y_k}{y_A y_{k\,max}} \qquad \textbf{2.8}$$

$y_{k\,max}$ is the final maximal fraction of phase k considering material chemistry and y_A is the fraction of austenite at the beginning of transformation k.

Using the additivity principle, it is possible to extend this model to continuous cooling transformation according to Pumphey and Jones [73]. The cooling curve $T(t)$ is subdivided into isothermal steps of size Δt_i. A schematic representation of the fictitious principle is shown in Figure 2.5.

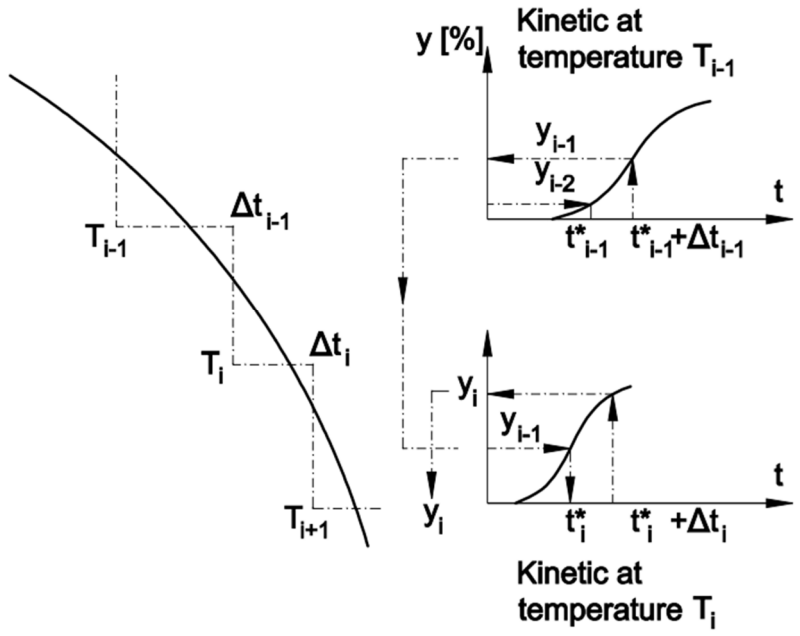

Figure 2.5. Fictitious time principle

At the end of the step at temperature T_{i-1}, the fictitious fraction $y_{i-1\,fic}$ is known by eq. 2.8. Therefore, the fictitious time t^*_{i-1} that would have given such a fraction phase for an isothermal transformation at temperature, can be computed using:

$$t^*_{i-1} = \left[\frac{-\ln(1 - y_{i-1\,fic})}{b_i}\right]^{1/n_i} \qquad \textbf{2.9}$$

where b_i, n_i are growth parameters for the isothermal transformation at temperature T_i.

At the end of the step of temperature T_i:

$$y_i = y_A y_{max}[1 - \exp(-b_i(t^*_{i-1} + \Delta t_i)^{n_i}] \qquad \textbf{2.10}$$

Finally, this formula precisely computes the microstructural state at the end of the step i.

2.2.3 Non-diffusive transformation

For martensite transformation, the Koistinen Marburger's model [74] is applied. The volume fraction y_M is computed from the current temperature gap with the transformation start temperature, M_s.

$$y_M = y_A\left[1 - exp\left(-A_M(M_s - T)\right)\right] \quad \textbf{2.11}$$

where A_M is the Koistinen-Marburger's coefficient, y_A the austenite volume fraction at transformation start M_s and T is the current temperature. Note that A_M can be easily identified if the temperatures at the start and at the end of the transformation are known. The M_s temperature depends on austenite carbon content and it evolves when the chemical carbon content of matrix austenite phase is modified.

2.3 Thermo-mechanical metallurgical model

2.3.1 Modifications of the transformation kinetic due to mechanical interactions

Diffusional transformations might be accelerated by strains. However, at the same time, transformations might be delayed due to the application of a hydrostatic pressure. In reality, only high pressures (>2500 MPa) have an effect on diffusional transformations [68]. In the implemented model, the shift of TTT curves depends only on the equivalent stress $\overline{\sigma}$:

$$D = g(\overline{\sigma}) \quad \textbf{2.12}$$

This modification on TTT curves have an effect on the modelling of anisothermal transformations.

Incubation times of isothermal transformation $\prod(T)$ are modified:

$$\Pi_\sigma(T) = (1 - D)\Pi(T) \quad \textbf{2.13}$$

By consequence, the Scheil's sum becomes:

$$\int_0^{t_j} \frac{dt}{\Pi_\sigma(T)} = 1 \qquad \textbf{2.14}$$

And the germination time is affected by the stress state.

The coefficient b of Johnson-Mehl-Avrami law is modified too and it accelerates the transformation:

$$b_\sigma = \frac{b}{(1-D)^n} \qquad \textbf{2.15}$$

For martensitic transformation, start temperature M_s is modified by the hydrostatic component σ_m of the stress tensor and also by the deviatoric part represented by the equivalent stress $\bar{\sigma}$. The shift of the martensite start temperature is computed by the model according to:

$$\Delta M_s = A\sigma_m + B\bar{\sigma} \qquad \textbf{2.16}$$

where A and B are constants related to the modelled steel.

2.3.2 Mechanical model with thermal and metallurgical interactions

An elasto-plastic behavior is assumed and the total strain rate $\dot{\varepsilon}$, is divided into five parts:

$$\underline{\dot{\varepsilon}} = \underline{\dot{\varepsilon}}^e + \underline{\dot{\varepsilon}}^p + \underline{\dot{\varepsilon}}^{th} + \underline{\dot{\varepsilon}}^{tr} + \underline{\dot{\varepsilon}}^{pt} \qquad \textbf{2.17}$$

The elastic strain rate $\underline{\dot{\varepsilon}}^e$ is computed by the Hooke's law depending on the Young's modulus E and the Poisson's ratio ν.

The computation of plastic strain rate $\underline{\dot{\varepsilon}}^p$ is based on the equivalent von Mises' yield criterion assuming isotropic hardening. The initial yield stress σ_y and the description of the hardening part are described by experimental points of the corresponding $\overline{\sigma} - \overline{\varepsilon}$ curve. Hardening curve is defined by a certain number of segments associated to different strain levels as it is presented in Figure 2.6.

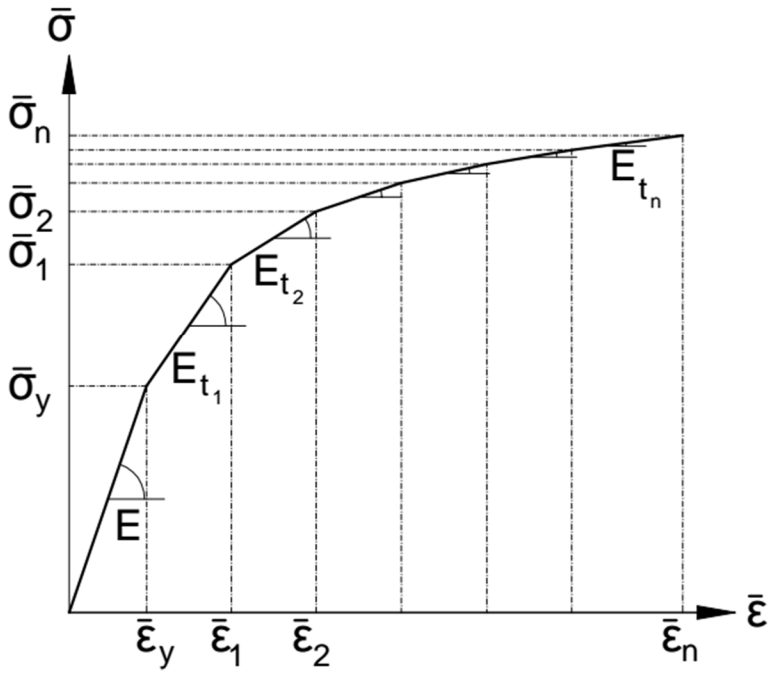

Figure 2.6. Mechanical behavior law

The parameters E, ν, σ_y and the hardening curve given by the set of E_{ti} are computed by the FE code using the mixture law (see eq. 2.1) since they depend on the temperature T and on the phase content.

The thermal strain rate $\underline{\dot{\varepsilon}}^{th}$ is characterized by the thermal expansion coefficient of each constituent and it is calculated according to:

$$\underline{\dot{\varepsilon}}^{th} = \frac{d}{dt}\left(\sum_{k=1}^{5} y_k \int_0^T \alpha_k(T)d\tau\right)\underline{I} \qquad \textbf{2.18}$$

where α_k is the thermal expansion coefficient and y_k the volume fraction of the constituent k, when $\underline{I}$ is the identity tensor.

The transformation strain rate $\underline{\dot{\varepsilon}}_k^{tr}$ (represents the expansion associated with the transformation from austenite to any constituent k) is calculated by:

$$\underline{\dot{\varepsilon}}^{tr} = \left(\sum_{k=2}^{5} \dot{y}_k \, \varepsilon_{k,0°C}^{tr}\right)\underline{I} \qquad \textbf{2.19}$$

The expansion coefficient $\varepsilon_{k,0°C}^{tr}$ is taken with respect to austenite at 0°C.

Transformation induced plasticity (TRIP) ε^{pt} is generated due to metallurgical transformations associated to an external loading inducing strain incompatibilities between phase interfaces. Numerous models are proposed in Denis' work [42, 75]. In the LAGAMINE code, transformation plasticity strain rates are computed using Giusty formula for ferrite, pearlite and martensite phase. They are given in eqs. 2.20, 2.21 and 2.22 respectively.

$$\underline{\dot{\varepsilon}}_{Fe}^{pt} = K_2(\bar{\sigma} - \sigma_y)\dot{y}_{Fe} \quad \textbf{2.20}$$

$$\underline{\dot{\varepsilon}}_{Pe}^{pt} = K_3(\bar{\sigma} - \sigma_y)\dot{y}_{Pe} \quad \textbf{2.21}$$

$$\underline{\dot{\varepsilon}}_{Ma}^{pt} = K_6\,\bar{\sigma}(2 - \dot{y}_M)\dot{y}_{Ma} \quad \textbf{2.22}$$

where $\bar{\sigma}$ is the equivalent stress, σ_y the initial yield limit and y the corresponding phase fraction already formed. K_2, K_3 and K_6 are the material transformation plasticity coefficients corresponding to ferrite, pearlite and martensite phase respectively.

2.3.3 Coupled thermo-mechanical metallurgical finite element

The finite element used for modelling of rolling mill roll is called CPL2D. It is an “8 node” element which has 4 integration points and it is appropriate for thermo-mechanical analysis on large deformations with or without metallurgical effects in plane or axisymmetric state. The interpolation functions are identical for the temperature T and displacement fields u and v displacements in X and Y directions.

$$T = \varphi_i T_i \;;\quad u = \varphi_i u_i \;;\quad v = \varphi_i v_i \quad \textbf{2.23}$$

where T_i is the nodal temperature; u_i, v_i nodal displacements and φ_i is the interpolation function from node i.

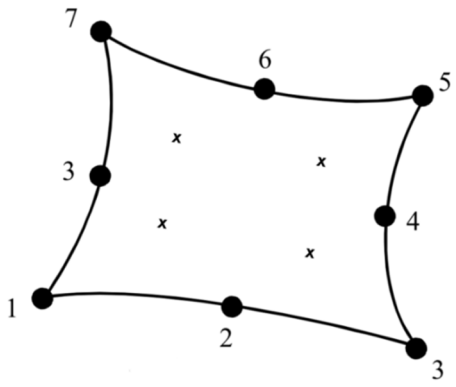

Figure 2.7. CPL2D finite element

Due to their cylindrical shape, rolling mill rolls might be modelled by axisymmetric analysis where X is the radial direction and Y the axial direction.

2.4 Damage model

Numerous criteria at room temperature i.e. Freudhental, Cockroft Latham, Oyane, Won & Oh, Ghosh and McClintock are described by Zhu in [54]. However their extension to high temperature is still limited. Cumulative damage for each criterion is implemented in the LAGAMINE code.

At fracture, a temperature dependent threshold value of a function of instantaneous principal stress values is defined by Ghosh criterion [55]:

$$\frac{\sigma_1 + \sigma_2 + \sigma_3}{3} \times \frac{\sigma_1 - \sigma_3}{2} = C_{Gh,T} \qquad \textbf{2.24}$$

The cumulative function of McClintock [56] based on the analysis of a cylindrical hole in an infinite matrix subjected to axial stress and to transversal stresses σ_a and σ_b also reaches a threshold value at fracture which is temperature dependent:

$$\int_0^{\varepsilon_f} \left[\frac{\sqrt{3}}{2(1-n)} sinh\left(\frac{\sqrt{3(1-n)}}{2} \times \frac{(\sigma_a + \sigma_b)}{\bar{\sigma}} \right) + \frac{3(\sigma_a - \sigma_b)}{4\bar{\sigma}} \right] d\bar{\varepsilon} = C_{Mc,T} \qquad \textbf{2.25}$$

Freudenthal [57] proposed that the absorbed energy per unit volume is the critical parameter at fracture.

$$\int_0^{\varepsilon_f} \overline{\sigma} d\bar{\varepsilon} = C_{Fr,T} \quad \textbf{2.26}$$

Cockroft and Latham [58] proposed that it is the principal tensile stress which is important in fracture initiation:

$$\int_0^{\varepsilon_f} \sigma_1 d\bar{\varepsilon} = C_{C-L,T} \quad \textbf{2.27}$$

Brozzo et al [59] proposed an empirical modification of Cockroft and Latham's model to consider the effect of hydrostatic stress explicitly:

$$\int_0^{\varepsilon_f} \frac{2\sigma_1}{3(\sigma_1 - \sigma_m)} d\bar{\varepsilon} = C_{Br,T} \quad \textbf{2.28}$$

Oyane et al [60] considered a void growth model:

$$\int_0^{\varepsilon_f} \left(A + \frac{\sigma_m}{\overline{\sigma}}\right) d\bar{\varepsilon} = C_{Oy,T} \quad \textbf{2.29}$$

For every criterion, the code computes the cumulative damage D assuming a simple linear additive damage rule for variable temperature using eq. 2.30.

$$D = \sum_{i=1}^{n} \frac{C_{i+1} - C_i}{C_{Max,T_i}} \quad \textbf{2.30}$$

where C_i and C_{i-1} are the current value of criterion at the step i and $i-1$ respectively. C_{Max,T_i} is the threshold value of criterion at T_i and can be obtained by applying eqs. 2.24- 2.29 to experimental tensile test.

2.5 Input data

For modelling of a rolling mill roll using LAGAMINE FE code, mechanical, thermal, metallurgical and coupled parameters are required for both core and shell materials. Table 2.1 summarizes the parameters which identification is presented in Chapter 3.

Table 2.1. Parameters required by the model as input data

Mechanical data	Thermal data	Metallurgical data	Coupled parameters
• Young Modulus: $E_k(T)$ • Yield stress: $\sigma_{y\,k}(T)$ • Plastic Modulus: $E_{t\,k}(T)$ • Poisson ratio: $\nu_k(T)$ • Hardness: $H_k(T)$	• Coefficient of thermal expansion: $\alpha_k(T)$ • Thermal capacity: $C_{p\,k}(T)$ • Thermal conductivity: $\lambda_k(T)$ • Density: $\rho_k(T)$ • Latent heat: $L_k(T)$	• TTT diagram • Martensite start T°: M_s • Martensite finish T°: M_f	• Transformation strain: ε_k^{tr} • Transformation plasticity coefficient: K_k • Shift of martensitic transformation coefficients: A, B

2.6 Materials

Spheroidal Graphite Iron (SGI) and High Chromium Steel (HCS) materials are used for the core and shell materials respectively in the fabrication of rolling mill rolls by MK industry. Note that the metallurgical properties of both materials are deeply investigated in [5], the parallel PhD thesis of J. Tchoufang Tchuindjang (MMS team). This PhD thesis is focused on the microstructure properties of rolling mill rolls that this senior scientist is focused on for more than 15 years. Only a brief description of both materials is given in this section.

2.6.1 Spheroidal Graphite Iron (SGI)

SGI material is similar to the EN-GJS-400 grade and it is usually considered for core material of rolling mill rolls since it is widely known by its high ductility. In addition, it has a high impact

and fatigue resistance provided by the spheroidal graphite inclusions. The chemical composition of the studied SGI grade is given in Table 2.2.

Table 2.2. Chemical compositions of SGI material in terms of wt.%

	C	Si	Mn	Ni	Cr	Mo	P	S	Fe
Min	3.3	1.5	0.2	0.1					Bal
Max	3.8	2.0	0.4	0.6	0.2	0.05	0.1	0.02	

Figure 2.8(a) shows the microstructure, obtained by Optical micrograph (OM), of SGI grade in as cast conditions, it can be observed that the matrix of the material is a mixture of pearlite and ferrite phases with spheroidal graphite distributed throughout the matrix. A closer view in Figure 2.8(b) allows the observation of the mostly pearlitic matrix with the characteristic layered structure and the graphite nodules surrounded by ferritic structure. The phase proportion was calculated using **Image J** tool obtaining an estimation of 75% Pe, 17% Fe with and 8% of spheroidal graphite.

For modeling effects, since the FE code is able to model only basic metallurgical phases, the graphite nodules are not considered and a phase content of 75% Pe and 25% Fe is predicted by the FE code. However, graphite influence is intrinsically included in materials properties used by the code for the modeling of SGI material.

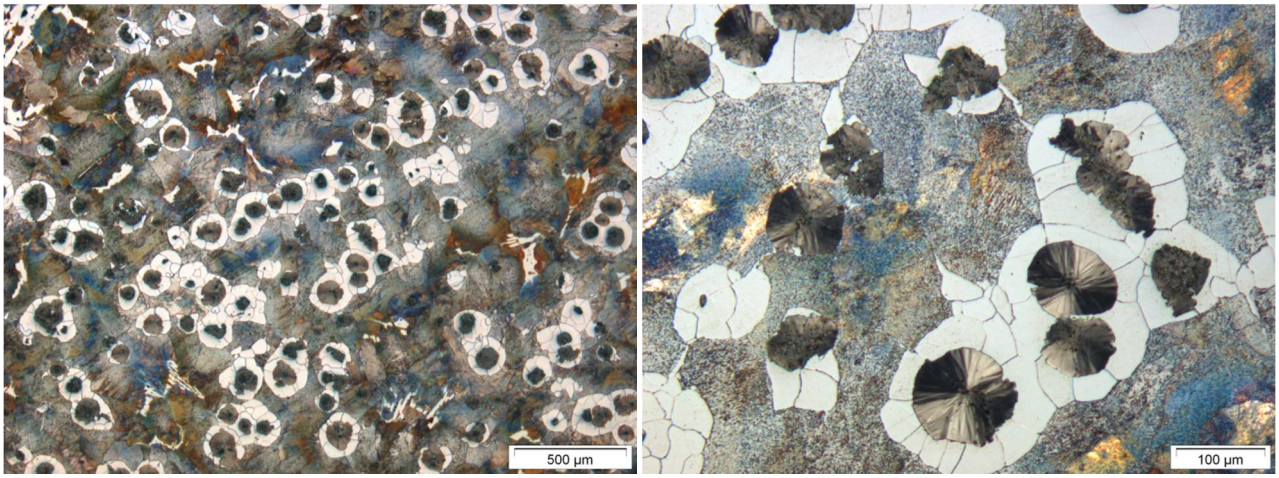

(a) OM, Nital 6% etching **(b) OM, Nital 6% etching**

Figure 2.8. Microstructure of SGI material

2.6.2 High Chromium Steel (HCS)

HCS grade is similar to the D2 grade and it is widely used as shell material of rolling mill rolls due to its high hardness and wear resistance. These properties of HCS material are explained by the microstructure in [76, 77]. The chemical composition of the HCS grade is given in Table 2.3.

Table 2.3. Chemical compositions of HCS material in terms of wt.%

	C	Si	Mn	Ni	Cr	Mo	V	Fe
Min	1.0	0.2	0.6	0.5	10.0	3.0	0.1	Bal
Max	1.5	1.0	1.0	1.5	14.0	6.0	0.5	

Figure 2.9 presents the microstructure of HCS material coming directly from casting. As it can be observed, HCS in as-cast conditions is mostly constituted by a matrix of martensite and residual austenite with a network of primary carbides at grain boundaries. Residual austenite is present due to the low cooling rate of around 0.5°C/min. Dilatometry curve of HCS grade presented in section 3.3.1, allows the confirmation of the residual austenite presence, since even at a considerably higher cooling rate of 3°C/s, the martensitic transformation is not complete.

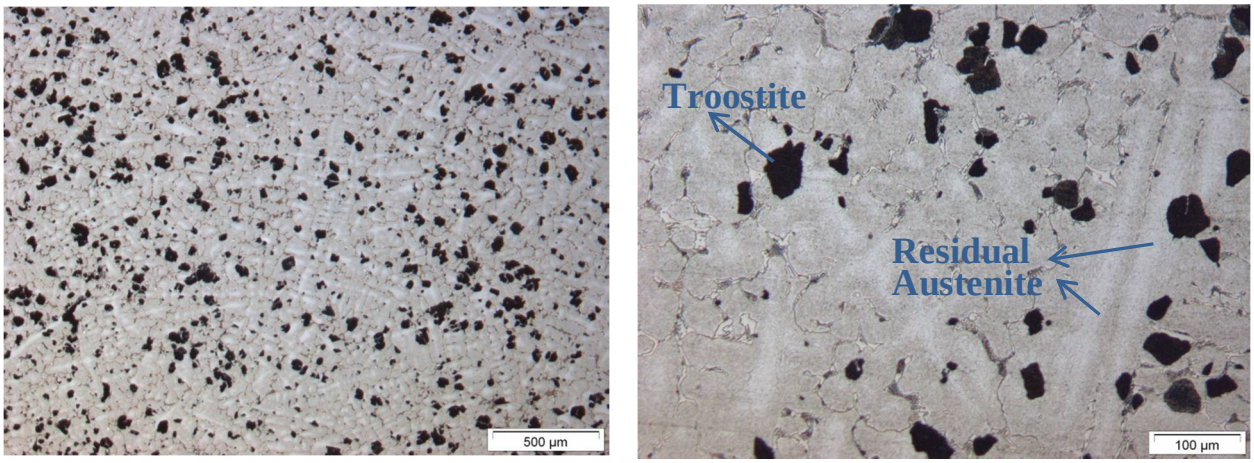

(a) OM, Nital 6% etching **(b) OM, Nital 6% etching**

Figure 2.9. Microstructure of HCS material in as-cast conditions

In Figure 2.9(b), mixed grains are observed more closely. The matrix is mostly martensite phase, it is observed as the darker areas inside grains surrounding residual austenite that is presented as columnar dendrite cores (lighter areas inside grains). From optical microscope, it is difficult to

estimate the phase proportion. However according to the industry, the martensite amount varies from 50 to 60 %. Troostite phase (soft phase with dark appearance) is sometimes also present in HCS material in as-cast conditions. This phase is suspected to reduce HCS material properties since hardness decreases in case of its presence. However, troostite phase will not be considered in this thesis and further analyses can be found in [5] and [78].

Figure 2.10 presents the images obtained by Scanning Electron Micrograph (SEM) after OPS (oxide polishing suspension) for HCS grade. Carbides present in the structure are enhanced.

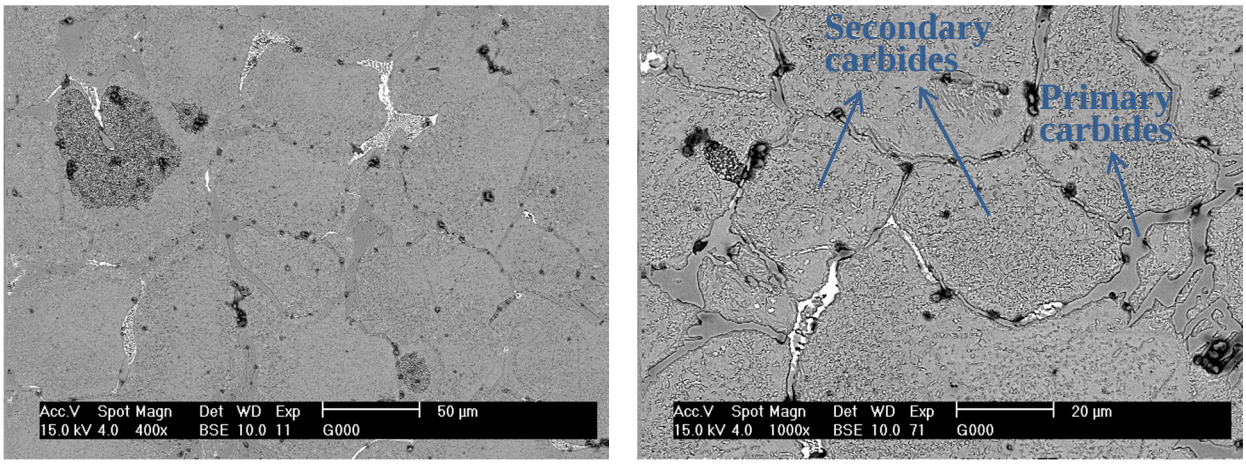

(a) SEM-BSE, OPS **(b) SEM-BSE, OPS**

Figure 2.10. SEM images of HCS material in as-cast conditions

Figure 2.10(a) shows a troostite nodule close to the grain boundary. Primary carbides are made of Cr-rich M_7C_3 and Mo-rich M_2C, their total amount is around 18% for the volume fraction (from quantitative metallography) and they are observed as a quasi-continuous network at grain boundaries. Secondary carbides Cr-rich M23C6 are observed more clearly in Figure 2.10(b) forming clusters inside grains.

In Figure 2.11, the microstructure of HCS material after a hardening treatment (1025°C/1hr/air cooling) is presented. Troostite phase disappeared and carbides are better observed.

Within the FE modeling, only martensite and austenite phases are modeled for HCS material, therefore, in order to discard troostite phase, the heat treated HCS material will be studied in this thesis. Nevertheless, the effect of carbides is modeled through the materials properties, since they are present in the HCS material during the experimental analyses presented in Chapter 3.

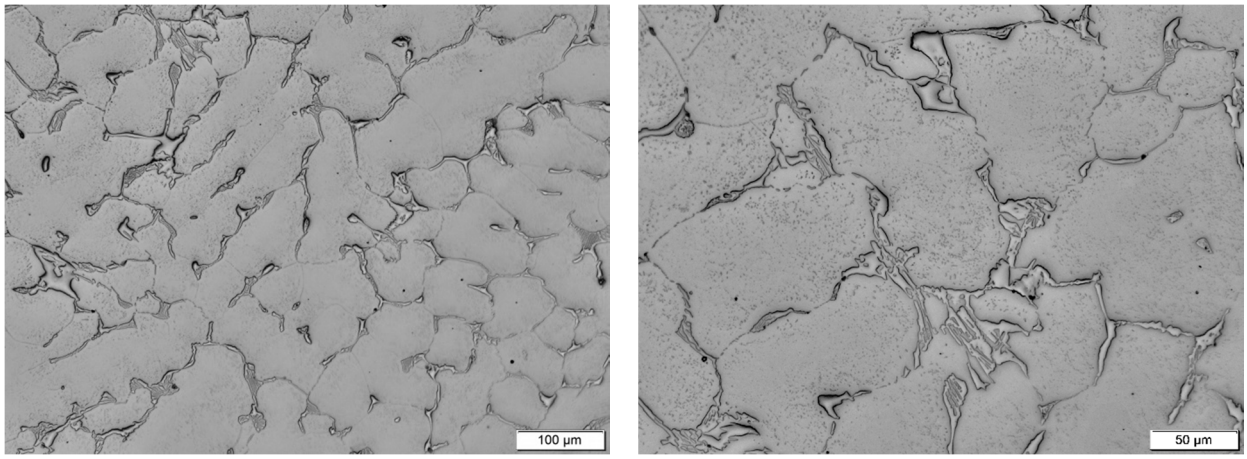

(a) OM, OPS **(b) OM, OPS**

Figure 2.11. Microstructure of HCS material after hardening heat treatment

2.7 Conclusions

The model implemented in the LAGAMINE finite element code, was summarized in this chapter. Thermal and metallurgical models for diffusional and martensite transformations, besides of mechanical and coupled models considering each interaction, were depicted by presenting corresponding theory and equations. The implemented damage model based on different rupture criteria was also presented. In addition, thermal, metallurgical, mechanical and coupled parameters required as input data for modelling were listed. Finally, a brief description of both spheroidal graphite iron and high chromium steel materials considered for the modelling of rolling mill rolls was given.

Chapter 3. Materials parameters identification and experimental campaign

For modelling of bimetallic rolling mill rolls through a thermo-mechanical metallurgical model, a series of parameters are required. A complete experimental campaign was performed to obtain mechanical and thermo-physical parameters. Compression tests at constant strain rate for each phase at different temperatures were performed. Tensile tests were performed at different temperatures for both materials. Thermophysical properties were obtained by dilatometry, DSC and laser-flash methods. Cryogenic cooling was applied for the martensite start temperature determination. Finally inverse method is applied for determination of lacking parameters.

3.1 Mechanical properties based on compression tests at constant strain rate

Compression tests at a constant strain rate for both SGI and HCS materials were developed using the equipment available in the Laboratory of Mechanics and Structures (ArGEnCo Department, University of Liège). In particular, SCHENCK Hydropuls 400kN machine (Figure 3.1(a)) with a quad elliptical radiant furnace 4x2000W was used. Cylindrical samples were compressed and

connected to a thermocouple for the temperature tracking. A zoom of the punch in contact with the sample during compression test is shown in Figure 3.1(b).

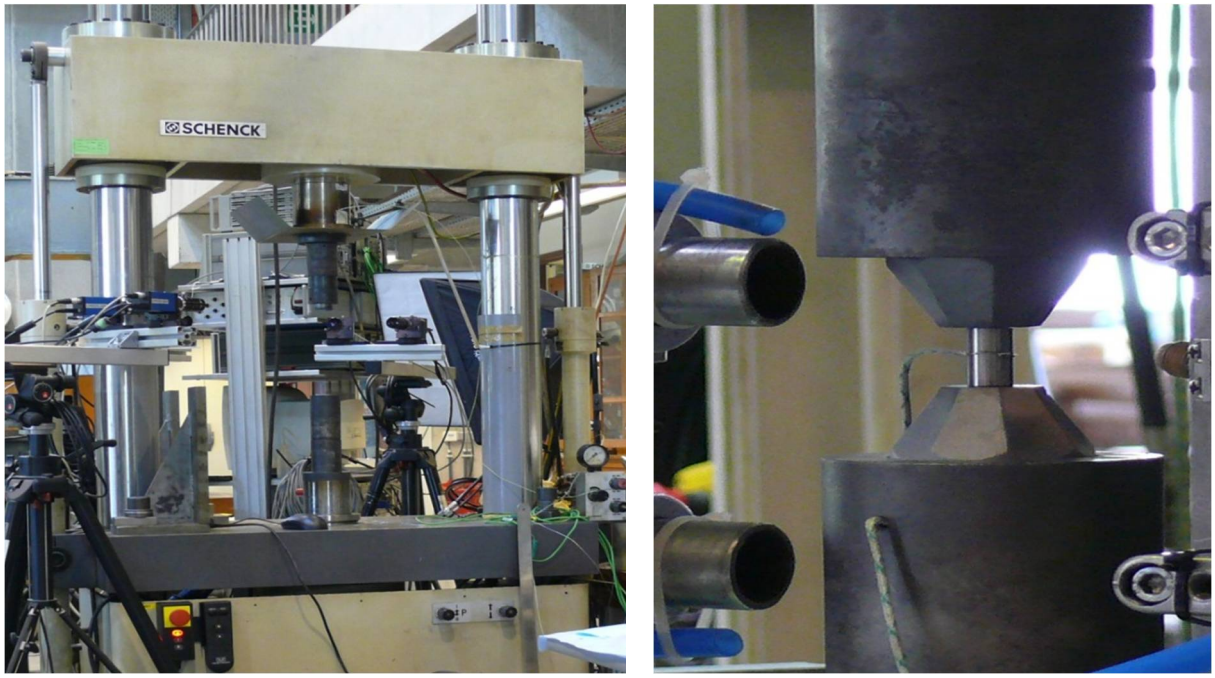

(a) **(b)**

Figure 3.1. (a)SCHENCK Hydropuls 400kN machine (b) Puncher-sample system

Ferrrite and pearlite phases for SGI material, and austenite and martensite phases for HCS material were tested at different temperatures [79]. This section presents the required procedure for the achievement of constant strain rate, the sample preparation and the mechanical properties identified from these compression tests. Additionally, an analysis of unexpected results obtained for HCS austenite and martensite phases is presented at the end of the section.

3.1.1 Procedure for achievement of constant strain rate in compression tests

Compression tests at a constant strain rate of $0.003s^{-1}$ were performed. A procedure for the achievement of compression tests at constant strain rate was developed in [80] and validated by DIC and extensometer measurements in [81]. The applied procedure will briefly be presented in this sub section.

3.1.1.1 General description of the procedure

Universal testing machines equipped with an online closed–loop control systems could be used for constant strain rate tests. However, all the required features were not available in the existing machines of the Laboratory of Mechanics and Structures (ArGEnCo, ULg). SCHENCK Hydropuls 400kN machine has the capacity to be configured for user–defined displacements of the cross–head before performing the test. However the sensor associated to the user–defined displacement is connected to the actuator (cross–die), therefore, a global displacement $X_{gl}(t)$ is measured. The identification of the specific specimen displacement $X_{ep}(t)$ needs a previous knowledge of the machine deflection $X_{ma}(t)$. In order to apply the proper user–defined displacements generating a compression test at constant strain rate, the proposed solution is to perform a series of tests. For the studied case, three steps are required for the achievement of a constant strain rate test. First, a compression test without sample is performed for the identification of the machine rigidity. Then a compression test is applied to one sample where a constant cross-head speed is imposed in order to obtain the deflection response of the system machine-sample. Finally a compression test at constant strain rate is achieved by imposing a corrected displacement function of time obtained from previous tests. This methodology must be applied for each material and temperature. The case of SGI Pearlitic phase at 20°C will be presented below for the procedure description.

3.1.1.2 Theoretical equations

The current true axial compression strain in the sample as a function of time is defined by:

$$\varepsilon(t) = ln\left(\frac{H_0 + X_{ep}(t)}{H_0}\right) \quad \textbf{3.1}$$

where H_0 is the initial height of the specimen and $X_{ep}(t)$ the specimen displacement (negative for compression) or height reduction.

Applying the time derivative to eq 3.1 and reordering the terms, a differential equation is obtained whose solution is presented in eq. 3.2

$$X_{ep}(t) = H_0(\exp(\dot{\varepsilon}t) - 1) \quad \textbf{3.2}$$

Therefore, the sample displacement $X_{ep}(t)$ required for a test at a constant strain rate $\dot{\varepsilon}$ can be computed using eq. 3.2. This displacement could be used as the user–defined displacement of the actuator $X_{gl}(t)$, if there was no machine deflection.

3.1.1.3 Compression test without specimen

A compression test without specimen at 20°C is performed, the obtained load-deflection curve of the testing machine is presented in Figure 3.2. From this test, the machine deflection X_{ma} can be identified as a function of load.

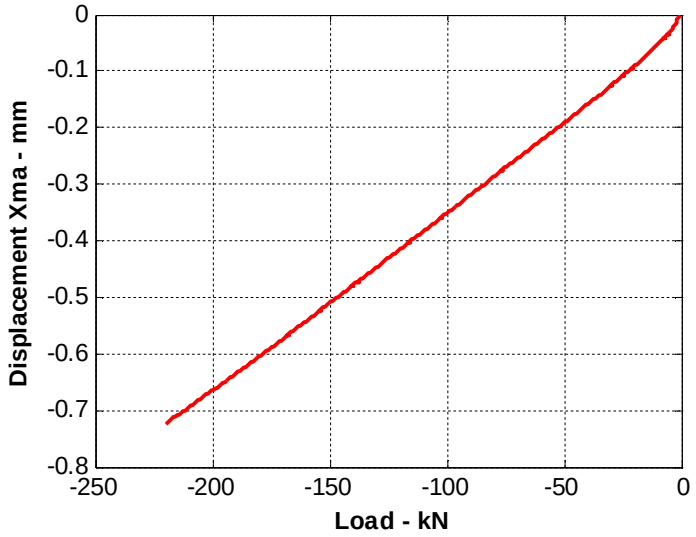

Figure 3.2. Load-deflection curve for the testing machine (SCHENCK Hydropuls 400kN) at 20°C

3.1.1.4 Compression test 1 at constant cross-head speed

In test 1, a constant average cross-head speed v is applied in order to obtain the deflection response of the system machine-sample. This speed v is computed using eq.3.3, where the target strain rate is used.

$$v = \frac{X_{gl}(t)}{\Delta t} = \frac{X_{ep}(t) + X_{ma}(t)}{\frac{\varepsilon_F}{\dot{\varepsilon}}} = \dot{\varepsilon}\frac{H_0(\exp(\varepsilon_F) - 1) + X_{ma}(t)}{\varepsilon_F} \qquad \textbf{3.3}$$

This equation is obtained from eq. 3.2 taking into account the machine deflection $X_{ma}(t)$ and considering $\Delta\varepsilon = \varepsilon_F$ (with initial strain $\varepsilon_0 = 0$) and $\dot{\varepsilon} = \Delta\varepsilon/\Delta t$.

For test 1, the displacement curve $X_{gl-1}(t)$ is generated from the assumption of constant cross–head speed v. $X_{ma}(t)$ is recovered from the measured load during test 1 and from graph of Figure 3.2. as shown in Figure 3.3.

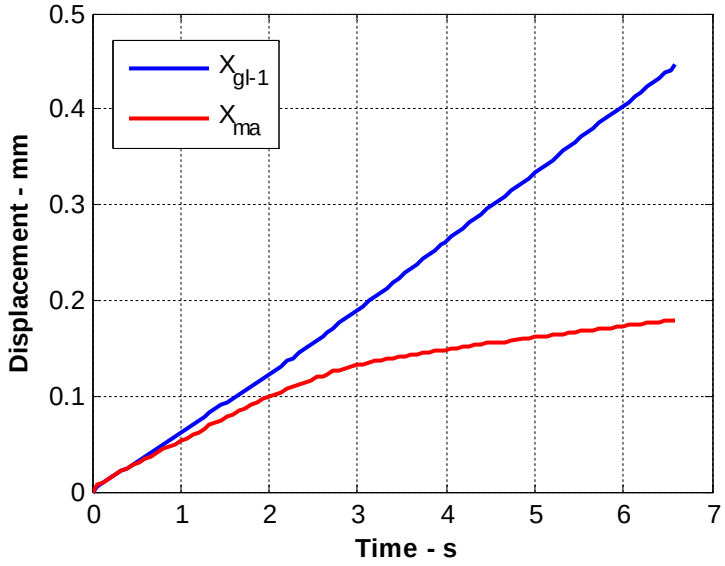

Figure 3.3. Specimen deformation for test 1 and machine deflection at 20°C

At this moment, the specimen deformation $X_{ep-1}(t)$ can be computed using eq. 3.4. Note that for this computation, the displacement curves of the testing machine and of the test 1 must be set at identical load sampling frequency.

$$X_{ep-1}(t) = X_{gl-1}(t) - X_{ma}(t) \quad \textbf{3.4}$$

For test 1, a constant cross-head speed is achieved as shown in Figure 3.3 and the constant strain rate is not achieved as can be observed in Figure 3.4(a). Therefore, a second test must be performed with a corrected user-defined displacement taking into account the machine deflection. A first stress-strain curve is shown in Figure 3.4(b).

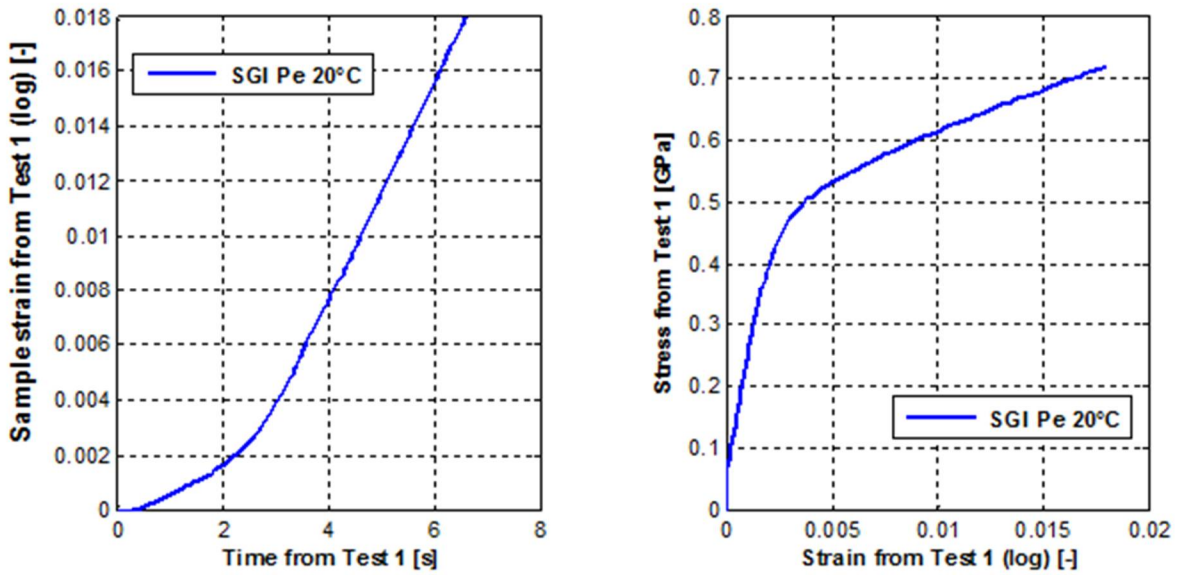

(a) Strain-time curve **(b) Stress-strain curve**

Figure 3.4. Strain-time and stress-strain curve from test 1 for SGI Pe sample at 20°C

3.1.1.5 Compression test 2 at constant strain rate

In test 2, the user-defined displacement X_{gl-2} must be determined in order that the specimen deformation X_{ep-2} follows theoretical equation of eq.3.2 (reminded here in eq.3.5 for a constant strain rate $\dot{\varepsilon} = 0.003\ s^{-1}$).

$$X_{ep-2}(t) = H_0(\exp(\dot{\varepsilon}t) - 1) = H_0(\exp(0.003t) - 1) \quad \textbf{3.5}$$

In order to impose an accurate X_{gl-2}, the behavior of the system-machine at constant strain rate $\dot{\varepsilon} = 0.003\ s^{-1}$ should be known, nevertheless it is not totally accurately known since the targeted constant strain rate was not achieved. However, the system-machine behavior of the cross-head speed in test 1 is assumed similar to the one of the targeted strain rate (test 2), i.e. $X_{ma-2} = X_{ma-1}$. Therefore, X_{gl-2} is determined as a function of time t_2, computed by shifting the curve X_{gl-1} (from test 1). Estimated shift is applied by using eq.3.5 rearranged in eq.3.6. A visual explanation is provided by Figure 3.5 issued from PhD thesis of V. Tuninetti who developed the method.

$$t_2 = -\frac{1}{\dot{\varepsilon}} \ln\left(\left(\frac{X_{ep-1}(t)}{H_0}\right) + 1\right) \quad \textbf{3.6}$$

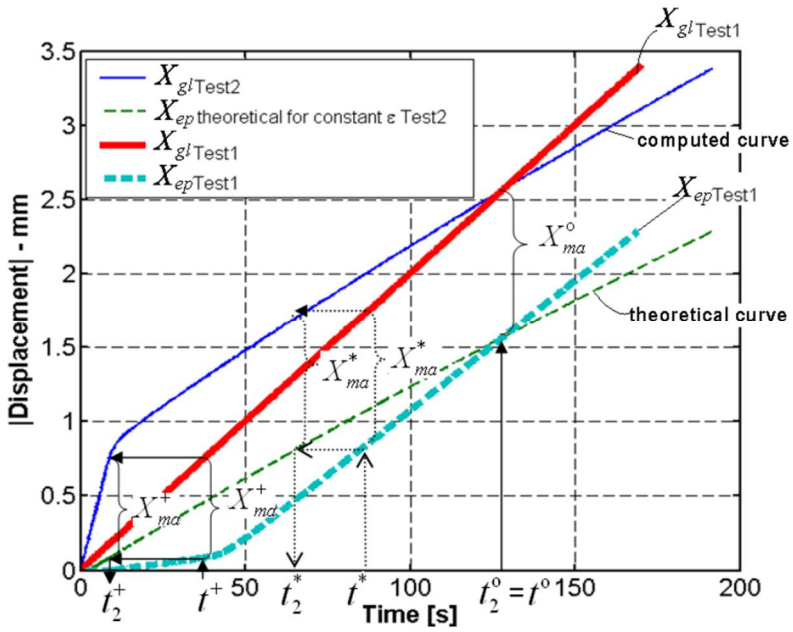

Figure 3.5. Schematic representation of the user–defined displacement computation

Finally, the constant strain rate is achieved by imposing $X_{gl-2}(t_2)$ in test 2 as it is observed in Figure 3.6(a). The corresponding stress-strain curve for test 2 is shown in Figure 3.6(b). The methodology presented here is applied for different temperatures and materials.

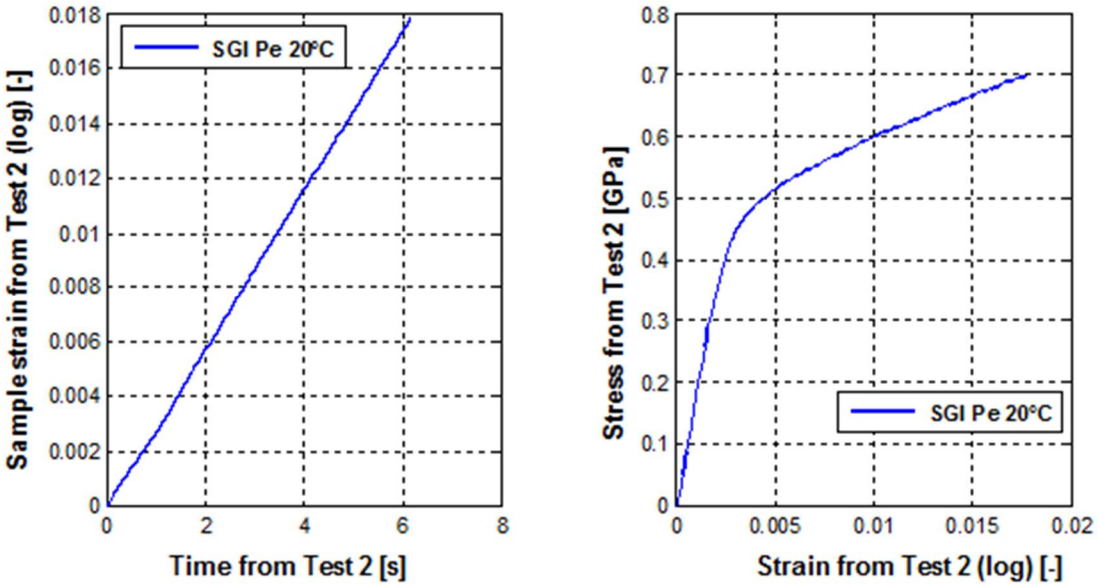

(a) Strain-time curve **(b) Stress-strain curve**

Figure 3.6. Strain-time and stress-strain curves from test 2 for SGI Pe sample at 20°C

3.1.2 Samples preparation

Cylindrical samples of core and shell material with 15 mm height and 9 mm diameter, were extracted from a mill roll manufactured in MK industry. Different heat treatments, using a BOUVIER TECHNOFOUR furnace equipped with a PID regulator and electrical resistances, were applied by MMS team to the samples, to generate different phase contents. For high temperatures compression tests, samples were reheated with the quad elliptical radiant furnace 4x2000W associated to the SCHENCK Hydropuls 400kN machine. Three samples were considered for each phase and test temperature. Table 3.1 summarizes the different microstructures generated by heat treatments and the temperatures chosen for compression tests. For each phase, thermal cycles applied are illustrated in Figure 3.7.

For core material SGI, graphite nodules are not considered since the FE code does not consider their modelling, however they are intrinsically included in the mechanical properties of the SGI material. Ferrite and pearlite phase were tested from room temperature until 650°C. For ferrite phase, the maximal amount obtained for SGI material is 55%Pe-45%Fe, called hereafter 45-Fe. It comes directly from casting stage for a very similar composition material. The maximal obtained proportion of pearlite is 95%Pe-5%Fe, hereafter called 95-Pe. It was generated by the thermal treatment of Figure 3.7(a) of the as cast samples, by heating samples at 1000°C with a holding time of 1h (austenitization), then cooling down to 800°C with a holding time of 30 hrs (isothermal treatment for “pearlitization”). The samples containing the maximal proportions of ferrite and pearlite, 45-Fe and 95-Pe were compressed at room temperature and at higher temperatures (see Figure 3.7(b)). The properties corresponding to pure ferrite and pearlite phases were later recovered by mixture law using eq. 2.1.

For shell material HCS, the initial state is the hardened state of Figure 2.11 in section 2.6.2 (troostite phase has been dissolved). Full martensite and austenite phases were tested and carbides are not considered. However, similarly to graphite nodules on SGI grade, primary and secondary carbides are included in the mechanical properties of HCS material. Fully martensite samples were obtained through an austenitization stage performed at 1025°C/1hr in an electric furnace (heating rate 2°C/s) prior to a subsequent cryogenic quenching into liquid nitrogen at -196°C. Martensitic samples were tested at 20°C or reheated in the radiant furnace (heating rate 3°C/s, holding time 60s) until the test temperature (80°C, 150°C) (see Figure 3.7(c)). HCS

austenite samples were tested from 300°C to 950°C. In order to test pure austenitic matrix, samples were subjected to the thermal cycle of Figure 3.7(d), austenitized at 950°C (heating rate 2°C/s) with a holding time of 60 seconds. The cooling stage was achieved inside the furnace (cooling rate 0.5°C/s), where the compression was applied at the chosen test temperature.

Table 3.1: Static compression tests summary

Material	Phase	Preliminary heat treatment	Compression test Temperature (°C)	Compression test treatment
SGI (Core)	Ferrite 45%Fe-55%Pe	As received	20	Test
			300	Reheating + Test
			650	Reheating + Test
	Pearlite 95%Pe-5%Fe	Austenitization + Annealing	20	Test
		Austenitization + Annealing	300	Reheating + Test
		Austenitization + Annealing	650	Reheating + Test
HCS (Shell)	Austenite 100%Au		300	Austenitization + Cooling in furnace + Test
			700	Austenitization + Cooling in furnace + Test
			950	Austenitization + Test
	Martensite 100%Ma	Austenitization + Quenching	20	Test
		Austenitization + Quenching	80	Reheating + Test
		Austenitization + Quenching	150	Reheating + Test

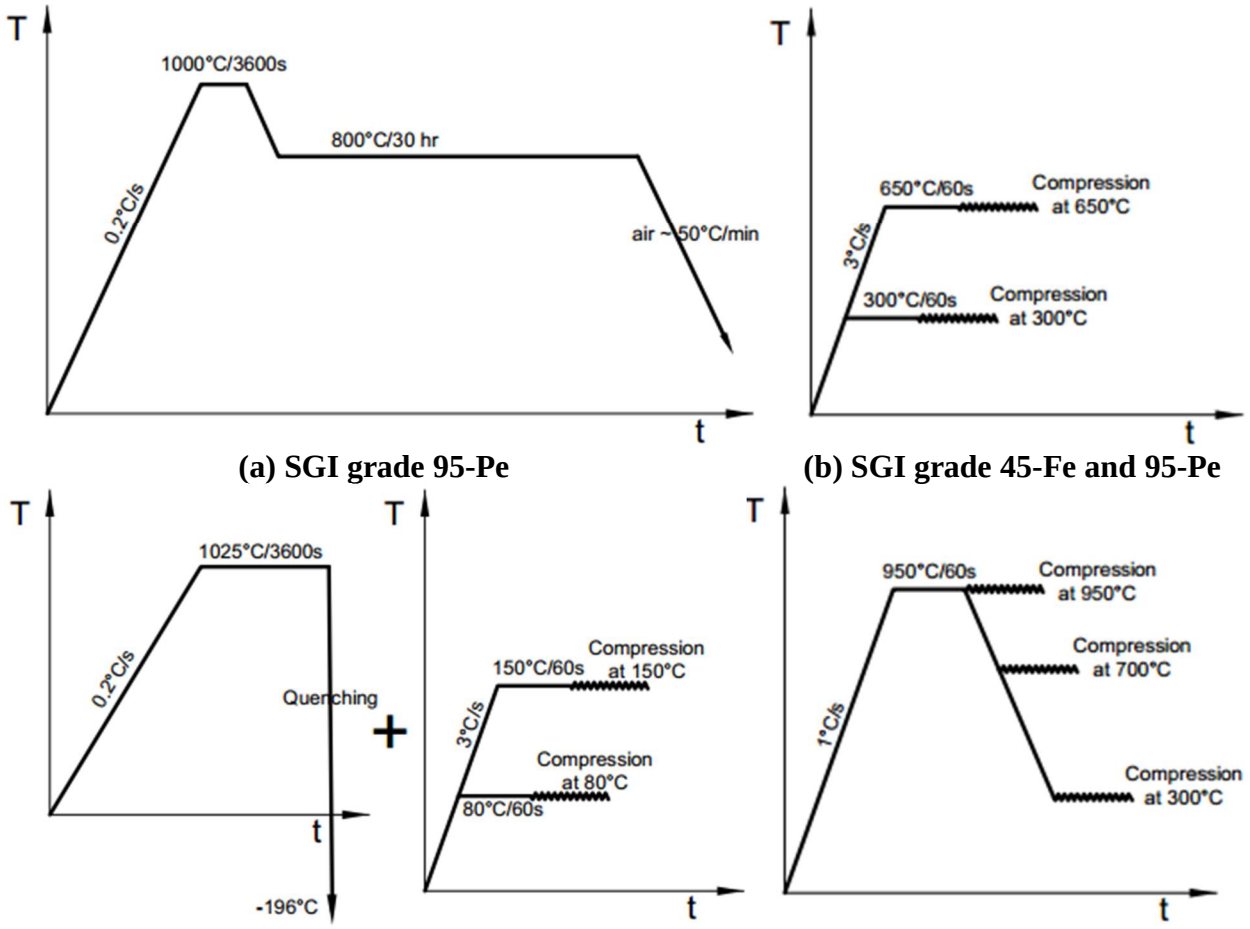

Figure 3.7. Thermal cycles applied in different phases of SGI and HCS grades for compression tests

3.1.3 Average curve computation

As three samples were tested for a same material phase and temperature, an average curve was computed from the set of results. The same discretization must be applied at each curve for the computation of average curve. As an example, three curves obtained for 95-Pe 20°C samples are presented in Figure 3.8(a) and the computed average curve is shown in Figure 3.8(b). The same procedure was applied for tests performed for each phase and temperature. In most cases, the average curves were easily obtained as the three curves were quite similar. However for the case of Au-300°C one of three samples presented a stress strain curve considerably different from other samples as it was reheated with a higher heating rate i.e. 2°C/s. From this unintentional

result, a full analysis about the behavior of HCS grade under hot compression is discussed in [82] and further presented in section 3.1.7.

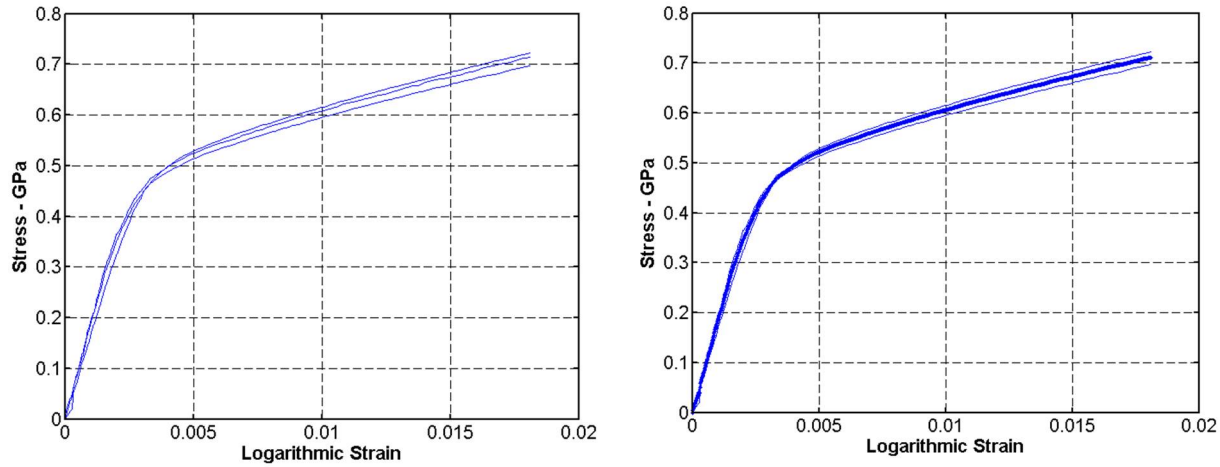

(a) **(b)**

Figure 3.8. Compression tests for 95-Pe 20°C (a) three tests results (b) average curve

3.1.4 Stress-strain curves

Average curves of compression test results for SGI material are presented in Figure 3.9. Results for the maximal proportions of pearlite and ferrite phases show, as expected, a higher strength for pearlite samples than for ferrite ones. For 95-Pe as well as for 45-Fe, the maximal strength was obtained for 20°C and it decreases with the increase of temperature. A similar behavior is observed for 95-Pe 20° and 95-Pe 300° since at moderate temperatures, the deformation mechanism for cementite (carbide composing pearlite phase together with ferrite phase) is limited to dislocation glide [83] and to only two slip systems [84], explaining a low plastic deformation at temperatures up to 300°C [85]. However, for higher temperatures, numerous phenomena take place as the grain boundary sliding [83, 85] and the spheroidization of cementite [86], in addition, more slip planes become operative due to the dynamic recovery [84] allowing a higher ductility as it is observed for 95-Pe 650°.

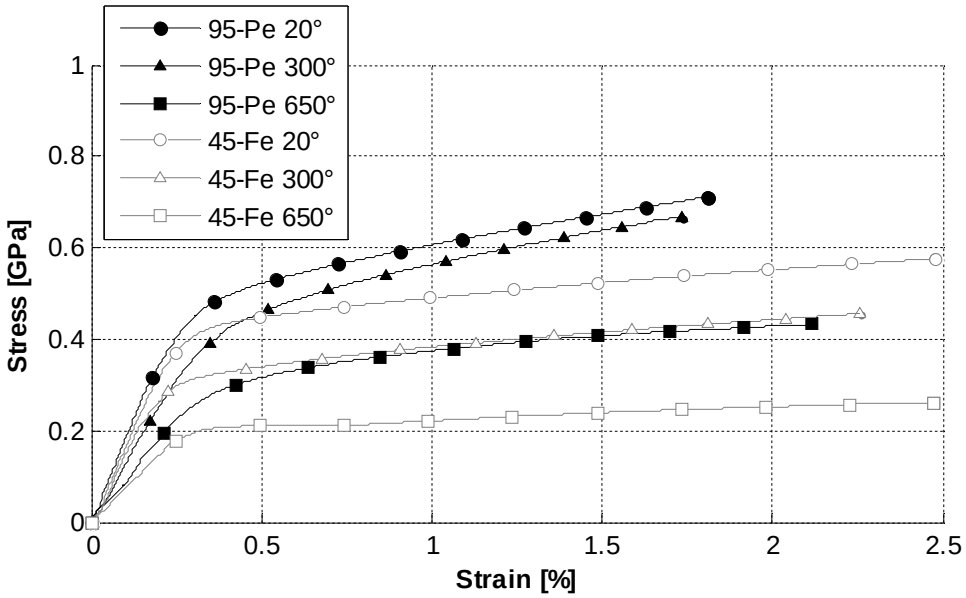

Figure 3.9. Stress-strain curves from monotone compression tests for SGI material

For HCS, average stress-strain curves are shown in Figure 3.10. Martensite samples exhibit a clearly higher strength than austenite samples as expected. In addition, for austenite samples, the strengthening effect is decreasing for higher temperatures. Moreover, for martensite phase a slightly higher strengthening effect is observed for Ma 20°C, while Ma 80° and Ma 150° curves overlap; a further analysis about this result will be presented in section 3.1.6.

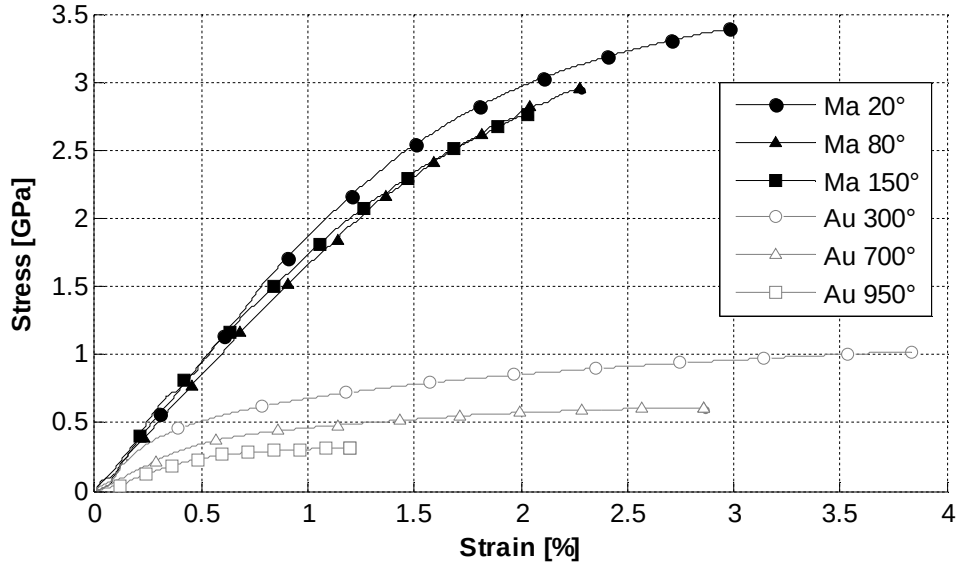

Figure 3.10. Stress-strain curves from monotone compression tests for HCS material

3.1.5 Properties

Mechanical properties as Young modulus E, yield limit σ_y, and tangent modulus E_t were computed from average stress-strain curves obtained from previous compression tests. The associated error corresponds to the standard deviation of the three tests performed. For HCS material, properties were directly obtained from stress-strain curves as they correspond to fully austenite and martensite phase. However for SGI material, values for fully ferrite and pearlite phases were computed based on mixture law applying eq.2.1 based on the curves of 45-Fe and 95-Pe samples respectively.

3.1.5.1 Young modulus and yield limit

Young modulus was computed from average stress-strain curve for each material, phase and temperature. From average stress-strain curve shown in Figure 3.11, corresponding to the case of 95-Pe 20°C, it is possible to distinguish the elastic and the plastic parts of the curve. The slope of the elastic line is considered as the Young modulus and measured for each case. Obtained results of Young modulus and their error are summarized in Table 3.2.

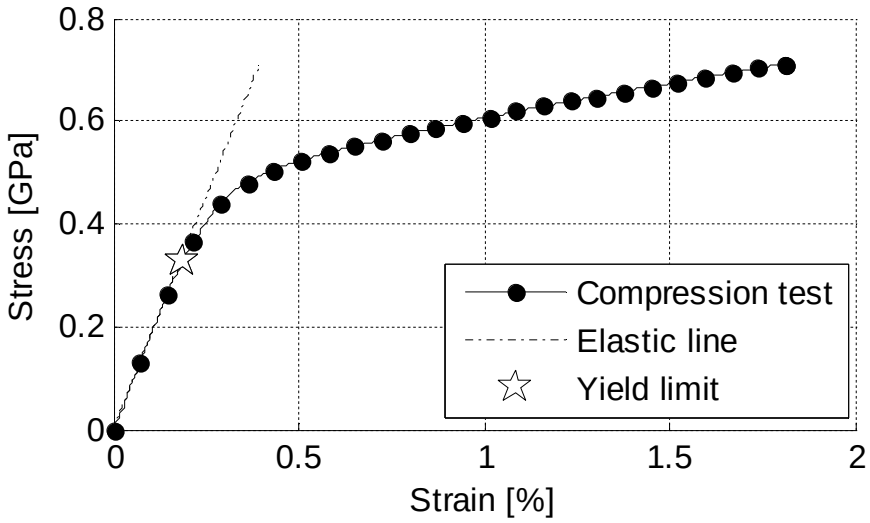

Figure 3.11. Young modulus and yield limit identification based on experimental compression test curve for 95-Pe 20°C

Table 3.2. Young modulus values obtained by compression tests

Material	Temperature (°C)	Samples microstructure	E from compression test (GPa)	Phase	E by mixture law (GPa)
SGI (Core)	20	45-Fe	164.10±17.85	Ferrite 100%	141.41±23.93
	300	As cast samples heated	146.30±17.30		151.59±34.81
	650	(45%Fe-55%Pe)	73.20±5.14		49.41±9.06
	20	95-Pe	180.60±13.44	Pearlite 100%	182.66±12.89
	300	Annealed samples heated	142.45±4.56		141.97±2.96
	650	(95%Pe- 5%Fe)	90.50±15.47		92.66±16.76
HCS (Shell)	300	Austenite	186.14±14.31		
	700	Annealed samples cooled	78.74±6.2		
	950	(100%Au)	50.98±9.48		
	20	Martensite	190.24±5.80		
	80	Quenched samples heated	167.6±1.80		
	150	(100%Ma)	187.5±5.80		

Furthermore, the yield limit σ_y was computed by taking the last point of the elastic behavior line and the compression test stress strain curve (see Figure 3.11). The stress corresponding to this intersection point gives the yield limit for each case. Obtained results of yield limit with the resulting error are summarized in Table 3.3.

Table 3.3. Yield limit values obtained by compression tests

Material	Temperature (°C)	Phase	σ_y from compression test (MPa)	Phase	σ_y by mixture law (MPa)
SGI (Core)	20	45-Fe	340±25	Ferrite 100%	313±42
	300	As cast samples heated	210±20		141±7
	650	(45%Fe-55%Pe)	160±5		50±15
	20	95-Pe	360±12	Pearlite 100%	363±11
	300	Annealed samples heated	260±40		266±42
	650	(95%Pe- 5%Fe)	240±20		250±22
HCS (Shell)	300	Austenite	270±40		
	700	Annealed samples cooled	240±30		
	950	(100%Au)	220±15		
	20	Martensite	1800±50		
	80	Quenched samples heated	1900±80		
	150	(100%Ma)	1300±20		

3.1.5.2 Tangent plastic modulus

Within Lagamine FE code [37] the stress strain curves at constant temperature are defined by a set of linear segments for each phase. For instance, Figure 3.12 shows the discretized experimental and numerical curve for 95Pe-20°C.

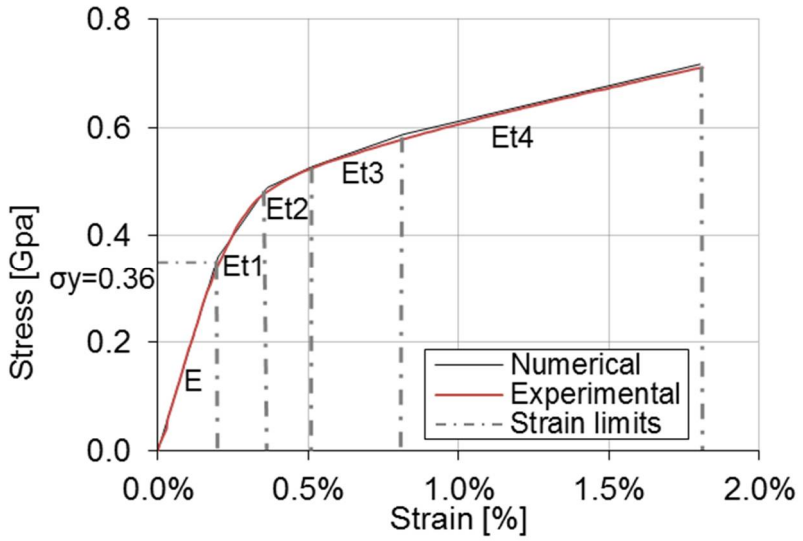

Figure 3.12. Experimental and numerical Stress Strain curves for Pearlite phase at 20°C

A series of tangent modulus E_{t1}, E_{t2}, E_{t3}, E_{t4} was considered in order to correctly define the plastic part of the stress strain curve and corresponding values are given by the slope of each segment. Results of the series of tangent plastic moduli obtained from compression tests at different temperatures for both materials and each phase with corresponding error are summarized in Table 3.4. For HCS material, values of martensite and austenite pure phases were directly obtained.

Table 3.4. Tangent plastic modulus values obtained by compression tests

Material	Temperature (°C)	Phase	Set of plastic modulus from compression tests			
			E_{t1} (GPa)	E_{t2} (GPa)	E_{t3} (GPa)	E_{t4} (GPa)
SGI (Core)	20	45-Fe As cast samples heated	57.7±3.5	20.0±1.5	8.33±0.6	6.5±0.3
	300		26.2±1.6	13.3±0.5	8.33±0.5	6.5±0.1
	650		16.2±0.7	2.94±0.3	2.94±0.3	2.94±0.3
	20	95-Pe Annealed samples heated	84.4±8.6	26.7±3.1	20.0±1.2	13.3±0.4
	300		73.6±6.5	33.3±4.0	21.7±1.3	15.8±1.3
	650		50.3±4.3	26.7±1.5	13.3±0.7	6.0±1.1
HCS (Shell)	300	Austenite Annealed samples cooled (100%Au)	68.6±6.5	33.3±4.0	16.7±0.6	10.0±0.4
	700		37.0±2.9	20.0±1.0	10.0±0.4	5.5±0.2
	950		48.9±5.2	12.0±0.6	8.0±0.4	2.5±0
	20	Martensite Quenched samples heated (100%Ma)	180.0±20	180.0±21	110.0±10	50.0±3.3
	80		160.0±15	160.0±16	115.0±9	62.5±6.0
	150		180.0±20	160.0±18	110.0±11	62.5±6.0

In contrast, for SGI material, the mixture law was applied for the computation of tangent plastic modulus for ferrite and pearlite pure phases. Results are presented in Table 3.5. Note that for ferrite pure phase, values of E_{t1}, E_{t2} and E_{t3} for 300 and 650°C are assumed to be a minimal value since computed values resulted negative due to mathematical errors. The true negative value obtained is reflected by the error for each case.

Table 3.5 Tangent plastic modulus values obtained by mixture law

Material	Temperature (°C)	Phase	Set of plastic modulus by mixture law			
			E_{t1} (GPa)	E_{t2} (GPa)	E_{t3} (GPa)	E_{t4} (GPa)
SGI (Core)	20	Ferrite 100%	39.9±4.3	15.6±0.7	0.55±0.1	1.95±0.2
	300		0.1±3.8	0.1±1.4	0.1±1.0	0.28±0.6
	650		0.1±3.0	0.1±2.9	0.1±1.1	0.9±0.1
	20	Pearlite 100%	87.8±7.8	27.5±1.7	21.5±1.2	14.2±0.4
	300		79.5±6.5	35.8±3.2	23.3±0.5	17.0±1.4
	650		54.5±4.0	29.6±1.1	14.6±1.2	6.4±1.2

In the literature, it is difficult to find values of Young modulus (E), yield limit (σ_y) and tangent plastic modulus (E_t) at different temperatures for similar materials. However for GGG40 [87] and SI-Mo [88, 89] (both similar to SGI), it has been possible to find Young modulus and yield limit ranges that are quite in agreement with values obtained by compression tests in this section. In addition, for classical metallic materials such as CK45 in [43] and C21980 in [90], it is found that E, σ_y and E_t are not too far from the results obtained by compression tests for SGI grade. Similarly, for classical metallic grades 42CD4 in [41] and 60NCD11 in [91], mechanical properties are in the same range than values obtained by compression tests for HCS grade.

Note: Sections 3.1.6 and 3.1.7 are based on the article published with the MMS team [82] as well as on the deep analysis that J. Tchoufang Tchuindjang did for his PhD thesis [5]. During my work in the University of Liège, a strong collaboration was established. My tasks were focused on the numerical modeling and global mechanical parameter identification. However my participation in the compression tests and in the analysis of obtained mechanical results and metallurgical microstructures justifies the summary provided here.

3.1.6 Further analysis of results for HCS martensite phase

3.1.6.1 Mechanical observations

As presented in section 3.1.2, HCS martensite samples were obtained by austenization treatment and subsequent cryogenic quenching in liquid nitrogen. Then samples were reheated at 80 and 150°C before applying compression stress (see Figure 3.7(c)). The stress-strain curves for HCS martensite samples shown in Figure 3.13 correspond to the average of three specimens compressed at 20°C, 80°C and 150°C. Although Ma-20°C presents a slightly higher strength, the three curves have a similar behavior suggesting that martensite phase is subjected to a hardening behavior during compression tests at 80 and 150°C.

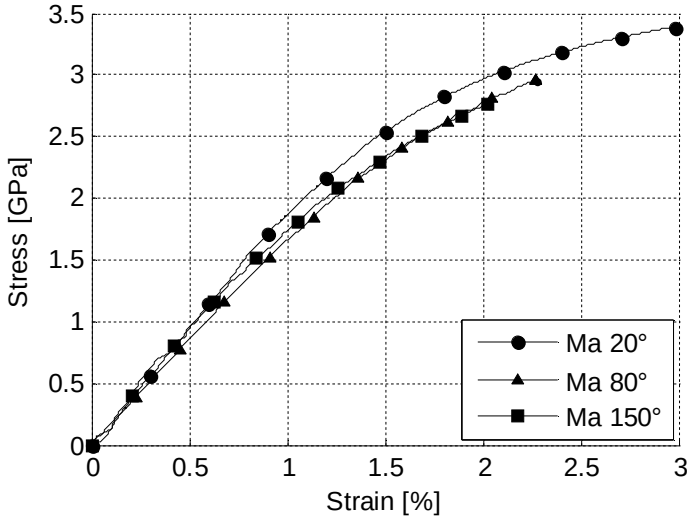

Figure 3.13. Stress-strain curves for HCS martensite samples

3.1.6.2 Microstructure analysis

Microstructure corresponding to Ma 150° samples is presented in Figure 3.14. The continuous network of carbides at grain boundaries and the martensitic matrix are observed in Figure 3.14(a). As shown in Figure 3.14(b), globular secondary carbides precipitating inside martensite hides the actual morphology of the martensite as the coarse carbides globules do not allow the observation of typical laths or plates of martensite. Same microstructure is exhibited by Ma 20° and Ma 80° at optical microscope.

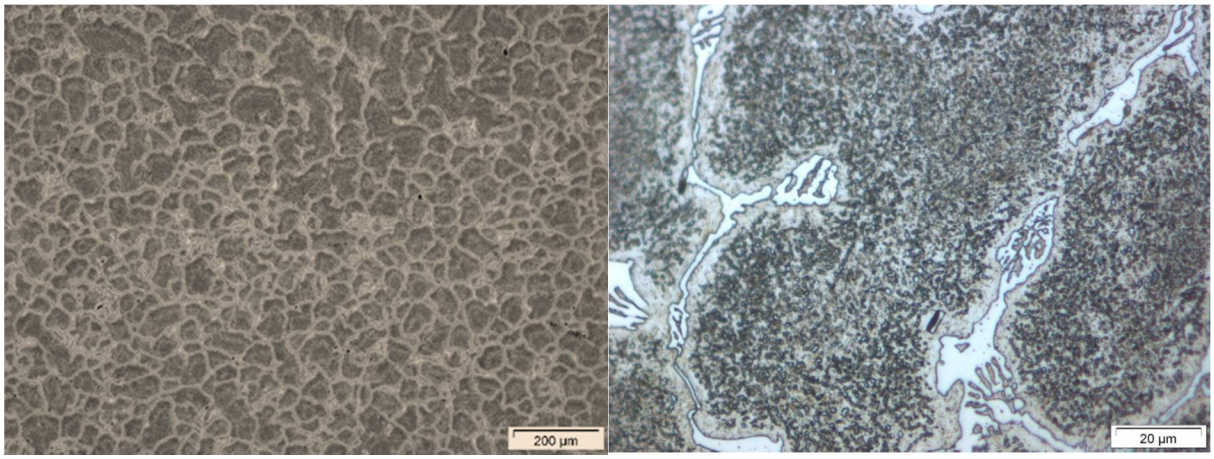

(a) OM, Vilella etching **(b) OM, Nital 6% etching**

Figure 3.14. Microstructure obtained for HCS martensite samples after cryogenic quenching

3.1.6.3 Discussion

To explain the microstructure observed in Figure 3.14 for HCS martensite phase, it is required to go further on the HCS martensite microstructural effects. The responsible phenomenon can be found by a broad literature review on Deep Cryogenic Treatment (DCT) [92–94], that is defined as a treatment performed at subzero temperatures in order to promote nucleation of carbides. The coarsening of carbides is achieved during a conventional tempering treatment at a temperature up to 300- 400°C to allow the coarsening of the previously precipitated fine carbides. In the case of HCS martensite samples, although no tempering treatment was done, it could be assumed that a soaking time as short as 5 minutes inside the liquid nitrogen together with the later warming up to room temperature might be sufficient to allow both the precipitation and the subsequent growing of the newly precipitated carbides within the fully martensitic HCS samples, achieving microstructures similar to those obtained after DCT. Gill and coworkers found that massive precipitation of small secondary carbides can be achieved from supersaturated martensite below Mf and later during warming up to room temperature. The microstructure observed on the cryogenic quenched HCS is in good agreement with this study, as both conditions on martensite supersaturation and final temperature well below Mf points are encountered. In fact the re-austenitization carried out at 1025°C allows complete dissolution of tertiary carbides [5] that yield a supersaturated austenite which should be transformed later into a supersaturated martensite during subsequent quenching. The martensitic transformation within the grains is

reported to begin at 266°c and to end at -41°C (see section 3.4). Therefore the temperature gap between Mf and the final temperature of the liquid nitrogen is sufficient to promote the precipitation of small secondary carbides, a phenomenon that still will go on during warming up to room temperature [95].

The explanation of similar strength at 80°C and at 150°C observed in Figure 3.14 can be set according to Bala and co-workers studies [96, 97]. In their work, these authors enhanced the effect of the heating rate on the kinetics of phase transformations of High Speed Steels (HSS) during continuous heating form as-quenched state, with a focus on the precipitation of ε transition carbides. Such carbides precipitate from the supersaturated martensite during heating in the first stage of the tempering treatment, the next stage corresponds to their dissolution. The temperature range of carbides precipitation is between 80 and 300°C and it depends on the chemical composition of the parent phase and on the heating rate. Therefore for the studied HCS, very few transition carbides may be present in the Ma 80° samples prior to the compression test. By increasing the temperature up to 150°C, the precipitation of an increased amount of ε transition carbides could be expected, having an effect more significant than the softening due to the stress relaxation occurring in the same time [98]. In addition, the applied compression stress may accelerate the atoms mobility and increase the transition carbides amount. Therefore, it could be assumed that for 80°C and 150°C samples, ε transition carbides precipitation had occurred leading to the enhancement of the strengthening effect.

Samples tested at 80 and 150°C may exhibit a strength slightly below that the one of the room temperature sample (see Figure 3.13). This result can be explained by the amount of dislocations that should remain maximal for Ma-20°C samples while Ma-80°C and Ma-150°C samples may undergo little intrinsic stress relaxation decreasing the dislocations density together with a more or less significant precipitation of ε transition carbides. Thus dislocations density which is maximal for the 20°C martensitic samples may be the key parameter to reach the high strength of fully martensitic samples.

3.1.6.4 Conclusions

Three phenomena subjected by HCS martensite samples were clarified. Precipitation and subsequent growing of carbides was explained by correlation with Deep Cryogenic Treatment (DCT). The similar strengthening behavior at 80°C and at 150°C was explained through ε transition carbides precipitation leading to the enhancement of the strengthening. The slightly higher strength for the Ma 20° samples is due to the higher dislocations density being the key parameter for the strengthening effect in fully martensitic samples.

3.1.7 Further analysis of results for HCS austenite phase

During compression tests of HCS austenite phase (see Figure 3.7(d)), one of the three samples reheated with a faster heating rate generated a higher strengthening effect. Only the two other samples were considered for the average stress-strain curve computation in section 3.1.3. The differences observed between these results were the starting base for a deep analysis presented in [82] about links between microstructure and austenite sample behavior under hot compression tests. Table 3.6 and Figure 3.15 summarize conditions for different samples studied. The effect of compression temperature was explained by comparing samples tested at 300°C (CT300) and 700°C (CT700). The effect of re austenitization heating rate was enlightened by comparison between samples reheated at 2°C/s (CT300-A, CT700-A) and at 1°C/s (CT300-B, CT700-B). Furthermore, a stress free sample (SF300-B) was re-austenized at 1°C/s in order to analyze the effect of compression stress applied at 700°C. A summary of important features is presented in this sub section.

Table 3.6. Summary of the thermal cycles applied to compression samples [82]

Temperature of the compression test	Sample designation	Number of samples	Heating rate achieved up to 950°C, prior to compression test
300°C	CT300-A	2	2°C/sec
	CT300-B	2	1°C/sec
Stress-free	SF300-B	1	1°C/sec
700°C	CT700-A	2	2°C/sec
	CT700-B	2	1°C/sec

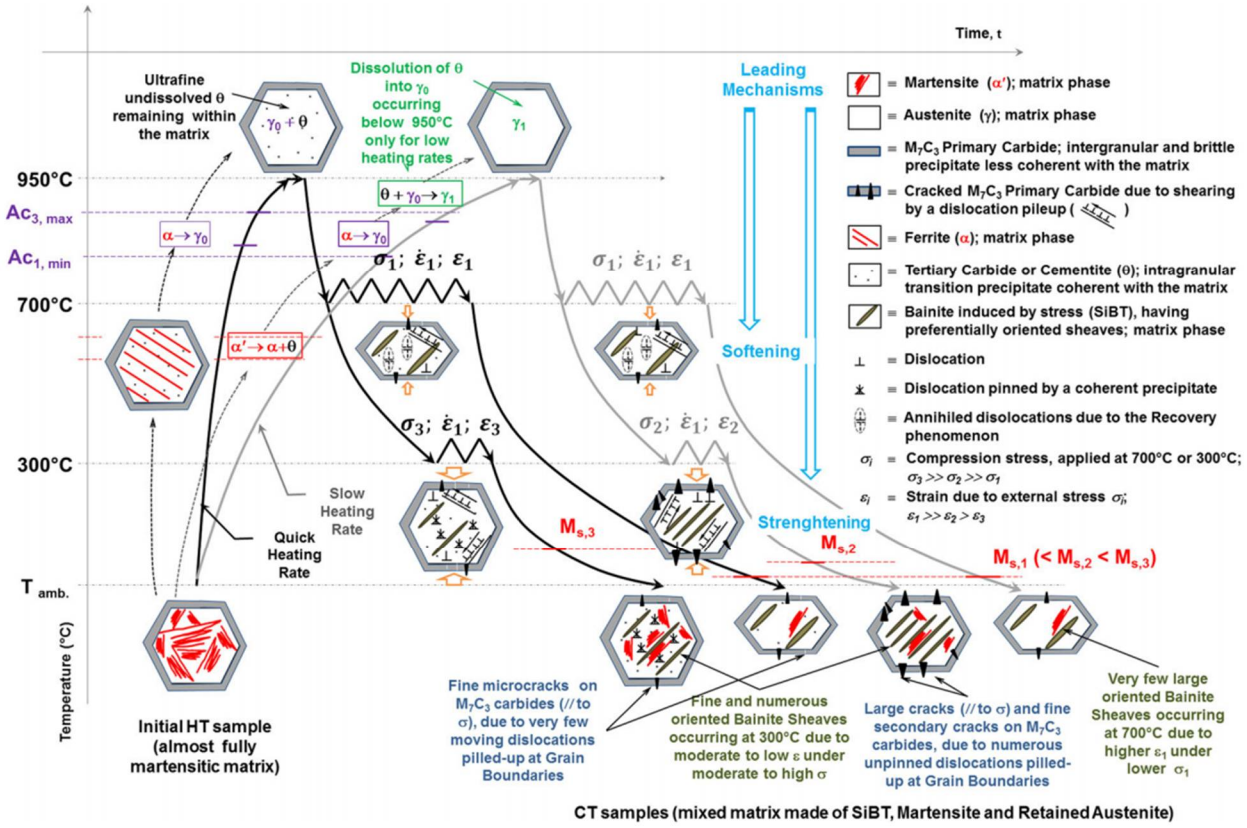

Figure 3.15. Sketch of the strengthening and softening mechanisms occurring on the HCS grade at different conditions [82]

3.1.7.1 Mechanical observation

Austenite samples were reheated before performing the compression tests. Two thermal histories illustrated in Figure 3.16(a); A (heating rate 2°C/s) and B (heating rate 1°C/s), were measured during the samples re-heating. The related stress-strain curves obtained from the average of compression tests of the two samples for each heating rate are given in Figure 3.16(b). Flow stress curves show a hardening stage that increases with decreasing compression temperatures.

For 700°C, flow stress curves obtained from the CT700-A samples are almost identical to the average of the CT700-B samples. This suggests similar hardening behavior for the batch of samples tested at 700°C, regardless of the prior reheating rate up to the austenitizing temperature. The four samples tested at 700°C will be referred to as CT700 hereinafter.

Conversely, different mechanical behavior was observed between the two samples reheated at 2°C/s (CT300-A) and the two other samples reheated at 1°C/s (CT300-B) prior to the

compression tests (Figure 3.16(b)). The CT300-A samples exhibit the higher hardening effect, while maximum elongation has been achieved on the CT300-B samples. This effect observed during experimental campaign must be explained.

The work hardening rate curves of all the tested samples are illustrated in Figure 3.17. A decreasing trend is presented below 0.02% logarithmic strain, before reaching the same asymptote above this limit. The decreasing trend in the work hardening rate is higher for the CT300-A samples, probably because the maximum strength reached is many times higher than the one of the other samples.

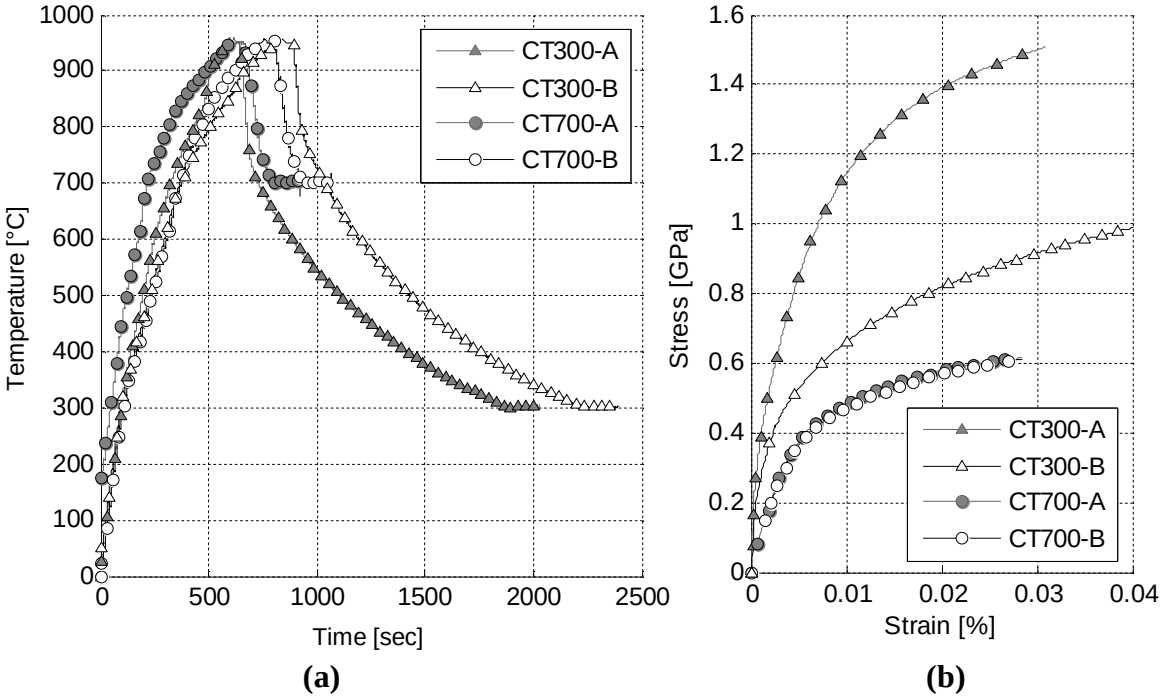

Figure 3.16. (a) Thermal histories on the austenite samples (b) Flow stress curves obtained after compression test performed during cooling stage either at 700°C or at 300°C [82]

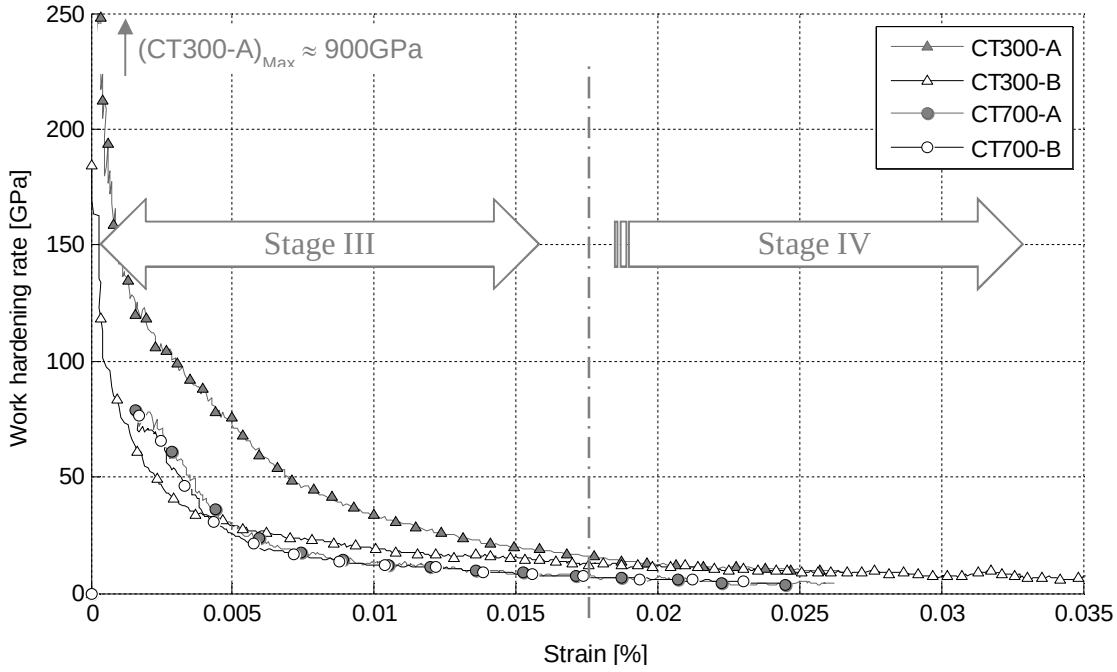

Figure 3.17. Work hardening rate curves for HCCS material at 300°C and 700°C [82]

3.1.7.2 Microstructure characteristic of CT300- A and B samples

The microstructures obtained after the compression tests performed at 300°C are illustrated in Figure 3.18 and Figure 3.19 for the high (CT300-A) and low (CT300-B) heating rates, respectively. The CT300-A samples contain bainite with few preferential oriented sheaves, the rest of the matrix being composed of martensite and possibly retained austenite (Figure 3.18(a)). The bainite sheaf structure probably resulted from the compression stress applied to the sample. The crack path observed in the CT300-A samples (Figure 3.18(b)) is composed of single oriented cracks within the grain boundary carbides, these cracks being parallel to the externally applied stress. In addition, evidence of the widespread of secondary carbide inside grains and precipitate free zones (PFZ) are enhanced in the optical micrograph after OPS (oxide polishing suspension) preparation (Figure 3.18(c)).

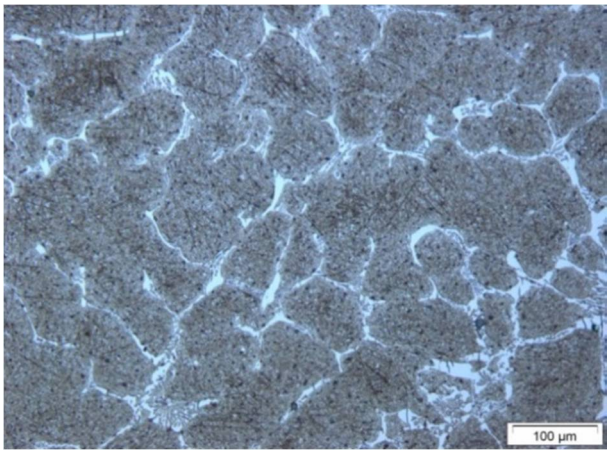

(a) OM, Nital 6% etching

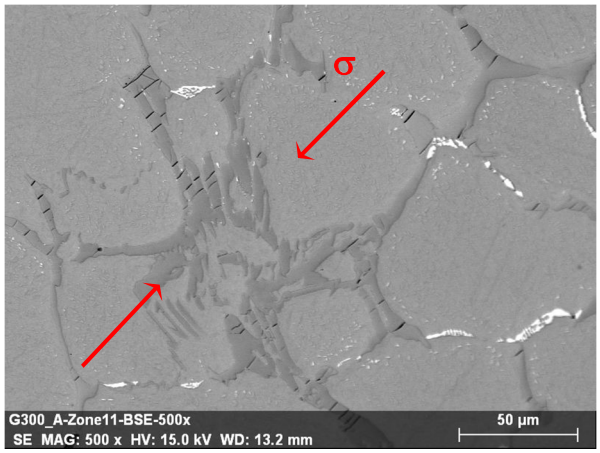

(b) SEM-BSE, OPS

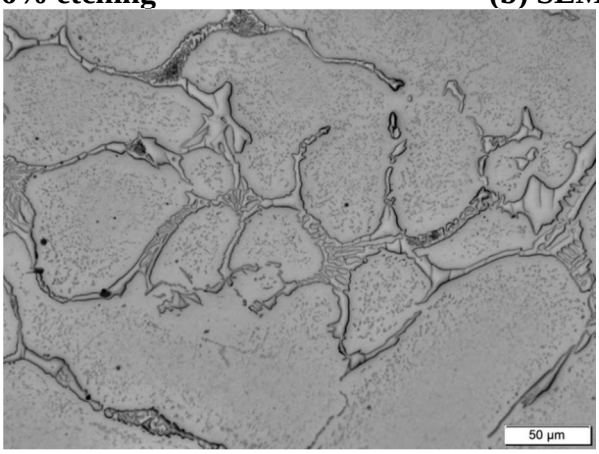

(c) OM, OPS

Figure 3.18. Microstructures obtained after compression tests on CT300-A [82]

The CT300-B samples exhibit bainite with numerous oriented sheaves in their matrix, as well as either martensite or some retained austenite in Figure 3.19(a). In addition, pitting corrosion approximately primary carbides is observed, probably due to the infiltration of the Nital etching into the large cracks that exist within the primary carbides. The crack path in the CT300-B clearly looks more complex and more extended than the previous one observed in CT300-A. It is due to multiple orientations for the crack path on primary carbides (Figure 3.19(b)). Similar to CT300-A, evidence of numerous intragranular secondary carbides and precipitate free zones (PFZ) are enhanced in the optical micrograph after OPS preparation (Figure 3.19(c)).

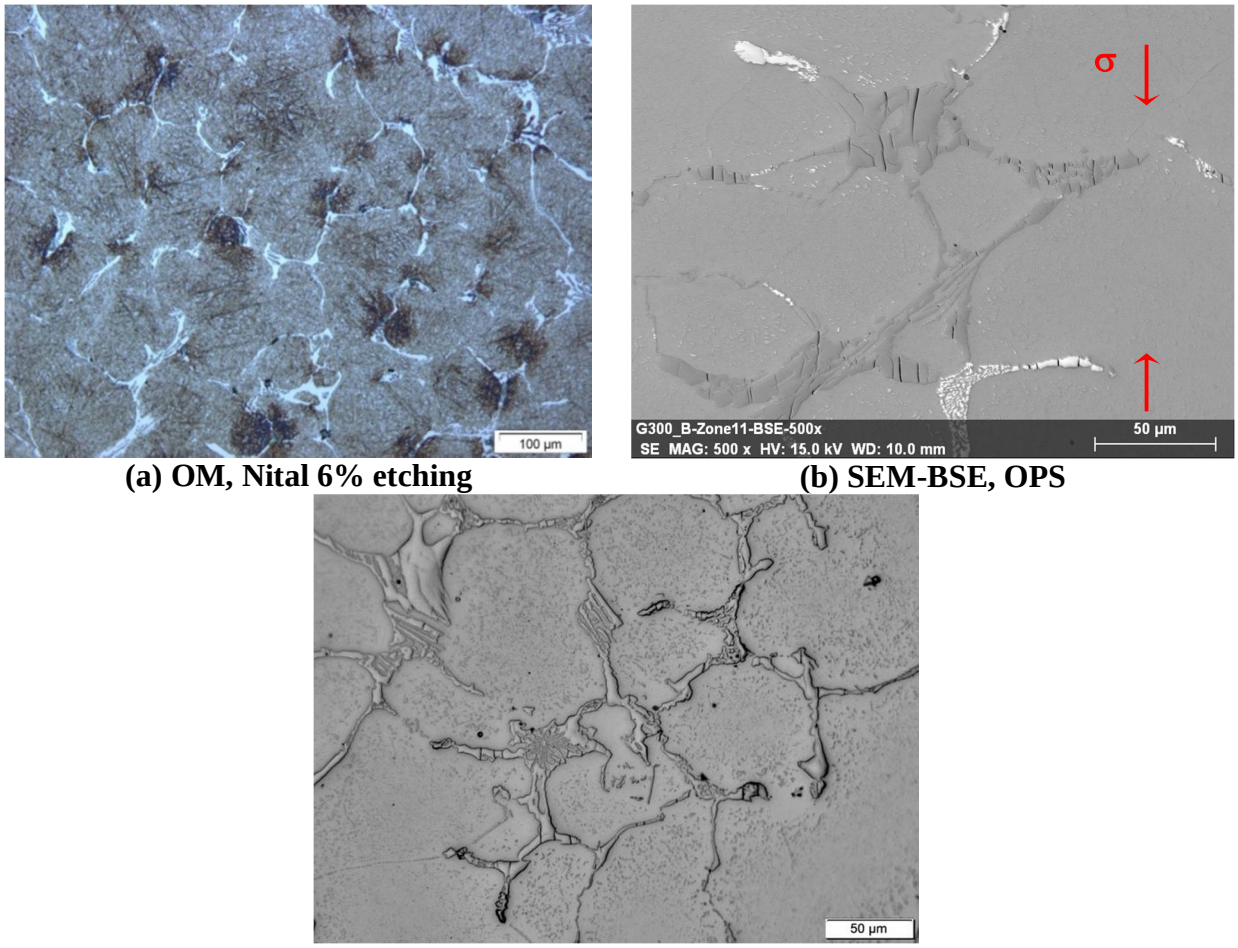

(a) OM, Nital 6% etching **(b) SEM-BSE, OPS**

(c) OM, OPS

Figure 3.19. Microstructures obtained after compression tests on CT300-B [82]

3.1.7.3 Microstructure characteristic of CT700 samples

For the CT700 samples, very few large oriented bainitic sheaves are observed inside the grains, the rest of the matrix being composed of martensite and retained austenite (Figure 3.20(a)). This later phase is probably present in an amount higher than that in the previous CT300 samples. Such an assumption is supported by two observations. First, the apparent volume fraction of the bainitic sheaves in the CT700 samples seems to be lower than the one observed within the CT300 samples. Second, the low sensitivity of the etched sample to the Nital reagent suggests that the austenite phase which remained un-etched is present in a significant amount. Similar to CT300-A, and CT300-B, intragranular secondary carbides and precipitate free zones (PFZ) are enhanced in the optical micrograph after OPS preparation (Figure 3.20 (b)). Cracks observed in

Figure 3.20 (b) are initiated on grain boundary of primary carbides and they are parallel to the applied stress.

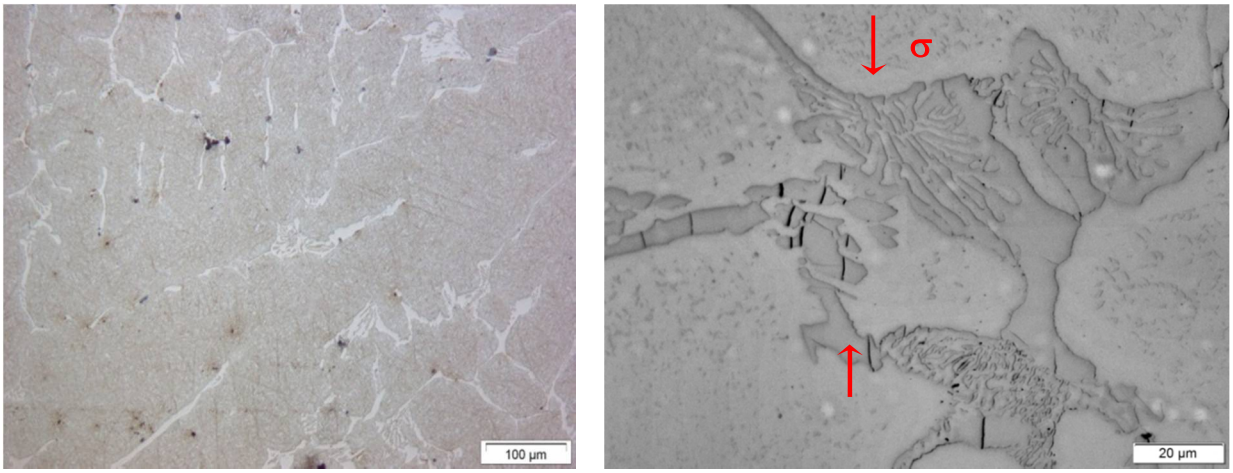

(a) OM, Nital 6% etching **(b) OM, OPS**

Figure 3.20: Microstructures obtained after compression tests on CT700 [82]

3.1.7.4 Microstructure characteristic of stress free sample

While all the compressed samples seem to exhibit preferential oriented bainitic sheaves in various amounts and sizes, the stress-free SF300 sample contains large quantities of sheave-like bainite structures with haphazard oriented directions inside grains (Figure 3.21(a)). In addition, the grain boundary carbides do not exhibit cracks as no external stress was applied. Widespread secondary carbides are present inside the grains with PFZs around them (Figure 3.21(b)).

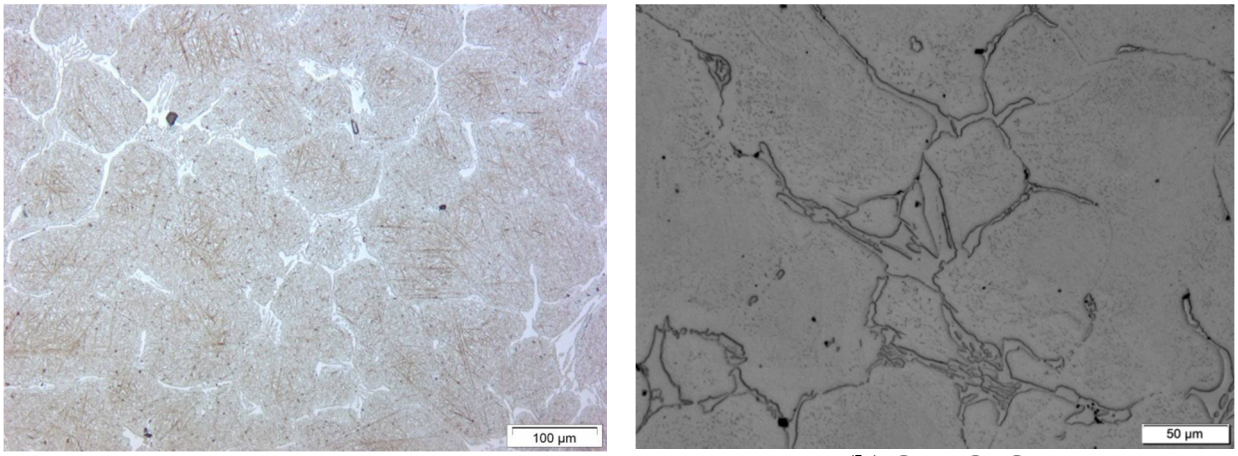

(a) OM, Nital 6% etching **(b) OM, OPS**

Figure 3.21: Microstructures obtained on the stress-free sample (SF 300) [82]

3.1.7.5 Discussion

From the microstructures presented in Figure 3.18 and Figure 3.19, it is possible to confirm that bainite phase has been transformed in austenite HCS compression test samples. It is known that chemical composition of the parent austenite may change the critical phase transformation temperatures and also that the uniaxial applied stress can increase the start of the bainitic reaction while hindering the transformation of non-favorable oriented grains at the same time [99, 100]. Optical micrographs of compressed samples either at 300°C (Figure 3.18(a) and Figure 3.19(a)) or at 700°C (Figure 3.20(a)) show typical bainitic sheaves oriented following preferential directions, contrary to the stress-free samples (Figure 3.21a), which exhibit haphazardly distributed sheaves of bainite. The stress applied at both 300 and 700°C enhance bainitic transformation under variant selection whereas that stress-free deformed austenite yield to haphazardly distributed sheaves of bainite [101] as observed in the SF300-B sample (Figure 3.21(a)).

At the same time, the microstructure of the samples tested at 700 °C is different from that of the samples tested at 300°C. In the former samples, bainitic sheaves are thicker but in relatively low quantity and the retained austenite seems to be present in a higher amount. These results are in good agreement with Hase et al. [99] who found that stress assisted transformation results in large blocks of bainite in identical orientation, the sheaves growing under the influence of stress being thicker than those occurring without stress. The fact that the apparent amount of bainitic sheaves seems to decrease with the increasing temperature of the compression tests seems to be consistent with previous works [102–105].

Furthermore, the work hardening rate curves of all the tested samples show Stage III and Stage IV (Figure 3.17). This observation is in agreement with the work of Kalidindi [106], where FCC polycrystals with high stacking fault energy (SFE), plastically deform by slip alone, contrary to low SFE FCC metals (plastic deformation by both slip and twinning). In addition, the first two stages (I and II) predicted by Kocks and Mecking [107], are hardly observed for FCC polycrystals with high SFE, which are similar to the HCS alloy studied in this thesis. HCS behavior at 700 and 300°C fits the above definitions of Stages III and IV very well, except for the CT300-A samples, which exhibit Stage III well above that of the other samples. This difference can only be explained through the microstructure itself. It is established that the

preliminary reheating and cooling sequence prior to the compression test can strongly influence the composition of the matrix and its contents in undissolved tertiary carbides θ.

Undissolved tertiary carbides θ-cementite (M_3C) significantly strengthen the HCS alloy under compression stress at 300°C, This phenomenon delays the cracking initiated on grain boundary primary carbides. The reason for the higher strengthening effect observed for the CT300-A samples when compared to the CT300-B samples, may be related to the presence of undissolved ultrafine and coherent with the austenite matrix transition carbides in the former samples, that should heavily impede dislocation glide under the Orowan mechanism [78, 107]. Similar transition carbides might have been more or less dissolved in the CT300-B samples due to their low reheating rate.

Secondary carbides present in the HCS alloy consist of $M_{23}C_6$ carbides. They remain undissolved after the reheating stage up to 950°C prior to compression, regardless of the reheating rate previously used. But contrary to tertiary carbides, the secondary carbides may have little influence on the strengthening effect due to the very few coherency relationships with the newly formed austenite.

Primary carbides are made of Cr-rich M_7C_3 carbides and Mo-rich M_2C carbides, which are located at grain boundaries. However only the M_7C_3 carbides, which are the majority of the grain boundary carbides, contain more or less cracks that are related to the total elongation achieved under the external compression stress applied (Figure 3.18(b), Figure 3.19(b) and Figure 3.20(b)). The crack path is made of primary carbides containing cracks parallel to the external compression stress (CT300-A samples, Figure 3.18(b)). However with increasing strain, the crack path changes to a more complex oriented one (CT300-B samples, Figure 3.19(b)) probably ascribed to the progress of the internal damage process with the micro-plastic strain evolution, which allows the occurrence of other critical shear directions within the carbides.

At 700°C the softening and damage phenomena are studied. In fact, all the samples tested at 700°C exhibit a similar flow curve regardless of the heating rate used to reach the austenitization at 950°C. Therefore, no strengthening effect can be expected from the presence (CT700-A samples) or the lack (CT700-B samples) of undissolved tertiary carbides within the matrix. Consequently, the leading mechanism occurring in the 700°C samples during the compression

tests may correspond to the ‘‘softening dynamic recovery’’ phenomenon, which involves a reduction of dislocation density by mutual annihilation [108–110]. The carbide micro-cracking observed at 700°C may be similar to the mechanism which occurs at 300°C, with narrow cracks for the higher compression temperature and large and branching cracks for the lower compression temperature. The final result is a smaller fracture strain at 700 than at 300°C.

3.1.7.6 Conclusions

Studied HCS material after casting and subsequent hardening treatment is made of a mixed martensite and retained austenite matrix with both Cr-rich M7C3 and Mo-rich M2C primary carbides located at the grain boundaries, and widespread Cr-rich M23C6 secondary carbides inside the grains. It was clarified that compressed austenite, either at 700 or at 300°C, yields bainite with preferentially oriented sheaves, this transformation is a key factor in the strengthening mechanism of the HCS material. The ‘‘softening dynamic recovery’’ phenomenon for samples compressed at 700°C was discussed. In addition, the influence of different carbides was elucidated. Primary carbides represent a critical feature in damage mechanism initiation. Secondary carbides increase the hardness of the matrix inside the grains. Finally, undissolved tertiary carbides influence significantly the strengthening mechanism, especially on samples compressed at 300°C. These tertiary carbides θ-cementite (M_3C), are not identified since they are instable and might disappear during cooling, however their presence during compression tests in the quickly heated sample has been supported through literature review [82] and by comparison of the mechanical behavior and the microstructure of two samples compressed at 300°C with different heating rate samples.

3.2 Fracture stress and strain by tensile tests

Tensile tests at different temperatures for SGI material were performed with the ZwickRoell 100kN press (Figure 3.22(a)) and H&K 3x400V+N furnace. For HCS material, the ZwickRoell 600kN press and Maytec 3x400V+N1 furnace were used. As cast samples were subjected to tensile tests, as the material must be characterized from real composition and not by phase as the case of compression tests [79]. Cylindrical samples were cut out from rolling mill rolls and

machined for giving the proper shape. The obtained shape for SGI samples is shown in Figure 3.22(b).

(a) Zwick 100kN machine

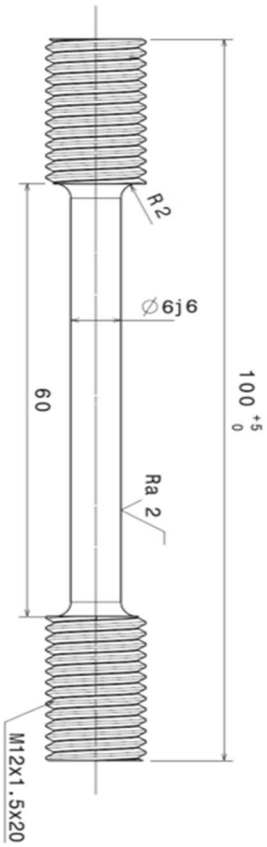

(b) Sample geometry of SGI material

Figure 3.22. Machine and sample shape for tensile tests

Samples were tested at room temperature but also at high temperatures. In the latter case, samples were reheated at 0.1°C/s until the test temperature and tensile force was applied until rupture. Two samples were tested for each temperature and material. Table 3.7 summarizes the details of the test campaign. This section presents the post treatment of the results to obtain significant curves, the fracture stress and strain from tensile tests and fractography analysis.

Table 3.7. Summary of data for tensile tests

Material	Temperature (°C)	Samples dimensions	Phase content at room temperature
SGI (Core)	20 150 300 500	ϕ: 6 mm L: 60 mm	Fe: 17% Pe: 83%
HCS (Shell)	20 150 300 500	ϕ: 6 mm L: 50 mm	Au: 50% Ma: 50%

3.2.1 Corrective procedure

In the Laboratory of Mechanics and Structures (ArGEnCo Department, University of Liège), the ZwickRoell 100kN and 600kN press are available and were used for the experimental determination of fracture stress and strain of samples. However, extensometer implementation is only possible for tests performed at room temperature. Therefore, at different temperatures, the machine elongation must be estimated and excluded from the tensile tests results ("brut" curve).

The corrective procedure applied for the machine deformation subtraction to reach true sample deformation for tensile tests performed at high temperatures (150°C - 500°C) is depicted presenting the case of SGI 150°C as example. The same methodology was performed for each tensile test performed at high temperature for both materials.

In fact, the "brut" tensile test defines the sample-machine system stiffness k_T, whereas for the obtaining of the true sample stiffness k_s an extensometer should be implemented at the machine. As for high temperatures, the implementation of extensometer is not possible; a reference curve must be defined. In this procedure, the Young modulus value obtained from compression tests was used for the definition of the reference curve.

The strain is computed by eq. 3.7 and the engineering stress is given by eq. 3.8.

$$\varepsilon = \ln\left(\frac{L_f}{L_i}\right) = \ln\left(\frac{L_i + d_s}{L_i}\right) = \ln\left(1 + \frac{d_s}{L_i}\right) \qquad \textbf{3.7}$$

$$\sigma = \frac{F}{A_0} \tag{3.8}$$

where L_i and L_f are the initial and the final lengths of the sample and d_s is the sample variation of length or displacement. F is the applied load and A_0 the initial area of the sample perpendicular to F.

Young modulus E, is defined as the quotient between elastic stress and strain, given by:

$$E = \frac{\sigma}{\varepsilon} \tag{3.9}$$

From eqs. 3.8 and 3.9. the strain can be written as:

$$\varepsilon = \frac{F}{E \cdot A} \tag{3.10}$$

Using eqs.3.7 and 3.10, the sample displacement can be computed as:

$$d_s = L_i \left(\exp\left(\frac{F}{E \cdot A} \right) - 1 \right) \tag{3.11}$$

For a tensile test, the total elongation d_T from the "brut" curve includes the displacement of the sample d_s and the machine d_m and can be written as eq. 3.12. In addition, the elongation can be expressed as the quotient between the load and the stiffness as in eq. 3.13.

$$d_T = d_s + d_m \tag{3.12}$$

$$\frac{F}{k_T} = \frac{F}{k_s} + \frac{F}{k_m} \tag{3.13}$$

Reordering previous equation, the machine stiffness can be computed by eq. 3.14.

$$k_m = \left(\frac{1}{k_T} - \frac{1}{k_s} \right)^{-1} \tag{3.14}$$

The sample-machine system stiffness k_T is given by the "brut" tensile test. The true sample stiffness k_s is given by the slope of the reference curve (defined by Young modulus) computed from eq. 3.11. Figure 3.23 shows the reference and the "brut" curves obtained for SGI 150°C tensile test. From both curves, k_T and k_s slopes are computed and the stiffness of the machine for SGI 150°C test k_m is retrieved.

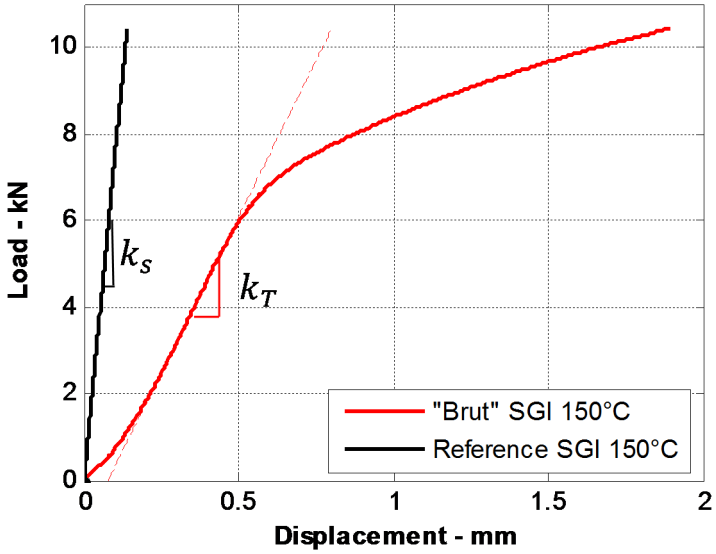

Figure 3.23. Reference and brut curves for SGI 150°C

The true sample displacement can be computed using eq.3.15. Figure 3.24 shows in red the "brut" curve, in black the reference curve and in blue the corrected load-displacement curve. Note that the mismeasured displacements at the beginning of the test are neglected shifting to 0 the corrected curve.

$$d_s = d_t - d_m = d_t - \frac{F}{K_m} \qquad \textbf{3.15}$$

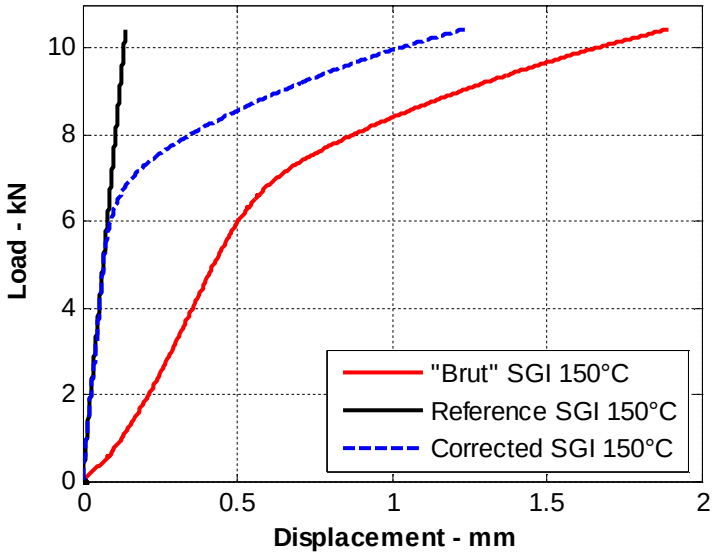

Figure 3.24. Brut and corrected curves for SGI 150°C

Finally, stress-strain curve can be computed from the final corrected load-displacement curve using eqs.3.7 and 3.8. Proper values of fracture stress and strain can be obtained by considering the last point of the curve.

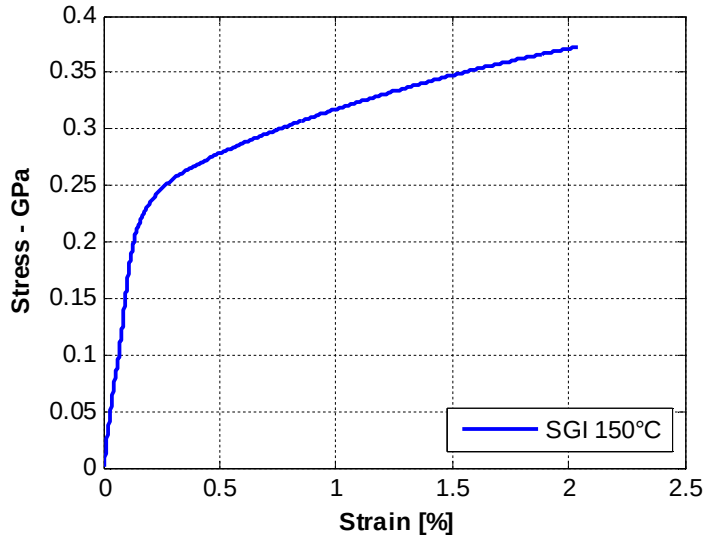

Figure 3.25. Stress-strain curve from corrected tensile test for SGI 150°C

3.2.2 Stress-strain curves

Corrected stress strain curves for tensile tests at different temperatures for both SGI and HCS materials are presented in Figure 3.26 and Figure 3.27 respectively.

For SGI grade, in Figure 3.26 it is possible to observe that between room temperature and 150°C, the fracture strain increases as the grain size is increased. This effect has been previously studied by [111]. However, from 150°C to 500°C, the ductility of the material is reduced due to oxidation phenomena as it has been analyzed by several authors as Hung-Mao, Tholence and Minnebo [112–114]. Note that SGI samples tested come from as-cast conditions and contain ferrite, pearlite and graphite nodules.

On the other hand, Figure 3.27 shows that for HCS material, the lower fracture strain is presented at 150°C. This embrittlement is explained due to the precipitation of ε carbides that is typically occurring between 80°- 300° as it is studied by Bala in [96, 97]. The same phenomenon has been previously observed for the strengthening of HCS material during compression tests and it was studied in section 3.1.6. These carbides are subsequently dissolved during heating as it is confirmed through the increment of the fracture strain for 300°C and 500°C. Note that HCS samples tested, come from heat treated HCS grade and contain martensite, residual austenite and carbides.

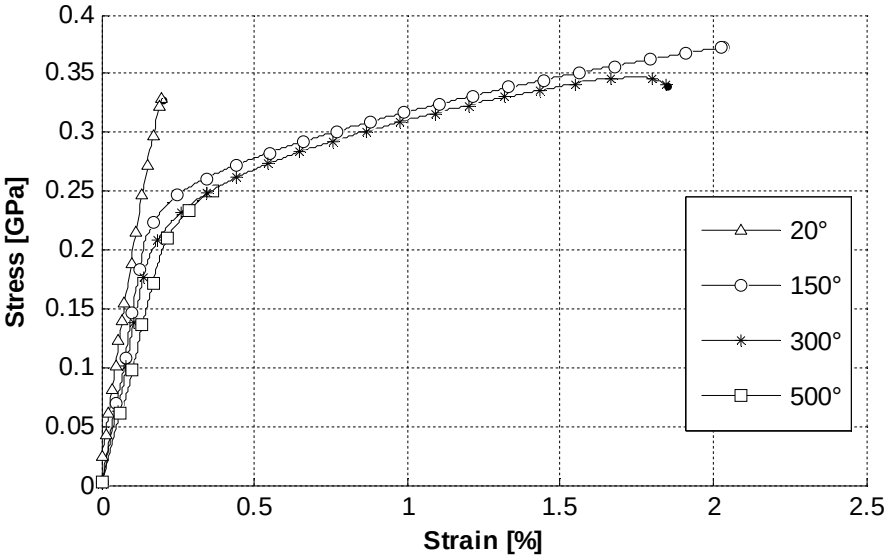

Figure 3.26. Experimental tensile stress-strain curves for SGI material

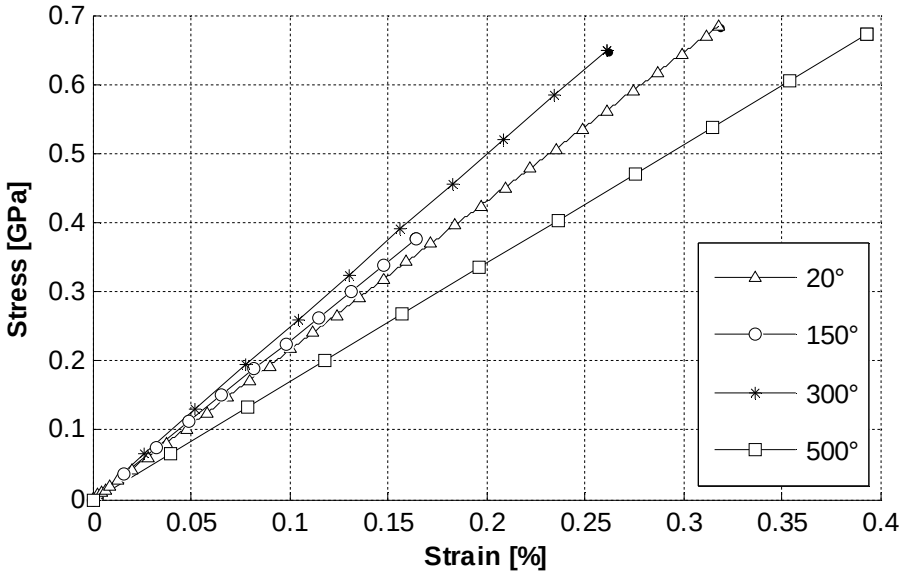

Figure 3.27. Experimental tensile stress-strain curves for HCS material

3.2.3 Properties

Fracture stresses and strains obtained from corrected tensile tests are summarized in Table 3.8 and can be used for rupture prediction of both SGI and HCS materials at different temperatures.

Table 3.8. Fracture stress and strain obtained by tensile tests

Material	Temperature (°C)	σ_{max} (MPa)	ε_{max} (%)
SGI (Core)	20	330	0.199
	150	372	2.033
	300	341	1.844
	500	250	0.364
HCS (Shell)	20	683	0.318
	150	375	0.165
	300	649	0.261
	500	672	0.393

3.2.4 Fractography analysis

Outcomes of fractography analyses performed on samples that failed after tensile tests for SGI material are presented in this section. Fractography analysis for HCS material is not included since it was not performed on time for this thesis. However it will be part of the PhD thesis of J. Tchoufang Tchuindjang [5]. Fractography analysis was performed by a Scanning Electron Microscope (SEM) using an XL30 FEG-ESEM Phillips apparatus equipped with a BRUKER 129 eV EDS microanalysis having a SDD.

For the two samples tested at each temperature, the same fracture surface is observed. Figure 3.28 shows the SEM image of broken samples at 150°C and 500°C. The fracture surface of SGI sample tested at 150°C illustrated in Figure 3.28(a) is quite similar to the fracture surface of sample tested at 300°C. For both samples, ductile failure mode is observed almost everywhere, except for primary cementite carbide. Typical dimples characteristic of the plastic deformation prior to failure have been observed on the fracture surface. These dimples can be spread over two distinct groups, depending on their size. The larger dimples ranging between 20 and 100 µm are always associated to graphite nodules while ultrafine dimples having size below 1 µm are located inside the matrix. For primary cementite carbides, brittle failure mode happens since typical transgranular cleavages are observed on the cracked carbide. For samples tested at 150 and 300°C (see Figure 3.28 (a)), the fracture surface seems to be free of surface oxidation, however for samples corresponding to 500°C, oxidation occurs quite everywhere making difficult to observe the fracture surface (Figure 3.28 (b)). Without surprise, oxidation already present during the test reduces the ductile behavior as it was presented in Figure 3.26 and Table 3.8. This effect has already been analyzed by others authors in [112–114].

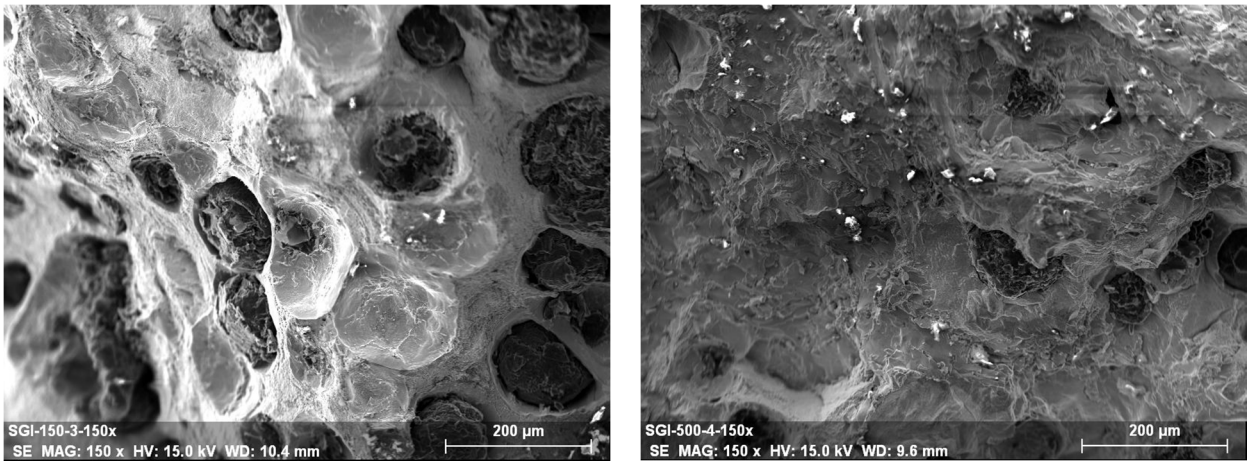

(a) 150°C **(b) 500°C**

Figure 3.28. Fracture surface corresponding to tensile test of SGI samples

3.3Thermophysical characterization

Experimental thermophysical characterization of SGI and HCS materials was performed in the MMS laboratory and it is fully described in [115][116]. In order to gather all the information and explain the characterization method, these test results and important features about experimental procedures are presented here. DSC, laser-flash and dilatometry methods were used. Samples used for testing come from a bimetallic mill roll after casting and associated heat treatment [79].

3.3.1 Coefficient of thermal expansion

Dilatometry method is useful for a precise measurement of volume expansion in materials during a controlled temperature variation. Dilatometer NETZSCH - 402C was used. Each tested sample was reheated at 3°C/min up to 1025°C with a holding time of 1 hr and then cooled to room temperature at 3°C/min. Results of linear dilatation curve are presented in Figure 3.29.

$$\alpha_{metallurgist}(T) = \frac{\frac{\Delta L(T)}{L_0}}{T - T_0} \qquad \textbf{3.16}$$

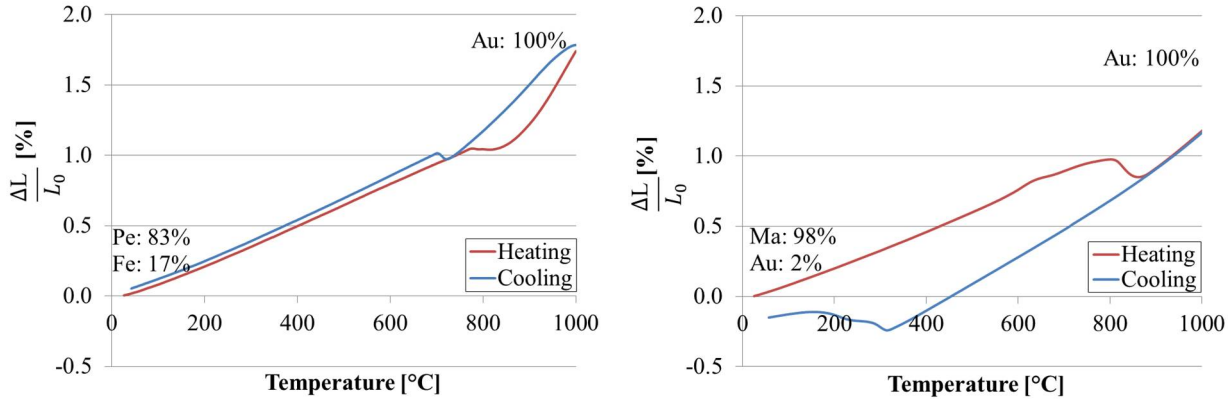

(a) SGI material **(b) HCS material**

Figure 3.29: Experimental dilatometry curves for SGI and HCS materials

From these experimental curves, it is possible to compute classical metallurgist Coefficient of Thermal Expansion (CTE) using eq. 3.16 (see results in Figure 3.30). Resultant incremental CTE for non-linear FE code α_{FE} for each case are computed [117] and correspond to the parameters considered for cooling and heating simulations.

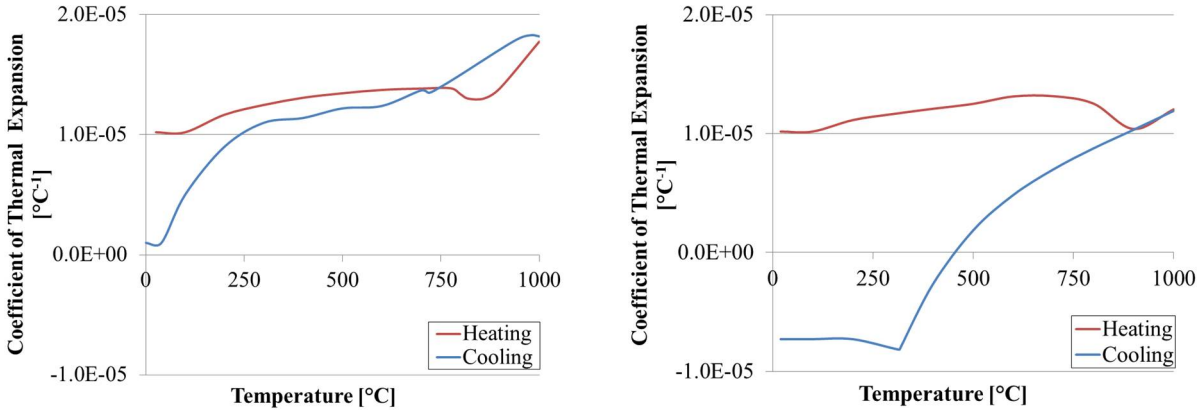

(a) SGI material **(b) HCS material**

Figure 3.30: Metallurgical CTE including phase transformation for SGI and HCS materials

3.3.2 Density

Density $\rho(T)$ at room temperature was measured by the double weighting method. Results of the computed density at different temperatures for SGI and HCS grades are presented in Figure 3.31 and are obtained using values of CTE previously computed by dilatometry tests.

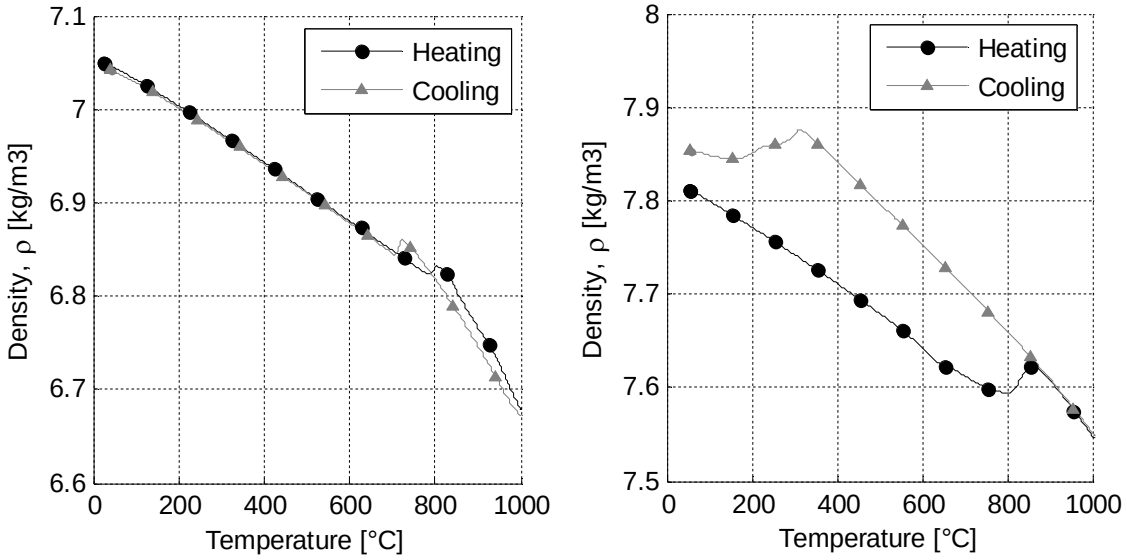

(a) SGI material **(b) HCS material**

Figure 3.31. Density measured for SGI and HCS materials

3.3.3 Thermal capacity

Differential Scanning Calorimetry (DSC) is a useful technique which measures the difference of heat required to increase the temperature of a new sample and for a reference sample. The device used was the NETZSCH DSC 404C. The result of this test is a curve of heat flux versus temperature or time. Post treatment is done by a software associated wiht the apparatus to compute thermal capacity $C_p(T)$. Results of the computed thermal capacity are presented in Figure 3.32.

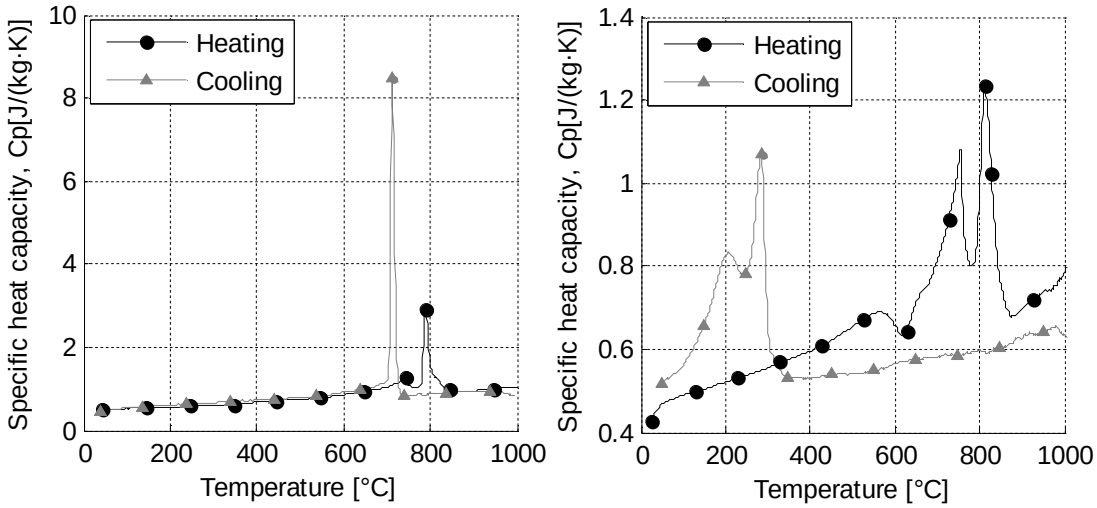

(a) SGI material **(b) HCS material**

Figure 3.32. Specific heat capacity evolution for SGI and HCS materials

3.3.4 Thermal diffusivity and Thermal conductivity

Thermal diffusivity $\alpha(T)$ was measured by the laser flash method using a NETZSCH LFA 427 device. Thermal conductivity $\lambda(T)$ can be retrieved from the previous parameters obtained by dilatometry, DSC and by the thermal diffusivity using eq. 3.17.

$$\lambda(T) = \alpha(T) \cdot \rho(T) \cdot C_p(T) \quad \textbf{3.17}$$

$\lambda(T)$ is the thermal conductivity in W/(m·K) if $\alpha(T)$ is the thermal diffusivity in mm^2/s, $\rho(T)$ the density in g/cm^3, and $C_p(T)$ the specific thermal capacity in J/(g·K).

Results obtained for thermal conductivity for both materials are presented in Figure 3.33.

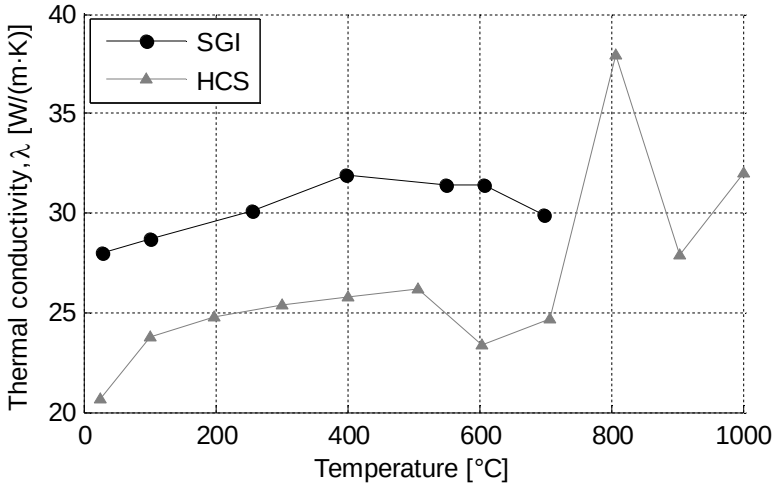

Figure 3.33. Thermal conductivity for SGI and HCS materials

3.3.5 Phase transformations from thermophysical results

From curves of **Figure** 3.29 and Figure 3.32, dilatometry and heat capacity curves allow confirming the phase transformations occurring for each material. During cooling of SGI grade, austenite phase is transformed to ferrite and pearlite phases within a short time period, generating one unique peak. Furthermore, the cooling of HCS material generates a coarser peak composed by three smaller peaks. This fact illustrates the carbides precipitation and that the austenite phase is transformed into martensite phase by parts and that transformation is not completed (see **Figure** 3.29(b)).

3.4 Martensite temperatures by cryogenic test

In order to find the start and end temperatures of martensite transformation, M_s and M_f respectively, cryogenic liquid nitrogen quenching was performed with one sample of HCS material (see Figure 3.34) with a continuous registration of the temperature. A brief description of experimental procedure and corresponding result are presented in this section.

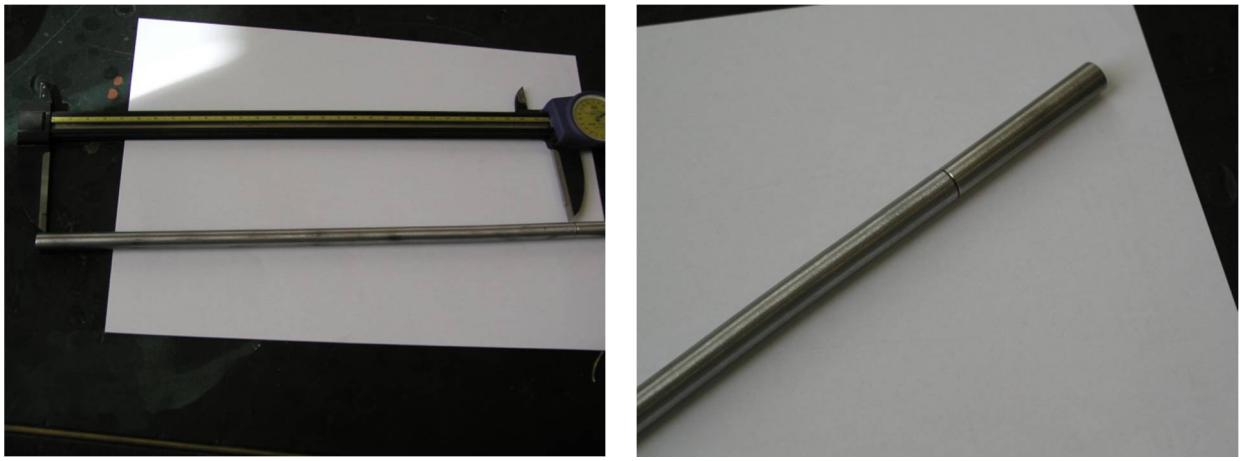

Figure 3.34. HCS sample for cryogenic test

3.4.1 Description

The HCS sample was subjected to an austenitization treatment prior to quenching. Figure 3.36 shows the heating curve, the sample is reheated in a BOUVIER TECHNOFOUR furnace equipped with a PID regulator and electrical resistances at 40°C/s until the austenitizing temperature of 1025°C (the furnace is at 1025°C when the sample is introduced) with a holding time of 1 hr. Then, from 1025°C direct quenching in liquid nitrogen is applied. During the whole procedure, the thermocouple placed into the sample allows registration of temperature by a data logger, achieving one acquisition every 0.105 sec. Sample was cylindrical of 80 mm height and 10 mm diameter with a hole of 40 mm for the thermocouple placement.

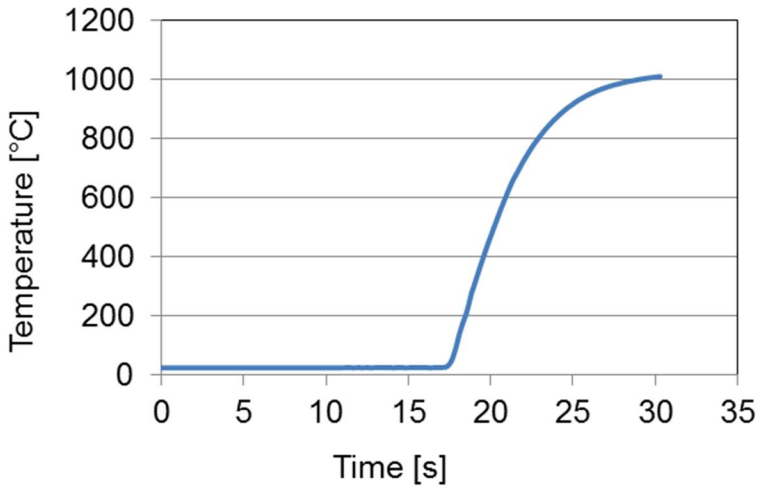

Figure 3.35. Temperature – time curve for heating of HCS sample

3.4.2 Results

Figure 3.36 shows the resulting temperature - time curve and the corresponding first derivative dT/dt curve computed in order to find critical points (slope changes) related to the different martensitic transformations that can occur. As shown in Figure 3.36, a zone with four noticeable peaks is registered in dT/dt curve, representing the growth of martensite phase inside grains and at grain boundaries (two types of carbides are present at grain boundaries). Further explanations can be found in [5]. However, for modelling purposes two points are important to identify; M_s point for the beginning of martensitic transformation in the matrix (266°C), and the M_f point corresponding to the end of transformation inside grains (-41°C). M_s temperature will be considered for the FE modelling of HCS phase transformation. M_f point helps to recover the coefficient of Koistinen-Marburger equation (see eq. 2.11)

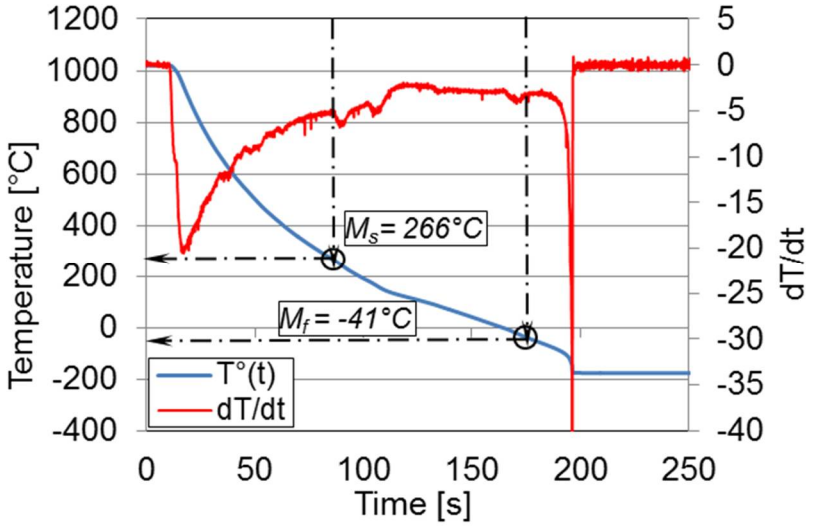

Figure 3.36. Temperature – time curve and first derivative from cryogenic quenching of a HCS sample

3.5 TTT diagrams by inverse method

The high difficulty and cost for the experimental determination of TTT and CCT diagrams is well known. Consequently, the available literature for SGI and HCS is quite limited. For both materials, TTT diagrams were obtained using inverse method through FE code using a CCT diagram as input data [118]. Important features are presented in this section.

The procedure schematized in Figure 3.37, starts from an experimental CCT diagram (CCT_{exp}) obtained from the literature for two materials quite similar to the studied SGI and HCS materials. In addition, an initial TTT diagram (TTT_{ini}) coming from a similar material for SGI and computed by Kirkaldy formulation [119] for HCS, is considered as a first approach in order to describe the kinetic of transformations. These data are the initial input data for the cooling modelling by one finite element of Figure 3.38 with four nodes and four integration points for a thermo-metallurgical analysis, the temperature history is imposed and the phase transformations are computed. Different cooling rates are modeled by LAGAMINE code, as result the code gives a numerical CCT diagram (CCT_{num}) associated to the input TTT diagram (TTT_{ini}). The TTT_{ini} diagram is modified until a CCT_{num} diagram closer to the experimental one is obtained. Additionally, a software complementary to "Lagamine" called "ManageLagTTT" allows the automatization of iteration process by automatically modifying the input TTT_{ini} diagram according to a set of parameters given by the user. Once a minimal error between CCT_{exp} and CCT_{num} is computed, the final TTT diagram (TTT_{final}) is found. Corresponding error is computed for each phase k using eq. 3.18 where $y_i\ exp$ and $y_i\ num$ are the amounts of phase k at each point i in experimental and numerical CCT diagrams respectively.

$$Error_k\ (\%) = \frac{\sum_{i=0}^{n}(y_i\ exp - y_i\ \text{num})}{\sum_{i=0}^{n} y_i\ exp} * 100 \qquad \textbf{3.18}$$

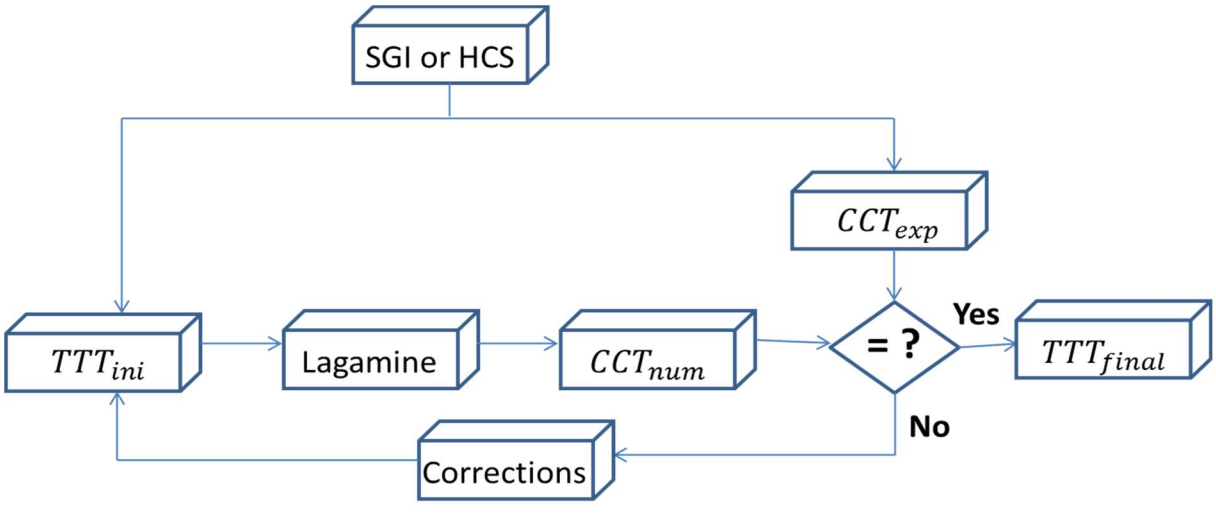

Figure 3.37. Scheme of TTT diagram obtaining by inverse method

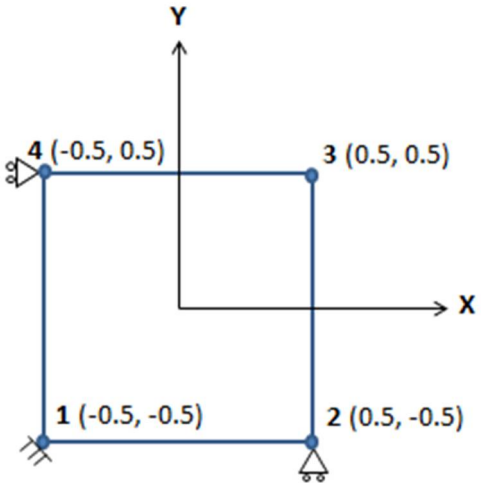

Figure 3.38. Finite element used for TTT diagrams determination (coordinates in m)

3.5.1 SGI grade

After several trials, the CCT_{num} diagram of Figure 3.39 (a) is found. It generates a minimal total error of 16% (using eq.3.18) in comparison with CCT_{exp} diagram [120], as it is presented in Table 3.9. This CCT_{num}diagram is associated to the TTT_{final} diagram of Figure 3.39 (b) corresponding to a ferritic SGI grade (solid lines) which contains 80% Ferrite and 20% Pearlite in the core of the rolling mill roll.

An updated version of this TTT_{final} diagram is obtained by considering red segmented lines that correspond to delayed curves of 10% and 90% of ferritic transformation. Curve of ferritic transformation start (0.1%) was not modified. This modified version of TTT_{final} diagram is useful for the representation of the kinetic of a pearlitic SGI grade and will be considered for the modelling of rolling mill rolls. Considering the roll temperature history and the modified TTT_{final} diagram, the FE simulation generates a core structure containing 75% Pearlite and 25% Ferrite phases.

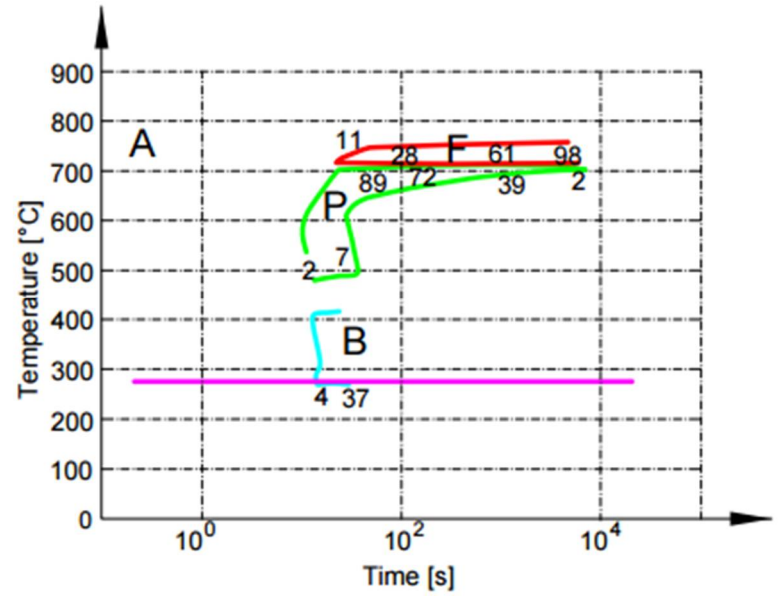

(a) CCT_{num} diagram

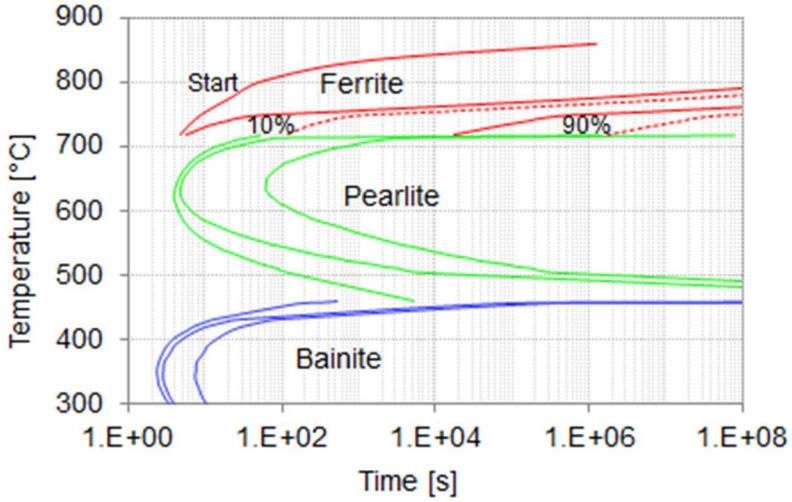

(b) TTT_{final} diagram

Figure 3.39: CCT diagram and TTT diagram used for SGI core material

Table 3.9. Phase rates predicted by experimental and numerical CCT diagrams for SGI grade

Phase	Cooling rate (°C/min)	%Phase CCT exp (y exp)	%Phase CCT num (y num)	y exp - y num
Ferrite	2790	0	0	0
	1860	0	0	0
	620	3	0	3
	350	10	11	1
	220	20	17	3
	20	50	59	9
	10	100	75	25
Pearlite	2790	0	0	0
	1860	3	2.5	0.5
	620	95	100	5
	350	90	89	1
	220	80	83	3
	20	50	41	9
	10	0	25	25
Bainite	2790	0	0	0
	1860	37	37	0
	620	2	0	2
	350	0	0	0
	220	0	0	0
	20	0	0	0
	10	0	0	0
Sum		540		86.5
Error (%)				16.02

3.5.2 HCS grade

For HCS, several trials allowed finding the CCT_{num} diagram shown in Figure 3.40 (a). The computed error in relation with the CCT_{exp} diagram [121] corresponds to 6% as it is presented in Table 3.10. The corresponding TTT_{final} diagram presented in Figure 3.40 (b) allows obtaining a shell structure containing 38% of retained Austenite and 62% of Martensite.

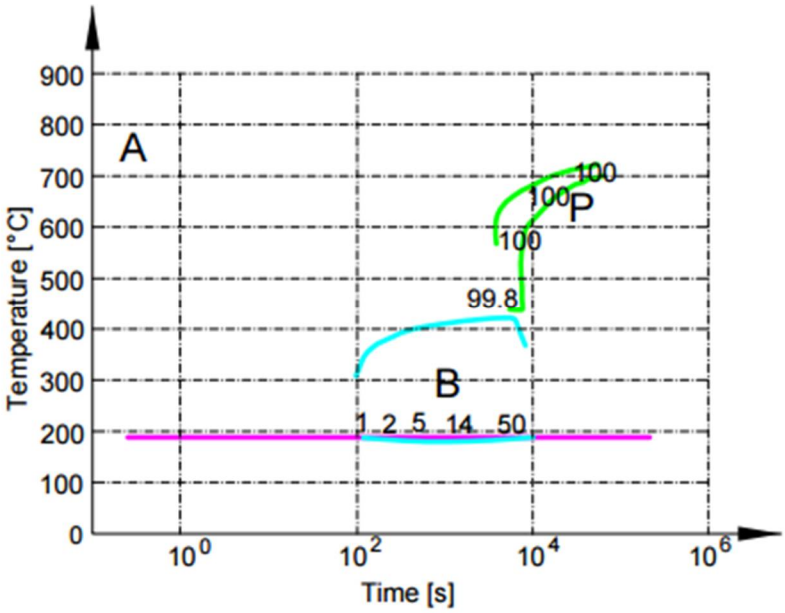

(a) CCT_{num} diagram

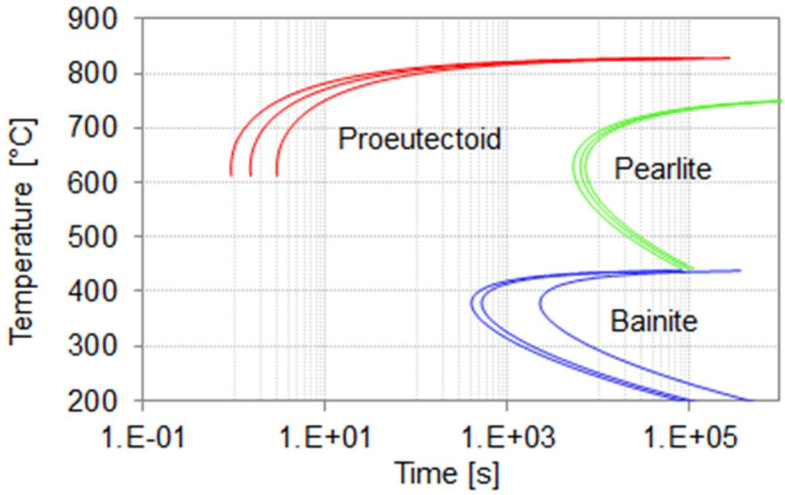

(b) TTT_{final} diagram

Figure 3.40: CCT diagram and TTT diagram used for HCS shell material

Note that for modelling of rolling mill rolls, only martensitic transformation is allowed in HCS as it has been confirmed by the quantitative analysis of phases performed. Therefore, HCS will be modelled considering only martensite transformation defined by martensite start transformation temperature M_s.

Table 3.10. Phase rates predicted by experimental and numerical CCT diagrams for HCS grade

Phase	Cooling rate (°C/min)	%Phase CCT exp (y exp)	%Phase CCT num (y num)	y exp - y num
Proeutectoid	29.4	0	0	0
	5.16	0	0	0
	3.78	0	0	0
	0.378	0	0	0
Pearlite	29.4	0	0	0
	5.16	8	12	4
	3.78	88	98	10
	0.378	100	100	0
Bainite	29.4	15	16	1
	5.16	65	64	1
	3.78	0	1.4	1.4
	0.378	0	0	0
Sum		276		17.4
Error (%)				6.30

3.6 Transformation strain by inverse method

For each phase transformation, a change of mass density is involved generating stresses and strains. The value of this parameter is specific for each material and each transformation undergone. Within the classical phase transformation model used in the LAGAMINE code [37], the transformation strain rate defined by eq. 2.19 is used to compute transformation strain for predicted phase of multiphase material. In this section, transformation strains for SGI and HCS materials are obtained through inverse modelling of dilatometry test during cooling (presented in section 3.3.1) [122].

3.6.1 Description

FE inverse modelling was performed in order to identify the correct value of austenite transformation strain to ferrite and pearlite phases ε_{Fe-Pe}^{tr} for SGI material and to martensite

phase ε_{Ma}^{tr} for HCS material. These parameters define the peaks at the moment of phase transformation within dilatation curves. The aim was to reproduce the cooling dilatometry curves provided by **Figure** 3.29 (a) and (b) by introducing the complete set of parameters found in this chapter as input data. The value of ε_{k}^{tr} was modified several times to reach accurate predictions of peaks appearing in the dilatometry curves for each material during the cooling sequence. Displacements computed must recover the variation of length experimentally measured. For SGI material, the same value of transformation strain was considered for ferritic and pearlitic transformation. For HCS material, only martensitic transformation case was studied.

3.6.2 Geometry and boundary conditions

Dilatometry test is modeled using one solid finite element with four nodes and four integration points for a plane thermo-mechanical analysis considering a generalized plane state problem where a fifth node defines the thickness of the element. Figure 3.41 presents the modeled geometry with corresponding initial coordinates and temperature. The cooling thermal history obtained from dilatometry tests presented in section 3.3.1 starting at 1000°C and finishing at room temperature is imposed at the four nodes. Node 1 is locked and the contraction or expansion of the element is computed by displacements of nodes 2 (only in x), 3 (in x and y) and 4 (only in y).

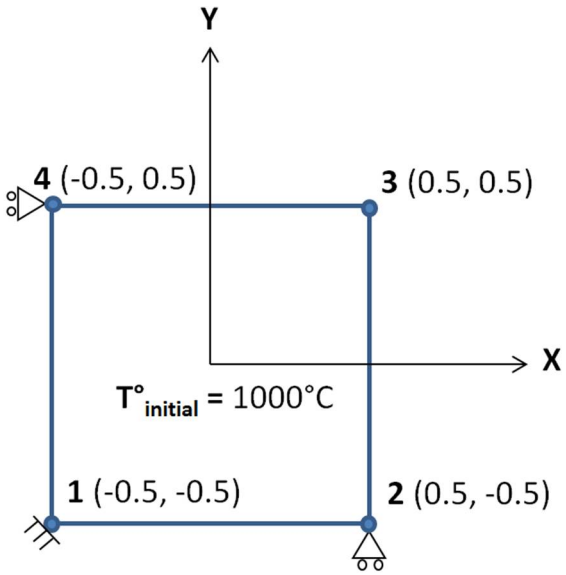

Figure 3.41. Finite element geometry for transformation strain determination

3.6.3 Results

Manual iterative simulations were performed to find suitable values of transformation strains. Some representative numerical curves are presented in Figure 3.42. For SGI grade, results obtained with values of ε_{Fe-Pe}^{tr} between 4.76E-04 and 11.76E-04 are shown in Figure 3.42(a) where it is possible to observe that a transformation strain of 7.76E-04 allows the closer peak shape to the experimental one. For HCS, in Figure 3.42(b) it is possible to observe that a couple of peaks in the experimental curve represent the different stages of martensitic transformation. However in the modelling of HCS martensite transformation only a single transformation strain at the end of cooling is required, therefore a value of ε_{Ma}^{tr} equal to 3.0E-03 allows the closer result as dilatation curve is adjusted at the test end. Values of transformation strain obtained through inverse method for SGI and HCS materials are summarized in Table 3.11.

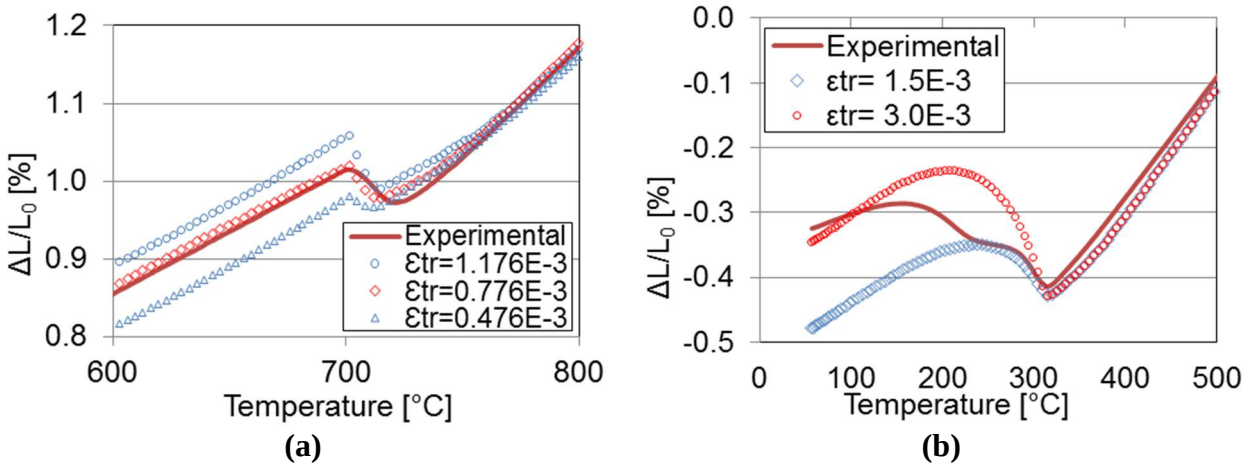

Figure 3.42. Modeling of dilatometry test for cooling (a) SGI (b)HCS.

Table 3.11: Transformation strain values

Material	Transformation strain
SGI (Ferritic and pearlitic transformation)	ε_{Fe-Pe}^{tr} = 7.76E-04
HCS (Martensitic transformation)	ε_{Ma}^{tr} = 3.00E-03

3.7 Latent heat by inverse method

The phase transformations happening during cooling, such as transformation from austenite to pearlite or ferrite phases in SGI and to martensite phase in HCS, generate a latent heat that increases the temperature. Latent heat L (J/m^3) is specific for each steel and can be measured by the area under the peaks of DSC (Differential Scanning Calorimetry) curves. However, this method needs the identification of a reference line without transformation. This procedure could not be followed as our trials with extrapolated reference curves yields to values far from the range found in literature. The determination of latent heat was finally achieved through inverse method.

3.7.1 Description

The target was to predict similar temperature histories to the measured curved affected by phase transformation during cooling of SGI and HCS materials. Cylindrical samples of 9 mm diameter and 16 mm height were heated at 1000°C (SGI) and 600°C (HCS) using a quad elliptical radiant furnace 4x2000W of MSM laboratory. Samples connected to a thermocouple (at the surface) for the temperature tracking were cooled until room temperature. Numerical simulations of samples cooling are performed using data obtained from previous sections. An iterative procedure until to reach a value of latent heat parameter that allows the reproduction of the experimental cooling curve was performed. Note that latent heat generated by ferrite and pearlite phase transformations in SGI material was assumed as a unique value. For HCS grade the experimental curve reproduced includes only martensitic transformation.

3.7.2 Geometry and boundary conditions

Axisymmetric simulations of the cooling of cylindrical samples are performed considering a thermo-mechanical analysis and the geometry shown in Figure 3.43. A quarter of the sample is modeled through 242 nodes and 210 elements with four integration points (CPL2D elements).

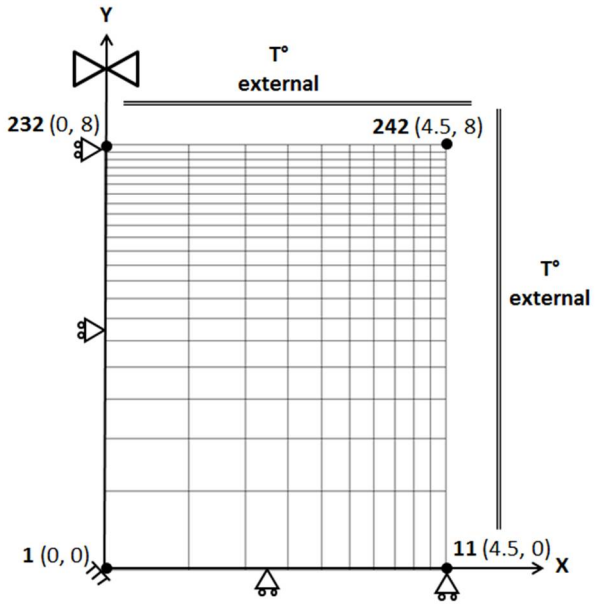

Figure 3.43. Finite element geometry for simulation of cooling for latent heat determination

An initial temperature of 1000°C and 600°C is imposed for SGI and HCS materials respectively while the room temperature is imposed and fixed near to the sample (CONRA elements). Therefore the cooling of the sample is achieved through thermal exchange. The heat exchange coefficient is identified through the beginning and the end of the thermal histories (outside transformations moments).

3.7.3 Results

Identified values of latent heat allowing close agreements with experimental curves (see Figure 3.44) are given in Table 3.12. They are in the range of literature values for other material grades [34, 79, 106].

Table 3.12. Summary of latent heat values obtained by inverse method with literature data

	Latent heat (J/m^3)			
	By inverse method	42CD4 grade [41]	60NCD11 grade [91]	18M5 grade [123]
Ferrite and Pearlite transformation	3.0E+08 (SGI)	5.9E+08		2.6E+08
Martensitic transformation	6.0E+08 (HCS)	6.4E+08	6.4E+08	

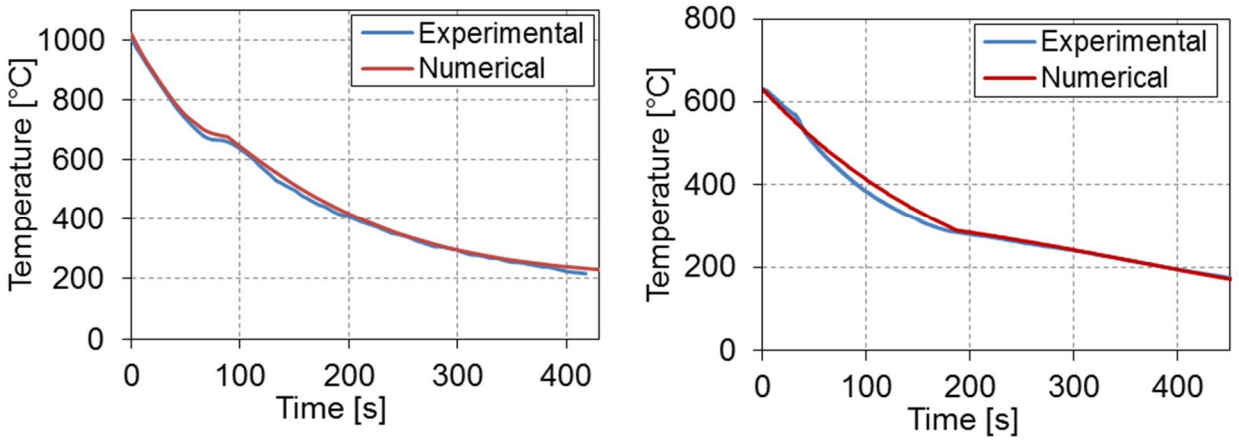

(a) SGI material **(b) HCS material**

Figure 3.44 Experimental and numerical cooling curve for latent heat determination of core and shell materials

3.8 Transformation plasticity coefficient by inverse method using compression tests and residual stress measurements

As it is shown in eq. 2.20, 2.21 and 2.22, transformation plasticity coefficients K_i are required by the FE code for the computation of transformation induced plasticity (TRIP) for ferrite and pearlite phases of SGI grade and for martensite phase of HCS grade. Two methods for computation of K_i coefficient were developed in this PhD thesis: inverse method applied on experimental compression tests and inverse method of experimental residual stresses measurements on real mill rolls of different sizes. The first method gives values of K_i quite in agreement with literature data which provides however a large range of possible values. However, their application in numerical simulations of bimetallic rolls, predicts residual stress profile of the mill roll considerably different from experimental measurements and previous predictions by other authors. Therefore, a second approach was developed in order to obtain transformation plasticity coefficients that generate results closer to the reality and still compatible with literature. Both methods are presented in this section.

3.8.1 Inverse method applied on compression tests

K_2, K_3 and K_6 coefficients corresponding to ferrite, pearlite and martensite transformation, are generated by inverse method of compression test results. The method as a combination of numerical predictions and experimental measurements is detailed in Figure 3.45.

Experimental compression tests considering thermal and load histories are modelled by introducing the set of parameters already obtained in this chapter (see Appendix B). Iterative simulations by shifting the value of K_i are performed until the achievement of a height reduction closer to the experimental one. The experimental and numerical procedures are applied for two samples of each material for two levels of loads.

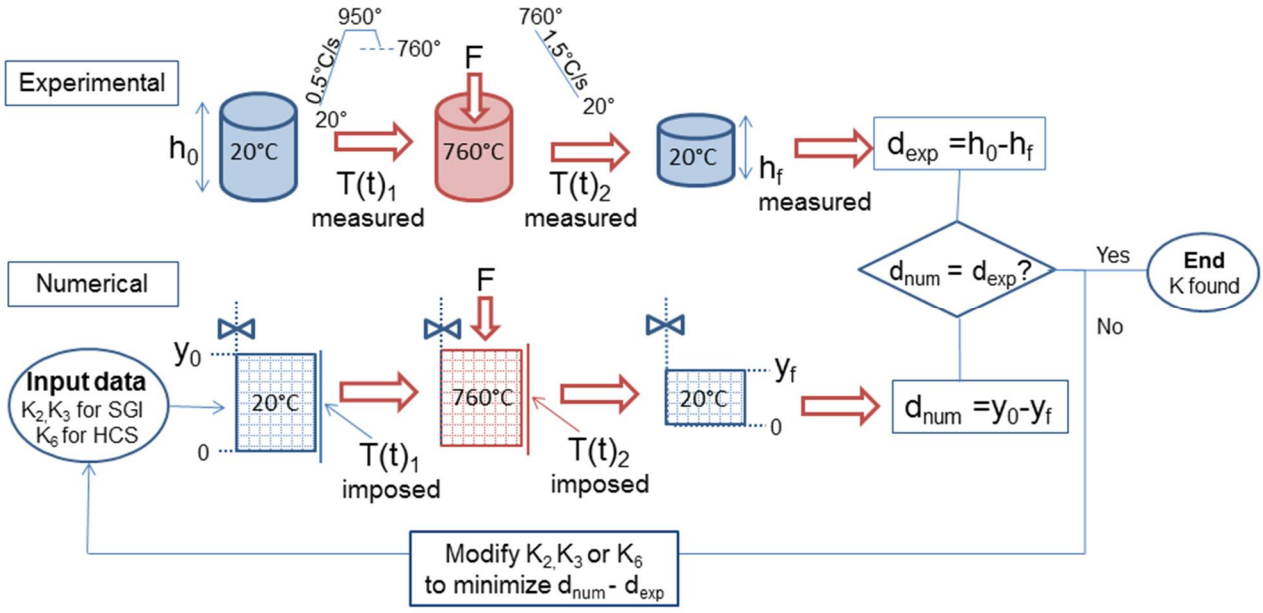

Figure 3.45. Flowchart of inverse method for determination of transformation plasticity coefficient (experimental temperature history is given for SGI samples)

3.8.1.1 Experimental compression tests

Experimental compression tests are performed in the SCHENCK Hydropuls 400kN press. For instance, for K_2 coefficient identification of SGI material, cylindrical samples are previously heated at 0.5°C/s until 950°C using a quad elliptical heater 4x2000W. Temperature is maintained during approximately 60s to achieve a fully austenite matrix. The next step is the sample cooling at 1.5°C/s until 760°C (fully austenitic state is assumed maintained) and compression force is

applied staying constant until the end of cooling (see Table 3.13). The same principal is applied to reach K_6 coefficient for HCS material, in this case the temperature values at the start of the compression is approximately 630°C. Within this experiment, phase transformations from the austenite matrix to martensite for HCS and to a mixture ferrite pearlite for SGI, happen under an applied stress. Transformation induced plasticity can be identified as two levels of force are defined (see Table 3.13). Each test is performed twice for identical force and temperature histories before and after the force is applied i.e. $T(t)_1$ and $T(t)_2$ are registered.

3.8.1.2 Numerical simulations

The simulations of compression tests on cylindrical samples take into account axisymmetric conditions and the mechanical behavior identified in section 3.1. The used thermophysical data are the dilatation coefficients and transformation strains obtained in section 3.3 and 3.6 respectively (see Appendix B). For SGI material, K_2 ferrite coefficient and K_3 pearlite one, equality is assumed [41]. Figure 3.46 presents the geometry of 210 elements and 242 nodes that model a quarter of the cylindrical sample. Simulations are performed in two stages. The first stage models the heating up to austenitization and the first cooling stage until the compression temperature, imposing the experimental temperature evolutions previously measured $T(t)_1$ at the surface of the sample. The second stage models the cooling step until room temperature under load through the imposed $T(t)_2$ experimental history and the measured compression force F applied at the top face of the sample.

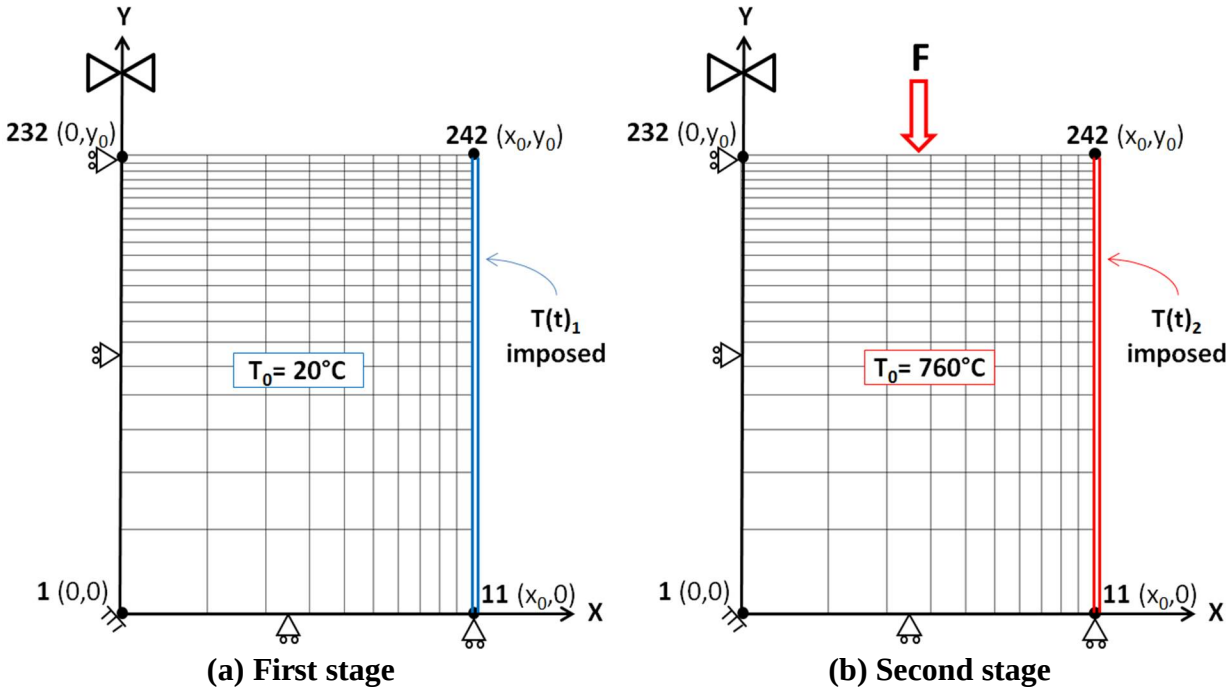

Figure 3.46. Simulation finite element geometry for determination of transformation plasticity coefficient

At the end of simulation, the final predicted sample height is recovered. The total displacement d_{num} is computed and compared to the experimental one d_{exp}. K_i parameter is modified in the input data until a right prediction of the experimental displacement is recovered (see Figure 3.45). A summary of the experimental results and the corresponding values of obtained K_i parameters are presented in Table 3.13., where A and B identifies the two tests performed in similar conditions. The accurate leak of thermal flow by the contact with punchers at the top and bottom edges is not modelled by correct boundary conditions. It could justify that homogeneous temperature did not happened and explain the inaccuracy of the results in the parameter identification.

Table 3.13. Summary of parameters for determination of transformation plasticity coefficient

	Force (kN)	Initial height h_0 (mm)	Experimental displacement d_{exp} (mm)	Dispersion of d_{exp} for the 2 tests (mm)	Numerical displacement d_{num} (mm)	Dispersion of d_{num} for the 2 tests (mm)	K_i (Pa)
SGI (Core)	6.0-A	13.88	0.90	0.02	0.91	0.04	K_2=K_3 5.00E-10
	6.0-B	13.88	0.88		0.87		K_2=K_3 4.70E-10
	8.5-A	13.85	3.11	0.02	3.07	0.07	K_2=K_3 5.7E-10
	8.5-B	13.89	3.13		3.14		K_2= K_3 5.8E-10
HCS (Shell)	20-A	14.47	0.25	0.02	0.24	0.01	K_6 0.65E-10
	20-B	14.95	0.23		0.23		K_6 0.60E-10
	30-A	14.82	0.50	0.05	0.49	0.05	K_6 0.63E-10
	30-B	14.65	0.55		0.54		K_6 0.60E-10

For HCS and SGI materials, close values for transformation plasticity coefficients were found through the four inverse modelling processes. The average value for martensite transformation coefficient K_6 is 0.62E-10 Pa whereas for SGI material, values for $K_2 = K_3$ linked to ferritic and pearlitic transformations induced plasticity is in average 5.30E-10. The sensitivity of d_{exp} (0.02-0.05 mm) could be associated to differences of sample geometry and to heating and cooling rates. The higher sensitivity of d_{num} (0.01-0.07) and the scattered values of K_i lead to think that inverse method is not an accurate method for computation of K_i coefficient. In addition, numerical simulations of mill rolls introducing these values of K_i as input data, predicted residual stress profiles quite different from the expected ones, which demonstrates that previous procedure is not reliable. Therefore, inverse method using industrial experimental stress measurements and other authors predictions is finally used.

3.8.2 Inverse method using experimental residual stress measurements

3.8.2.1 Inverse method for K_6

Residual stresses experimentally measured at the surface of cylinders are provided by the manufacturing industry. Such measurements were obtained at the end of heat treatment in the surface of cylinders of different diameters and shell thickness using the bore-hole method. In particular, the average of stress measurements $\sigma_{r\ exp}$ obtained for cylinders of 1200 mm diameter and 80 mm shell thickness (called 1200/80 mm hereafter) is taken into account for computing K_6 parameter through inverse method [79].

Details about numerical simulations of rolling mill rolls are presented in Chapter 4, however this section presents simulation results of post casting cooling (PCC) and tempering heat treatment (THT) of cylinders 1200/80 mm predicting the residual stress in the surface at the end of heat treatment, called $\sigma_{r\ num}$. The value of K_6 coefficient is found by a manual iterative procedure yielding to a value of $\sigma_{r\ num}$ close to $\sigma_{r\ exp}$. Values of K_6 coefficient within a range of 0 to 0.6E-10 MPa^{-1} were tested finding that K_6=0.25E-10 MPa^{-1} allows a minimal difference of 1.5% (see eq. 3.19) between numerical and average experimental results. Residual axial stress profiles obtained by different simulations are shown in Figure 3.47(a). Note that the value obtained by previous inverse method from compression tests K_6=0.6E-10 MPa^{-1}, would generate a very different result with a residual stress at the surface of approximately -100 MPa when experimental measurements give a value of approximately -400 MPa.

$$error(\%) = \frac{\sigma_{r\ exp} - \sigma_{r\ num}}{\sigma_{r\ exp}} \qquad \textbf{3.19}$$

From here, it is possible to realize that K_6 is a key parameter. A series of simulations for cylinders with different diameters and shell thickness were performed using K_6=0.25E-10 MPa^{-1}. Residual stresses in the surface predicted by numerical simulations are compared with experimental measurements in Figure 3.47(b) (c) and (d) where a good agreement is observed for all the different cases with different diameters and shell thicknesses.

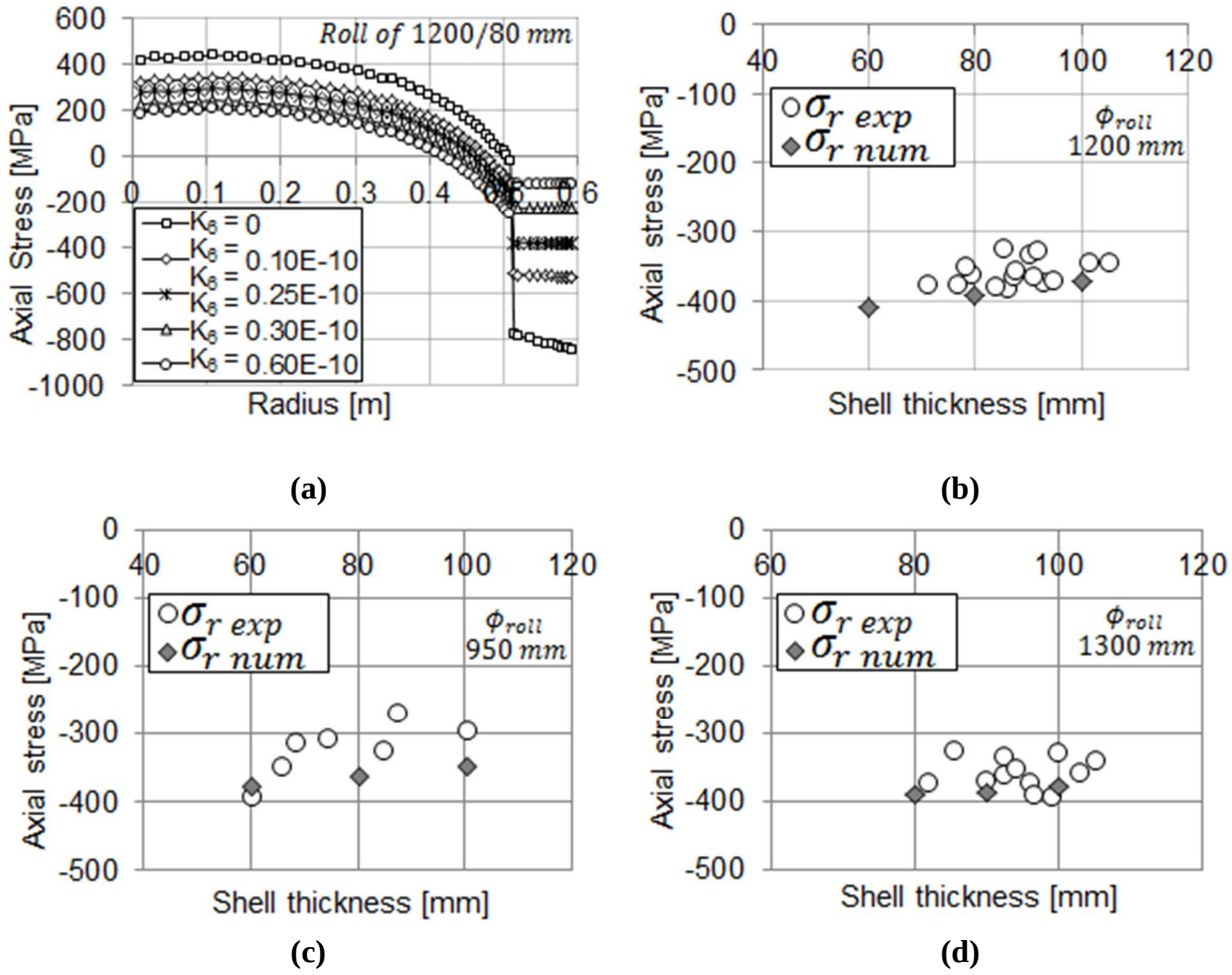

Figure 3.47. (a) Residual stresses along the radius obtained through numerical simulations for different K_6 coefficients. Experimental and numerical values of residual stresses at the surface of cylinder for diameters (b) 1200 mm (c) 950 mm (d) 1300 mm

Even if industrial measurements are scattered, numerical values are well in the same order of magnitude for each case and predict the correct trends allowing the validation of K_6 coefficient obtained by the current inverse method. In addition, the observed trend of residual stresses at the surface from numerical and experimental results is the same. It shows that for smaller diameters, a bigger shell thickness reduces the value of the compression residual stress at the surface when the contrary effect is observed for a thinner shell. The same trend is observed for higher diameters although less pronounced.

Note that for simulations presented here, data obtained from previous experimental and numerical methods (sections 3.1 to 3.7) is used as input data (see Appendix B). A value of $K_2 = K_3$ coefficient equal to 1.7E-10 coming from literature [124] is considered as a first approach, however this parameter does not affect the value of residual stresses predicted at the surface of the roll as will be conformed below.

3.8.2.2 Inverse method for, K_2 and K_3

Residual stress profiles for similar rolling mill rolls are predicted by Assaker in [36] and by Ziehenberger in [7]. In both works a decreasing shape from the center to the interface is found for the core material predicting higher tensile stresses at the center of the roll. These predictions are in good agreement with industrial observations since they observe star cracks in broken rolls that seem to begin in the center of the roll.

Several numerical simulations were performed using input data form sections 3.1 to 3.7 and a value of K_6=0.25E-10 MPa^{-1}. The value of K_2=K_3 coefficient is shifted from 0 to 5.0E-10 MPa^{-1}. Residual stress profiles predicted by different simulations are shown in Figure 3.48 where it is possible to notice that a value of 0.3E-10 MPa^{-1} is the maximal value generating a decreasing tensile stresses profile in the core material. Lower values will highly increase tensile state in the center of the roll. Higher values will generate a tensile reduction on the center of the roll. This is the case of the value K_2=K_3=5.3E-10 MPa^{-1} obtained by previous method from compression tests, where low compression stresses are predicted in the center of the roll. Based on other authors, results predicting a decreasing tensile stress profile in the core material and in agreement with industrial observations, the value of coefficients K_2=K_3=0.3E-10 MPa^{-1} will be used for next simulations of SGI grade.

Note that the cross effect from K_6 and $K_2 = K_3$ coefficients has been checked confirming that the results presented in previous sections are indeed valuable.

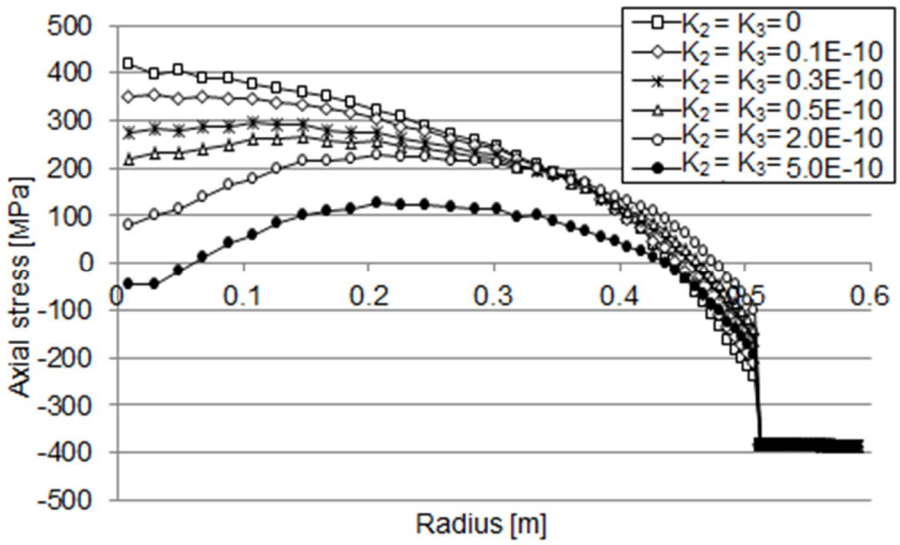

Figure 3.48. Residual stresses along the radius obtained through numerical simulations for different K2, K3 coefficient

3.8.3 Comparison with literature

In literature, values of K_6 for martensitic transformation between 0.10E-10 MPa^{-1} and 0.97E-10 MPa^{-1} have been found in [11, 91, 125]. Otherwise, wide range of K_3 pearlite coefficient from lower values as 0.1E-10 MPa^{-1} to higher values of 1.7E-10 MPa^{-1}can be found in [11, 124]. From both methods, it was possible to obtain values of transformation plasticity coefficient within the range found in literature for martensite transformation and for ferrite – pearlite transformation as can be noticed in Table 3.14. However for modelling of rolling mill rolls, values obtained using residual stresses measurements will be considered as results close to reality are attended.

Table 3.14. Summary of transformation plasticity coefficient obtained by inverse method

Material	K_i using compression tests (MPa^{-1})	K_i using residual stresses (MPa^{-1})	K_i ranges from literature (MPa^{-1})
SGI (Fe and Pe)	K_2=K_3=0.62E-10	K_2=K_3=0.3E-10	K_2=K_3=0.1E-10 - 1.7-10
HCS (Ma)	K_6=0.53E-10	K_6=0.19E-10	K_6=0.1E-10 - 0.97E-10

3.9 Trials for the shift of martensitic transformation coefficients

The start of martensitic transformation is known to be modified due to the generated stress state as it is defined in 2.3.1. The magnitude of this modification is given by eq. 2.16, where A and B parameters are characteristic of each material. In this thesis, a wide research for determination of these parameters was performed with the aim of finding experimental tests that could be useful to identify them. However, all the trials were not successful. Nevertheless, the effect of these parameters on simulation predictions of rolling mill rolls is negligible, as will be presented in section 5.3. Therefore, values found in the literature were adopted for reference simulations. A summary of the performed research is given in Appendix A.

3.10 Conclusions

In this chapter, characterization of SGI and HCS materials was achieved by experimental and numerical methods. Mechanical parameters such as Young modulus, yield limit and tangent modulus at different temperatures have been obtained through experimental compression tests at constant strain rate. Experimental tensile tests were performed for finding the fracture stresses and strains at different temperatures. Thermophysical characterization was achieved through DSC, dilatometry and laser-flash experimental methods. Furthermore, inverse method was applied for the determination of transformation strain, transformation plasticity coefficients, latent heat and TTT diagrams. Finally martensitic start and end temperatures for HCS material were obtained through experimental cryogenic quenching. Modelling of bimetallic rolling mill rolls can be performed using as input data the set of parameters obtained in this chapter. The complete set of data is given in Appendix B.

Chapter 4. Industrial application - FE simulation of a reference rolling mill roll.

Numerical simulations of **P**ost **C**asting **C**ooling (PCC) and **T**empering **H**eat **T**reatment (THT) of a reference bimetallic rolling mill roll composed by SGI and HCS materials are performed using LAGAMINE code by introducing the complete set of data obtained through experimental and numerical methods in Chapter 3. The geometry of a reference roll with failure risk is modelled considering 1200 mm of total diameter and 80 mm of shell thickness. Thermal history and stress fields are analyzed as well as damage predictions allowing the proposal of two rupture hypotheses.

4.1 Geometry and boundary conditions

The model is focused on the cooling stage within solid state of the rolling mill roll and its heat post treatment with residual stress field and stress history as the main targets. The simulations of the cooling of the solid roll assume an initial constant temperature of 1000°C within the roll at an initial computing time t_0. While the stress states associated to higher temperature than 1000°C are very low, this hypothesis is acceptable. For PCC stage, at the external surface of the roll, a convection radiation is applied through an interface thermal element. Note that the used air convective coefficient was identified from an experimental surface thermal history recorded by

the industry for a smaller mill roll of similar grades [36]. This cooling step approximately takes 11 days for the modelled roll as observed in the industry. Then a THT is applied, the measured temperature history is imposed at the surface: heating at 0.1°C/hr until 500°C and the subsequent cooling at -0.1°C/hr until room temperature (see Figure 4.2).

Due to the cylindrical shape and the large size of the rolls (diameter larger than 1 m and axial length approximately 8 m), axisymmetric analyses are performed and only one slice at the middle of the roll is meshed. The bimetallic geometry of 1200 mm diameter with 80 mm of shell thickness is defined by considering 77 finite elements CPL2D as shows Figure 4.1. The mesh is indeed refined near the surface to avoid spurious numerical oscillations in presence of high thermal gradients due to the air quench. CPL2D is a "8 node" finite element with a fully thermo-mechanical metallurgical coupling and 4 integration points. It gives the evolution of state variables and stresses results at different simulation times (see section 2.3.3). Note that a mesh sensitivity was done. Coarser and finer meshes from 40 to 224 elements were used with no effects on the results.

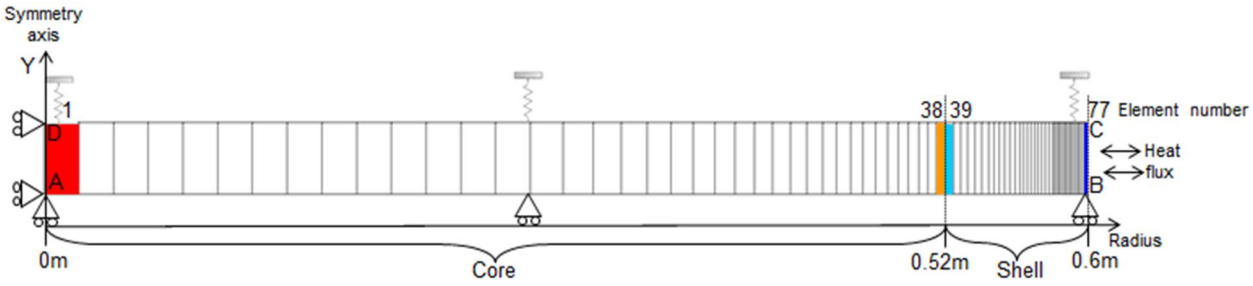

Figure 4.1. Axisymmetric geometry for reference simulation (diameter 1200 mm / shell thickness 80 mm) of bimetallic mill roll

38 elements model the core material SGI and 39 elements correspond to the shell material HCS. The red element (1) is located in the **center** of the roll, the yellow (38) and light blue (39) elements model the **core interface** and **shell interface** respectively. Note that a discrete jump of materials happens between element 38 and 39 associated to the core and the shell metals respectively. The **surface** of the roll is modelled by the dark blue element (77) where the heat flux is imposed. These four elements will be used hereinafter for the presentation of results, using the color code of Figure 4.1. Boundary conditions are listed below and reflect the hypothesis of an infinitely long cylinder which is free of dilatation along Y axis.

- A-B line: Nodes are locked along Y direction.
- A-D line: Nodes are locked along symetry axis X.
- C-D line: Same displacement is imposed along Y axis for all nodes using spring elements in order to constrain nodes to remain in a plane perpendicular to the Y axis.
- B-C line: Convection radiation exchange are imposed for PCC stage while for THT, temperature evolution is imposed in surface nodes.

4.2 Results

The simulation of PCC and THT stages of a rolling mill roll of 1200 mm diameter and 80 mm of shell thickness by LAGAMINE code gives the history of coordinates i.e. X, Y, T° for each node, as well as the history of state variables and stresses for each element. In this section, the analysis of temperature, state variables corresponding to phase rates and stresses will be presented.

4.2.1 Temperature evolution

The temperature evolution of reference simulation for center and surface nodes can be seen in Figure 4.2. Seven critical times t1-t7 are enhanced since for these times, peaks on stress profiles are generated as it will be presented below.

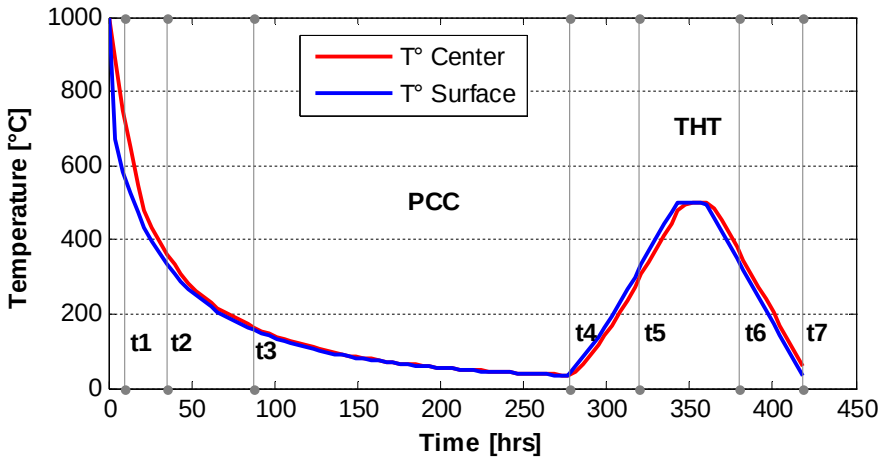

Figure 4.2. Predicted temperature evolution during PCC and THT stages (except for T° surface in THT where temperature is imposed)

The temperature distribution along the whole simulated roll is illustrated in Figure 4.3 for critical times t1 (10 hr), t4 (278 hr) end of PCC stage, t5 (320 hr) middle of temperature increase of THT stage, t6 (380 hr) middle of temperature decrease of THT stage, and t7 (418 hr) end of THT stage. For each time, the difference between temperature at the center and at the surface of the roll is given ($\Delta T = T_{center} - T_{surface}$).

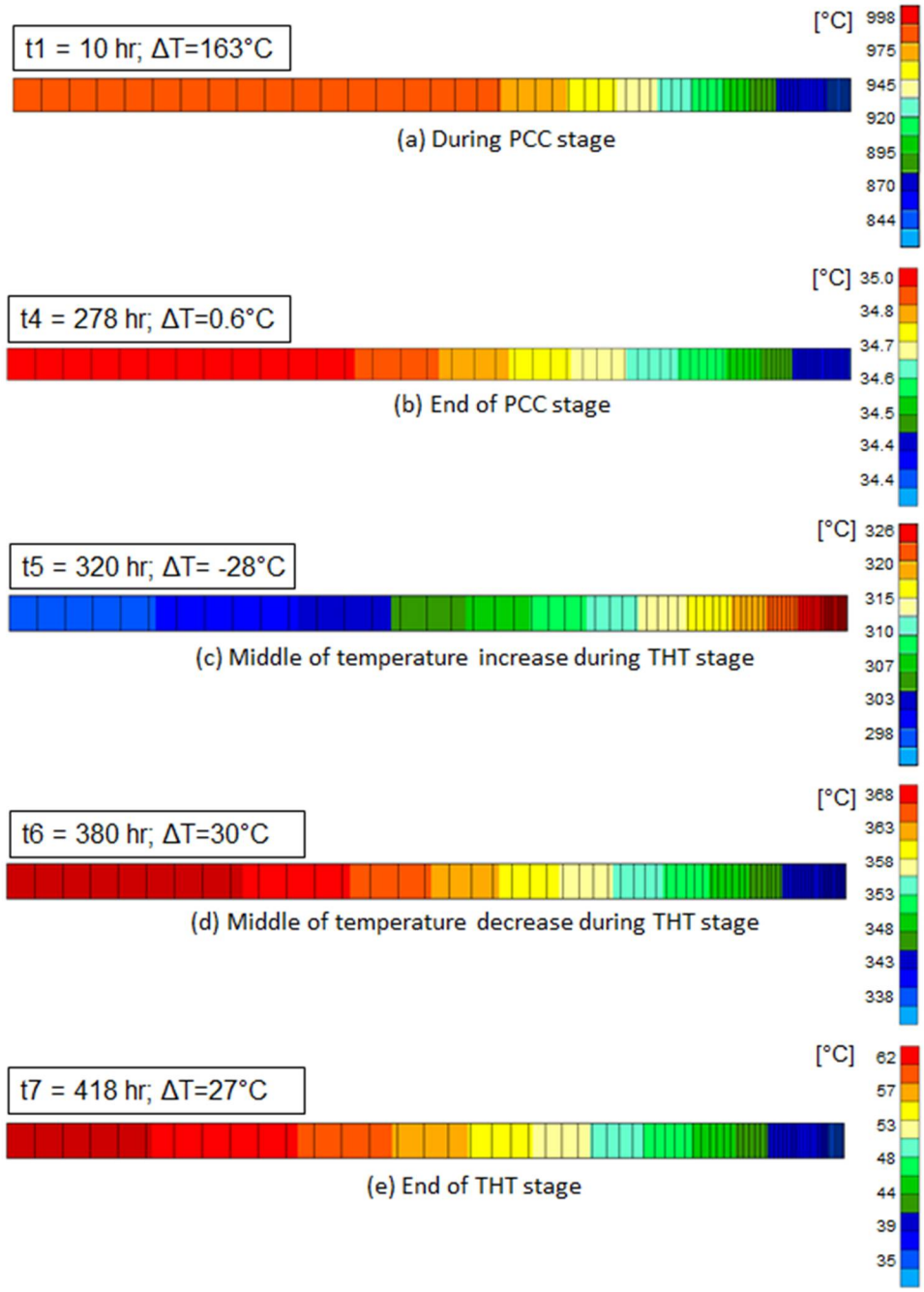

Figure 4.3. Temperature distribution along the radius of the rolls for some critical times

The thermal gradients along the radius for different times are presented in Figure 4.4. From Figure 4.4, it is observed that during the first 20 hrs of PCC stage, the temperature is considerably higher at the center than at the surface of the roll. A difference of 163°C is observed at 10 hrs (see Figure 4.3 (a)). The thermal gradient decreases with time. After 30 hrs of cooling, differences are becoming insignificant until the end of PCC stage at 278 hrs where homogeneous temperature is presented within the whole mill roll (see Figure 4.3 (b)). During THT stage, at time t5 (320 hrs) the surface of the roll is 28°C higher than the center since the roll is subjected to heating (see Figure 4.3 (c)). The contrary effect is observed at time t6 (380 hrs) when the roll is being cooled and the center is 30°C higher than the surface (see Figure 4.3 (d)). At time t7 (418 hrs, end of THT stage), a moderate difference of temperature (27°C) is still present between center and surface of the rolling mill roll (see Figure 4.3 (e)).

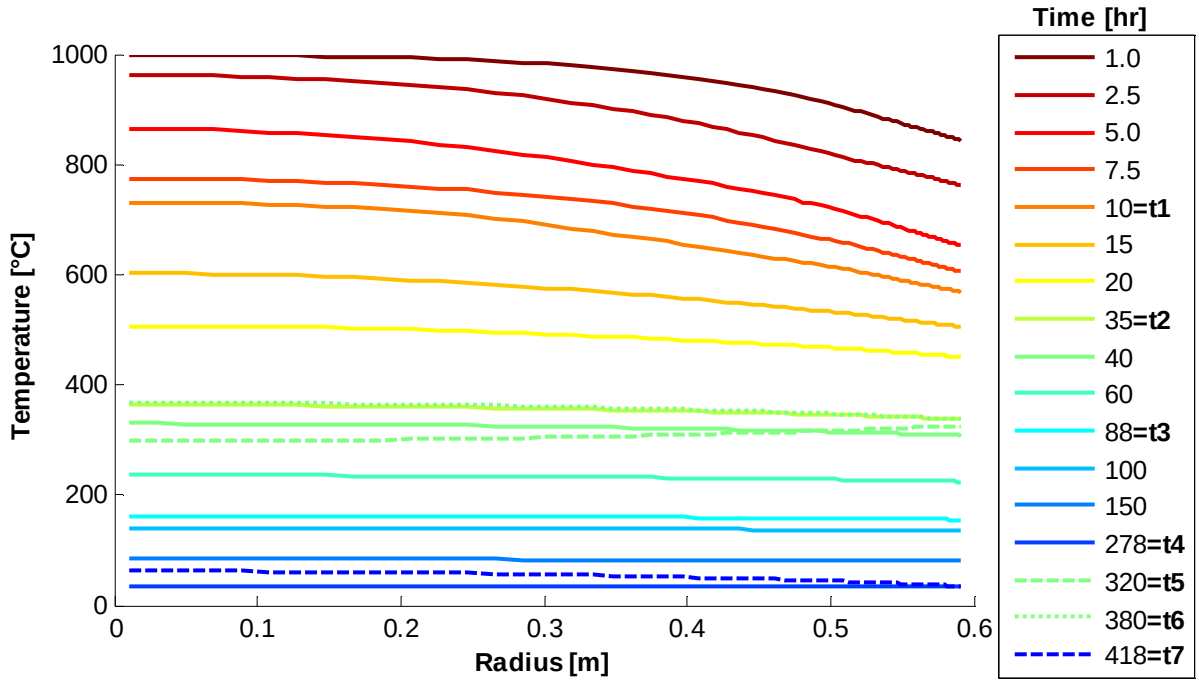

Figure 4.4. Thermal gradients along the radius during PCC and THT stages

A summary of the temperature reached at critical times for different position within the roll is presented in Table 4.1.

Table 4.1 Summary of temperature reached at critical times

Critical times	Temperature (°C)			
	Center	Core interface	Shell interface	Surface
t1=10 hrs (3.6E+04 s)	731	611	609	568
t2=35 hrs (1.26E+05 s)	363	345	344	337
t3=88 hrs (3.17E+05 s)	162	157	157	155
t4=278 hrs (1.0E+06 s)	35.0	34.6	34.6	34.4
t5=320 hrs (1.15E+06 s)	298	317	318	326
t6=380 hrs (1.37E+06 s)	367	347	346	337
t7=418 hrs (1.50E+05 s)	62	44	43	35

4.2.2 Stresses and phase transformations evolution

Axial stress predicted for elements corresponding to center, surface and interface of the mill roll together with their interactions with corresponding phase transformations during PCC stage are presented in Figure 4.5. A zoom of the first 100 hrs is presented in Figure 4.6.

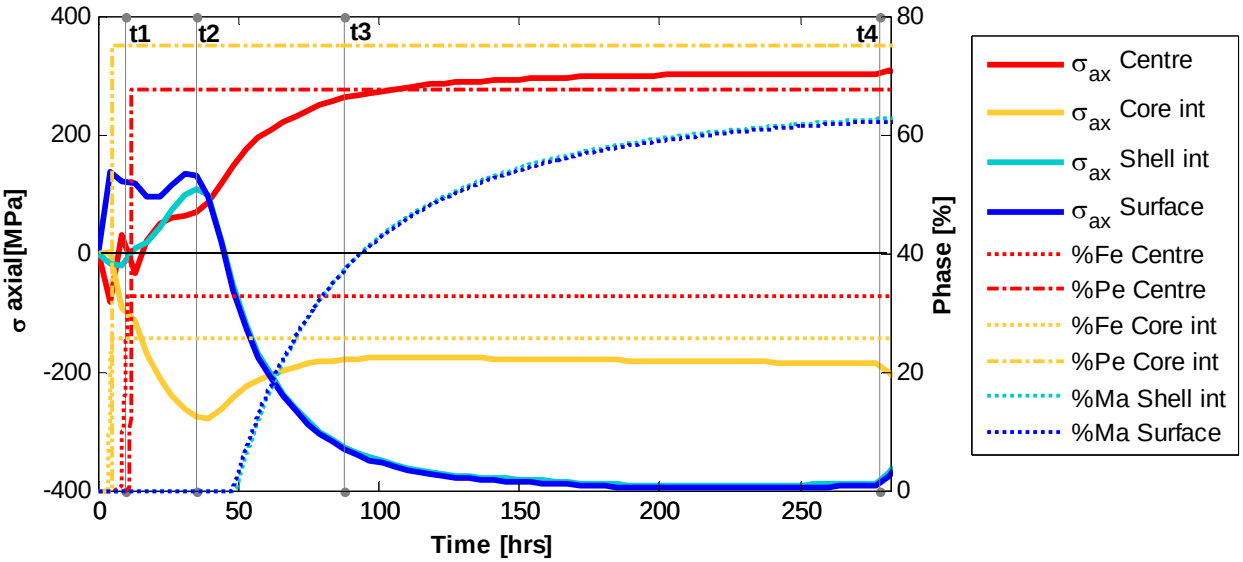

Figure 4.5. Axial stress and phase amount evolution during PCC stage for the four color elements identified in Figure 4.1

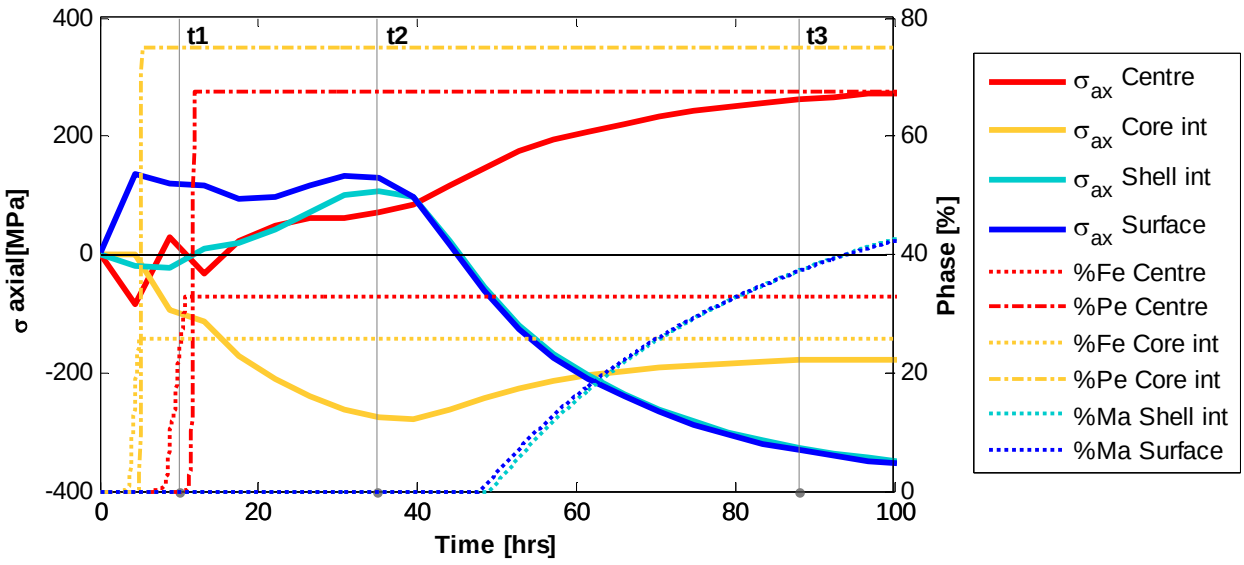

Figure 4.6. Axial stress and phase amount evolution during PCC stage for the four color elements identified in Figure 4.1. Zoom for first 100 hrs

The axial stress peaks generated can be explained by the phase transformation happening in the core and shell materials.

- During the first 10 hrs the core material is being transformed as can be observed in Figure 4.6. First, the ferritic and pearlitic transformations of the core interface (in yellow) generate a compression state in the center of the roll (in red) and a tensile state of the surface (in blue) by equilibrium. Later, the ferritic transformation of the center of the roll generates a relaxation in its stress state and a compression state in the core interface.
- For t1=10 hr, the core interface is completely transformed while the center of the roll is in the middle of its transformation; ferritic transformation has almost achieved but not yet pearlitic transformation. The center of the roll is subjected to a slight compression due to the pearlitic transformation and the compression state in the core interface increases. The shell material is subjected to tensile state by equilibrium (see Figure 4.6). The distribution of phases along the modelled structure at time t1 can be seen in Figure 4.7. Note that for this time, the temperature at the center is approximately 730°C and at the surface is approximately 560°C (see Figure 4.3 (a)).

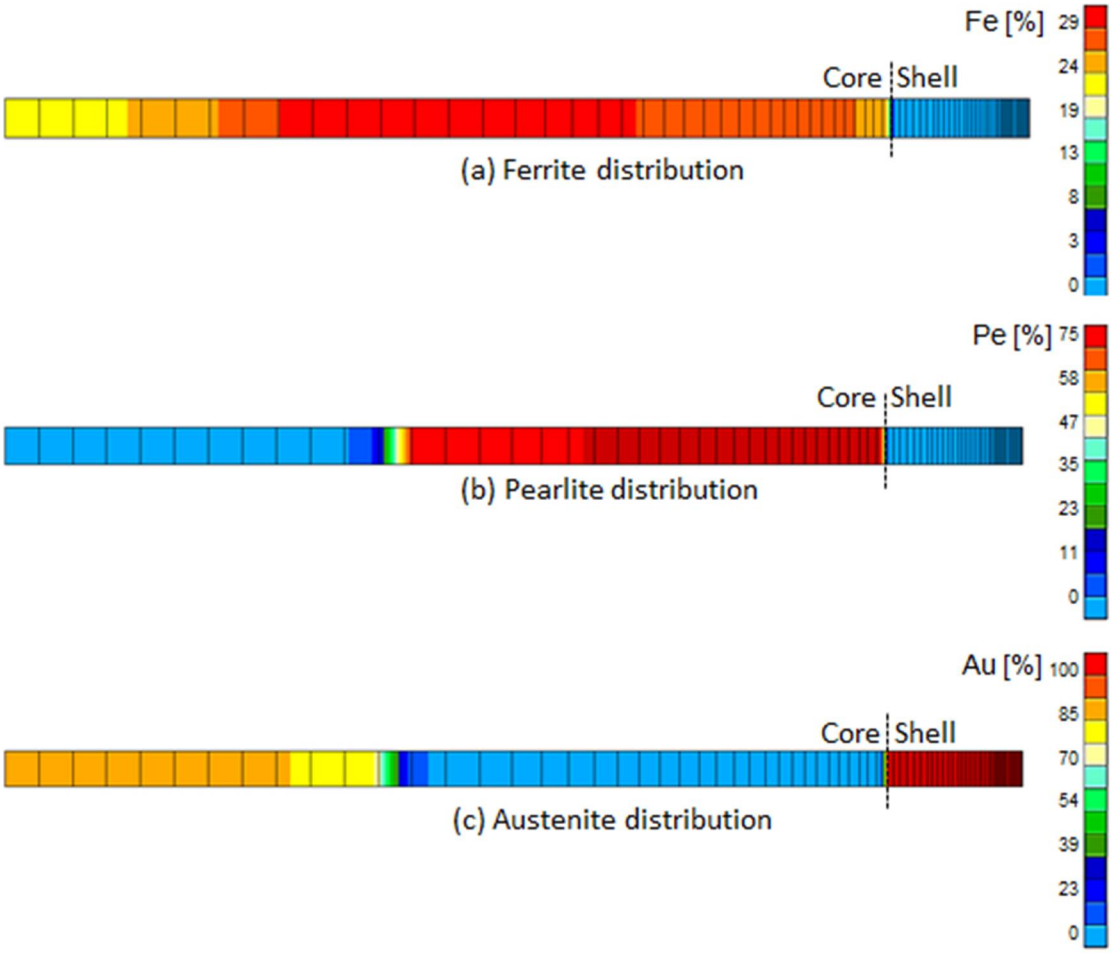

Figure 4.7. Phase distribution at t1=10 hrs along the modelled structure

- For t2=35 hrs, the whole core material is transformed to ferrite and pearlite phases. Note that for this time, the roll presents a nearly homogeneous temperature of 300°C (see Figure 4.4). From Figure 4.6 it is possible to observe that the center of the roll is in tensile state while the core interface is in compression and the whole shell material is subjected to tensile state by equilibrium. Generated peaks at this time are associated to the difference between coefficients of thermal expansion of core and shell materials since the difference between both coefficients is maximal for 300°C as can be observed in Figure 4.8.

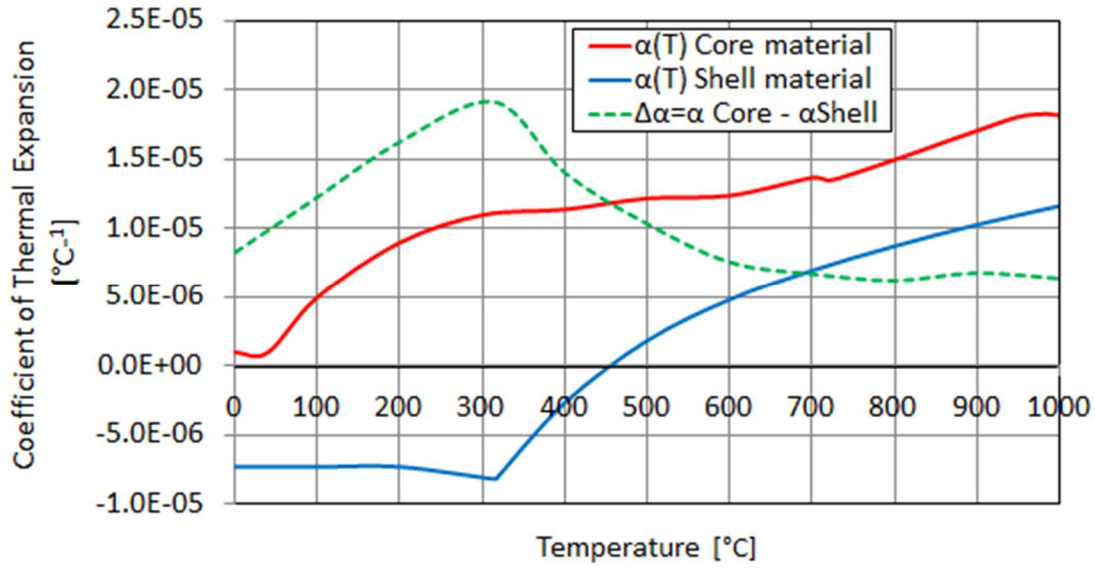

Figure 4.8. Coefficient of thermal expansion for core and shell materials together with the computed difference between both coefficients

- At t3=88 hrs, the roll presents a homogeneous temperature of about 200°C (see Figure 4.4). Martensitic transformation of the whole shell material has started (martensitic transformation happens at almost the same time for surface and shell interface) and it generates a high compression state in shell material while the center of the roll goes to tensile state by equilibrium and the core interface slightly decreases its compressive state. This trend continues until the end of martensitic phase transformation at t4 time as can be observed in Figure 4.5.
- At t4=278 hrs (corresponding to the end of the PCC stage), room temperature is achieved in the whole roll (see Figure 4.3 (b)) and the higher stresses are generated; the shell material is highly compressed whereas the core material goes from a high tensile state at the center to a medium compression state at the interface due to the phase transformation previously described. At this time, Figure 4.9 presents the distribution of metallurgical phases on the modelled structure allowing confirming that the predicted phase rate is the same one obtained in a real mill roll composed by SGI and HCS materials (see section 2.6). The core material contains a mixed ferrite/pearlite structure with a distribution that changes within the core. In the center of the roll, the phase amount is 68%Pe-32%Fe and in the core interface it is 75%Pe-25%Fe (see Figure 4.9(a) (b)). On the other hand, the whole shell material exhibits

the same amount of austenite and martensite that corresponds to 38%Au-62%Ma (see Figure 4.9(c) (d)).

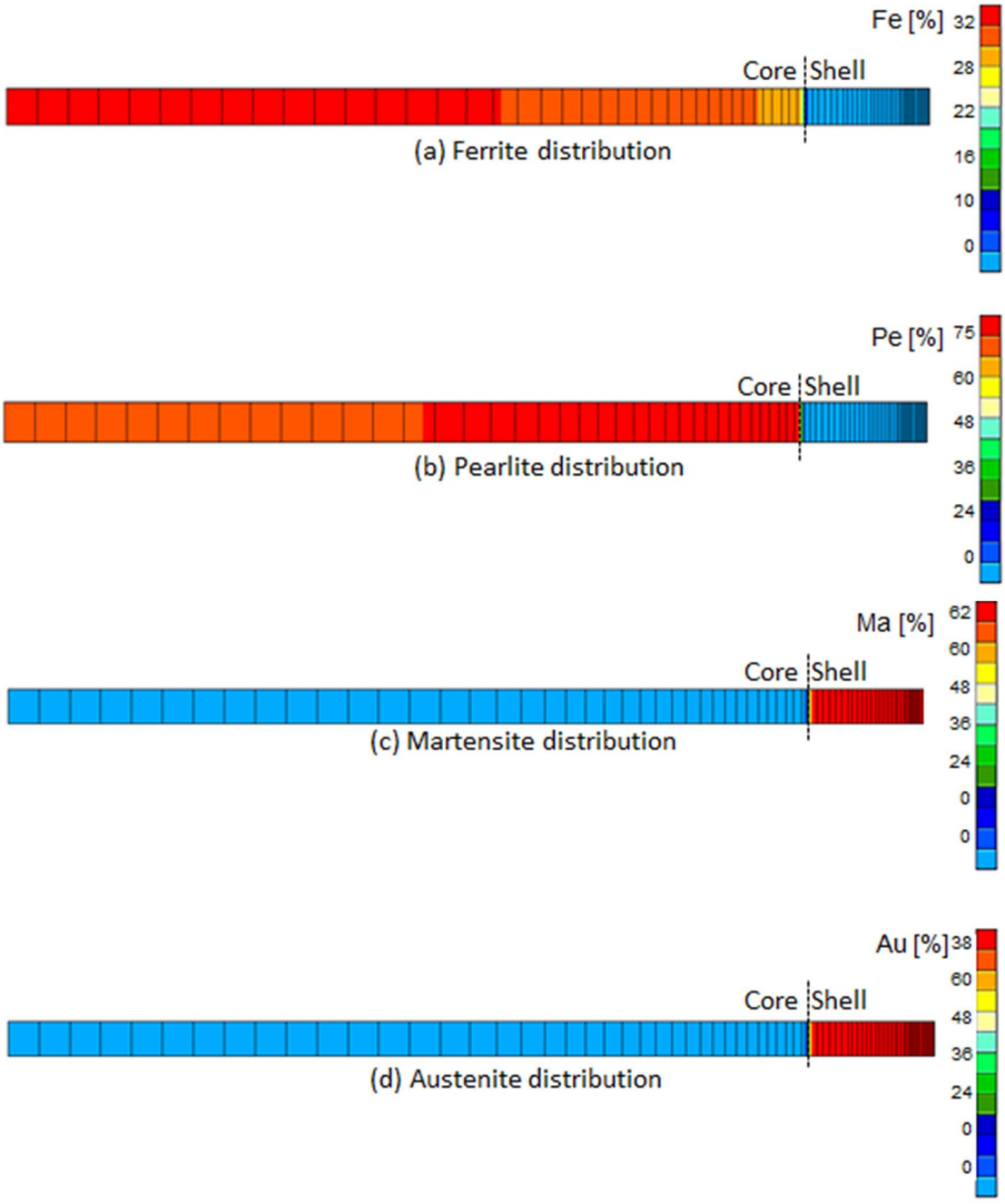

Figure 4.9. Phase distribution at t4 end of PCC stage along the modelled structure

The axial stress evolution for reference simulation during both PCC and THT stages can be seen in Figure 4.10. It is possible to observe that during this complete simulation the highest tensile stress state in the roll center is generated at the end of PCC stage i.e. time t4. During THT stage, this stress decreases, whereas for the core interface element, compression stress slightly increases. For the whole shell material, compression stresses are completely relaxed and a low tensile stress state is generated. Two peaks are generated at t5=320 hrs (300°C) and t6=380 hrs (300°C). They are linked to differences in dilatation coefficients of the core and shell materials that vary with the temperature. Finally at t7=420 hrs, the final state, it is possible to observe that almost the same stress state as in t4 (end of cooling stage) is recovered.

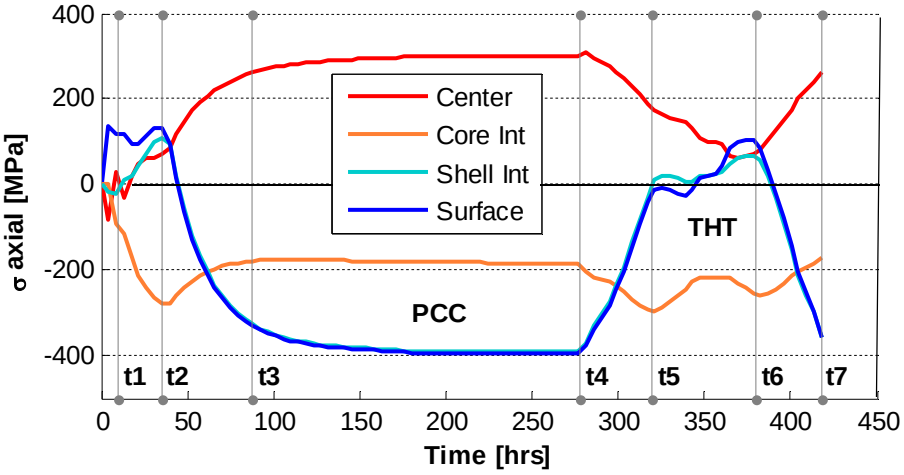

Figure 4.10. Axial stress evolution with time during PCC and THT stages

The histories of circumferential and radial stresses are given in Figure 4.11 and Figure 4.12 respectively. Circumferential stresses present similar critical times, order of magnitude and feature than axial stresses. On the contrary, the radial stress is high at the center of the roll and null for the surface as expected. However its level is lower than previous stresses. The tangential stresses are very low (in a range of -1.5 and 1 Pa) justifying that we do not study them. Indeed x, y, z axes roughly define the principal directions.

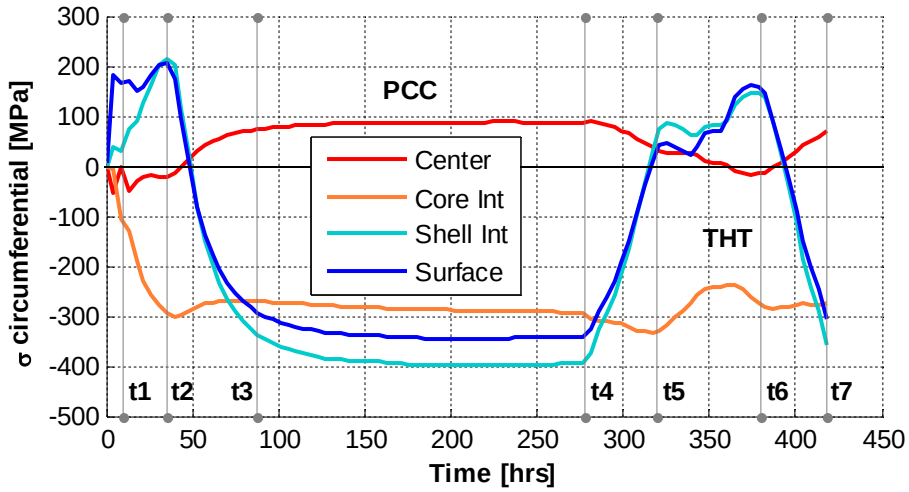

Figure 4.11. Circumferential stress evolution during PCC and THT stages

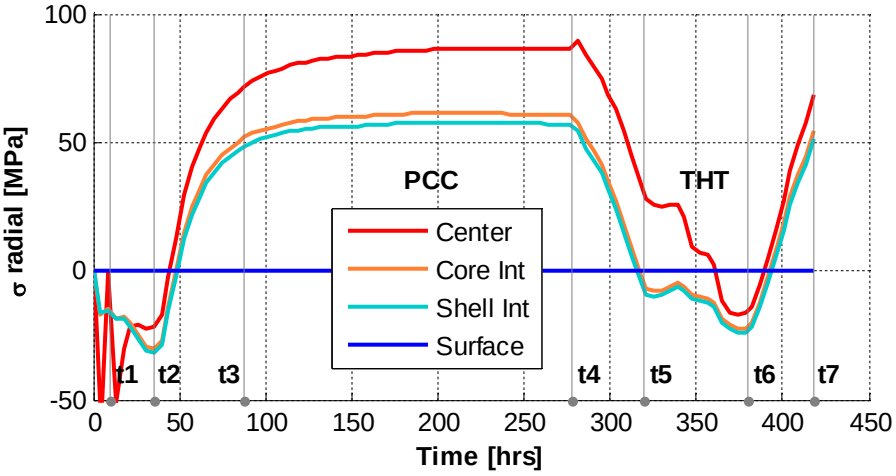

Figure 4.12. Radial stress evolution during PCC and THT stages

Summarizing the observations, each stress component presents high values peaks during PCC stage between t3 and t4 times corresponding to the cooling between 200°C and 35°C. Maximal values for each stress component for the four critical elements are summarized in Table 4.2. This stress field evolution is related to the material difference in grade and phase contents between core and shell metals, which is coupled to different levels of the dilatation coefficients as it was shown in Figure 4.8.

Table 4.2 Summary of maximal stress values reached at time t4

	Center	Core interface	Shell interface	Surface
$\boldsymbol{\sigma_{max}}\ Axial$ (MPa)	328.2	-295.1	-391.5	-395.1
$\boldsymbol{\sigma_{max}}\ Circumferential$ (MPa)	91.12	-334	-398.8	-344.9
$\boldsymbol{\sigma_{max}}\ Radial$ (MPa)	89.36	60.96	57.65	0.18

4.2.3 Axial stress evolution along radius

For critical times t1-t7, Figure 4.13 shows the axial stress profiles along radius and the rupture stresses at the associated temperatures obtained by tensile tests (see section 3.2.3).

In Figure 4.13 (a) corresponding to PCC stage, the core material presents the highest tensile states at t3 time (88 hrs) when temperature is 150°C and at t4 (278 hrs) time for a temperature of 35°C. The rupture stress at room temperature (330 MPa, see Table 3.8) is reached at t4, however at t3 time (150°C) the rupture stress (372 MPa, see Table 3.8) is approximately 100 MPa higher than maximal values predicted. The shell material goes from tensile state at t1 and t2 moments to a compression state at t3 and t4 ones. However rupture tensile stresses (from 375 to 683 MPa, see Table 3.8) are far from the generated tensile stresses.

On the other hand, during THT (Figure 4.13 (b)), stresses in the core are decreasing for times t5 and t6. At t7 when room temperature is achieved, stresses are increased again almost recovering the same level as at time t4. Nevertheless in this case, the rupture stress is not reached. For the shell, the highest tensile state is predicted at time t6 (98 MPa), for a temperature 300°C. It is significantly lower than the rupture stress at 300°C for this material (649 MPa, see Table 3.8). Note that a high gap of approximately 500 MPa is generated at the interface, being a critical zone where high stress gradients are present.

Residual axial stress distribution along modelled geometry can be observed in Figure 4.14 at the end of PCC (278 hr) and THT (418 hr) stages. A very similar distribution of stress state is predicted for both moments, however axial stresses (tensile for the core and compression for the shell) are relaxed during THT stage.

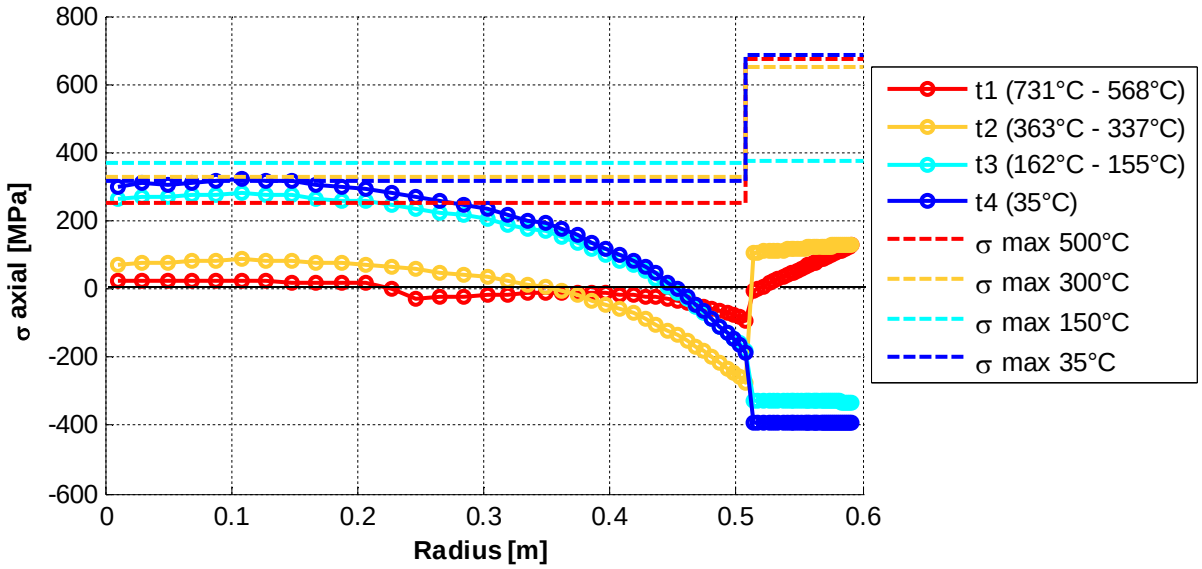

(a) PCC stage

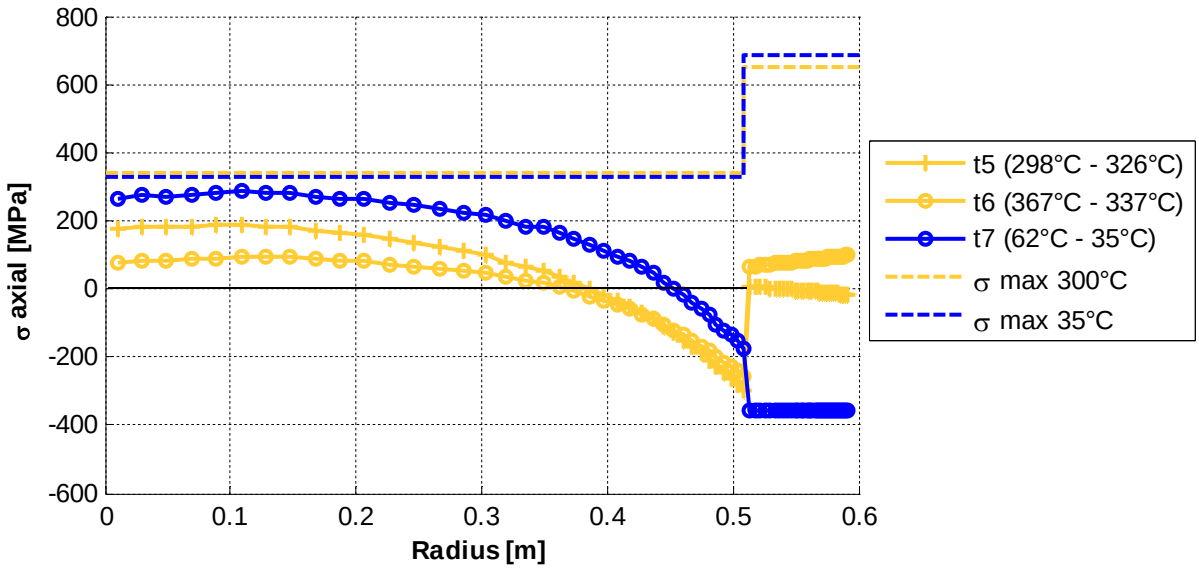

(b) THT stage

Figure 4.13. Rupture stresses and axial stress profiles at different critical times during PCC and THT stages

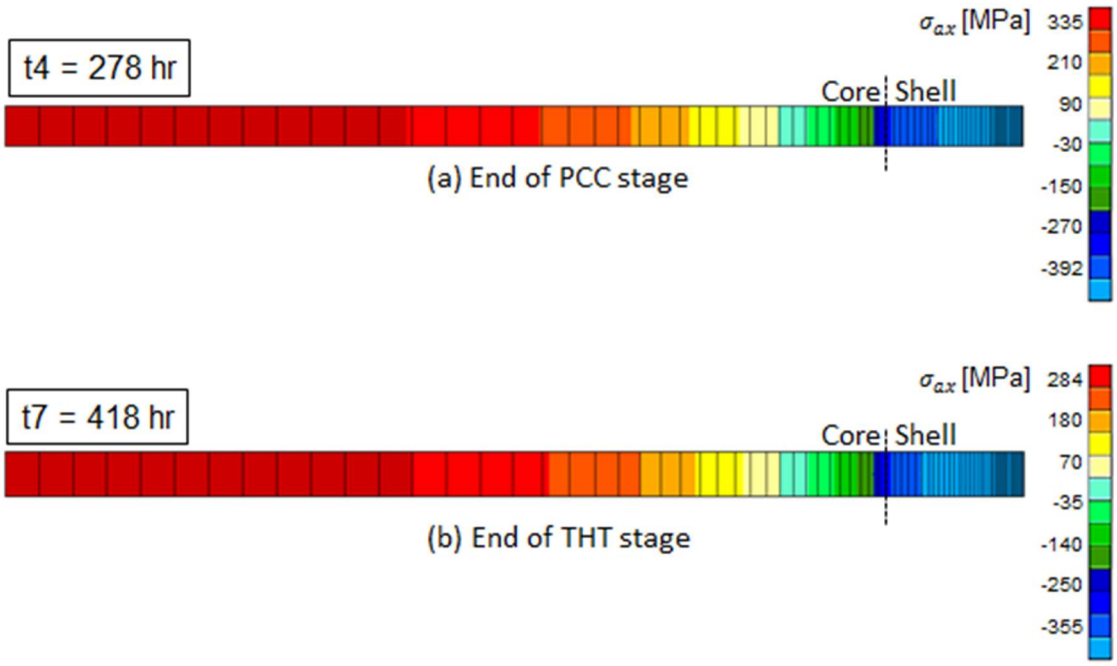

Figure 4.14. Axial stress distribution along modelled structure at the end of PCC and THT stages

4.3 Damage analysis

In previous section, stresses and phase transformations evolution obtained within the simulation of PCC and THT stages for the reference rolling mill roll were presented. To analyze damage, different approaches are proposed. The first one considers both the axial stress and triaxiality evolution and a second one is based on the analysis of different rupture criteria. Both approaches are presented in this section for a rupture hypothesis establishment.

4.3.1 Axial stress and triaxiality evolution

The fact that the level of axial stress at t4 observed in Figure 4.10 and Figure 4.13 overlaps the maximum fracture stress in tensile state for core material, leads to assume that high damage and potential crack take place during the last stage of PCC in the core material without reaching the surface due to the shell strength. However during THT stage, the propagation of the crack into the interface could become possible due to the non-negligible tensile state of the shell material

and the high stress gradient generated at the interface. This assumption is enhanced by the existence of radial and circumferential stresses within the shell that modifies triaxiality state.

In practice, triaxiality state (ratio between hydrostatic and von Misses stresses) is known to strongly reduce the fracture strain. For instance, [61] presented the three branch fracture locus of Figure 4.15. From where, it is settled that for triaxiality value from -1/3 to 0 and upper 1/3, the fracture strains decrease. On the contrary, for triaxiality values from 0 to 1/3 fracture strain is increased. Let us remind that 1/3 and -1/3 are characteristic values of uniaxial tensile and compression state respectively.

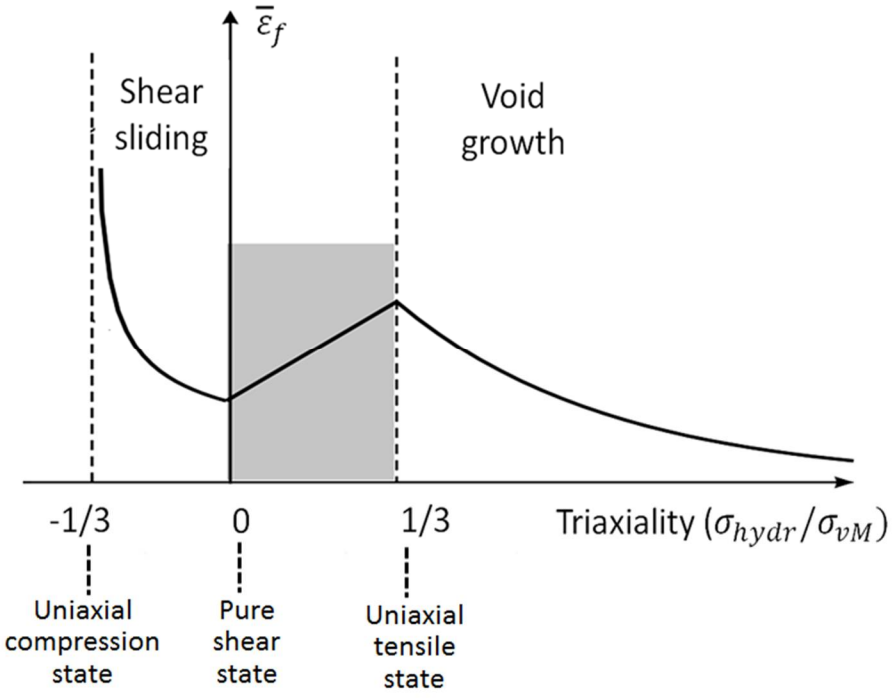

Figure 4.15. Scheme of the three-branch fracture locus

For the mill roll studied in this thesis, von Misses and hydrostatic stresses and triaxiality value along the radius are shown in Figure 4.16 at critical time t4 (end of PCC stage). Clearly, one can notice that for t4 time, the most part of cylinder is presenting values of triaxialities that reduce fracture strain. In our FE model, when triaxiality is positive, only 3 finite elements between 0.42 m and 0.44 m have a triaxiality value between 0 and 1/3 where fracture strain is not exponentially decreasing. The stress field in the most part of cylinder induces a smaller fracture

strain than in pure tension. This fact takes especial importance at the center of the roll from 0 to 0.2 m since the tensile rupture stress is already achieved at time t4 (see Figure 4.13).

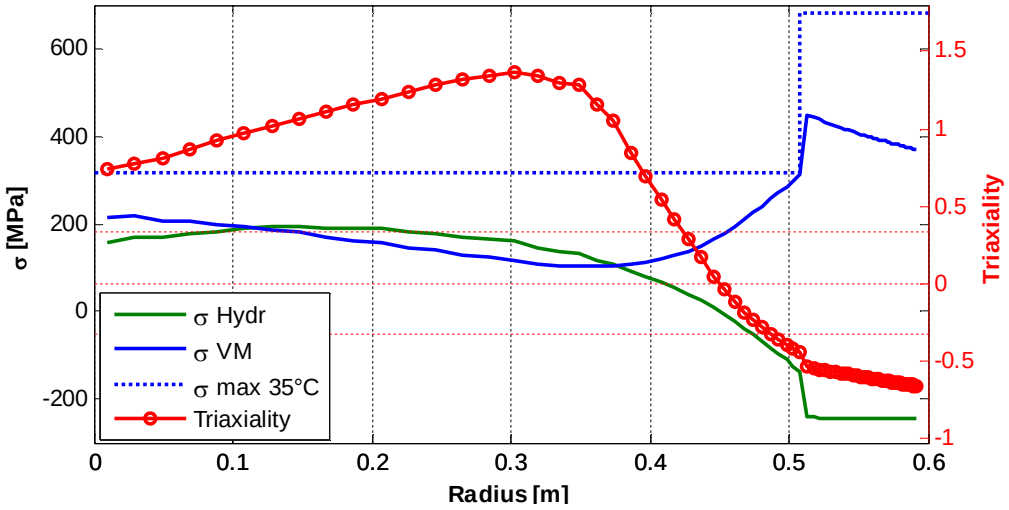

Figure 4.16. Von Misses stress, Hydrostatic stress and triaxiality value along the radius for time t4

4.3.2 Rupture criteria

Damage analysis from FE simulations performed by LAGAMINE code can also be based on Ghosh [55], McClintock [56], Freudenthal [57], Cockroft-Latham [58], Brozzo et al. [59] and Oyane [60] criteria (see section 2.4) linked to a linear cumulative damage assumption. This strongly phenomenological and simplified approach only provides a potential rupture history as accurate damage model is far from being validated and identified. The threshold values were identified using available experimental tensile data for some temperatures (see eqs. 2.24 to 2.30). Figure 4.17 provides for t4 to t7 times, the damage state along the radius for each criterion computed by LAGAMINE code for the studied reference roll (diameter 1200 mm and shell thickness 80 mm). For each criterion, it is observed that damage increases with time, since it is cumulative through the roll history.

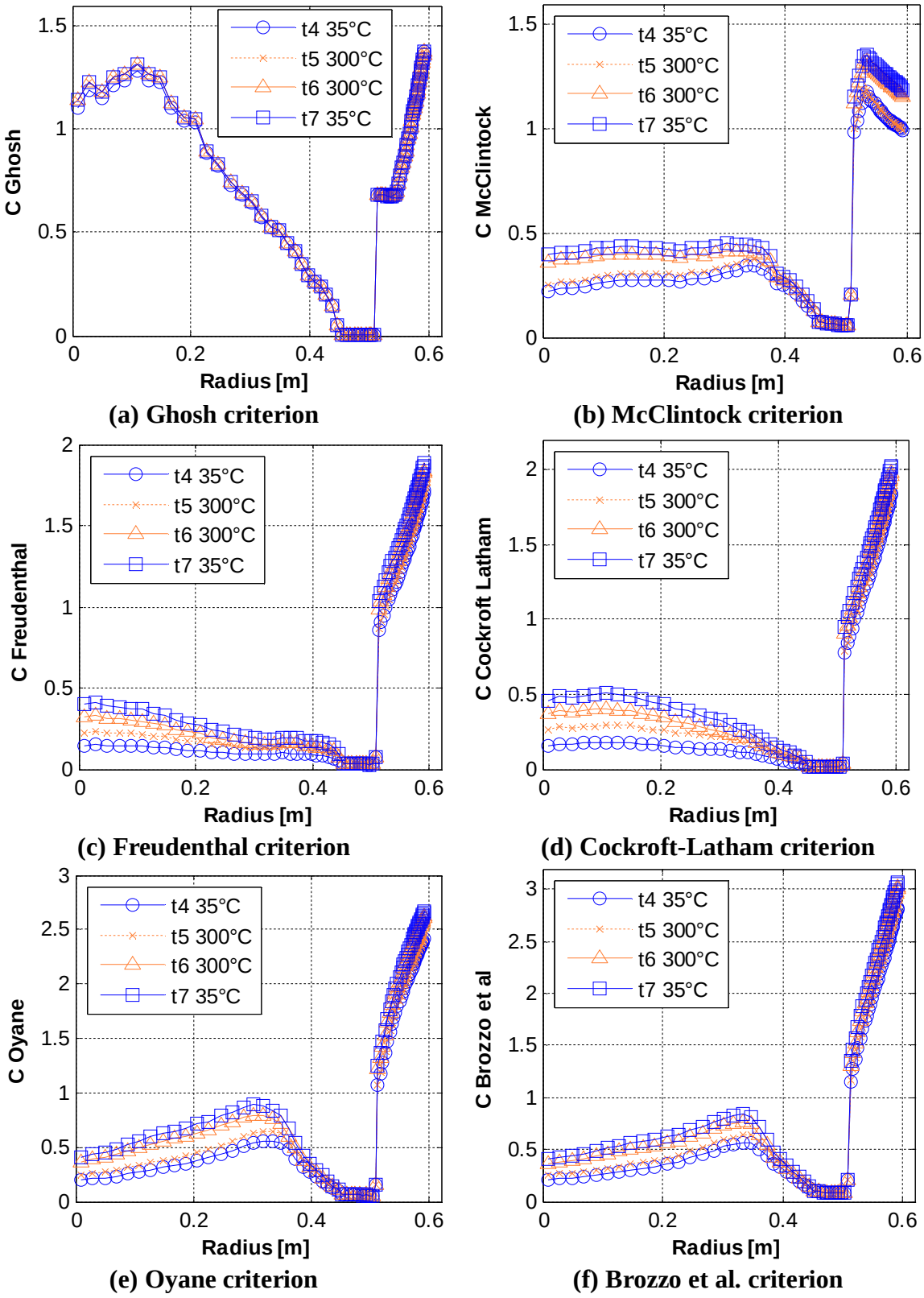

(a) Ghosh criterion

(b) McClintock criterion

(c) Freudenthal criterion

(d) Cockroft-Latham criterion

(e) Oyane criterion

(f) Brozzo et al. criterion

Figure 4.17. Value of rupture criteria along radius for times t4 to t7

Figure 4.17(a) and (b) provide the values of Ghosh and McClintock criteria respectively. Let us remind that Ghosh criterion takes the maximal rupture stress as reference while McClintock is based on the rupture energy. Regarding to Ghosh criterion, the critical damage during THT stage is confirmed for the core material from 0 to 0.22 m and for the shell from 0.57 m to the surface for times t4 to t7 as the criterion value is higher than 1. According to McClintock criterion, as it takes values higher than the unity, damage is generated at the shell material during THT stage. Furthermore according to McClintock, damage at the shell is increasing at the first 1/3 section close to the interface and it decreases for the 2/3 part of the section close to the surface.

Figure 4.17(c) and (d) show the evolution along radius of Freudenthal and Cockroft-Latham criteria respectively. For both criteria, identical trends are observed. For core material, the damage is decreasing from the center of the roll to the interface however no critical damage is predicted at the whole core material. Both criteria predict critical damage for the most part of shell material increasing from the interface to the roll surface.

Figure 4.17(e) and (f) provide values of Oyane and Brozzo et al criteria respectively. For both criteria, no critical damage is predicted for core material even if a peak of damage value is presented at approximately 0.32 m. Regarding to shell material, damage increases from the interface to the surface of the roll and damage is predicted for the 2/3 section close to the surface. Note that the discrepancy of rupture criteria predictions is far from being seldom and justify the development of continuous damage mechanics.

4.3.3 Rupture hypothesis

Numerical results obtained by LAGAMINE code show that during PCC stage, phase transformations happen inducing an important stress state in the whole mill roll. This stress state is strongly modified at the high temperatures of THT stage. However, during cooling of the THT stage, the important stress state is almost recovered. An elasto-viscoplastic model would simulate some stress relaxation, however the length of the THT stage and the level of measured residual stress confirm that this phenomenon is not a process dominant feature, still the elasto-plastic model provides interesting results. From the stress state and rupture criteria analysis, it is possible to propose three rupture hypotheses.

1. Considering a simple criteria of maximal tensile stress, it is possible to predict rupture in the core material in particular **in the center of the roll** at the end of PCC stage. However as the shell is highly compressed, cracks do not propagate within the shell. Ghosh criterion predicts fracture within the core and the surface. Although other fracture criteria are not supporting this hypothesis of core fracture. A core fracture is in agreement with reality as seldom cases of star cracks starting in the roll center have been observed within industry in broken rolls at the end of PCC.
2. Furthermore, damage predicted by McClintock criterion for the shell material during THT stage and the fact that shell is in high tensile state with an important gap at the interface, allow expecting cracks events in the shell material **starting at the interface**. Even if others criteria are predicting damage increasing to the surface. McCLintock predictions seem more physic and similar to the industrial knowledge. Indeed, some industrial observations as butterfly cracks are observed in the shell material close to the interface in rolls broken after THT stage. These kinds of cracks do not propagate more than 1/3 of shell material and the roll is restrained by a ring of external shell material. This fact can be explained by the potential low quality of the material since polluted composition is generated at the interface. The simulation results could suggest that cracks are generated at the interface and propagated until approximately 1/3 of the shell from where damage start to decrease.
3. Based on all criteria, shell ruptures are predicted already at time t4, which is not in agreement with industrial observation and does not validate these phenomenological criteria. Note that a simple correction of the criteria could be done to correct all the formula by preventing damage cumulative when σ_1 or σ_{Hydr} is in compression. This would avoid the shell crack prediction for compression state.

4.4 Conclusion

Numerical simulation of a reference rolling mill roll is performed by introducing parameters obtained in Chapter 3 as input data. FE code LAGAMINE predicts the history of stresses, phase amount and different rupture criteria during PCC and THT stages. Phase transformations occurring during PCC stage generate a high axial stress state along the whole mill roll. The

center of the roll is subjected to tensile stress, while a compression stress state is generated in the whole shell material. The triaxiality level generated at critical time t4 (end of PCC) confirms damage at the core material as the fracture strain is reduced. During THT stage, tensile stresses at the center of the roll are slightly relaxed while the shell material is subjected to a low tensile stress state. At the end of THT stage, almost the same stress state than at the end of PCC stage is recovered. The analysis of axial stresses together with Ghosh criteria allows proposing a first rupture hypothesis: initial star cracks can be generated in the center of cylinder at the end of post casting cooling but do not propagate in shell material until tempering heat treatment, when cracks could propagate through the shell subjected to tensile stresses. The second rupture hypothesis is based on McClintock criteria: butterfly cracks happen during THT stage at the core-shell interface. Both hypotheses are supported by industrial observations.

Chapter 5. Sensitivity analysis

Sensitivity analysis to metallurgical, mechanical and thermal input data for the modeling of a reference rolling mill roll was presented in [126]. Results established that the most important effect is observed by the modification of metallurgical data. In this chapter, metallurgical input data of core and shell materials is modified by modeling of a higher ferrite core material and a lower martensite shell material. The effect of the roll geometry is studied by using different roll diameters and shell thicknesses. In addition, modifications of lacking parameters are performed in order to evaluate their impact on results. Predictions obtained from modified simulations are compared with reference simulation predictions allowing the study of the effect of eventual manufacturing process modifications. Sensitivity analysis performed allows the exploitation and validation of the model by comparing obtained results with industrial observations.

5.1 Core material

In order to analyze the effect of a different core material, a modified TTT (time, transformation, temperature) diagram is introduced as input data. FE simulation similar to the reference one presented in Chapter 4 is performed considering the same data obtained in Chapter 3 modifying only the TTT diagram. Ferritic SGI grade TTT diagram is obtained by the inverse method described in section 3.5.1 based on the CCT diagram from [120]. Let us remind that for reference simulation presented in Chapter 4, a TTT diagram corresponding to a pearlitic SGI grade was introduced as input data. Figure 5.1 shows both the reference (pearlitic SGI) and the modified (ferritic SGI) TTT diagram used for FE simulations. It is possible to observe that for the reference TTT diagram (Figure 5.1(a)), kinetic of ferritic transformation is slower in comparison

with the modified TTT diagram (Figure 5.1(b)) as the 10% and 90% curves of ferritic transformation are shifted.

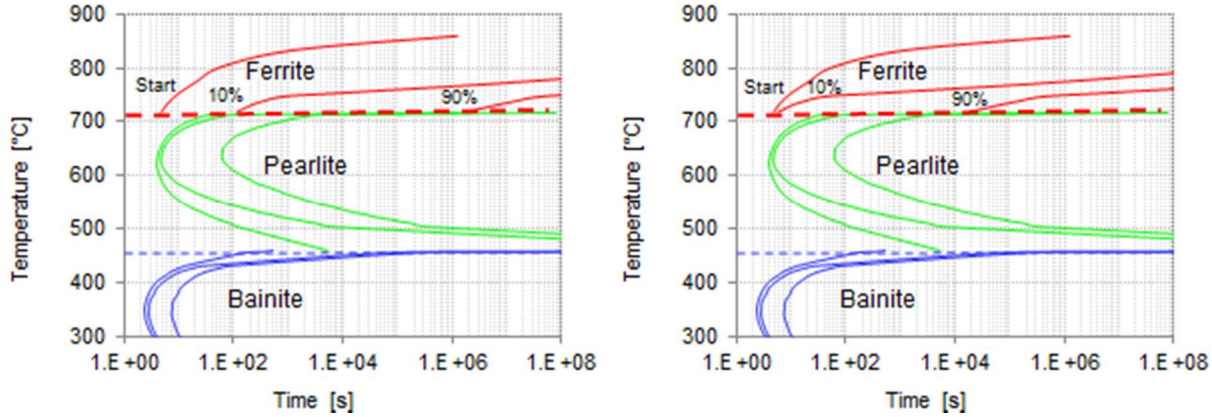

(a) SGI pearlitic grade (reference) **(b) SGI ferritic grade (modified)**

Figure 5.1. Reference and modified TTT diagram for SGI core material

Note that the other curves corresponding to ferrite transformation start and to pearlite and bainite phases are identical for both diagrams. A comparison between simulations considering a SGI ferritic or a SGI pearlitic grade as core material is presented in this section. Modified TTT diagram correspond to a material different from the core material of the reference simulation only from a metallurgical point of view. Mechanical properties are computed by LAGAMINE code using mixture law (see eq. 2.1) based on the same mechanical and thermal data obtained in Chapter 3 by lack of other information. However, finite elements results are slightly modified since phase transformation events (ferrite or pearlite) are modified by the TTT diagram and the mechanical properties of ferrite and pearlite are indeed used. They were identified within the ferritic material studied in section 3.1.5.

The rupture criteria threshold values for reference simulation using reference TTT diagram were computed using eqs 2.24 to 2.30 considering experimental data obtained from tensile tests performed for the pearlitic SGI grade (see section 3.2.2). For the SGI ferritic grade, this data was not obtained experimentally. However, it is known that a ferritic SGI grade is more ductile than a pearlitic one. In addition, the MK industry informs that at room temperature, the ductility (in tension) of a ferritic SGI grade is two times higher than for a pearlitic SGI grade. Therefore, for the computation of the right rupture criterion threshold values at different temperatures, the

fracture strains for ferritic SGI grade were assumed to be two times higher than the ones obtained for pearlitic SGI grade. Fracture strains for both ferritic and pearlitic SGI grades, used for computation of rupture criteria threshold values are summarized in Table 5.1.

Table 5.1. Fracture stress and strain for ferritic and pearlitic SGI grade

Temperature (°C)	ε_{max} SGI Pe (%) (by tensile tests)	ε_{max} SGI Fe (%) (2 x ε_{max} SGI Pe)
20	0.199	0.398
150	2.033	4.066
300	1.844	3.688
500	0.364	0.728

The evolution of axial stress with time for both simulations using reference and modified TTT diagram is shown in Figure 5.2. For SGI ferritic TTT diagram (dotted lines) tensile stress generated at the center of the roll is increased by approximately 30 MPa while for the core interface, the compression stresses are reduced. For shell material, very low differences are observed between simulations using reference and modified TTT diagrams.

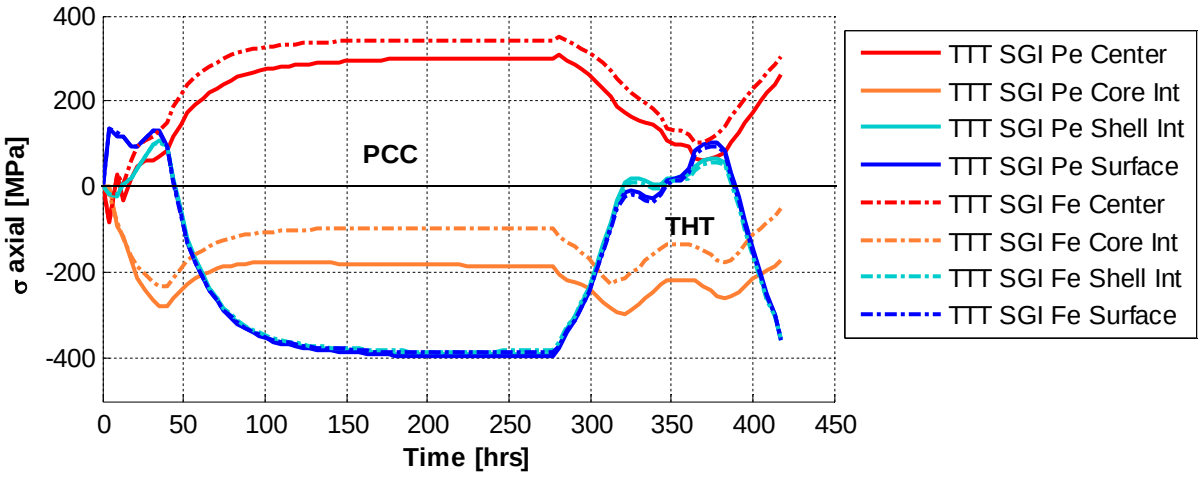

Figure 5.2. Axial stress evolution with time for pearlitic and ferritic TTT diagrams

The evolution of ferrite and pearlite phase transformations obtained in core material by considering both TTT diagrams is shown in Figure 5.3. Figure 5.3 (a) shows that for the reference TTT diagram, a phase rate between 75% and 68% of pearlite is transformed in the core material (SGI pearlitic). Additionally, Figure 5.3 (b) allows confirming that by using the modified TTT diagram, a higher amount of ferrite phase between 80% and 82% is transformed in the core material (SGI ferritic).

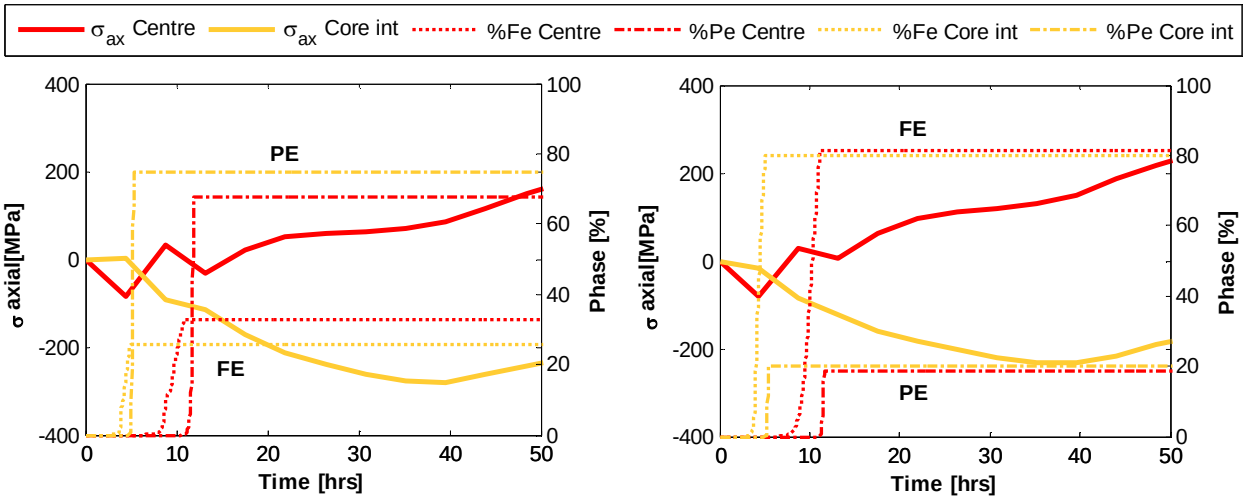

(a) SGI pearlitic grade (reference) **(b) SGI ferritic grade (modified)**

Figure 5.3. Phase transformation evolution for reference and modified TTT diagrams

Axial stress profiles along radius for both simulations at times t4 and t7 (end of PCC and THT stages) are presented in Figure 5.4(a) and (b) respectively. For both times, axial tensile stress is slightly increased at the center of the roll while axial compression stress in the core interface is slightly reduced, using modified TTT diagram (SGI ferritic). However for the rest of the roll, no difference is observed. By comparison of Figure 5.4(a) and Figure 5.4(b) it is possible to confirm that at t7 (end of THT stage) almost the same stress state of time t4 (end of PCC stage) is recovered for both simulations, nevertheless a small relaxation has occurred during THT stage.

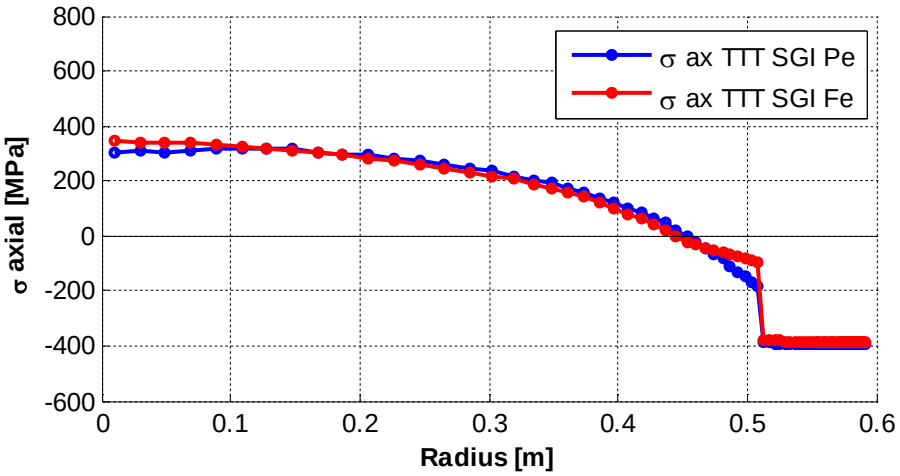

(a) t4 end of PCC stage

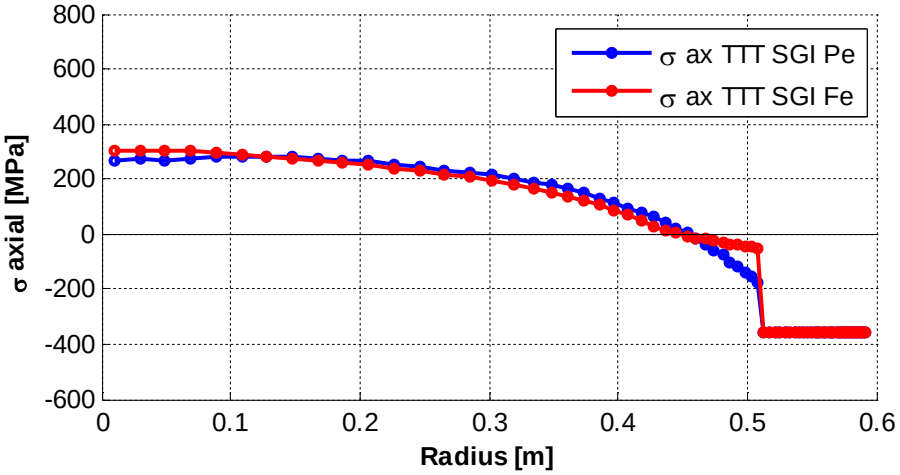

(b) t7 end of THT stage

Figure 5.4. Axial stress profiles for reference and modified TTT diagrams

Rupture criteria values along radius for both simulations are presented in Figure 5.5(a) to (e). Note that for each case, the rupture criteria threshold values were computed using data from Table 5.1. By using modified TTT diagram (SGI ferritic) and ferritic SGI grade crack strain, each criterion predicts a lower damage discarding damage in the core material. Furthermore, according to McCLintock, Freudenthal and Cockroft-Latham criteria damage in the shell material is also decreased.

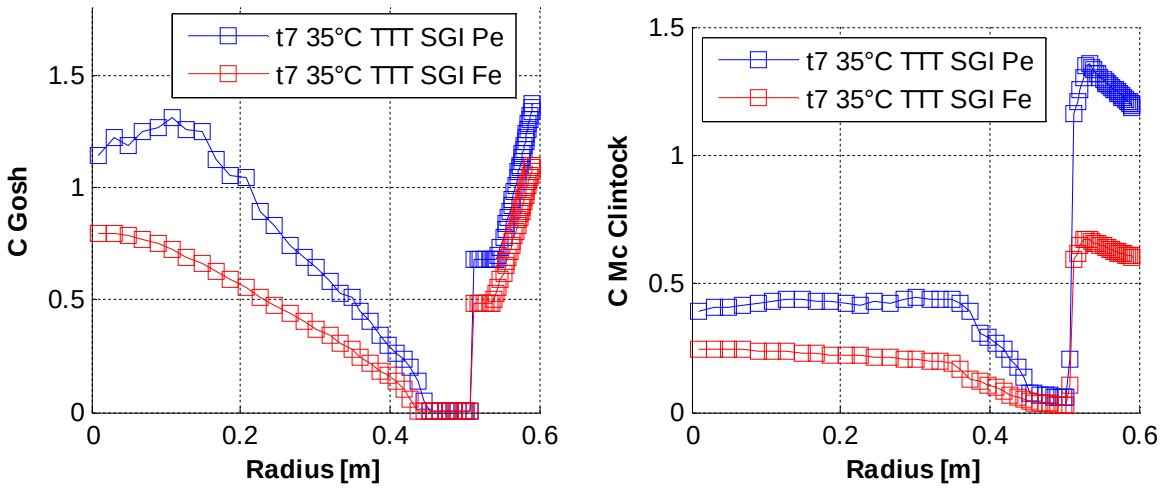

(a) Ghosh criterion

(b) McClintock criterion

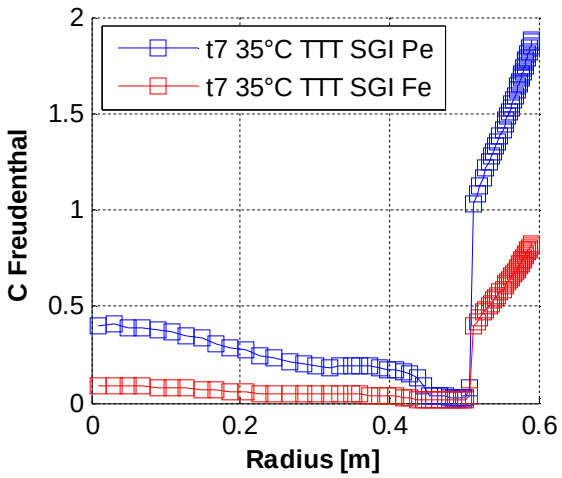

(c) Freudenthal criterion

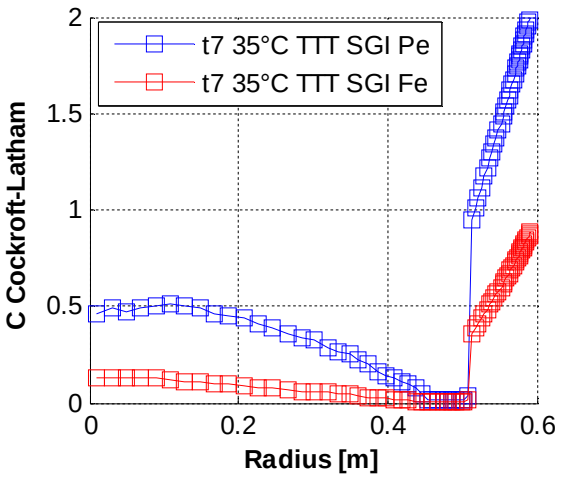

(d) Cockroft-Latham criterion

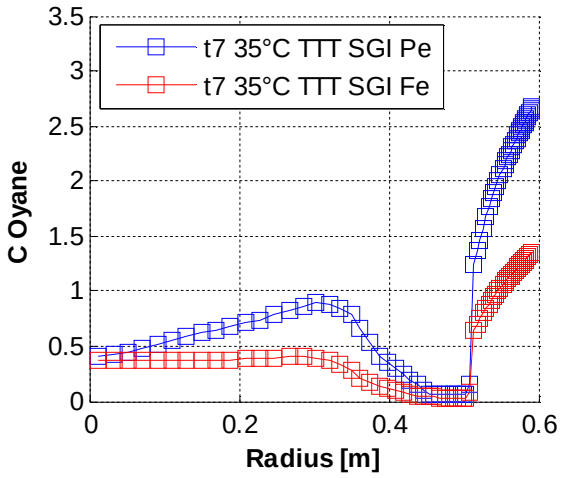

(f) Oyane criterion

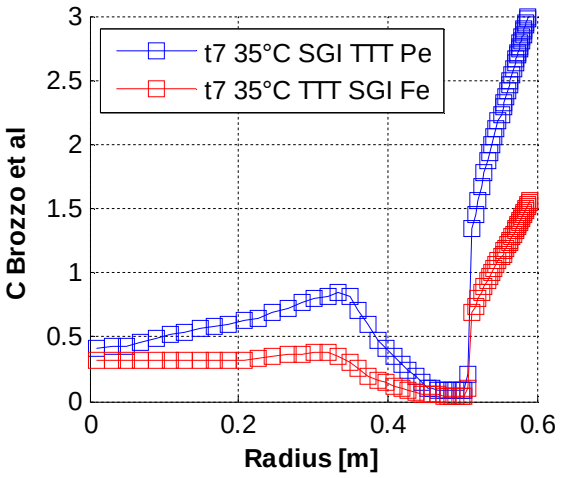

(e) Brozzo et al criterion

Figure 5.5. Value of rupture criteria along radius for reference and modified TTT diagram at the end of THT stage

Summarizing, using a modified TTT diagram which corresponds to a ferritic SGI core material, generates a very slight effect on the axial stress profile. Tensile stress at the center and compression stress at the core interface and shell material are slightly increased and reduced respectively. However, the six rupture criteria analyzed agree in the prediction of a lower damage in the core material using a ferritic SGI core material and discard damage in the core material. A half of the criteria also discard damage in the shell material for a ferritic SGI material. Predictions are in agreement with industrial observations since a lower rate of failure is obtained for bimetallic rolling mill rolls using a ferritic SGI core material.

5.2 Martensite start temperature

In order to analyze the effect of using a different material corresponding to a Semi HSS grade at the shell of the rolling mill roll, martensitic start temperature (Ms) is modified. Let us remind that for reference simulation, the martensitic start temperature of HCS grade is equal to 266°C. It was obtained through cryogenic quenching (see section 3.4). A value of 190°C will be used for the modified simulation and corresponds to the Semi HSS material also used for the shell in rolling mill roll fabrication. However, the mechanical and rupture properties used in this simulation are still the ones identified for the reference material. In Table 5.2, a summary of obtained results through both simulations is presented. The difference for the start of martensitic transformation between both simulations is of 76°C and generates a difference of 14% on the martensite phase final amount.

Table 5.2. Summary of results for reference and modified Ms temperature

	Reference simulation (HCS grade)	**Modified simulation (Semi HSS grade)**
Ms temperature	266°C	190°C
% Martensite phase at the surface	62.2%	48.3%
Residual axial stress in the surface at the end of PCC stage	-393 MPa	-337 MPa
Residual axial stress in the surface at the end of THT stage	-356 MPa	-300 MPa

Note that a difference in the martensite phase amount will affect the mechanical properties of shell material since they are computed by LAGAMINE code using mixture law (see eq. 2.1). The effect of the difference between reference and modified Ms temperatures is a reduction of the axial stress state in 56 MPa in the surface of the roll at the end of both PCC and THT stages.

The evolution of axial stress for both simulations is shown in Figure 5.6. The simulation with the semi HSS grade predicts the reduction of axial stress for the shell material during PCC stage, however during the THT stage, tensile stresses are considerably increased generating a lower compression state at the end of the thermal history. For the core material, a small reduction of tensile stress at the center of the roll and a small increment on compression stress in the core interface, are generated using the modified Ms temperature (semi HSS).

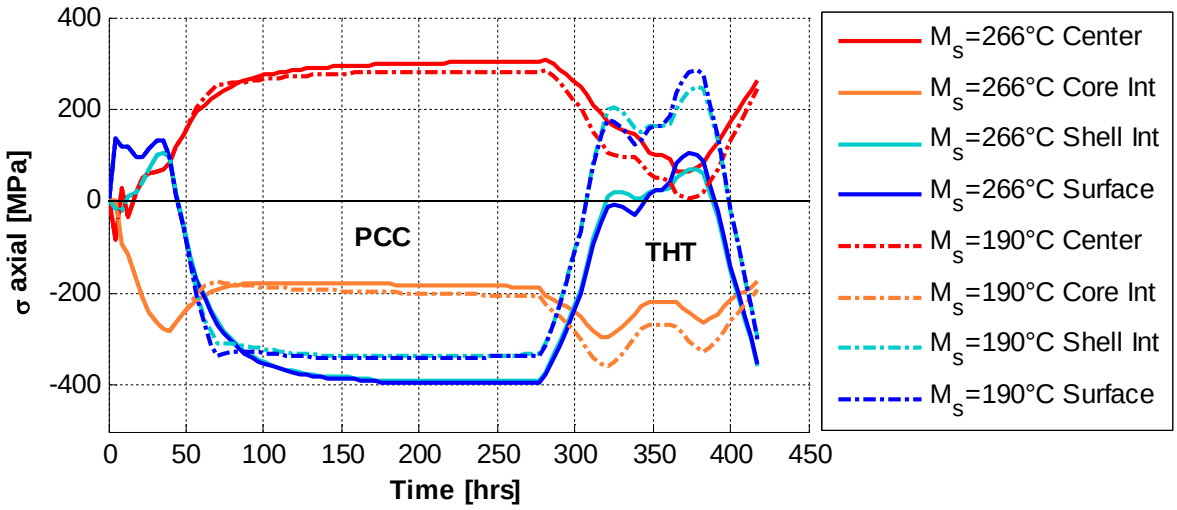

Figure 5.6. Axial stress evolution with time for reference and modified Ms temperature

The evolution of martensite phase transformation obtained in shell material by considering both Ms temperatures is shown in Figure 5.7.

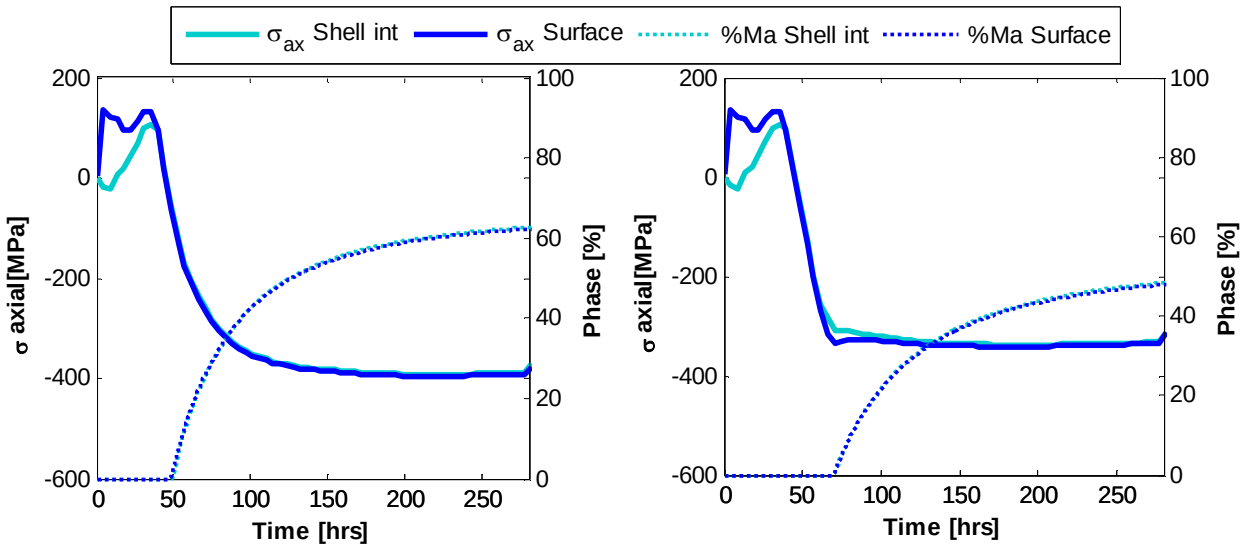

(a) Ms=266°C (reference) **(b) Ms=190°C (modified)**

Figure 5.7. Phase transformation evolution for reference and modified TTT diagrams

Figure 5.7 (a) shows that for the reference Ms temperature equal to 266°C, a phase rate of 62% of martensite phase is transformed in the whole shell material (HCS grade), while Figure 5.7 (b) allows confirming that using the modified Ms temperature equal to 190°C, martensitic transformation is delayed (starting at 48 hrs for reference Ms and at 70 hrs for modified Ms) and a lower amount of martensite phase is transformed in the shell material reaching a 48% of martensite phase in shell material (semi HSS grade).

Residual stress profile along the radius at the end of PCC and THT stages are presented respectively in Figure 5.8(a) and (b). It is confirmed that using the modified Ms (semi HSS material), generates a lower compression stress in the shell material for both times. However, for the center of the roll negligible differences are presented.

Since in Figure 5.6 it was observed that during THT stage high differences are generated for the center of the roll and for the shell material, axial stress profile at times t5=320 hrs (corresponding to approximately 300°C during the heating of THT stage) and t6=380 hrs (corresponding to approximately 300°C during the cooling of THT stage) are presented in Figure 5.9.

For core material, at both t5 (Figure 5.9(a)) and t6 (Figure 5.9(b)) times, tensile axial stresses are reduced in about 70 MPa by using the modified Ms (semi HSS grade), while for the shell material, tensile stresses are highly increased in approximately 200 MPa.

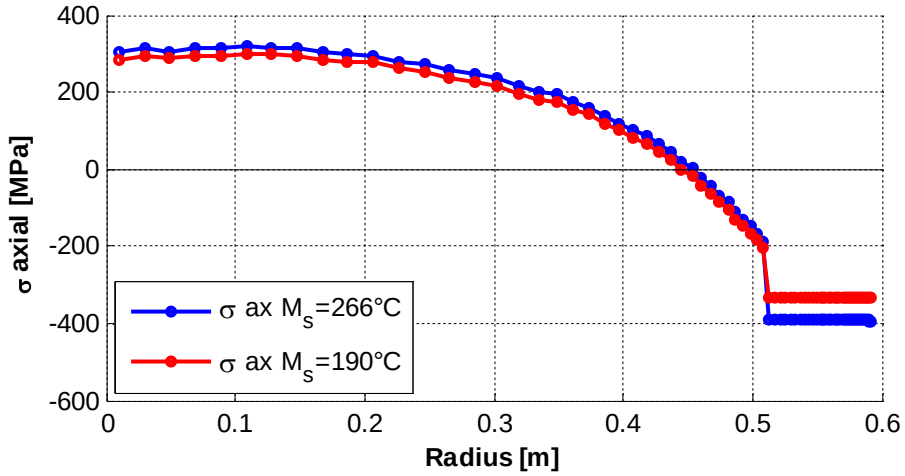

(a) t4 end of PCC stage

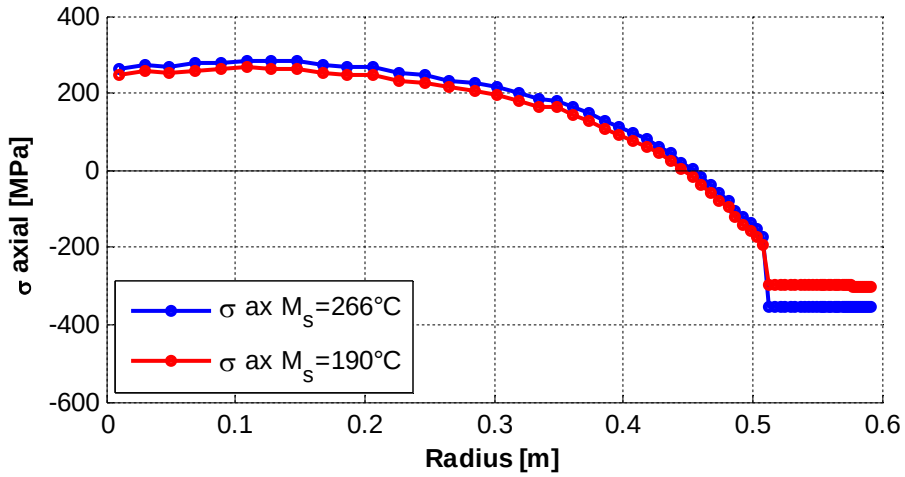

(b) t7 end of THT stage

Figure 5.8. Axial stress profiles for reference and modified Ms temperature at the end of PCC and THT stages

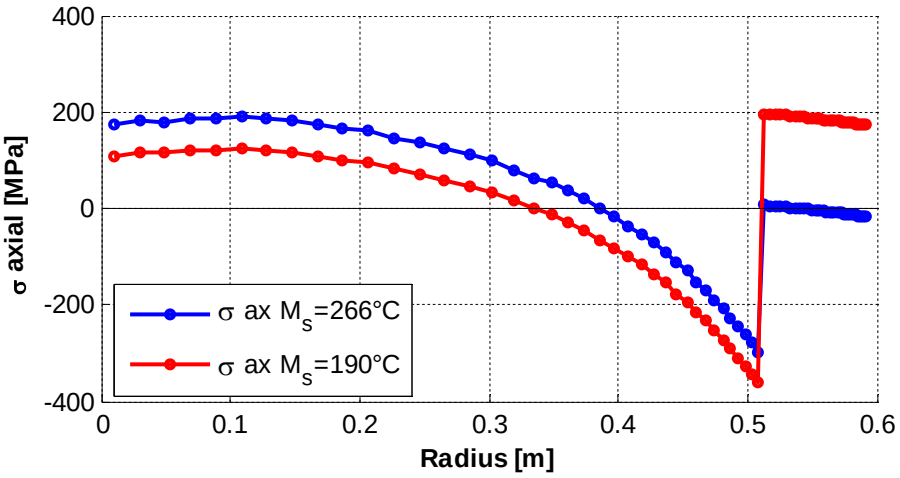

(a) t5 heating of THT at approximately 300°C

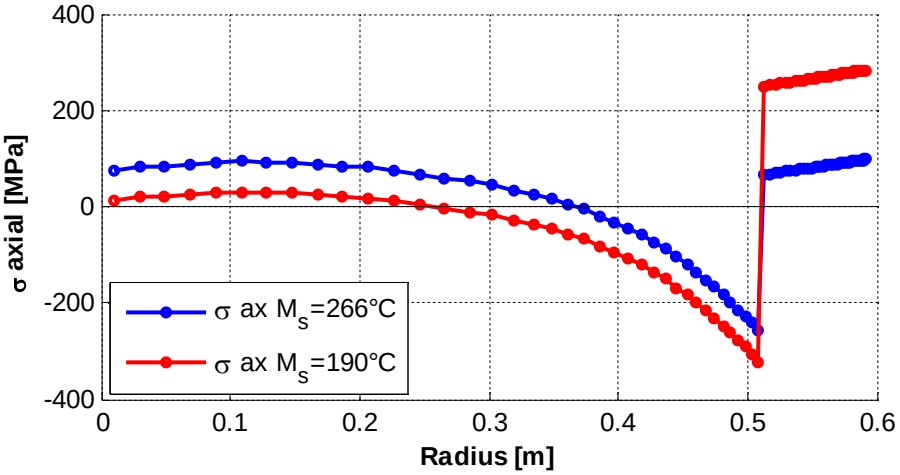

(b) (a) t6 cooling of THT at approximately 300°C

Figure 5.9. Axial stress profiles for reference and modified Ms temperatures at critical times of THT stages

Rupture criteria values along radius for both simulations are presented in Figure 5.10(a) to (e). For core material, a slightly lower damage is predicted by Ghosh criterion using a modified Ms temperature (semi HSS grade), however the five other criteria analyzed do not predict differences between both simulations. For shell material, each criterion predicts a higher damage at the end of THT stage using modified Ms temperature corresponding to semi HSS grade, where high differences are predicted by Ghosh criterion.

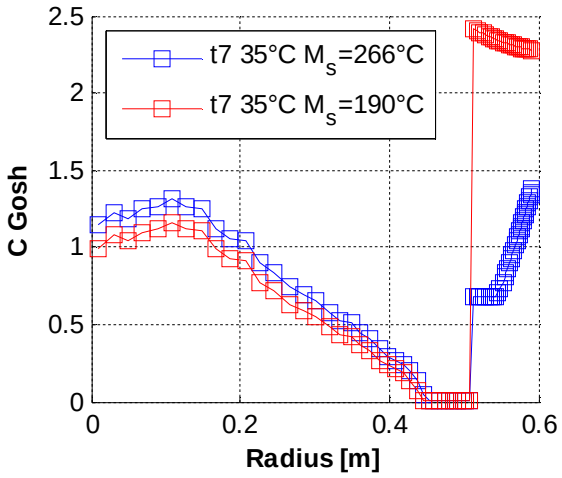

(a) Ghosh criterion

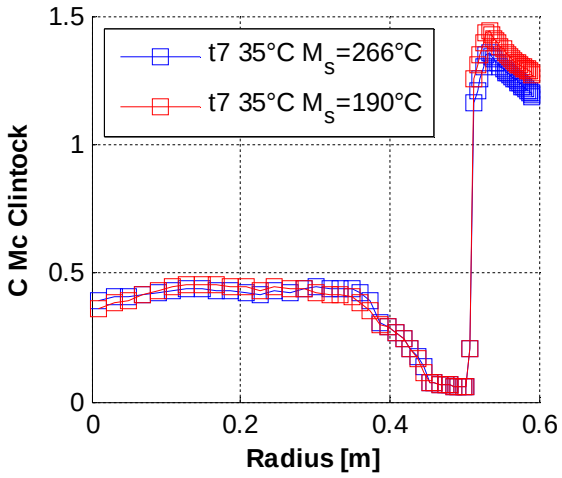

(b) McClintock criterion

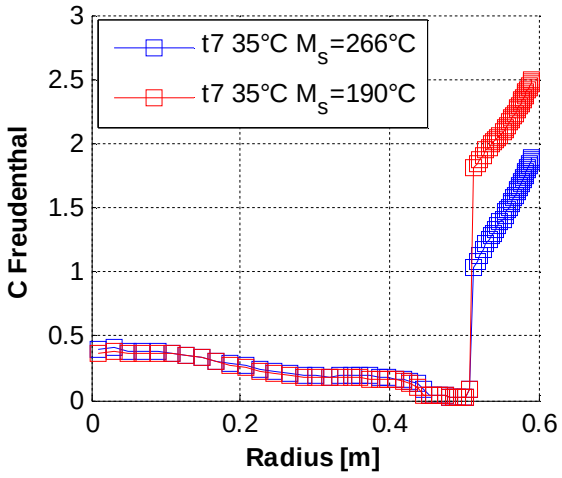

(c) Freudenthal criterion

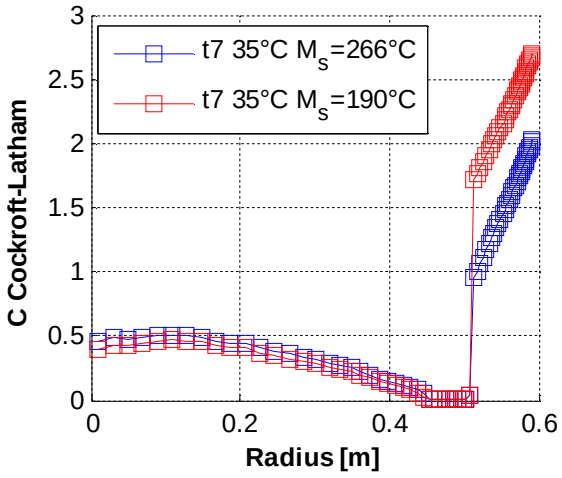

(d) Cockroft-Latham criterion

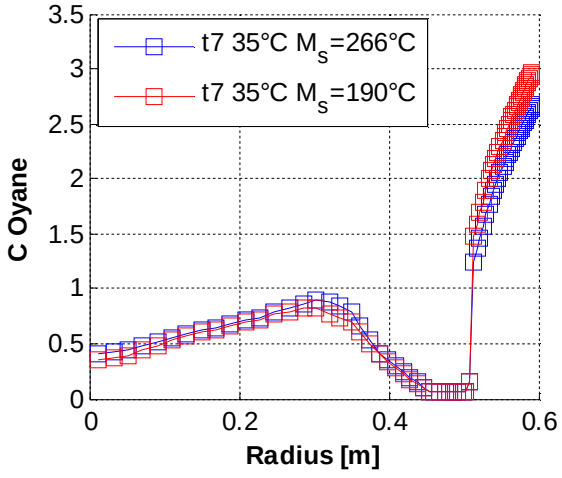

(f) Oyane criterion

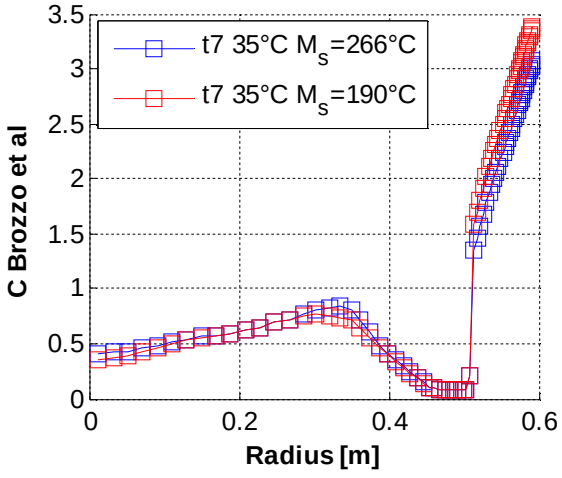

(e) Brozzo et al criterion

Figure 5.10. Value of rupture criteria along radius for reference and modified Ms temperatures

Summarizing, considering a Ms temperature of 190°C corresponding to a semi HSS grade as shell material, predicts a higher damage at the shell even if residual stresses at the end of PCC and THT stages are reduced, since a considerable higher tensile state is generated during THT stage. For the core material, tensile stresses are reduced in the center of the roll and a slightly lower damage is predicted by Ghosh criterion. Using a semi HSS grade, predicts a higher probability of damage since the cumulative damage in the shell material is increased, under the **big assumption** of identical mechanical and rupture properties of both materials. The industry provides the information of a lower ductility for the semi HSS material with respect to HCS material. This fact would enhance predictions obtained here, confirming that a higher probability of damage is expected by using the semi HSS as shell material of rolling mill rolls.

5.3 Shift of martensitic transformation due to stress state

As it was told in section 3.9, several trials were performed for the experimental determination of A and B parameters that define the shift of martensitic transformation due to stress state (see Appendix A). However, since all the trials performed failed, values of A and B parameters from the literature were used in simulations of rolling mill rolls. The sensitivity of simulations to A and B parameters is presented in this section in order to analyze the importance of this eventual inaccuracy of parameters. Several set of parameters were used, nevertheless the most representative result is presented in this section. The effect is amplified by multiplying A and B coefficients used for reference simulations by five. A summary of used parameters and their effect on results is presented in Table 5.3.

Reference simulation predicts a shift of only 2°C on martensitic transformation start. Modified parameters corresponding to five times literature values are chosen since they predict a shift of 54°C in martensitic transformation. This value is considered high enough for the analysis of sensitivity. The impact of this shift in stress results is of about 20 MPa since martensite phase amount is slightly modified of 2 %.

Table 5.3. Summary of results for reference and modified A, B parameters

	Reference simulation	Modified simulation
A, B parameters	A= 5.0E-08 B= 3.3E-08	A= 25.0E-08 B= 16.0E-08
Input Ms temperature	266°C	266°C
ΔMs	2°C	54°C
Final Ms temperature	268°C	320°C
% Martensite phase at the shell interface	62.2%	64.1%
Residual axial stress in the surface at the end of PCC stage	-393 MPa	-414 MPa
Residual axial stress in the surface at the end of THT stage	-356 MPa	-376 MPa

The evolution of axial stress for both simulations is presented in Figure 5.11, where small differences are observed. A slight increment of axial compression stress state is generated in the shell material during PCC stage using modified A, B parameters. During THT stage, tensile stresses at the shell material are slightly decreasing for modified simulation. In the core material no differences are observed between both simulation results.

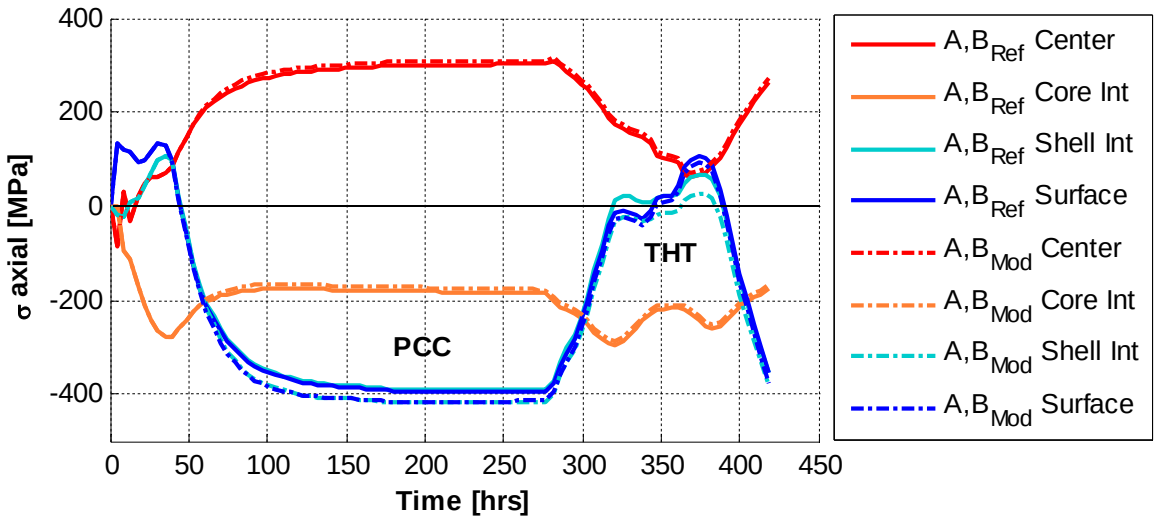

Figure 5.11. Axial stress evolution with time for reference and modified A, B parameters

The evolution of martensite phase transformation obtained in shell material by considering reference and modified A, B parameters, is shown in Figure 5.12.

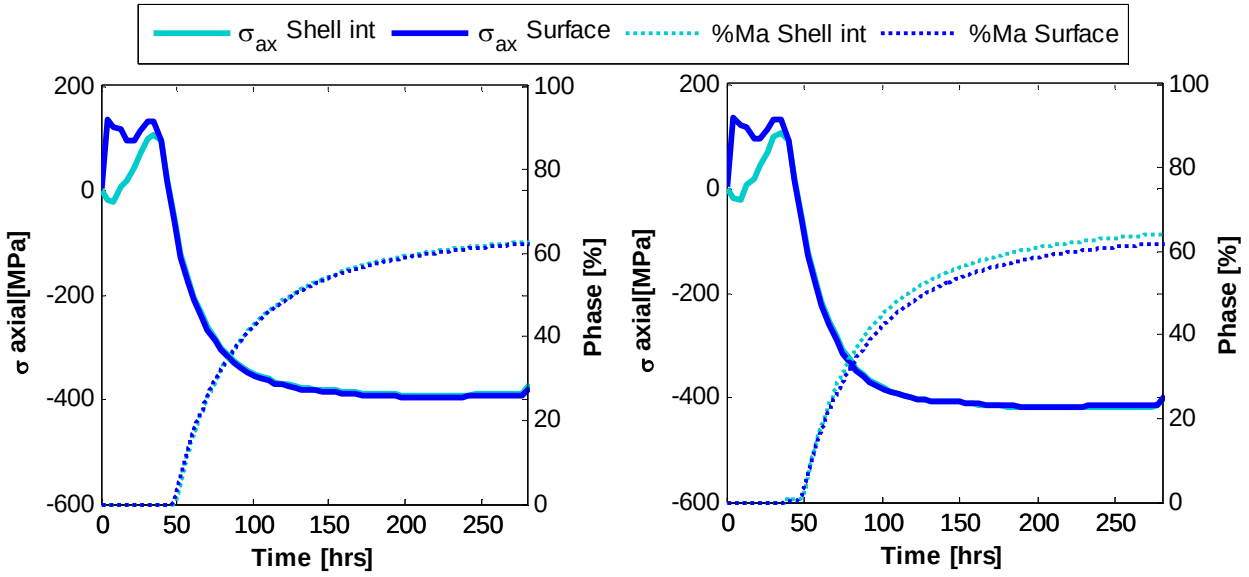

(a) A, B reference parameters **(b) A, B modified parameters**

Figure 5.12. Phase transformation evolution for reference and modified A, B parameters

Figure 5.12 (a) shows that for the reference A, B parameters, a phase rate of 62% Ma is transformed in the shell material. However, Figure 5.8 (b) shows that by using the modified A, B parameters, the start of phase transformation is slightly accelerated (starting at 48 hrs for reference and at 40 hrs for modified A,B parameters) and it is confirmed that almost the same amount of martensite phase is transformed in the shell material, although in the shell interface a slightly higher martensite content of 64% is predicted.

Axial stress profile for both simulations at the end of PCC and THT stages are presented in Figure 5.13(a) and (b) respectively. No difference is observed at the tensile state of core material. In the shell material, a small increment of compression stress is observed for simulation using modified A, B parameters for both moments; the end of PCC and THT stages. However, as presented in Table 5.3 the increment is only 20 MPa.

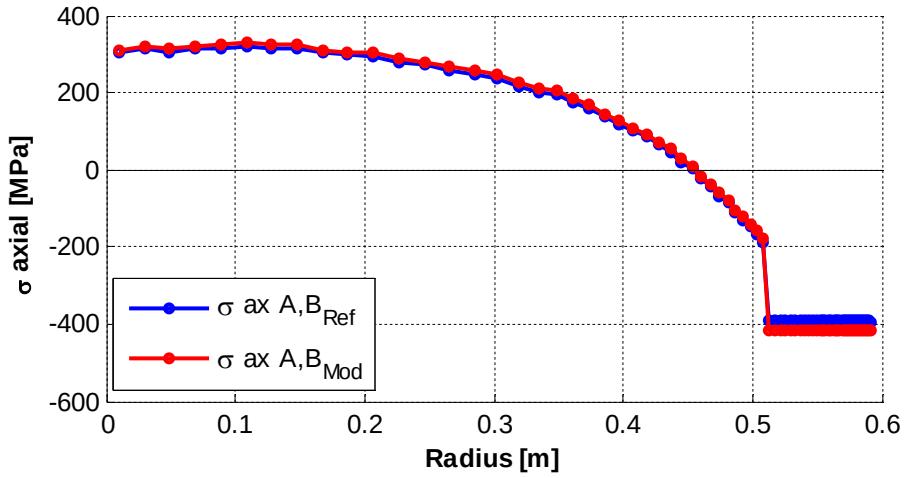

(a) t4 end of PCC stage

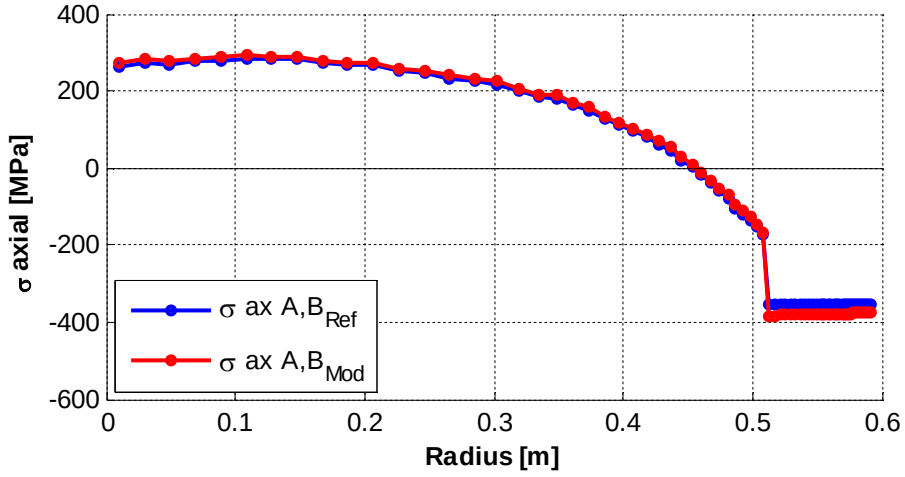

(b) t7 end of THT stage

Figure 5.13. Axial stress profiles for reference and modified A, B parameters

From rupture criteria values, it is possible to notice in Figure 5.14(a) and (b) that according to Ghosh and McClintock respectively; nearly no differences are presented between both simulation predictions.

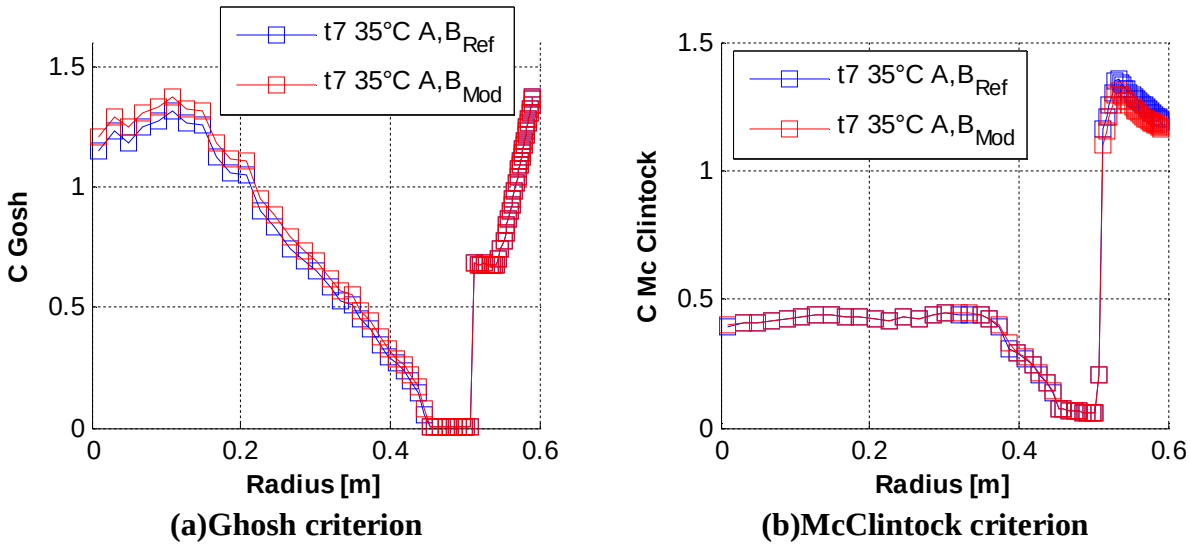

Figure 5.14. Value of rupture criteria along radius for reference and modified A, B parameters at the end of THT stage

Summarizing, using modified A, B parameters that generate a shift of 54°C in martensitic transformation start, will generate a very small effect on simulation results. The axial compression stress is reduced in approximately 20 MPa at the shell material at the end of PCC and THT stages. This result allows confirming that A and B parameters accuracy is not a key feature within the model for this type of simulations, their effect on predictions is negligible.

5.4 Shell thickness

The effect of using a thicker or thinner layer of shell material is studied in this section by comparing results obtained by reference simulation with two other modified simulations. This thickness is imposed by the roll customer and is not a choice by the manufacturer. For reference simulation, a diameter of 1200 mm and a shell thickness of 80 mm is considered. The set of material parameters of the reference simulation is considered for modified simulations, however 50 mm and 120 mm are used as shell thickness by shifting the position of the interface between core and shell material. Schemes of different geometries modelled are presented in Figure 5.15.

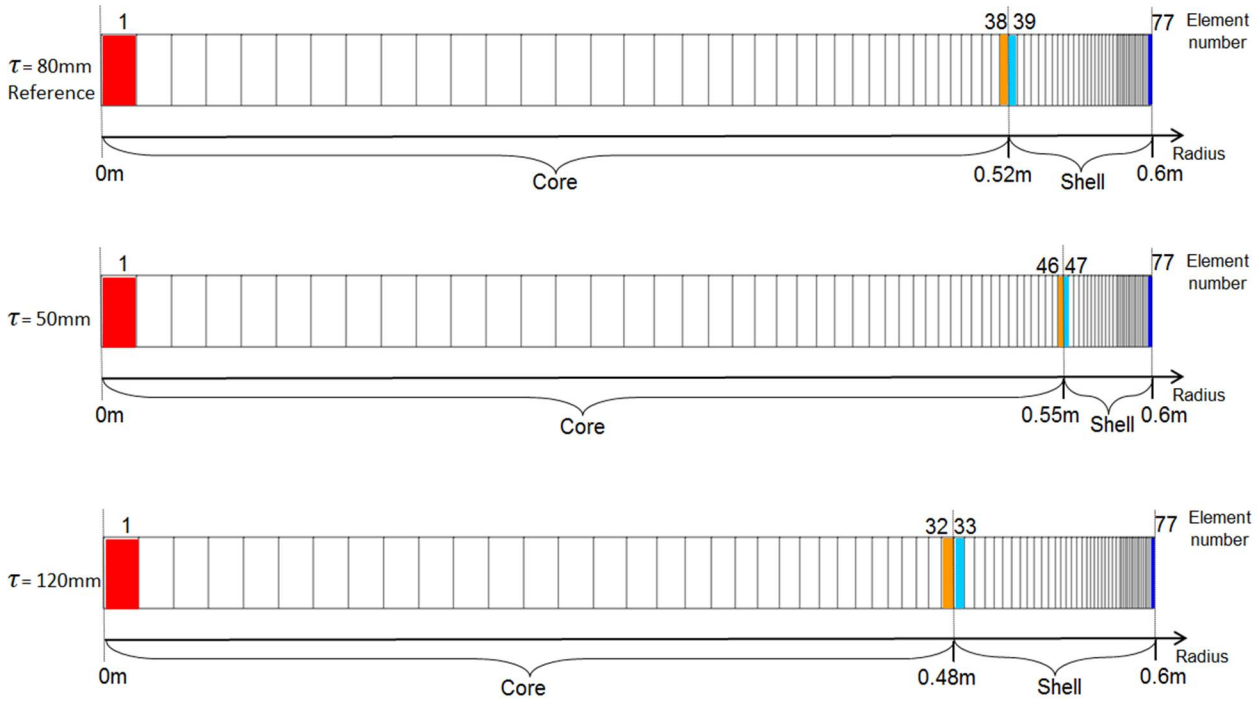

Figure 5.15. Different geometries modelled for shell thickness modification

Axial stress history for different shell thickness is shown in Figure 5.16. It is observed that in comparison with reference simulation (τ=80 mm), a bigger shell thickness (τ=120 mm) generates a slight increment of tensile stresses for the center of the roll while for the core interface an important reduction of compression stresses is observed. For the shell material, compression and tensile stresses are reduced during PCC and THT stages respectively. Furthermore, for a smaller shell thickness (τ=50 mm) the contrary effect is observed for core and shell materials of a rolling mill roll.

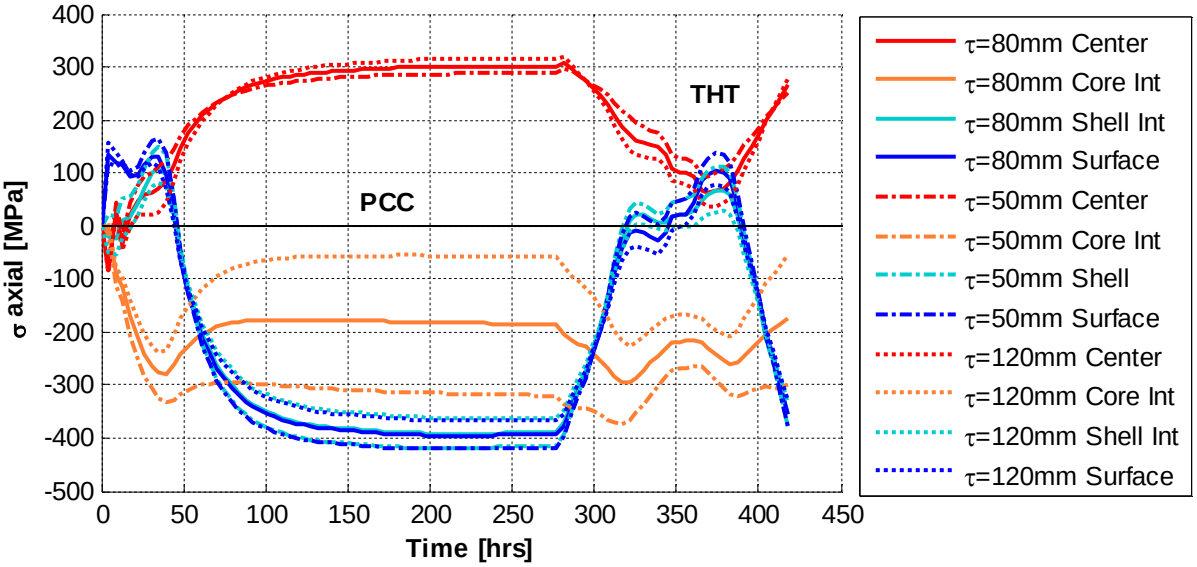

Figure 5.16. Axial stress evolution with time for different shell thicknesses

For reference and modified shell thickness simulations, residual stress profile along radius after PCC and THT stages are presented in Figure 5.17(a) and (b) respectively. For a bigger shell thickness (τ=120 mm), a slightly higher tensile stress is generated at the center of the roll while for the core interface, compression stresses are reduced due to the fact that the interface is shifted. In shell material, using a bigger shell thickness generates a slightly lower compression stress. The contrary effect is generated using a smaller shell thickness (τ=50 mm). However for both moments (t4 and t7), in the center of the roll and in the shell material, the effect on stresses of using a bigger or smaller shell thickness is approximately ±20 Mpa between reference and modified simulations.

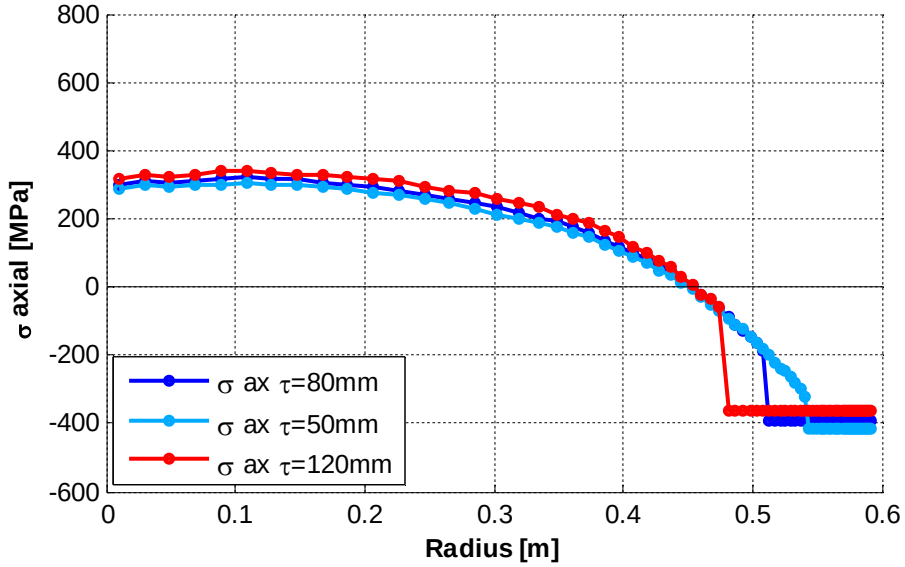

(a) t4 end of PCC stage

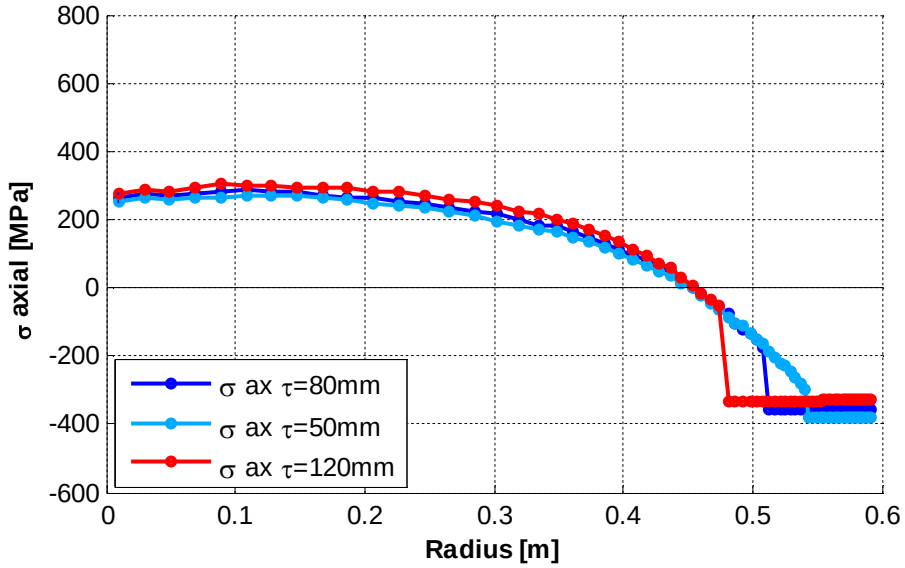

(b) t7 end of THT stage

Figure 5.17. Axial stress profiles for different shell thicknesses

Figure 5.18 shows rupture criterion values according to Ghosh and McClintock at the end of THT stage for different shell thickness simulations. Ghosh criterion (Figure 5.18(a)) predicts a higher (lower) damage at the core material using a bigger (smaller) shell thickness. However the same damage is predicted at the shell material for three simulations. On the contrary, McClintock criterion (Figure 5.18(b)) predicts a lower (higher) damage for core material for the simulation

using a bigger (smaller) shell thickness, while for shell material using smaller shell thickness, damage is predicted only at the external part of the shell material.

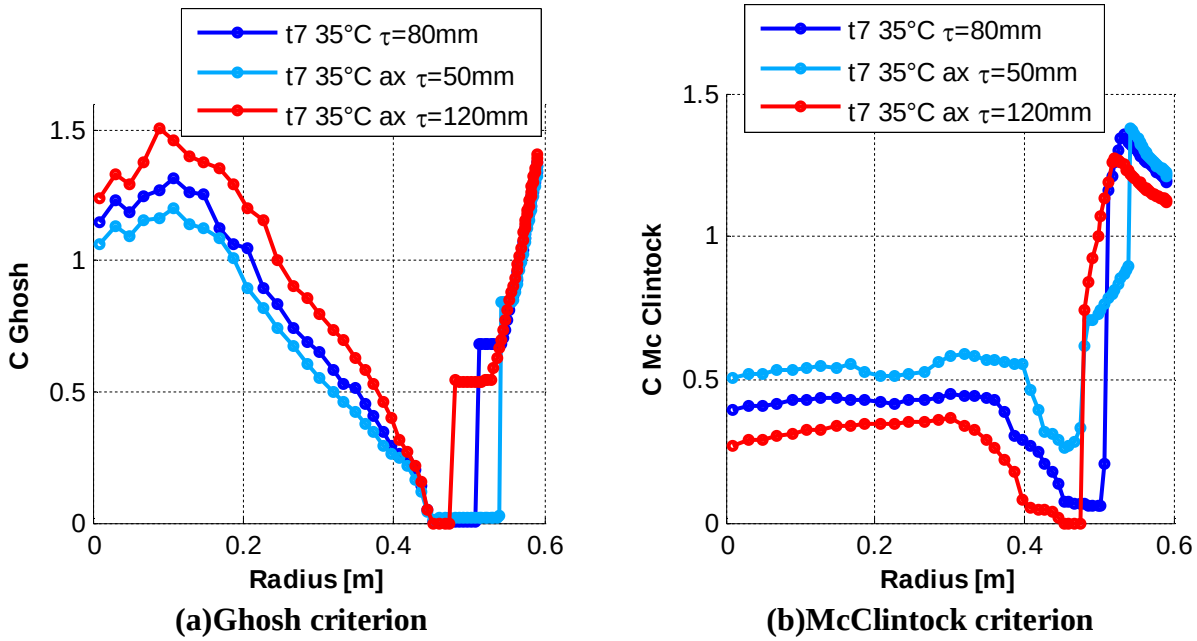

Figure 5.18. Value of rupture criteria along radius for different shell thicknesses at the end of THT stage

Summarizing, using a **bigger shell thickness** (τ=120 mm); a higher tensile state at the center of the roll is predicted and damage at the core material according to Ghosh is increased. For the shell material, compression stresses are reduced. The opposite effect is observed **for a smaller shell thickness** (τ=50 mm) where tensile stresses are reduced in the core and compression stresses are increased in the shell. In addition, the gap between axial stress in the core and shell material at the interface is considerably reduced and McClintock predicts damage only at the external part of the shell material. In conclusion, the reduction of axial stresses in the core material and in the gap at the interface together with McClintock and Ghosh predictions lead to think in a lower damage probability using a smaller shell thickness.

5.5 Diameter

The effect of modelling a bigger or a smaller rolling mill roll is studied in this section by comparing results obtained from reference simulation with two modified simulations results. For reference simulation a diameter of 1200 mm and a shell thickness of 80 mm is considered. The same set of material parameters from reference simulation were considered for modified simulations, however 950 mm and 1300 mm are considered as rolling mill roll diameter. Schemes of different geometries modelled are presented in Figure 5.19.

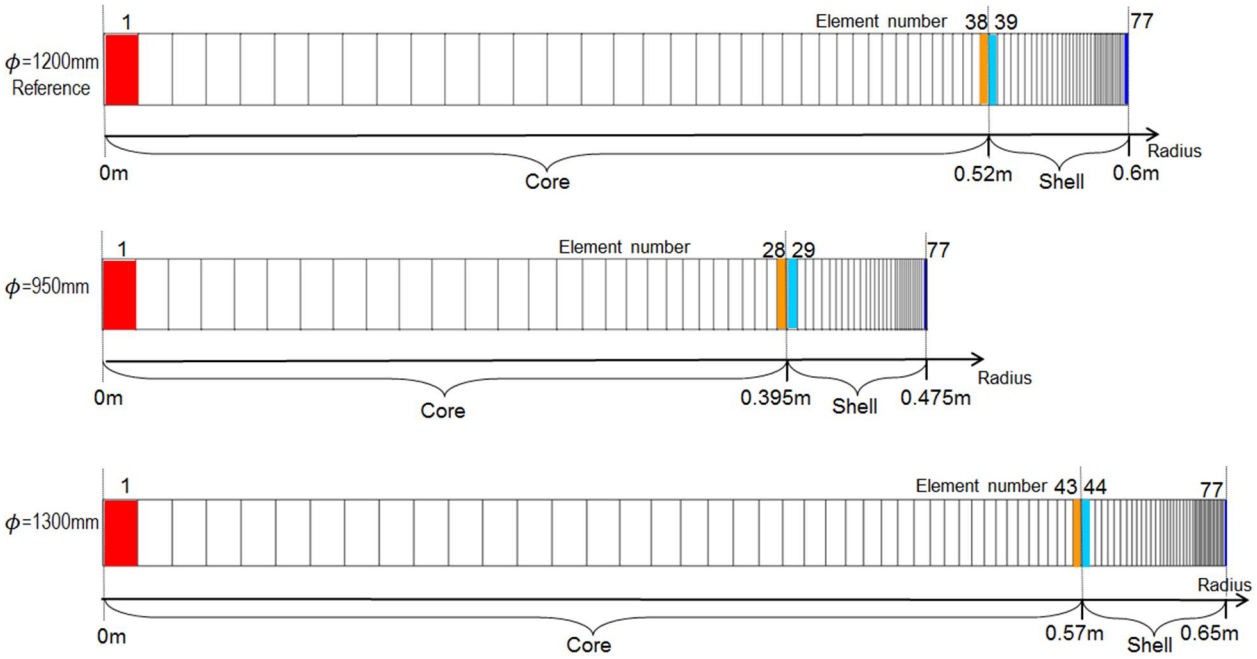

Figure 5.19. Different geometries modelled for diameter modification

Axial stress evolution with time during PCC and THT stages for the three simulations using a different diameter is shown in Figure 5.20.

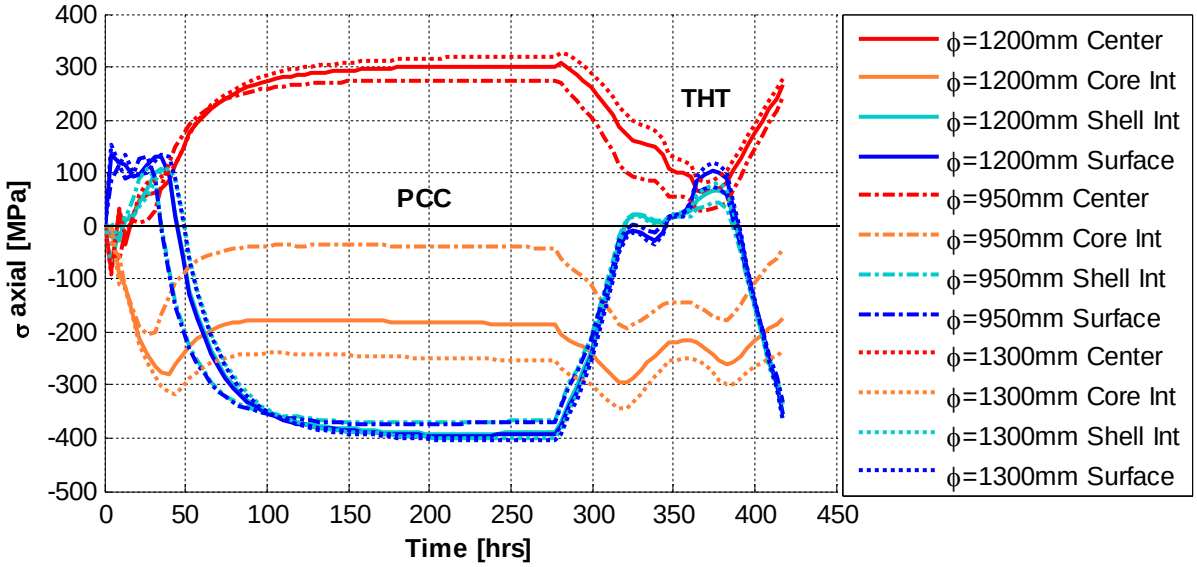

Figure 5.20. Axial stress evolution with time for different diameters

An increment of tensile and compression stresses is predicted at the center of the roll and at the core interface respectively for a bigger diameter (ϕ=1300 mm) while for the shell material, compression stresses are slightly increased. The opposite effect is observed for a smaller diameter (ϕ=950 mm).

Residual stress profile along the radius at the end of PCC and THT stages are presented in Figure 5.21(a) and (b) respectively for three different diameters modelled. Using a bigger diameter (ϕ=1300 mm), slightly increases tensile stresses in the center of the roll. In addition, as the interface is shifted, a higher compression stress is generated at the core interface. For shell material, a slightly higher compression stress is predicted. The contrary effect is generated using a smaller diameter (ϕ=950 mm).

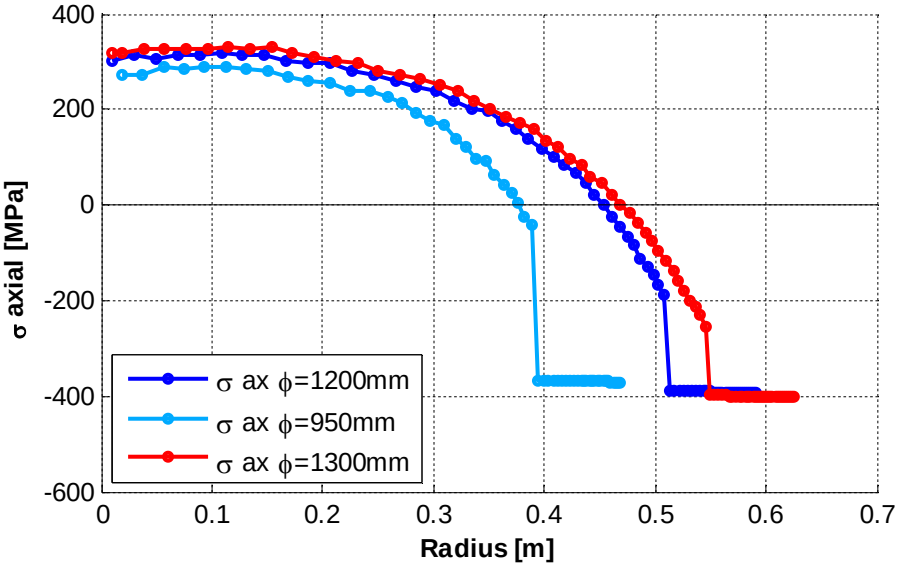

(a) t4 end of PCC stage

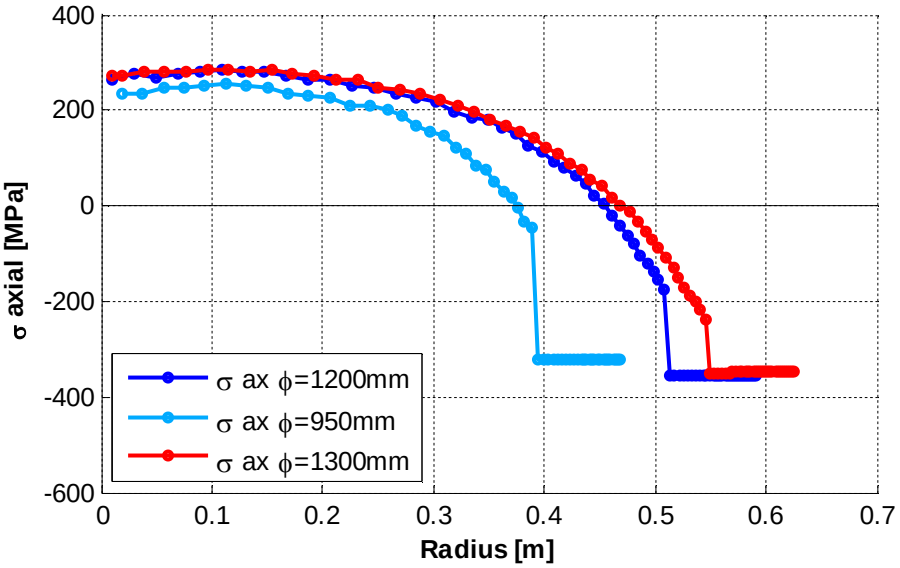

(b) t7 end of THT stage

Figure 5.21. Axial stress profiles for different diameter

Values of rupture criteria at the end of THT stage for different diameters are presented in Figure 5.22(a) and (b) according to Ghosh and McClintock criteria respectively. Both criteria are predicting a higher damage for core and shell materials using a bigger roll diameter while the opposite prediction is made for a smaller roll diameter. In fact, for diameter 950 mm according to Ghosh criterion, damage is generated only at a small part of the core material while the center

and the rest of the roll are damage free. According to McClintock for diameter 950 mm, damage is generated only at the outer part of shell material.

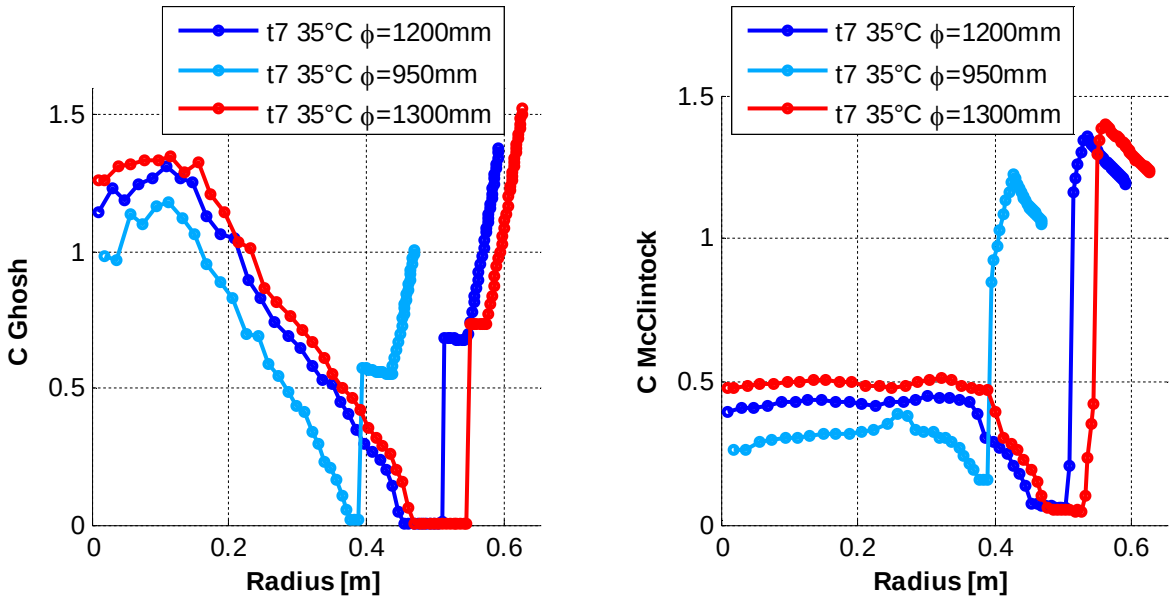

(a) Ghosh criterion **(b) McClintock criterion**

Figure 5.22. Value of rupture criteria along radius for different diameter ϕ at the end of THT stage

Using a **smaller roll diameter** allows reducing the stress state generated and damage prediction at the core and shell material. The contrary effect is obtained for a **bigger roll diameter** increasing the stress state and damage prediction at the whole rolling mill roll. Predictions are supported by industrial observations since for smaller diameters, no rupture case of rolling mill rolls is observed.

5.6 Conclusions and suggestions

From the sensitivity analysis presented in this chapter, generated by modifications of material parameters and geometries, it is possible to affirm following statements:

- Using a modified TTT diagram corresponding to a ferritic SGI core material, predicts a very slight effect on axial stress profiles. However the rupture criteria analysis considering the higher ductility of SGI ferritic grade, allows discarding damage in the core material by using

a ferritic SGI as core material. Predictions are in agreement with industrial observations since the use of a ferritic SGI core material has reduced the failure problem of bimetallic rolling mill rolls.

- A Ms temperature of 190°C corresponding to a semi HSS shell material with similar mechanical and fracture properties, generates a higher damage at the shell material and a higher probability of damage is predicted.
- Considering higher A, B parameters (shift of Ms temperature in presence of stress state) generating a shift of 54°C in martensitic transformation start, a very small effect on simulation results (stress and rupture) is observed. Therefore, even if A, B parameters were not accurately achieved in this thesis; their effect on simulation predictions is negligible.
- The rupture probability can be reduced using a smaller shell thickness, since axial stresses in the center of the roll and the gap of axial stresses at the interface between core and shell materials are reduced, this hypothesis is supported by both Ghosh and McClintock criteria.
- Industrial observations of rupture phenomena occurring for diameter equal or larger than 1200 mm are confirmed by simulations result since a lower rupture probability using smaller roll diameters is predicted.

Conclusions and perspectives

Within this research, following results have been established:

- The modelling of bimetallic rolling mill rolls is settled, since the parameters of both core and shell materials were experimentally measured or obtained by inverse method.
- For a reference simulation, the stress profile obtained by numerical simulation at the end of PCC stage (t4) predicts rupture at the center of mill rolls since rupture stress is surpassed. However at this stage, the shell is highly compressed avoiding crack propagation. During THT stage, the shell is subjected to tensile stresses and a high gradient of stresses at the interface leads to think that the crack propagation into the shell material is achieved in this stage. Damage criteria allow confirming this hypothesis of rupture as “star cracks”, since the analyzed rupture criteria predict shell damage during THT step.
- If the core is strong enough to resist high tensile stresses, due to a lower pollution effect or another factor, the shell material might also be the origin of cracks in a zone closer to the interface with core material. This hypothesis of rupture as “butterfly” cracks is based on McClintock criteria predicting rupture during THT stage starting at the core-shell interface.
- Both rupture hypotheses derived from numerical results are quite in agreement with industrial observations of the real phenomena occurring to bimetallic mill rolls.
- From the sensitivity analysis; it is possible to establish that a higher probability of damage is predicted by considering a lower Ms temperature. The opposite effect is expected by using a SGI ferritic core material, a smaller shell thickness and a smaller roll diameter since a lower probability of damage is predicted for each case. In addition, it is confirmed that the effect of the lacking accurate A, B parameters is negligible.
- Predictions for reference rolling mill roll in comparison with predictions for smaller diameters and for a ferritic SGI core material, are quite in agreement with experimental

observations since for both modifications in manufacturing process, the failure rate is reduced.

The FE model and all the experimental work, allowed the development of a tool able to explain potential rupture scenarios linked to industrial observation trends. Its validity was confirmed by the observations of Chapters 4 and 5, since the model was capable of correctly predicting the same industrial observations of rupture events and modifications of diameter and core material. However, the model is still far from quantitative predictions considering the rupture or even accurate residual fields and its limitations must be also clarified. Let us remind that the tempering heat treatment is applied principally to reduce the fragility of martensite phase and to increase its toughness, but also for the structure homogenization and relaxation of the residual stress levels. The simple law of Koistinen-Marburger for the initial composition of austenite phase does not allow the modeling of transformations during the tempering heat treatment. It would be required to model the carbides dissolution considering the changes of composition as it has been done in [127]. In addition, the use of an elasto-plastic law and no an elasto-viscoplastic one is not adapted for the prediction of the residual stress relaxation. These two elements missing in the model, as well as the simplistic hypothesis of the binary interface between core and shell materials, dismissing the pollution effect and the progressive composition change, justify the difference between modeling and complex reality. As reported in [59], the studied materials are complex. The phenomenological model of phase transformation and rough damage analysis used here provide only a macroscopic average of the behavior, when rupture is often related to local event. However, the presented simplified model allows realistic predictions since it has been calibrated by the real stresses measured in the manufacturer industry. It can help to understand the roll behavior and predict trends when geometry, materials or other manufacturing parameters are modified.

Appendix A. Research for shift of martensitic transformation coefficients

In this thesis, a wide research was performed with the aim of proposing experimental tests that could be useful and achievable for the estimation of the shift in the start of martensitic transformation due to the generated stress state; however several trials were not successful. A summary of the performed research is provided in this appendix.

Shift of martensitic transformation due to stress state

The start of martensitic transformation M_s can be modified due to the generated stress state according to:

$$\Delta M_s = A\sigma_m + B\bar{\sigma} \qquad \text{A.1}$$

where σ_m is the hydrostatic component of the stress tensor and $\bar{\sigma}$ is the equivalent stress. A and B are coefficients specific of each material. A and B parameters could be identified from two linear relations. A first one could be obtained from compression tests and a second one from shear tests.

Compression tests research

Trials for compression tests were achieved in the MSM laboratories using the SCHENCK Hydropuls 400kN machine with a quad elliptical radiant furnace 4x2000W. The studied material corresponds to the Semi HSS grade. Cylindrical samples with 15 mm height and 9 mm diameter are compressed and connected to a thermocouple for the temperature tracking. The aim was an

accurate measurement of the temperature history in order to detect a variation of the curve associated to the martensitic transformation. Two tests were proposed. For both tests, samples must be heated at 0.5°C/s up to 950°C for achieving the austenitization, then the cooling until room temperature is performed for a load free sample (test 1) and for a loaded sample (test 2). The cooling of samples would allow the registration of the martensitic transformation temperature with and without load.

- For first trials of test 1, it was very difficult to detect the M_s temperature due to fact that the large puncher affected the cooling history of the sample as shows the Figure A.1 (a) (red curve).
- A second trial was performed starting the cooling of the sample at 2400 seconds and extracting the sample from the puncher contact. This trial allowed observing a change of slope related to martensitic sample at approximately 289°C in Figure A.1 (a) (blue curve).
- Two additional trials were performed starting the cooling at 2500 seconds (green and magenta curves). These trials were correctly reproducible since for both cases the slope change is detected at 190°C for two samples as it is observed in Figure A.1 (b). In addition this last result was in agreement with the M_s temperature experimentally measured in [5] for Semi HSS grade.

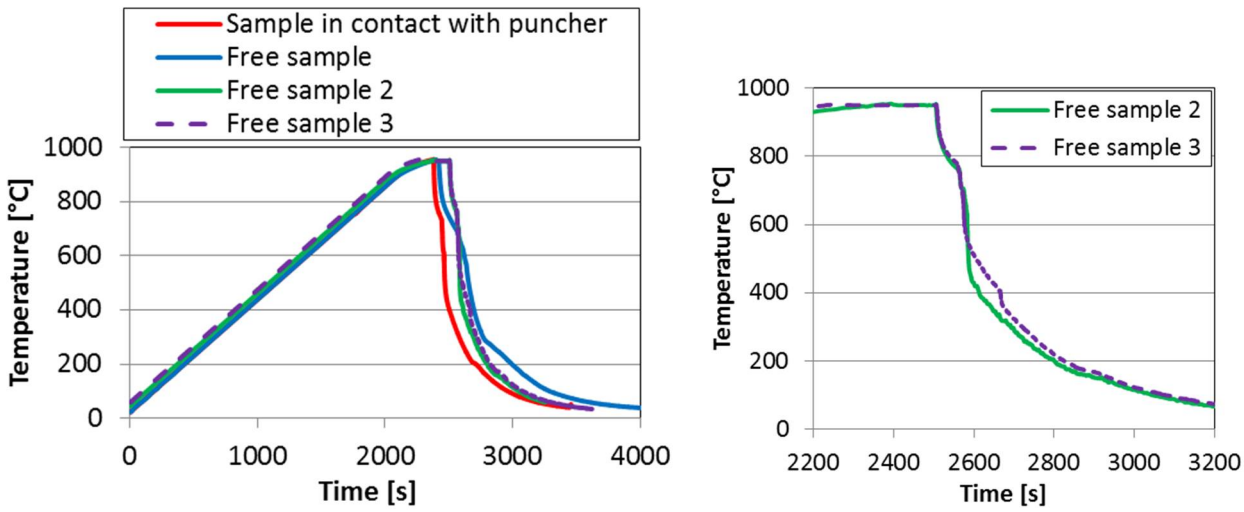

(a) Trials without load **(b) Zoom for trials 2 and 3**

Figure A.1. Cooling curve for trials without load for martensitic transformation start

Since test consisted in the cooling of the sample while a certain load that could affect the martensitic transformation start is applied, the extraction of the sample was not possible for this case. Therefore, trials by cooling the puncher using compressed air were performed as it is shown in Figure A.2. However, no change of slope is detected since the puncher continues affecting the sample cooling as shows Figure A.3.

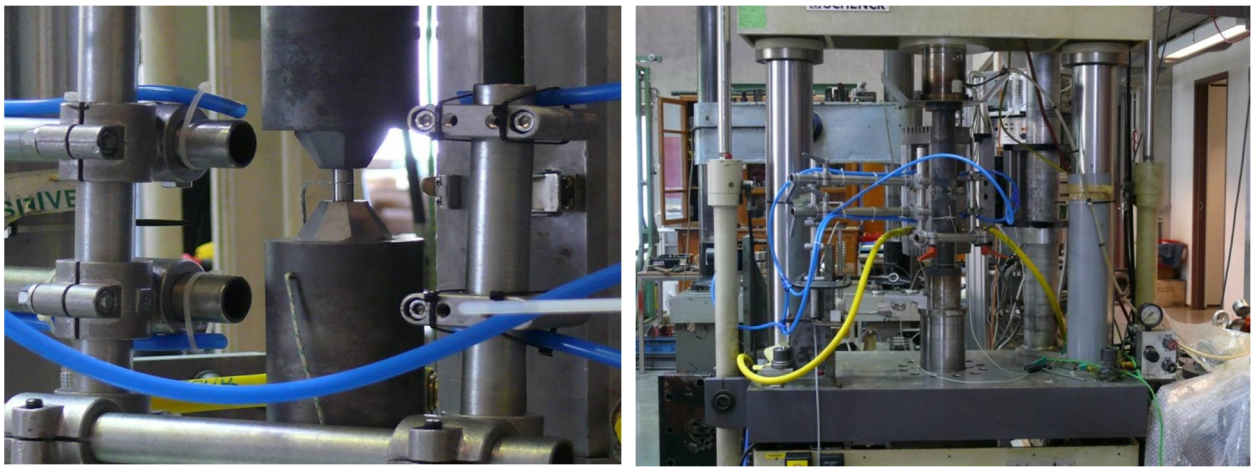

Figure A.2. Image of the puncher cooled by compressed air

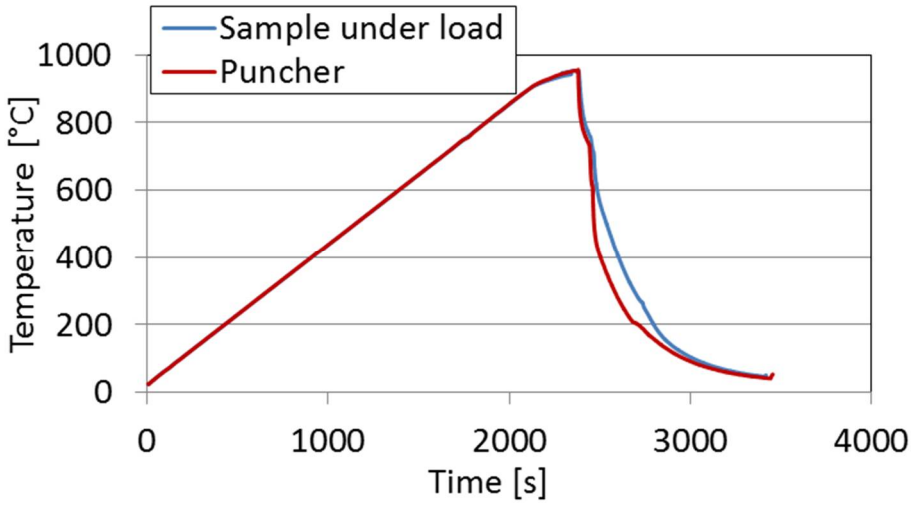

Figure A.3. Cooling curve with load (puncher cooled by compressed air)

Due to the high influence of cooling rate and holding time, it was not possible to reproduce tests correctly by managing the compression load and the cooling rate applying the compressed air at the same time.

Shear tests research

In addition, shear tests are also required for establishing a second linear relation between both A and B coefficients. Numerical simulations were performed to find an optimized geometry inducing shear stress state under compression loads that allows the observation of a different M_s temperature in zones subjected to shear state. In addition the geometry should fit into the puncher diameter of 65 mm. The first proposed geometry is shown in Figure A.4. Compression would be applied in Y direction subjecting the middle thinner sections to shear stress state. A difference of approximately 20°C in the M_s temperature is predicted between shear and shear free sections (see Figure A.5).

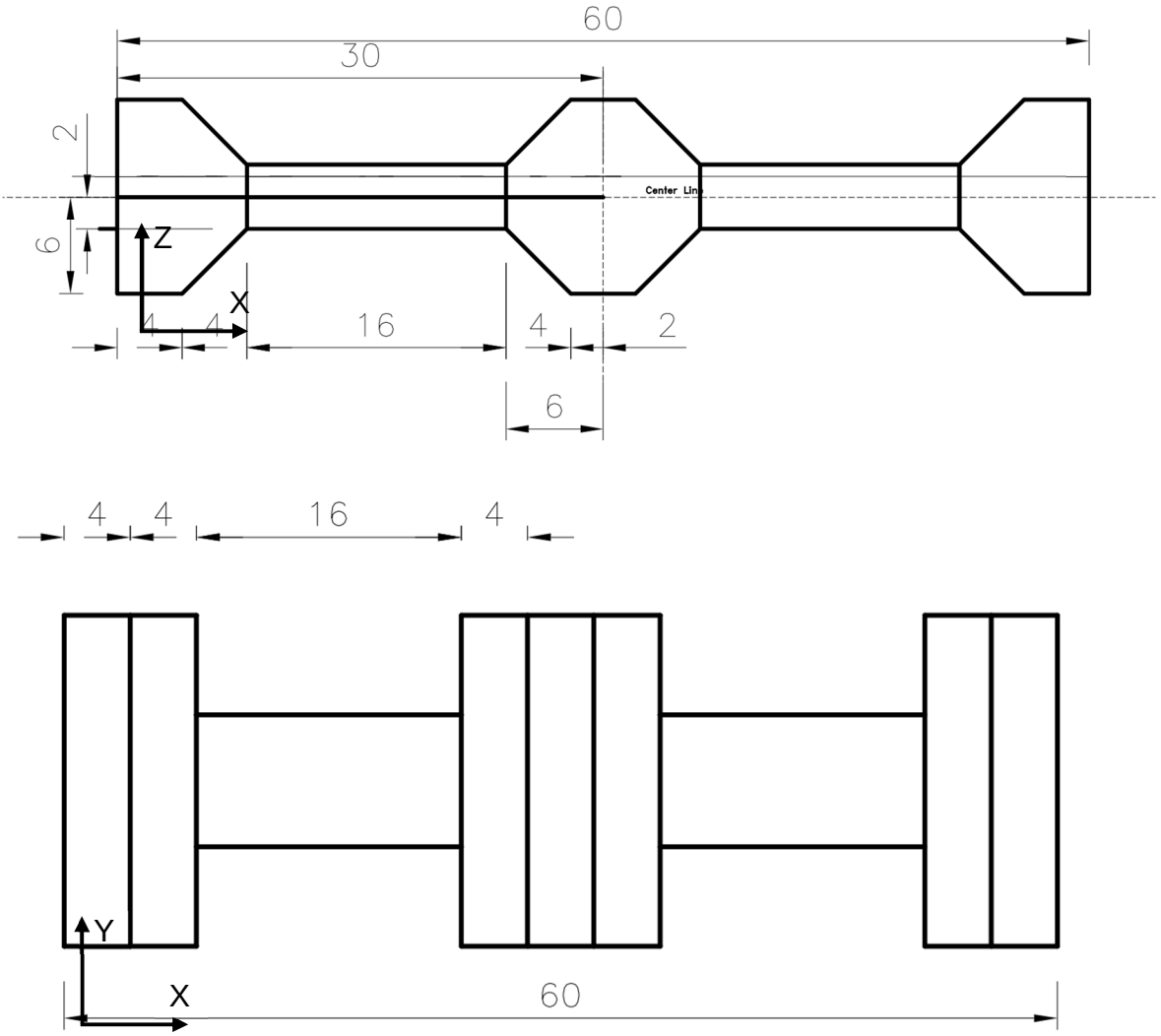

Figure A.4. First geometry proposed for shear tests (dimensions in mm)

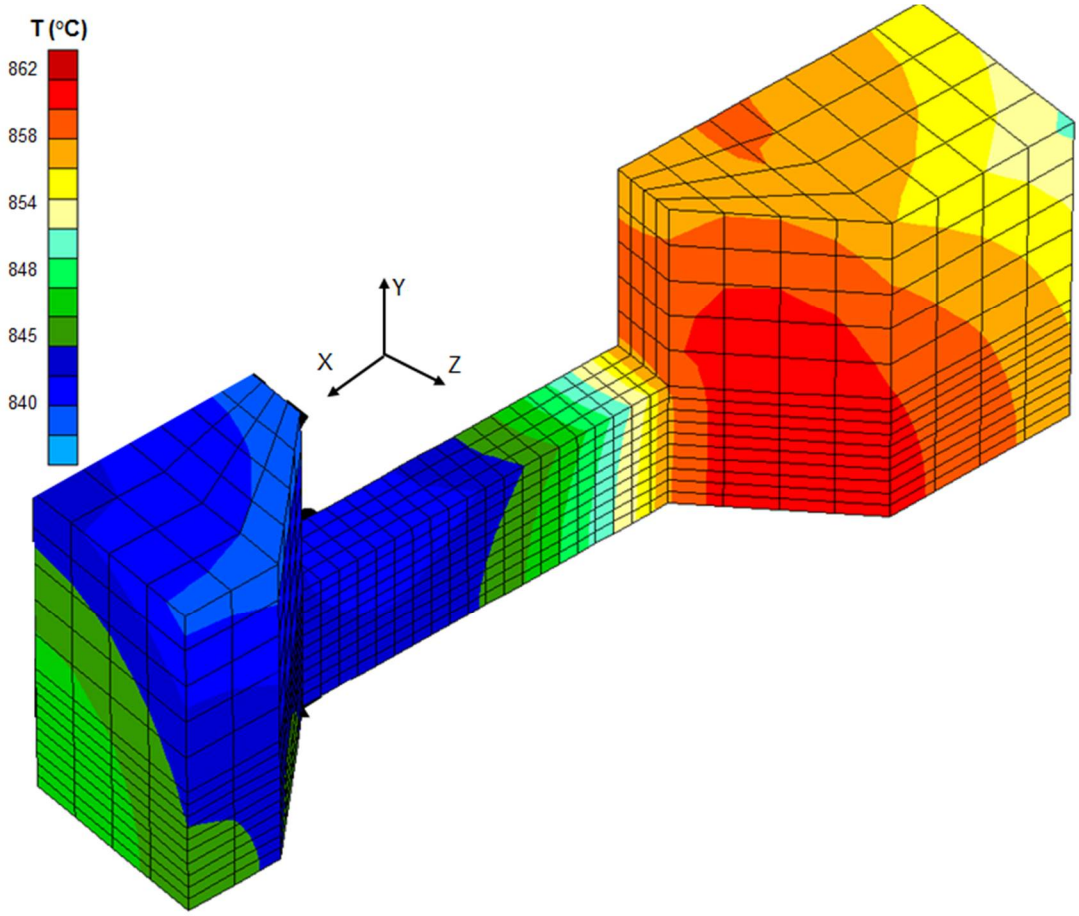

Figure A.5. Modeling of first geometry proposed for shear tests

However previous geometry was not possible to be mechanized due to the complicated shape together with the high hardness of the material. Therefore, it was proposed to modify the geometry using circular sections as shown in Figure A.6.

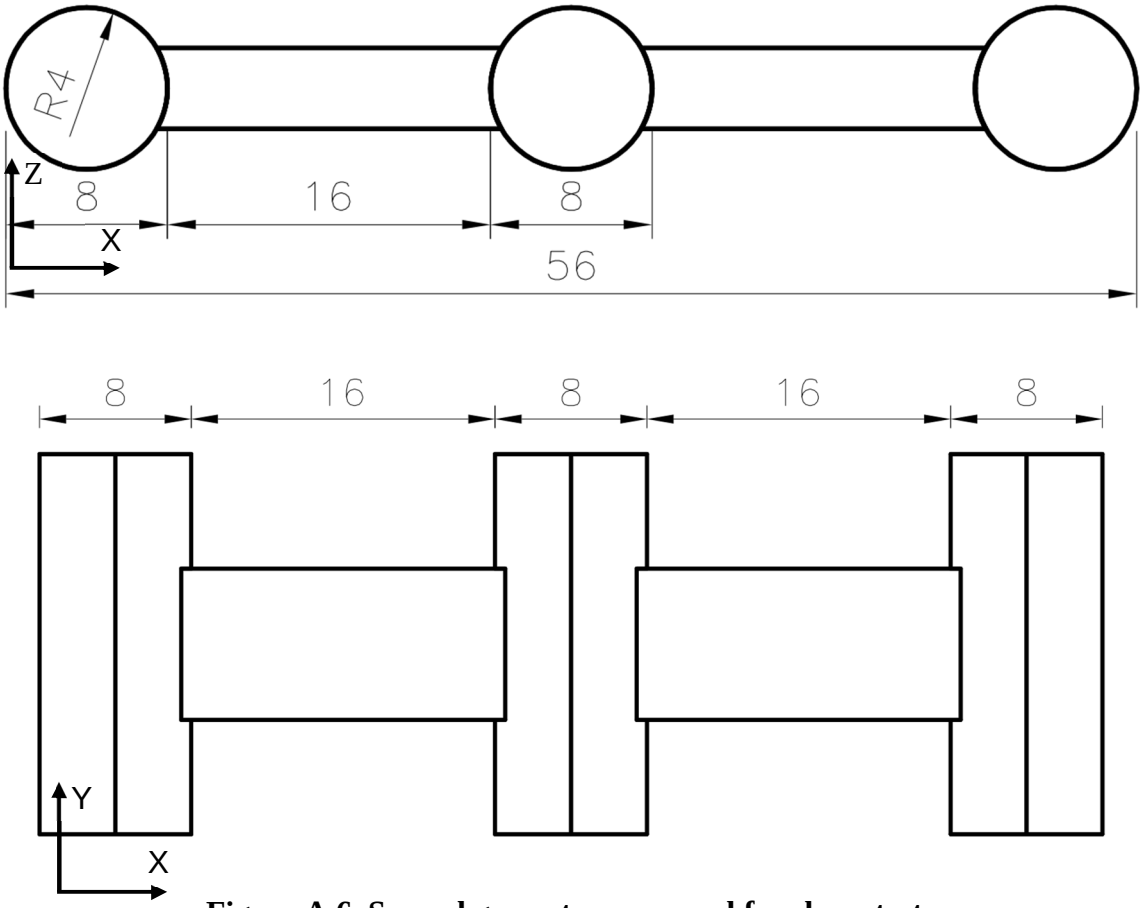

Figure A.6. Second geometry proposed for shear tests

This new geometry allowed predicting a difference of approximately 15°C in the M_s temperature between shear and shear free zones as shown in Figure A.7. However, the available equipment did not allowed the achievement of experimental tests due to the limitations of the furnace since it was not possible to perform the homogeneous cooling of the whole sample allowing a complete transformation of the austenite into martensite phase.

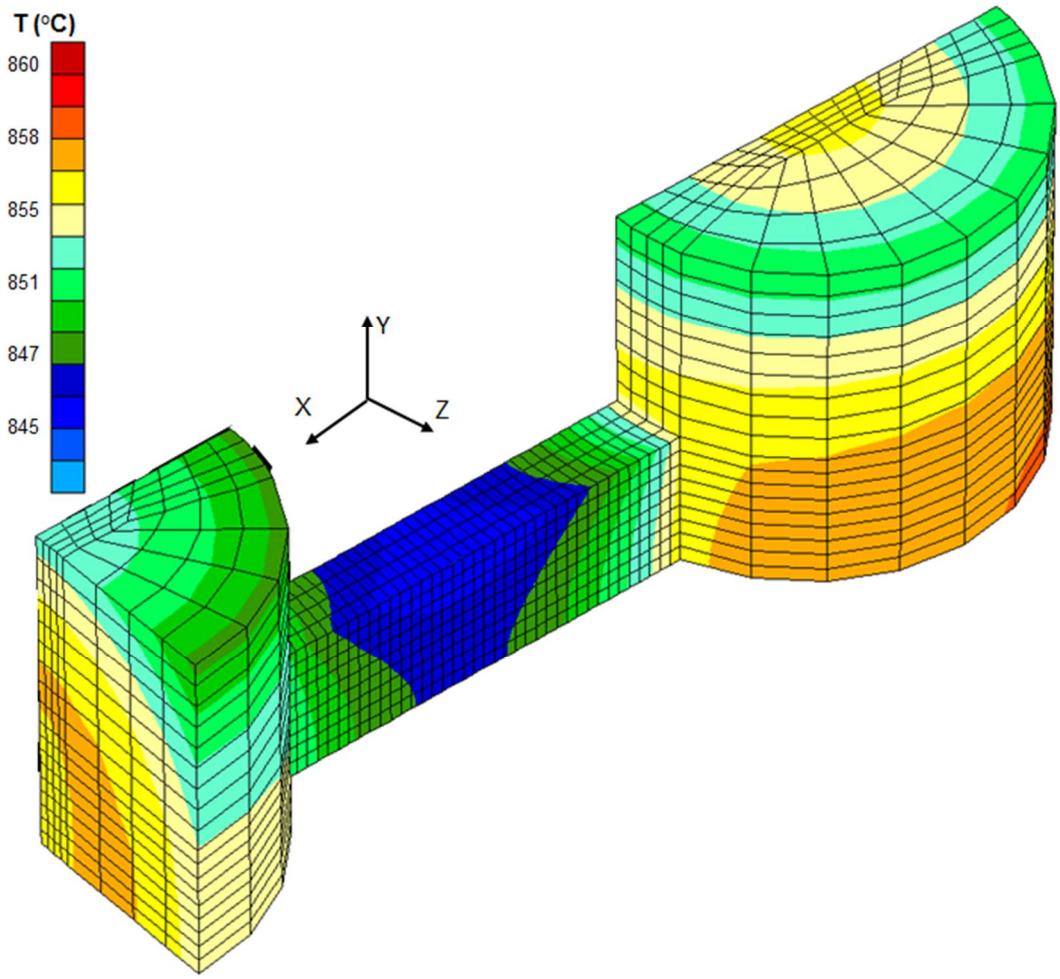

Figure A.7. Modeling of second geometry proposed for shear tests

Appendix B. Input data for numerical simulations (OUM file)

This appendix allows archiving material data, author and promoter are aware that the reader would need Lagamine used guide to better understand data structure.

Line	Text
1	**
2	SGI grade - Unites: m. s. C. kg. Pa. J. W/(m.K). kg/m3. J/(kg.K). J/m3
3	
4	Number of steel described = 1
5	Print index = 1
6	Number of characteristic temperatures = 20
7	Number of param. descr. by polynomials = 0
8	Maximal degree of polynomials = 3
9	Number of mechanical parameters = 10
10	Number of temp. in proeutectoid tables = 68
11	Number of temp. in pearlite tables = 68
12	Number of temp. in bainite tables = 68
13	Number of temp. in mechanical tables = 29
14	Value of temperature shift = 0.000
15	Index for pamet structure (Studer) = 0
16	ET at different strain levels = 1
17	Number of strain levels = 4
18	
19	ACM A3 A1 TH BS BF MS AM FINCUB
20	860. 755. 718. 460. 267. 273. 0.420E-02 0.00
21	
22	C F P C BA A (DMS) B (DMS) EXP PR EXP PE EXP BA EXP MA
23	0.00 0.00 0.00 0.00 0.776E-03 0.776E-03 0.00 0.00
24	K3 EPT SHOLD K6 EPT LIQUID
25	0.300E-10 0.00 0.00 0.130E+04
26	
27	STRAIN LEVELS (VARIABLE TANGENT MODULUS)
28	0.003500 0.005000 0.008000 0.018000
29	

Modified in section 3.6 until finding ε_{Fe-Pe}^{tr} for SGI

Modified in section 3.8.2.2 until finding $K_2 = K_3$ for SGI grade

Line	Text
30	YOUNG MODULUS
31	
32	AUSTE
33	*****
34	20.0 0.141E+12
35	300. 0.152E+12
36	650. 0.494E+11
37	0.140E+04 0.00
38	0.00 0.00
39	
40	PROEU
41	*****
42	20.0 0.141E+12
43	300. 0.152E+12
44	650. 0.494E+11
45	0.140E+04 0.00
46	0.00 0.00
47	
48	PERLI
49	*****
50	20.0 0.183E+12
51	300. 0.142E+12
52	650. 0.927E+11
53	0.140E+04 0.00
54	0.00 0.00
55	
56	BAINI
57	*****
58	0.00 0.00
59	0.00 0.00
60	
61	MARTE
62	*****
63	0.00 0.00
64	0.00 0.00
65	
66	POISSON MODULUS
67	
68	AUSTE
69	*****
70	20.0 0.286
71	100. 0.286
72	200. 0.285
73	300. 0.288
74	400. 0.291
75	500. 0.294
76	600. 0.298
77	0.100E+04 0.311
78	0.120E+04 0.318
79	0.140E+04 0.324
80	0.00 0.00
81	
82	PROEU
83	*****
84	20.0 0.286
85	100. 0.286

Line	Text
86	200. 0.285
87	300. 0.288
88	400. 0.291
89	500. 0.294
90	600. 0.298
91	0.100E+04 0.311
92	0.120E+04 0.318
93	0.140E+04 0.324
94	0.00 0.00
95	
96	PERLI
97	*****
98	20.0 0.286
99	100. 0.286
100	200. 0.285
101	300. 0.288
102	400. 0.291
103	500. 0.294
104	600. 0.298
105	0.100E+04 0.311
106	0.120E+04 0.318
107	0.140E+04 0.324
108	0.00 0.00
109	
110	BAINI
111	*****
112	0.00 0.00
113	0.00 0.00
114	
115	MARTE
116	*****
117	0.00 0.00
118	0.00 0.00
119	
120	THERMAL EXPANSION COEFFICIENT
121	
122	AUSTE
123	*****
124	0.00 0.100E-05
125	40.0 0.233E-05
126	100. 0.103E-04
127	200. 0.150E-04
128	300. 0.146E-04
129	400. 0.137E-04
130	500. 0.146E-04
131	600. 0.168E-04
132	700. 0.146E-04
133	720. 0.157E-04
134	750. 0.275E-04
135	800. 0.310E-04
136	900. 0.350E-04
137	950. 0.302E-04
138	980. 0.188E-04
139	0.100E+04 0.130E-04
140	0.00 0.00
141	

```
PROEU
*****
 0.00     0.100E-05
 40.0     0.233E-05
 100.     0.103E-04
 200.     0.150E-04
 300.     0.146E-04
 400.     0.137E-04
 500.     0.146E-04
 600.     0.168E-04
 700.     0.146E-04
 720.     0.157E-04
 750.     0.275E-04
 800.     0.310E-04
 900.     0.350E-04
 950.     0.302E-04
 980.     0.188E-04
0.100E+04 0.130E-04
 0.00      0.00

PERLI
*****
 0.00     0.100E-05
 40.0     0.233E-05
 100.     0.103E-04
 200.     0.150E-04
 300.     0.146E-04
 400.     0.137E-04
 500.     0.146E-04
 600.     0.168E-04
 700.     0.146E-04
 720.     0.157E-04
 750.     0.275E-04
 800.     0.310E-04
 900.     0.350E-04
 950.     0.302E-04
 980.     0.188E-04
0.100E+04 0.130E-04
 0.00      0.00

BAINI
*****
 0.00      0.00
 0.00      0.00

MARTE
*****
 0.00      0.00
 0.00      0.00

   YIELD LIMIT

AUSTE
*****
 20.0     0.313E+09
 300.     0.141E+09
 600.     0.500E+08
0.150E+04  0.00
 0.00      0.00

PROEU
*****
 20.0     0.313E+09
 300.     0.141E+09
 600.     0.500E+08
0.150E+04  0.00
 0.00      0.00

PERLI
*****
 20.0     0.363E+09
 300.     0.266E+09
 600.     0.250E+09
0.150E+04  0.00
 0.00      0.00


BAINI
*****
 0.00      0.00
 0.00      0.00

MARTE
*****
 0.00      0.00
 0.00      0.00

   TANGENT PLASTIC MODULUS

AUSTE
*****
 20.0     0.399E+11 0.156E+11 0.550E+09 0.195E+10
 300.      100.      100.      100.     0.280E+09
 650.      100.      100.      100.     0.900E+09
 0.00      0.00      0.00      0.00      0.00

PROEU
*****
 20.0     0.399E+11 0.156E+11 0.550E+09 0.195E+10
 300.      100.      100.      100.     0.280E+09
 650.      100.      100.      100.     0.900E+09
 0.00      0.00      0.00      0.00      0.00

PERLI
*****
 20.0     0.844E+11 0.267E+11 0.200E+11 0.133E+11
 300.     0.736E+11 0.333E+11 0.217E+11 0.158E+11
 650.     0.503E+11 0.267E+11 0.133E+11 0.600E+10
 0.00      0.00      0.00      0.00      0.00


BAINI
```

Line	Text
254	*****
255	0.00 0.00 0.00 0.00 0.00
256	0.00 0.00 0.00 0.00 0.00
257	
258	MARTE
259	*****
260	0.00 0.00 0.00 0.00 0.00
261	0.00 0.00 0.00 0.00 0.00
262	
263	THERMAL CONDUCTIVITY
264	
265	AUSTE
266	*****
267	29.0 28.0
268	100. 28.7
269	255. 30.1
270	377. 31.9
271	550. 31.4
272	609. 31.4
273	699. 29.9
274	0.00 0.00
275	
276	PROEU
277	*****
278	29.0 28.0
279	100. 28.7
280	255. 30.1
281	377. 31.9
282	550. 31.4
283	609. 31.4
284	699. 29.9
285	0.00 0.00
286	
287	PERLI
288	*****
289	29.0 28.0
290	100. 28.7
291	255. 30.1
292	377. 31.9
293	550. 31.4
294	609. 31.4
295	699. 29.9
296	0.00 0.00
297	
298	BAINI
299	*****
300	0.00 0.00
301	0.00 0.00
302	
303	MARTE
304	*****
305	0.00 0.00
306	0.00 0.00
307	
308	DENSITY
309	

Line	Text
310	AUSTE
311	*****
312	42.0 0.704E+04
313	100. 0.703E+04
314	200. 0.700E+04
315	300. 0.697E+04
316	400. 0.694E+04
317	500. 0.691E+04
318	600. 0.688E+04
319	700. 0.685E+04
320	800. 0.682E+04
321	900. 0.675E+04
322	0.100E+04 0.667E+04
323	0.00 0.00
324	
325	PROEU
326	*****
327	26.0 0.705E+04
328	100. 0.703E+04
329	200. 0.700E+04
330	300. 0.697E+04
331	400. 0.694E+04
332	500. 0.691E+04
333	600. 0.688E+04
334	700. 0.685E+04
335	800. 0.683E+04
336	900. 0.677E+04
337	0.100E+04 0.668E+04
338	0.00 0.00
339	
340	PERLI
341	*****
342	26.0 0.705E+04
343	100. 0.703E+04
344	200. 0.700E+04
345	300. 0.697E+04
346	400. 0.694E+04
347	500. 0.691E+04
348	600. 0.688E+04
349	700. 0.685E+04
350	800. 0.683E+04
351	900. 0.677E+04
352	0.100E+04 0.668E+04
353	0.00 0.00
354	
355	BAINI
356	*****
357	0.00 0.00
358	0.00 0.00
359	
360	MARTE
361	*****
362	0.00 0.00
363	0.00 0.00
364	
365	THERMAL CAPACITY

Line	Text
366	
367	AUSTE
368	*****
369	38.0 468.
370	100. 536.
371	200. 608.
372	300. 670.
373	400. 734.
374	500. 793.
375	600. 922.
376	700. 0.117E+04
377	800. 868.
378	900. 943.
379	0.100E+04 761.
380	0.00 0.00
381	
382	PROEU
383	*****
384	46.0 513.
385	100. 530.
386	200. 566.
387	300. 603.
388	400. 675.
389	500. 751.
390	600. 856.
391	700. 0.105E+04
392	800. 0.160E+04
393	900. 942.
394	0.100E+04 0.103E+04
395	0.00 0.00
396	
397	PERLI
398	*****
399	46.0 513.
400	100. 530.
401	200. 566.
402	300. 603.
403	400. 675.
404	500. 751.
405	600. 856.
406	700. 0.105E+04
407	800. 0.160E+04
408	900. 942.
409	0.100E+04 0.103E+04
410	0.00 0.00
411	
412	BAINI
413	*****
414	0.00 0.00
415	0.00 0.00
416	
417	MARTE
418	*****
419	0.00 0.00
420	0.00 0.00
421	

Line	Text
422	HARDNESS
423	
424	AUSTE
425	*****
426	100. 230.
427	200. 230.
428	400. 230.
429	600. 230.
430	800. 230.
431	900. 230.
432	0.00 0.00
433	
434	PROEU
435	*****
436	100. 230.
437	200. 230.
438	400. 230.
439	600. 230.
440	800. 230.
441	900. 230.
442	0.00 0.00
443	
444	PERLI
445	*****
446	100. 230.
447	200. 230.
448	400. 230.
449	600. 230.
450	800. 230.
451	900. 230.
452	0.00 0.00
453	
454	BAINI
455	*****
456	0.00 0.00
457	0.00 0.00
458	
459	MARTE
460	*****
461	0.00 0.00
462	0.00 0.00
463	
464	LATENT HEAT
465	
466	AUSTE
467	*****
468	0.00 0.00
469	0.00 0.00
470	
471	PROEU
472	*****
473	100. 0.300E+09
474	200. 0.300E+09
475	400. 0.300E+09
476	600. 0.300E+09
477	800. 0.300E+09

Line	Text
478	900. 0.300E+09
479	0.102E+04 0.300E+09
480	0.00 0.00
481	
482	PERLI
483	*****
484	100. 0.300E+09
485	200. 0.300E+09
486	400. 0.300E+09
487	600. 0.300E+09
488	800. 0.300E+09
489	900. 0.300E+09
490	0.102E+04 0.300E+09
491	0.00 0.00
492	
493	BAINI
494	*****
495	0.00 0.00
496	0.00 0.00
497	
498	MARTE
499	*****
500	0.00 0.00
501	0.00 0.00
502	
503	TTT DIAGRAM
504	
505	PROEU
506	*****
507	TP Y MAX
508	869. 0.00
509	854. 100.
510	788. 100.
511	718. 100.
512	
513	TP TPS DE
514	859. 0.126E+07
515	833. 0.132E+04
516	801. 55.8
517	775. 21.3
518	755. 10.6
519	748. 8.63
520	743. 7.62
521	739. 6.96
522	732. 5.99
523	718. 4.72
524	
525	TTPIS 10.0 99.0
526	
527	TP TPS PER1 TPS PER2 COEF N COEF B
528	859. 0.252E+16 0.158E+21 0.342 0.570E-06
529	833. 0.252E+13 0.158E+18 0.342 0.605E-05
530	801. 0.252E+11 0.158E+16 0.342 0.292E-04
531	775. 0.252E+08 0.158E+13 0.342 0.310E-03
532	755. 0.170E+05 0.106E+10 0.342 0.376E-02
533	748. 0.101E+04 0.548E+08 0.347 0.958E-02

Modified in section 3.7 until finding values for latent heat of SGI ferrite and pearlite phases

Line	Text
534	743. 0.501E+04 0.229E+08 0.448 0.231E-02
535	739. 371. 0.158E+08 0.354 0.129E-01
536	732. 216. 0.711E+07 0.363 0.150E-01
537	718. 107. 0.174E+07 0.390 0.170E-01
538	
539	PERLI
540	*****
541	TP Y MAX
542	727. 0.00
543	712. 100.
544	588. 100.
545	460. 100.
546	
547	TP TPS DE
548	717. 53.0
549	713. 35.6
550	711. 27.4
551	708. 23.4
552	705. 19.6
553	700. 14.0
554	697. 12.2
555	695. 11.2
556	691. 9.98
557	689. 9.27
558	684. 8.05
559	676. 6.57
560	673. 6.16
561	663. 5.26
562	659. 4.97
563	653. 4.63
564	645. 4.31
565	632. 4.01
566	628. 3.94
567	624. 3.91
568	620. 3.87
569	611. 4.12
570	608. 4.23
571	600. 4.42
572	596. 4.58
573	593. 4.70
574	587. 5.04
575	579. 5.61
576	573. 6.23
577	567. 7.06
578	561. 8.13
579	554. 10.0
580	552. 10.8
581	548. 12.4
582	543. 14.6
583	539. 17.1
584	533. 23.5
585	530. 27.6
586	527. 32.4
587	523. 38.7
588	522. 43.0
589	518. 50.4

Line	Text
590	516. 60.2
591	513. 70.7
592	511. 84.4
593	504. 116.
594	460. 0.526E+04
595	
596	TTPIS 10.0 99.0
597	
598	TP TPS PER1 TPS PER2 COEF N COEF B
599	717. 0.141E+07 0.794E+08 0.937 0.182E-06
600	713. 54.5 0.323E+04 0.925 0.261E-02
601	711. 38.7 0.230E+04 0.924 0.359E-02
602	708. 26.7 0.161E+04 0.922 0.510E-02
603	705. 17.0 0.105E+04 0.917 0.784E-02
604	700. 11.4 708. 0.916 0.113E-01
605	697. 7.19 461. 0.908 0.176E-01
606	695. 5.99 388. 0.906 0.208E-01
607	691. 4.57 303. 0.901 0.268E-01
608	689. 3.82 258. 0.897 0.317E-01
609	684. 2.64 186. 0.888 0.445E-01
610	676. 1.58 119. 0.874 0.707E-01
611	673. 1.29 101. 0.866 0.845E-01
612	663. 0.930 76.7 0.856 0.112
613	659. 0.850 70.7 0.855 0.121
614	653. 0.710 60.9 0.848 0.141
615	645. 0.680 57.8 0.850 0.146
616	632. 0.700 57.6 0.857 0.143
617	628. 0.770 61.5 0.862 0.132
618	624. 0.810 63.9 0.865 0.126
619	620. 0.980 72.9 0.877 0.107
620	611. 1.27 90.8 0.885 0.853E-01
621	608. 1.55 107. 0.892 0.713E-01
622	600. 2.14 141. 0.902 0.530E-01
623	596. 2.57 166. 0.907 0.448E-01
624	593. 3.08 195. 0.911 0.378E-01
625	587. 3.96 246. 0.915 0.299E-01
626	579. 6.92 415. 0.923 0.177E-01
627	573. 10.9 640. 0.927 0.115E-01
628	567. 15.1 881. 0.929 0.847E-02
629	561. 23.3 0.135E+04 0.931 0.562E-02
630	554. 38.4 0.220E+04 0.933 0.351E-02
631	552. 45.6 0.261E+04 0.933 0.299E-02
632	548. 60.5 0.346E+04 0.934 0.229E-02
633	543. 94.3 0.537E+04 0.935 0.151E-02
634	539. 135. 0.765E+04 0.935 0.108E-02
635	533. 224. 0.127E+05 0.935 0.668E-03
636	530. 302. 0.171E+05 0.936 0.504E-03
637	527. 474. 0.268E+05 0.936 0.330E-03
638	523. 615. 0.348E+05 0.936 0.258E-03
639	522. 735. 0.415E+05 0.936 0.218E-03
640	518. 0.121E+04 0.685E+05 0.937 0.136E-03
641	516. 0.164E+04 0.924E+05 0.937 0.103E-03
642	513. 0.202E+04 0.114E+06 0.937 0.839E-04
643	511. 0.310E+04 0.175E+06 0.937 0.565E-04
644	504. 0.588E+04 0.331E+06 0.937 0.309E-04
645	460. 0.141E+13 0.794E+14 0.937 0.434E-12

Line	Text
646	
647	Computed value for perlite beginning when
648	proeutectoid is still in formation
649	
650	TP TPS DE
651	
652	BAINI
653	*****
654	
655	TP Y MAX
656	470. 0.00
657	455. 40.0
658	366. 40.0
659	273. 40.0
660	
661	TP TPS DE
662	460. 526.
663	459. 425.
664	457. 277.
665	456. 154.
666	431. 12.7
667	428. 10.4
668	420. 6.92
669	415. 5.99
670	412. 5.38
671	409. 4.82
672	405. 4.23
673	402. 3.90
674	397. 3.55
675	390. 3.14
676	383. 2.87
677	376. 2.69
678	368. 2.52
679	360. 2.40
680	354. 2.35
681	347. 2.35
682	340. 2.39
683	331. 2.45
684	327. 2.53
685	311. 2.91
686	303. 3.27
687	300. 3.46
688	290. 4.15
689	283. 4.82
690	278. 5.51
691	273. 7.44
692	
693	TTPIS 10.0 99.0
694	
695	TP TPS PER1 TPS PER2 COEF N COEF B
696	460. 0.562E+11 0.214E+12 2.83 0.449E-31
697	459. 0.562E+09 0.214E+10 2.83 0.201E-25
698	457. 0.562E+07 0.214E+08 2.83 0.898E-20
699	456. 0.561E+05 0.214E+06 2.82 0.406E-14
700	431. 13.9 71.0 2.31 0.241E-03
701	428. 8.49 47.3 2.20 0.952E-03

Line	Text				
702	420.	3.42	23.0	1.98	0.919E-02
703	415.	2.18	16.9	1.85	0.250E-01
704	412.	1.84	14.8	1.81	0.348E-01
705	409.	1.64	13.2	1.81	0.430E-01
706	405.	1.44	11.6	1.81	0.544E-01
707	402.	1.32	10.6	1.81	0.637E-01
708	397.	1.05	9.09	1.75	0.967E-01
709	390.	0.760	7.42	1.66	0.166
710	383.	0.750	7.00	1.69	0.171
711	376.	0.650	6.36	1.66	0.215
712	368.	0.470	5.41	1.55	0.339
713	360.	0.440	5.11	1.54	0.373
714	354.	0.490	5.24	1.59	0.329

Line	Text				
715	347.	0.440	5.06	1.55	0.375
716	340.	0.410	4.99	1.51	0.406
717	331.	0.470	5.30	1.56	0.342
718	327.	0.490	5.52	1.56	0.321
719	311.	0.520	6.17	1.53	0.286
720	303.	0.540	6.75	1.50	0.265
721	300.	0.540	7.03	1.47	0.261
722	290.	0.640	8.40	1.47	0.203
723	283.	0.710	9.65	1.45	0.173
724	278.	0.770	10.8	1.43	0.153
725	273.	0.780	13.7	1.32	0.146
726					

Line	Text
727	**
728	HCS grade - Unites: m. s. C. kg. Pa. J. W/(m.K). kg/m3. J/(kg.K). J/m3
729	
730	Number of steel described = 2
731	Print index = 1
732	Number of characteristic temperatures = 20
733	Number of param. descr. by polynomials = 0
734	Maximal degree of polynomials = 3
735	Number of mechanical parameters = 10
736	Number of temp. in proeutectoid tables = 68
737	Number of temp. in pearlite tables = 98
738	Number of temp. in bainite tables = 68
739	Number of temp. in mechanical tables = 29
740	Value of temperature shift = 0.000
741	Index for pamet structure (Studer) = 0
742	ET at different strain levels = 1
743	Number of strain levels = 4
744	
745	ACM A3 A1 TH BS BF MS AM FINCUB
746	830. 760. 610. 440. 220. 266. 0.420E-02 0.00
747	
748	C F P C BA A (DMS) B (DMS) EXP PR EXP PE EXP BA EXP MA
749	0.00 0.00 0.500E-07 0.330E-07 0.00 0.00 0.00 0.300E-02
750	K3 EPT SHOLD K6 EPT LIQUID
751	0.00 0.00 0.250E-10 0.145E+04
752	
753	STRAIN LEVELS (VARIABLE TANGENT MODULUS)
754	0.005000 0.010000 0.020000 0.028000
755	

Modified in section 3.6 until finding ε_{Ma}^{tr} for HCS grade

Modified in section 3.8.2.1 until finding K_6 for HCS grade

Line	Text
756	YOUNG MODULUS
757	
758	AUSTE
759	*****
760	0.00 0.186E+12
761	300. 0.186E+12
762	700. 0.787E+11
763	950. 0.510E+11
764	0.150E+04 0.510E+11
765	0.00 0.00
766	
767	PROEU
768	*****
769	0.00 0.00
770	0.00 0.00
771	
772	PERLI
773	*****
774	0.00 0.00
775	0.00 0.00
776	
777	BAINI
778	*****
779	0.00 0.00
780	0.00 0.00
781	
782	MARTE
783	*****
784	0.00 0.190E+12
785	20.0 0.190E+12
786	80.0 0.168E+12
787	150. 0.188E+12
788	0.100E+04 0.188E+12
789	0.00 0.00
790	
791	POISSON MODULUS
792	
793	AUSTE
794	*****
795	20.0 0.288
796	100. 0.290
797	200. 0.292
798	300. 0.298
799	400. 0.301
800	500. 0.306
801	600. 0.312
802	0.150E+04 0.500
803	0.00 0.00
804	
805	PROEU
806	*****
807	0.00 0.00
808	0.00 0.00
809	
810	PERLI
811	*****

Line	Text
812	0.00 0.00
813	0.00 0.00
814	
815	BAINI
816	*****
817	0.00 0.00
818	0.00 0.00
819	
820	MARTE
821	*****
822	20.0 0.288
823	100. 0.290
824	200. 0.292
825	300. 0.298
826	400. 0.301
827	500. 0.306
828	600. 0.312
829	0.150E+04 0.500
830	0.00 0.00
831	
832	THERMAL EXPANSION COEFFICIENT
833	
834	AUSTE
835	*****
836	0.00 -0.729E-05
837	100. -0.730E-05
838	200. -0.807E-05
839	315. -0.150E-05
840	320. 0.106E-04
841	400. 0.195E-04
842	500. 0.205E-04
843	600. 0.202E-04
844	700. 0.206E-04
845	800. 0.219E-04
846	900. 0.232E-04
847	0.102E+04 0.254E-04
848	0.00 0.00
849	
850	PROEU
851	*****
852	0.00 0.00
853	0.00 0.00
854	
855	PERLI
856	*****
857	0.00 0.00
858	0.00 0.00
859	
860	BAINI
861	*****
862	0.00 0.00
863	0.00 0.00
864	
865	MARTE
866	*****
867	0.00 0.102E-04

```
 100.    0.106E-04
 200.    0.125E-04
 300.    0.129E-04
 400.    0.137E-04
 500.    0.137E-04
 600.    0.124E-04
 700.    0.124E-04
 800.    0.124E-04
 900.    0.124E-04
0.102E+04 0.123E-04
 0.00     0.00

   YIELD LIMIT

AUSTE
*****
 0.00    0.270E+09
 300.    0.270E+09
 700.    0.240E+09
 950.    0.220E+09
0.150E+04 0.220E+08
 0.00     0.00

PROEU
*****
 0.00     0.00
 0.00     0.00

PERLI
*****
 0.00     0.00
 0.00     0.00

BAINI
*****
 0.00     0.00
 0.00     0.00

MARTE
*****
 0.00    0.800E+09
 20.0    0.800E+09
 80.0    0.700E+09
 150.    0.800E+09
0.150E+04 0.800E+09
 0.00     0.00

   TANGENT PLASTIC MODULUS

AUSTE
*****
 300.    0.686E+11 0.333E+11 0.167E+11 0.100E+11
 700.    0.370E+11 0.200E+11 0.100E+11 0.556E+10
 950.    0.489E+11 0.120E+11 0.800E+10 0.250E+10
 0.00     0.00      0.00      0.00      0.00

PROEU
*****
 0.00     0.00      0.00      0.00      0.00
 0.00     0.00      0.00      0.00      0.00

PERLI
*****
 0.00     0.00      0.00      0.00      0.00
 0.00     0.00      0.00      0.00      0.00

BAINI
*****
 0.00     0.00      0.00      0.00      0.00
 0.00     0.00      0.00      0.00      0.00

MARTE
*****
 20.0    0.180E+12 0.180E+12 0.110E+12 0.500E+11
 80.0    0.160E+12 0.160E+12 0.115E+12 0.625E+11
 150.    0.180E+12 0.160E+12 0.100E+12 0.625E+11
 0.00     0.00      0.00      0.00      0.00

   THERMAL CONDUCTIVITY

AUSTE
*****
 25.0     20.6
 102.     23.7
 199.     24.8
 301.     25.4
 403.     25.8
 507.     26.1
 606.     23.3
 708.     24.7
 807.     38.0
 905.     27.9
0.100E+04  32.0
 0.00     0.00

PROEU
*****
 0.00     0.00
 0.00     0.00

PERLI
*****
 0.00     0.00
 0.00     0.00

BAINI
*****
 0.00     0.00
 0.00     0.00

MARTE
*****
```

Line	Text
980	25.0 20.6
981	102. 23.7
982	199. 24.8
983	301. 25.4
984	403. 25.8
985	507. 26.1
986	606. 23.3
987	708. 24.7
988	807. 38.0
989	905. 27.9
990	0.100E+04 32.0
991	0.00 0.00
992	
993	DENSITY
994	
995	AUSTE
996	*****
997	0.00 0.780E+04
998	200. 0.780E+04
999	300. 0.780E+04
1000	400. 0.780E+04
1001	500. 0.780E+04
1002	550. 0.778E+04
1003	600. 0.775E+04
1004	650. 0.773E+04
1005	700. 0.771E+04
1006	750. 0.768E+04
1007	800. 0.766E+04
1008	850. 0.764E+04
1009	900. 0.761E+04
1010	950. 0.758E+04
1011	0.100E+04 0.755E+04
1012	0.102E+04 0.754E+04
1013	0.00 0.00
1014	
1015	PROEU
1016	*****
1017	0.00 0.00
1018	0.00 0.00
1019	
1020	PERLI
1021	*****
1022	0.00 0.00
1023	0.00 0.00
1024	
1025	BAINI
1026	*****
1027	0.00 0.00
1028	0.00 0.00
1029	
1030	MARTE
1031	*****
1032	0.00 0.782E+04
1033	30.0 0.782E+04
1034	100. 0.780E+04
1035	150. 0.779E+04

Line	Text
1036	200. 0.777E+04
1037	250. 0.776E+04
1038	300. 0.774E+04
1039	350. 0.773E+04
1040	400. 0.771E+04
1041	800. 0.771E+04
1042	0.100E+04 0.771E+04
1043	0.00 0.00
1044	
1045	THERMAL CAPACITY
1046	
1047	AUSTE
1048	*****
1049	0.00 533.
1050	300. 533.
1051	400. 530.
1052	450. 541.
1053	500. 541.
1054	550. 546.
1055	600. 564.
1056	650. 577.
1057	700. 582.
1058	750. 584.
1059	800. 595.
1060	850. 605.
1061	900. 625.
1062	950. 650.
1063	0.100E+04 634.
1064	0.102E+04 600.
1065	0.00 0.00
1066	
1067	PROEU
1068	*****
1069	0.00 0.00
1070	0.00 0.00
1071	
1072	PERLI
1073	*****
1074	0.00 0.00
1075	0.00 0.00
1076	
1077	BAINI
1078	*****
1079	0.00 0.00
1080	0.00 0.00
1081	
1082	MARTE
1083	*****
1084	0.00 437.
1085	30.0 437.
1086	100. 490.
1087	150. 504.
1088	200. 521.
1089	250. 537.
1090	300. 555.
1091	350. 576.

Line	Text
1092	400. 595.
1093	600. 595.
1094	800. 595.
1095	0.100E+04 595.
1096	0.00 0.00
1097	
1098	HARDNESS
1099	
1100	AUSTE
1101	*****
1102	0.00 500.
1103	100. 500.
1104	200. 500.
1105	300. 500.
1106	400. 500.
1107	500. 500.
1108	600. 500.
1109	700. 500.
1110	800. 500.
1111	900. 500.
1112	0.100E+04 500.
1113	0.110E+04 500.
1114	0.120E+04 500.
1115	0.130E+04 500.
1116	0.140E+04 500.
1117	0.150E+04 500.
1118	0.00 0.00
1119	
1120	PROEU
1121	*****
1122	0.00 0.00
1123	0.00 0.00
1124	
1125	PERLI
1126	*****
1127	0.00 0.00
1128	0.00 0.00
1129	
1130	BAINI
1131	*****
1132	0.00 0.00
1133	0.00 0.00
1134	
1135	MARTE
1136	*****
1137	0.00 650.
1138	100. 650.
1139	200. 650.
1140	300. 650.
1141	400. 650.
1142	500. 650.
1143	600. 650.
1144	700. 650.
1145	800. 650.
1146	900. 650.
1147	0.100E+04 650.

Line	Text
1148	0.110E+04 650.
1149	0.120E+04 650.
1150	0.130E+04 650.
1151	0.140E+04 650.
1152	0.150E+04 650.
1153	0.00 0.00
1154	
1155	LATENT HEAT
1156	
1157	AUSTE
1158	*****
1159	0.00 0.00
1160	0.00 0.00
1161	
1162	PROEU
1163	*****
1164	0.00 0.00
1165	0.00 0.00
1166	
1167	PERLI
1168	*****
1169	0.00 0.00
1170	0.00 0.00
1171	
1172	BAINI
1173	*****
1174	0.00 0.00
1175	0.00 0.00
1176	
1177	MARTE
1178	*****
1179	0.00 0.600E+09
1180	100. 0.600E+09
1181	200. 0.600E+09
1182	300. 0.600E+09
1183	400. 0.600E+09
1184	500. 0.600E+09
1185	600. 0.600E+09
1186	700. 0.600E+09
1187	800. 0.600E+09
1188	900. 0.600E+09
1189	0.100E+04 0.600E+09
1190	0.110E+04 0.600E+09
1191	0.120E+04 0.600E+09
1192	0.130E+04 0.600E+09
1193	0.140E+04 0.600E+09
1194	0.150E+04 0.600E+09
1195	0.00 0.00
1196	
1197	TTT DIAGRAM
1198	
1199	PROEU
1200	*****
1201	
1202	TP Y MAX
1203	828. 0.00

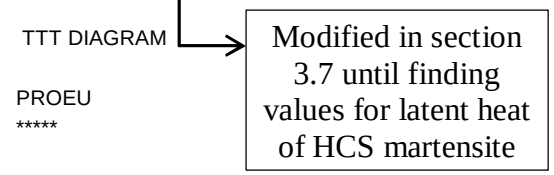

Line	Text
1204	802. 0.00
1205	772. 0.00
1206	742. 0.00
1207	712. 0.00
1208	682. 0.00
1209	652. 0.00
1210	622. 0.00
1211	612. 0.00
1212	
1213	TP TPS DE
1214	828. 0.880E+05
1215	825. 0.580E+04
1216	822. 0.146E+04
1217	817. 357.
1218	812. 141.
1219	807. 71.3
1220	802. 41.6
1221	797. 26.7
1222	792. 18.4
1223	787. 13.4
1224	782. 10.2
1225	777. 7.97
1226	772. 6.42
1227	767. 5.29
1228	762. 4.44
1229	757. 3.79
1230	752. 3.29
1231	747. 2.89
1232	742. 2.57
1233	737. 2.30
1234	732. 2.09
1235	727. 1.91
1236	722. 1.75
1237	717. 1.63
1238	712. 1.52
1239	707. 1.43
1240	702. 1.35
1241	697. 1.28
1242	692. 1.22
1243	687. 1.17
1244	682. 1.12
1245	677. 1.08
1246	672. 1.05
1247	667. 1.02
1248	662. 1.00
1249	657. 0.980
1250	652. 0.960
1251	647. 0.950
1252	642. 0.940
1253	637. 0.930
1254	632. 0.930
1255	627. 0.930
1256	622. 0.930
1257	617. 0.930
1258	612. 0.940
1259	

Line	Text
1260	TTPIS 10.0 90.0
1261	
1262	TP TPS PER1 TPS PER2 COEF N COEF B
1263	828. 0.560E+05 0.192E+06 2.50 0.135E-12
1264	825. 0.366E+04 0.127E+05 2.48 0.147E-09
1265	822. 920. 0.318E+04 2.48 0.457E-08
1266	817. 225. 780. 2.48 0.151E-06
1267	812. 89.2 309. 2.48 0.151E-05
1268	807. 45.0 156. 2.49 0.819E-05
1269	802. 26.2 90.8 2.48 0.315E-04
1270	797. 16.9 58.4 2.48 0.942E-04
1271	792. 11.6 40.3 2.48 0.237E-03
1272	787. 8.47 29.3 2.49 0.521E-03
1273	782. 6.41 22.2 2.48 0.105E-02
1274	777. 5.03 17.4 2.49 0.190E-02
1275	772. 4.05 14.0 2.49 0.326E-02
1276	767. 3.33 11.5 2.48 0.532E-02
1277	762. 2.81 9.70 2.49 0.805E-02
1278	757. 2.40 8.29 2.49 0.119E-01
1279	752. 2.08 7.19 2.49 0.171E-01
1280	747. 1.82 6.31 2.48 0.238E-01
1281	742. 1.62 5.60 2.49 0.317E-01
1282	737. 1.46 5.04 2.49 0.411E-01
1283	732. 1.31 4.56 2.47 0.540E-01
1284	727. 1.20 4.16 2.48 0.670E-01
1285	722. 1.11 3.84 2.49 0.813E-01
1286	717. 1.02 3.55 2.47 0.100
1287	712. 0.960 3.32 2.49 0.117
1288	707. 0.900 3.11 2.49 0.137
1289	702. 0.840 2.94 2.46 0.162
1290	697. 0.800 2.79 2.47 0.183
1291	692. 0.770 2.66 2.49 0.202
1292	687. 0.730 2.54 2.47 0.229
1293	682. 0.710 2.46 2.48 0.247
1294	677. 0.690 2.37 2.50 0.266
1295	672. 0.670 2.30 2.50 0.287
1296	667. 0.650 2.24 2.49 0.308
1297	662. 0.630 2.19 2.48 0.331
1298	657. 0.620 2.14 2.49 0.346
1299	652. 0.610 2.11 2.49 0.360
1300	647. 0.600 2.08 2.48 0.374
1301	642. 0.600 2.06 2.50 0.378
1302	637. 0.590 2.05 2.48 0.389
1303	632. 0.590 2.03 2.50 0.393
1304	627. 0.580 2.02 2.47 0.405
1305	622. 0.580 2.03 2.46 0.403
1306	617. 0.590 2.03 2.50 0.393
1307	612. 0.590 2.04 2.49 0.391
1308	
1309	PERLI
1310	*****
1311	
1312	TP Y MAX
1313	758. 0.00
1314	755. 100.
1315	752. 100.

Line	Text
1316	747. 100.
1317	742. 100.
1318	737. 100.
1319	732. 100.
1320	727. 100.
1321	722. 100.
1322	717. 100.
1323	712. 100.
1324	707. 100.
1325	702. 100.
1326	697. 100.
1327	692. 100.
1328	687. 100.
1329	682. 100.
1330	677. 100.
1331	672. 100.
1332	667. 100.
1333	662. 100.
1334	657. 100.
1335	652. 100.
1336	647. 100.
1337	642. 100.
1338	637. 100.
1339	632. 100.
1340	627. 100.
1341	622. 100.
1342	617. 100.
1343	612. 100.
1344	607. 100.
1345	602. 100.
1346	597. 100.
1347	592. 100.
1348	587. 100.
1349	582. 100.
1350	577. 100.
1351	572. 100.
1352	567. 100.
1353	562. 100.
1354	557. 100.
1355	552. 100.
1356	547. 100.
1357	542. 100.
1358	537. 100.
1359	532. 100.
1360	527. 100.
1361	522. 100.
1362	517. 100.
1363	512. 100.
1364	507. 100.
1365	502. 100.
1366	497. 100.
1367	492. 100.
1368	487. 100.
1369	482. 100.
1370	477. 100.
1371	472. 100.

Line	Text
1372	467. 100.
1373	462. 100.
1374	457. 100.
1375	452. 100.
1376	447. 100.
1377	442. 100.
1378	
1379	TP TPS DE
1380	758. 0.114E+09
1381	755. 0.766E+07
1382	752. 0.197E+07
1383	747. 0.502E+06
1384	742. 0.207E+06
1385	737. 0.109E+06
1386	732. 0.660E+05
1387	727. 0.442E+05
1388	722. 0.318E+05
1389	717. 0.241E+05
1390	712. 0.191E+05
1391	707. 0.156E+05
1392	702. 0.131E+05
1393	697. 0.113E+05
1394	692. 0.993E+04
1395	687. 0.887E+04
1396	682. 0.805E+04
1397	677. 0.740E+04
1398	672. 0.689E+04
1399	667. 0.648E+04
1400	662. 0.616E+04
1401	657. 0.590E+04
1402	652. 0.571E+04
1403	647. 0.556E+04
1404	642. 0.545E+04
1405	637. 0.538E+04
1406	632. 0.535E+04
1407	627. 0.534E+04
1408	622. 0.537E+04
1409	617. 0.542E+04
1410	612. 0.551E+04
1411	607. 0.562E+04
1412	602. 0.576E+04
1413	597. 0.592E+04
1414	592. 0.612E+04
1415	587. 0.636E+04
1416	582. 0.663E+04
1417	577. 0.693E+04
1418	572. 0.727E+04
1419	567. 0.767E+04
1420	562. 0.811E+04
1421	557. 0.861E+04
1422	552. 0.917E+04
1423	547. 0.980E+04
1424	542. 0.105E+05
1425	537. 0.113E+05
1426	532. 0.122E+05
1427	527. 0.132E+05

Line	Text
1428	522. 0.143E+05
1429	517. 0.156E+05
1430	512. 0.171E+05
1431	507. 0.187E+05
1432	502. 0.206E+05
1433	497. 0.227E+05
1434	492. 0.252E+05
1435	487. 0.280E+05
1436	482. 0.311E+05
1437	477. 0.348E+05
1438	472. 0.390E+05
1439	467. 0.439E+05
1440	462. 0.495E+05
1441	457. 0.560E+05
1442	452. 0.636E+05
1443	447. 0.724E+05
1444	442. 0.827E+05
1445	
1446	TTPIS 10.0 90.0
1447	
1448	TP TPS PER1 TPS PER2 COEF N COEF B
1449	607. 0.110E+04 0.201E+04 5.09 0.341E-16
1450	602. 0.112E+04 0.206E+04 5.08 0.323E-16
1451	597. 0.116E+04 0.213E+04 5.10 0.247E-16
1452	592. 0.120E+04 0.220E+04 5.10 0.215E-16
1453	587. 0.124E+04 0.228E+04 5.09 0.185E-16
1454	582. 0.129E+04 0.237E+04 5.08 0.165E-16
1455	577. 0.135E+04 0.248E+04 5.07 0.142E-16
1456	572. 0.143E+04 0.262E+04 5.11 0.821E-17
1457	567. 0.150E+04 0.275E+04 5.09 0.719E-17
1458	562. 0.158E+04 0.291E+04 5.08 0.584E-17
1459	557. 0.168E+04 0.308E+04 5.09 0.413E-17
1460	552. 0.179E+04 0.328E+04 5.08 0.321E-17
1461	547. 0.191E+04 0.351E+04 5.08 0.234E-17
1462	542. 0.205E+04 0.376E+04 5.09 0.144E-17
1463	537. 0.221E+04 0.405E+04 5.09 0.103E-17
1464	532. 0.238E+04 0.437E+04 5.09 0.700E-18
1465	527. 0.258E+04 0.473E+04 5.08 0.474E-18
1466	522. 0.280E+04 0.514E+04 5.08 0.321E-18
1467	517. 0.305E+04 0.560E+04 5.08 0.209E-18
1468	512. 0.334E+04 0.613E+04 5.07 0.140E-18
1469	507. 0.366E+04 0.670E+04 5.09 0.754E-19
1470	502. 0.403E+04 0.739E+04 5.08 0.526E-19
1471	497. 0.445E+04 0.815E+04 5.09 0.285E-19
1472	492. 0.492E+04 0.903E+04 5.08 0.185E-19
1473	487. 0.546E+04 0.100E+05 5.09 0.100E-19
1474	482. 0.610E+04 0.112E+05 5.10 0.525E-20
1475	477. 0.682E+04 0.125E+05 5.10 0.287E-20
1476	472. 0.764E+04 0.140E+05 5.11 0.156E-20
1477	467. 0.858E+04 0.157E+05 5.10 0.936E-21
1478	462. 0.966E+04 0.177E+05 5.07 0.659E-21
1479	457. 0.109E+05 0.201E+05 5.08 0.313E-21
1480	452. 0.124E+05 0.228E+05 5.09 0.151E-21
1481	447. 0.141E+05 0.259E+05 5.07 0.960E-22
1482	442. 0.162E+05 0.293E+05 5.20 0.139E-22
1483	

Line	Text
1484	Computed value for perlite beginning when
1485	proeutectoid is still in formation
1486	
1487	TP TPS DE
1488	
1489	TP TPS PER1 TPS PER2 COEF N COEF B
1490	758. 0.220E+08 0.400E+08 5.16 0.138E-38
1491	755. 0.149E+07 0.274E+07 5.06 0.584E-32
1492	752. 0.390E+06 0.710E+06 5.15 0.173E-29
1493	747. 0.980E+05 0.180E+06 5.07 0.503E-26
1494	742. 0.400E+05 0.740E+05 5.01 0.889E-24
1495	737. 0.210E+05 0.390E+05 4.98 0.307E-22
1496	732. 0.128E+05 0.236E+05 5.07 0.159E-21
1497	727. 0.864E+04 0.158E+05 5.09 0.101E-20
1498	722. 0.622E+04 0.114E+05 5.10 0.493E-20
1499	717. 0.471E+04 0.864E+04 5.10 0.202E-19
1500	712. 0.373E+04 0.684E+04 5.09 0.703E-19
1501	707. 0.305E+04 0.559E+04 5.09 0.202E-18
1502	702. 0.256E+04 0.470E+04 5.09 0.483E-18
1503	697. 0.221E+04 0.405E+04 5.08 0.106E-17
1504	692. 0.194E+04 0.356E+04 5.08 0.204E-17
1505	687. 0.173E+04 0.318E+04 5.08 0.366E-17
1506	682. 0.157E+04 0.288E+04 5.09 0.560E-17
1507	677. 0.145E+04 0.265E+04 5.08 0.931E-17
1508	672. 0.134E+04 0.247E+04 5.07 0.141E-16
1509	667. 0.127E+04 0.232E+04 5.10 0.156E-16
1510	662. 0.120E+04 0.221E+04 5.07 0.257E-16
1511	657. 0.115E+04 0.212E+04 5.07 0.315E-16
1512	652. 0.111E+04 0.204E+04 5.07 0.387E-16
1513	647. 0.109E+04 0.199E+04 5.09 0.376E-16
1514	642. 0.106E+04 0.195E+04 5.07 0.483E-16
1515	637. 0.105E+04 0.193E+04 5.09 0.446E-16
1516	632. 0.105E+04 0.192E+04 5.10 0.428E-16
1517	627. 0.104E+04 0.192E+04 5.07 0.504E-16
1518	622. 0.105E+04 0.192E+04 5.08 0.477E-16
1519	617. 0.106E+04 0.195E+04 5.10 0.384E-16
1520	612. 0.108E+04 0.197E+04 5.10 0.364E-16
1521	
1522	BAINI
1523	*****
1524	
1525	TP Y MAX
1526	438. 0.00
1527	417. 100.
1528	392. 100.
1529	367. 100.
1530	342. 100.
1531	317. 100.
1532	292. 100.
1533	267. 100.
1534	242. 100.
1535	217. 100.
1536	
1537	TP TPS DE
1538	438. 0.649E+05
1539	435. 0.113E+05

Line	Text
1540	432. 0.478E+04
1541	427. 0.208E+04
1542	422. 0.125E+04
1543	417. 887.
1544	412. 693.
1545	407. 579.
1546	402. 508.
1547	397. 462.
1548	392. 433.
1549	387. 416.
1550	382. 408.
1551	377. 407.
1552	372. 412.
1553	367. 422.
1554	362. 439.
1555	357. 461.
1556	352. 489.
1557	347. 523.
1558	342. 565.
1559	337. 615.
1560	332. 675.
1561	327. 746.
1562	322. 831.
1563	317. 931.
1564	312. 0.105E+04
1565	307. 0.119E+04
1566	302. 0.136E+04
1567	297. 0.157E+04
1568	292. 0.182E+04
1569	287. 0.212E+04
1570	282. 0.248E+04
1571	277. 0.292E+04
1572	272. 0.347E+04
1573	267. 0.414E+04
1574	262. 0.496E+04
1575	257. 0.600E+04
1576	252. 0.729E+04
1577	247. 0.891E+04
1578	242. 0.110E+05
1579	237. 0.136E+05
1580	232. 0.169E+05
1581	227. 0.212E+05
1582	222. 0.268E+05
1583	217. 0.341E+05
1584	212. 0.436E+05
1585	207. 0.562E+05
1586	202. 0.730E+05
1587	197. 0.955E+05
1588	192. 0.126E+06
1589	
1590	TTPIS 10.0 90.0
1591	
1592	TP TPS PER1 TPS PER2 COEF N COEF B
1593	438. 0.192E+05 0.302E+06 1.12 0.171E-05
1594	435. 0.334E+04 0.526E+05 1.12 0.120E-04
1595	432. 0.142E+04 0.223E+05 1.12 0.315E-04

Line	Text
1596	427. 617. 0.972E+04 1.12 0.799E-04
1597	422. 370. 0.585E+04 1.12 0.142E-03
1598	417. 262. 0.414E+04 1.12 0.208E-03
1599	412. 205. 0.323E+04 1.12 0.273E-03
1600	407. 171. 0.270E+04 1.12 0.335E-03
1601	402. 150. 0.237E+04 1.12 0.388E-03
1602	397. 137. 0.216E+04 1.12 0.431E-03
1603	392. 128. 0.202E+04 1.12 0.463E-03
1604	387. 123. 0.194E+04 1.12 0.485E-03
1605	382. 121. 0.190E+04 1.12 0.496E-03
1606	377. 120. 0.190E+04 1.12 0.497E-03
1607	372. 122. 0.192E+04 1.12 0.490E-03
1608	367. 125. 0.197E+04 1.12 0.476E-03
1609	362. 130. 0.205E+04 1.12 0.456E-03
1610	357. 136. 0.215E+04 1.12 0.431E-03
1611	352. 144. 0.228E+04 1.12 0.405E-03
1612	347. 155. 0.244E+04 1.12 0.374E-03
1613	342. 167. 0.263E+04 1.12 0.344E-03
1614	337. 182. 0.287E+04 1.12 0.315E-03
1615	332. 200. 0.315E+04 1.12 0.282E-03
1616	327. 221. 0.348E+04 1.12 0.252E-03
1617	322. 246. 0.387E+04 1.12 0.223E-03
1618	317. 275. 0.434E+04 1.12 0.196E-03
1619	312. 310. 0.490E+04 1.12 0.172E-03
1620	307. 353. 0.557E+04 1.12 0.150E-03
1621	302. 404. 0.636E+04 1.12 0.128E-03
1622	297. 463. 0.732E+04 1.12 0.110E-03
1623	292. 537. 0.847E+04 1.12 0.931E-04
1624	287. 625. 0.987E+04 1.12 0.788E-04
1625	282. 733. 0.116E+05 1.12 0.658E-04
1626	277. 864. 0.136E+05 1.12 0.549E-04
1627	272. 0.103E+04 0.162E+05 1.12 0.453E-04
1628	267. 0.122E+04 0.193E+05 1.12 0.372E-04
1629	262. 0.147E+04 0.232E+05 1.12 0.303E-04
1630	257. 0.177E+04 0.280E+05 1.12 0.245E-04
1631	252. 0.216E+04 0.340E+05 1.12 0.196E-04
1632	247. 0.263E+04 0.415E+05 1.12 0.158E-04
1633	242. 0.324E+04 0.511E+05 1.12 0.125E-04
1634	237. 0.401E+04 0.633E+05 1.12 0.992E-05
1635	232. 0.500E+04 0.789E+05 1.12 0.768E-05
1636	227. 0.628E+04 0.988E+05 1.12 0.591E-05
1637	222. 0.793E+04 0.125E+06 1.12 0.462E-05
1638	217. 0.101E+05 0.159E+06 1.12 0.353E-05
1639	212. 0.129E+05 0.203E+06 1.12 0.266E-05
1640	207. 0.166E+05 0.262E+06 1.12 0.199E-05
1641	202. 0.216E+05 0.340E+06 1.12 0.150E-05
1642	197. 0.285E+05 0.445E+06 1.12 0.106E-05
1643	192. 0.370E+05 0.587E+06 1.12 0.842E-06

References

1. Martiny F, Sinnaeve M (2002) Rolls for the metalworking industries. Iron Steel Soc 160–166.

2. Studer L (2008) Modelling the vertical spincasting of large bimetallic rolling mills. DEA thesis. Université de Liège, Belgium.

3. Heinrich Schroder K (2003) A basic understanding of the mechanics of rolling mill rolls.

4. Marichal Ketin (2012) Confidential Company presentation. Liège, Belgium

5. Tchoufang Tchuindjang J Influence of the Supersaturation on the Solidification and the Solid State Phase Transformations of Multicomponents Fe-Cr-C-X Alloys: Case Studies. PhD thesis. In Progress. Université de Liège, Belgium.

6. Redkin K, Hrizo C, Mardsen K, et al. (2015) Advanced analytical and non-destructive technologies for engineered roll production. Conference communication Rolls 5.

7. Ziehenberger K, Windhager M (2005) Recent Developments in HSM Rougher Rolls: Risks and Chances. Conf. Mater. Sci. Technol.

8. Van der Walls J (1979) The thermodynamic theory of capillarity under the hypothesis of a continuous variation of density. J. Stat. Phys. 20:

9. Cahn JW (1958) Free energy of a non uniform system. I. Interfacial free energy. J Chem Phys 28:258–267.

10. Levitas VI, Lee DW, Preston DL (2010) Interface propagation and microstructure evolution in phase field models of stress-induced martensitic phase transformations. Int J Plast 26:395–422.

11. Otsuka T (2014) Micromechanical modelling of transformation plasticity in steels based on fast Fourier transform numerical scheme. PhD thesis. Paris 13 University, France.

12. Fu H, Xiao Q, Xing JD (2008) A study on the crack control of a high-speed steel roll fabricated by a centrifugal casting technique. Mater Sci Eng A 474:82–87. doi: 10.1016/j.msea.2007.03.101

13. Gao JW, Wang CY (2000) Modeling the solidification of functionally graded materials by centrifugal casting. Mater Sci Eng A 292:207–215. doi: 10.1016/S0921-5093(00)01014-5

14. Wu SP, Li CY, Guo JJ, et al. (2006) Numerical simulation and experimental investigation of two filling methods in vertical centrifugal casting. Trans Nonferrous Met Soc China 16:1035–1040. doi: 10.1016/S1003-6326(06)60373-7

15. Mercado-Solis RD, Talamantes-Silva J, Beynon JH, Hernandez-Rodriguez M a. L (2007) Modelling surface thermal damage to hot mill rolls. Wear 263:1560–1567. doi: 10.1016/j.wear.2006.12.062

16. Domazet Z, Lukša F, Stanivuk T (2014) An optimal design approach for calibrated rolls with respect to fatigue life. Int J Fatigue 59:50–63. doi: 10.1016/j.ijfatigue.2013.09.015

17. Corral RL, Colás R, Pérez a. (2004) Modeling the thermal and thermoelastic responses of work rolls used for hot rolling steel strip. J Mater Process Technol 153-154:886–893. doi: 10.1016/j.jmatprotec.2004.04.090

18. Jin YM, Artemev A, Khachaturyan AG (2001) Three-dimensional phase field model of low-symmetry martensitic transformation in polycrystal: Simulation of ζ'2 martensite in AuCd alloys. 49:2309–2320.

19. Cottura M, Appolaire B, Finel A, Le Bouar Y (2014) Phase field study of acicular growth: Role of elasticity in Widmanstätten structure. Acta Mater 72:200–210. doi: 10.1016/j.actamat.2014.03.045

20. Levitas VI (2014) Phase field approach to martensitic phase transformations with large strains and interface stresses. J Mech Phys Solids 70:154–189. doi: 10.1016/j.jmps.2014.05.013

21. Parisier G, Schaffinit P, Steinbach I, Bleck W (2001) Simulation of the γ-α transformation using the phase-field method. Steel Res 72:354–360.

22. Militzer M, Mecozzi MG, Sietsma J, van der Zwaag S (2006) Three-dimensional phase field modelling of the austenite-to-ferrite transformation. Acta Mater 54:3961–3972. doi: 10.1016/j.actamat.2006.04.029

23. Zhu B, Chen H, Militzer M (2015) Phase-field modeling of cyclic phase transformations in low-carbon steels. Comput Mater Sci. doi: 10.1016/j.commatsci.2015.01.023

24. Nakajima K, Apel M, Steinbach I (2006) The role of carbon diffusion in ferrite on the kinetics of cooperative growth of pearlite: A multi-phase field study. Acta Mater 54:3665–3672.

25. Vaks VG, Stroev AY, Urtsev VN, Schmakov AV (2011) Experimental and theoretical study of the formation and growth of pearlite colonies in eutectoid steels. J Exp Theor Phys 112:961–978.

26. Cottura M, Le Bouar Y, Finel A, et al. (2012) A phase field model incorporating strain gradient viscoplasticity: Application to rafting in Ni-base superalloys. J Mech Phys Solids 60:1243–1256.

27. Cho YG, Kim JY, Cho HH, et al. (2012) Analysis of transformation plasticity in steel using a finite element method coupled with a phase field model. PLoS One 7 e35987.

28. Vasconcelos P, Gießmann a., Dias-de-Oliveira J, Andrade-Campos a. (2015) Heat treatment analysis of multiphase steels through the use of a coupled phase field and finite element model methodology. Comput Mater Sci 107:139–150. doi: 10.1016/j.commatsci.2015.05.005

29. Steinbach I, Apel M (2007) The influence of lattice strain on pearlite formation in Fe–C. Acta Mater 55:4817–4822.

30. Steinbach I, Pezzolla F, Nestler B, et al. (1996) A phase field concept for multiphase systems. Phys D 94:135–147.

31. Yamanaka A, Yamamoto T, Takiki T, Tomita Y (2008) Multi-phase-field study for pearlite transformation with grain boundary diffusion. In: Proc. Forth Int. Conf. Multiscale Mater. Model. Florida, USA, pp 425–428

32. Lebensohn R a., Kanjarla AK, Eisenlohr P (2012) An elasto-viscoplastic formulation based on fast Fourier transforms for the prediction of micromechanical fields in polycrystalline materials. Int J Plast 32-33:59–69. doi: 10.1016/j.ijplas.2011.12.005

33. Geers MGD, Kouznetsova VG, Brekelmans WAM (2010) Multi-scale computational homogenization: trends and challenges. J Comput Appl Methematics 234:2175–2182.

34. McDowell DL (2010) A perspective on trends in multiscale plasticity. Int J Plast 26:1280–1309.

35. Denis S, Gautier E, Simon A, Beck G (1985) Stress phase transformation interactions - basic principles, modelling and calculation of internal stresses. Mater Sci Technol 1:805–814.

36. Assaker D (1990) Analyse thermomecanique non lineaire par elements finis des traitements thermiques des metaux. PhD thesis. University of Liege, Belgium.

37. Habraken AM, Bourdouxhe M (1992) Coupled thermomechanical- metallurgical analysis during the cooling of steel pieces. Eur J Mech - A/Solids 11:381–402.

38. Lequesne C (2009) Modeling of fracture in heavy steel welded beam-to-column connection submitted to cyclic loading by finite elments. PhD thesis. Université de Liège, Belgium. http://bictel.ulg.ac.be/ETD-db/collection/available/ULgetd-07062009-125347/

39. Pascon F (2003) 2D1/2 Thermal-mechanical model of continuous casting of steel using finite element method. PhD thesis. Université de Liège, Belgium. http://bictel.ulg.ac.be/ETD-db/collection/available/ULgetd-06262007-100522/

40. Schwartz R (2011) Study of the continuous casting of peritectic steel grades by a mesoscopic damage approach. PhD thesis. Université de Liège, Belgium. http://bictel.ulg.ac.be/ETD-db/collection/available/ULgetd-08252011-194757/

41. Casotto S, Pascon F, Habraken AM, Bruschi S (2005) Thermo-mechanical-metallurgical model to predict geometrical distortions of rings during cooling phase after ring rolling operations. Int J Mach Tools Manuf 657–664.

42. Denis S, Sjostrom S, Simon A (1987) Coupled temperature, stress, phase transformation calculation model numerical illustration of the internal stresses evolution during cooling of an Eutectoid carbon steel cylinder. Metall Trans 18A:1203–1212.

43. Geijselaers HJM (2003) Numerical simulation of stresses due to solid state transformations: The simulations of laser hardening. University of Twente.

44. Li J, Tang L, Li S, Wu X (2013) Finite element simulation of deep cryogenic treatment incorporating transformation kinetics. Mater Des 47:653–666. doi: 10.1016/j.matdes.2012.12.076

45. Lee SJ, Matlock DK, Van Tyne CJ (2013) Comparison of two finite element simulation codes used to model the carburizing of steel. Comput Mater Sci 68:47–54. doi: 10.1016/j.commatsci.2012.10.007

46. Bok HH, Choi J, Barlat F, et al. (2014) Thermo-mechanical-metallurgical modeling for hot-press forming in consideration of the prior austenite deformation effect. Int J Plast 58:154–183. doi: 10.1016/j.ijplas.2013.12.002

47. Lee CH, Chang KH (2011) Prediction of residual stresses in high strength carbon steel pipe weld considering solid-state phase transformation effects. Comput Struct 89:256–265. doi: 10.1016/j.compstruc.2010.10.005

48. Johnson GR, Cook WH (1985) Fracture characteristics of three metals subjected to various strains, strain rates, temperatures and pressures. Eng Fract Mech 21:31.

49. Gurson a. L (1977) Continuum Theory of Ductile Rupture by Void Nucleation and Growth: Part I—Yield Criteria and Flow Rules for Porous Ductile Media. J Eng Mater Technol 99:2. doi: 10.1115/1.3443401

50. Rousselier G, Devaux JC, Mottet G, Devesa G (1989) A methodology for ductile fracture analysis based on damage mechanics: an illustration of local approach of fracture. In: ASTM Spec. Tech. Publ., 995th ed. pp 332–354

51. Lemaitre J (1985) Coupled elasto-plasticity and damage constitutive equations. Comput Methods Appl Mech Eng 51:31–49.

52. Cerri O (2007) Rupture a chaud dans les aciers au cours de leur solidification - Caracterisation experimentale et modelisation thermomecanique. PhD thesis. Ecole des mines de Paris.

53. Clift SE, Hartley P, et al (1990) Fracture prediction in plastic deformation processes. Int J Mech Sci 32:1–17.

54. Zhu Y, Cescotto S, Habraken AM (1992) A fully coupled elastoplastic damage modeling and fracture criteria in metalforming processes. J Mater Process Technol 32:197–204.

55. Ghosh AK (1976) A criterion for ductile fracture in sheets under biaxial loading. Metall Trans 7a:523–533.

56. McClintock FA, Kaplan SM, Berg CA (1986) Ductile fracture by hole growth in shear bands. Int J Mech Sci 2:614–627.

57. Freudenthal AM (1950) The inelastic behaviour of engineering materials and structures. Wiley, New York.

58. Cockroft MG, Latham DJ (1968) Ductile fracture characterization for medium carbon steel using continuum damage mechanics. J Inst Met 96:33–39.

59. Brozzo P, Deluca B, Rendina R (1972) A new method for the prediction of formability limits in metal sheets. 7th Bienn. Conf. Int. Deep Draw. Res. Gr.

60. Oyane M (1972) Criteria of ductile fracture strain. Bull JSME 105:1507–1513.

61. Bao Y, Wierzbicki T (2004) On fracture locus in the equivalent strain and stress triaxiality space. Int J Mech Sci 46:81–98. doi: 10.1016/j.ijmecsci.2004.02.006

62. Mae H, Teng X, Bai Y, Wierzbicki T (2008) Comparison of ductile fracture properties of aluminum castings: Sand mold vs. metal mold. Int J Solids Struct 45:1430–1444.

63. Bai Y, Wierzbicki T (2008) A new model of metal plasticity and fracture with pressure and Lode dependence. Int J Plast 24:1071–1096. doi: 10.1016/j.ijplas.2007.09.004

64. Barsoum I, Faleskog J (2007) Rupture mechanisms in combined tension and shear-micromechanics. Int J Solids Struct 44(17):5481–5498.

65. Xue L (2008) Constitutive modeling of void shearing effect in ductile fracture of porous materials. Eng Fract Mech 75(11):3343–3366.

66. Basaran M, Wölkerling SD, Feucht M, et al. (2010) An Extension of the GISSMO Damage Model Based on Lode Angle Dependence. LS-DYNA Anwenderforum.

67. El Bartali A, Zhang L, Studer L, Habraken AM (2009) Validation d'un calcul thermique métallurgique in Mécanique et mécanismes des changements de phases. In: Appolaire B. A, Chirani, S.; Calloch, S.; Denis, S.; Leal, M.; Tailleur M, Aussois (eds) MECAMAT. pp 254–258

68. Habraken AM (1989) Contribution à la modélisation du formage des métaux par la méthode des éléments finis. PhD thesis. Université de Liège, Belgium. http://bictel.ulg.ac.be/ETD-db/collection/available/ULgetd-12022009-154016/

69. Sjostrom S (1985) Interactions and constitutive models for calculating quench stresses in steel. Mater Sci Technol 1:823–828.

70. Fernandes F, Denis D, Simon A (1986) Prévision de l'évolution thermique et structurales des aciers au cours de leur refroidissement continu. Mémoires Études Sci Rev Métall 335–365.

71. Bardelcik A, Worswick MJ, Wells M a. (2014) The influence of martensite, bainite and ferrite on the as-quenched constitutive response of simultaneously quenched and deformed boron steel – Experiments and model. Mater Des 55:509–525. doi: 10.1016/j.matdes.2013.10.014

72. Johnson WA, Mehl RF (1939) Reaction kinetics in processes of nucleation and growth. Trans AIME, Iron Steel Div 135:416.

73. Pumphrey WI, Jones FW (1948) Inter-relation of hardenability and isothermal transformation data. JISI 159:137–144.

74. Koistinen D, Marburger R. (1959) A General Equation prescribing extent of the austenite-martensite transformation in pure Fe-C alloys and plain carbon steels. Acta Metall 7:59–60.

75. Giusti J (1988) Numerical study of some types of distorsions due to quench of carburized steel pieces. Int. Conf. residual Stress. 3

76. Lecomte-Beckers J, Sinnaeve M, Tchoufang Tchuindjang J (2012) Current Developments of Alloyed Steels for Hot Strip Roughing Mills : Characterization of High-Chromium Steel and Semi-High Speed Steel. Iron Steel Technol 33–40.

77. Hwang KC, Lee S, Lee HC (1998) Effects of alloying elements on microstructure and fracture properties of cast high speed steel rolls: Part II. Fracture behavior. Mater Sci Eng A 1–8. doi: 10.1016/S0921-5093(98)00626-1)

78. Tchoufang Tchuindjang J, Sinnaeve M, Lecomte-Beckers J (2011) Influence of High Temperature Heat Treatment on in situ Transformation of Mo-rich Eutectic Carbides in HSS and Semi-HSS Grades. In: Abrasion 2011. Liege, pp 61–75

79. Neira-Torres I, Gilles G, Tchoufang Tchuindjang J, et al. (2015) FE modeling of the cooling and tempering steps of bimetallic rolling mill rolls. Int J Mater Form. doi: 10.1007/s12289-015-1277-0

80. Tuninetti V (2014) Experimental and numerical study of the quasi-static behavior of Ti-6Al-4V. PhD thesis. Université de Liège, Belgium. http://bictel.ulg.ac.be/ETD-db/collection/available/ULgetd-04252014-163021/

81. Tuninetti V, Habraken AM (2014) Impact of anisotropy and viscosity to model the mechanical behavior of Ti-6Al-4V alloy. Mater Sci Eng A 605:39–50.

82. Tchoufang Tchuindjang J, Neira Torres I, Flores V. P, et al. (2015) Phase Transformations and Crack Initiation in a High-Chromium Cast Steel Under Hot Compression Tests. J Mater Eng Perform 24:2025–2041.

83. Ghaffarian H, et al (2015) Molecular dynamics simulation study of the effect of temperature and grain size on the deformation behavior of polycrystalline cementite. Scr Mater 95:23–26.

84. Inoue A, Ogura T, Masumoto T (1977) Microstructures of Deformation and Fracture of Cementite in Pearlitic Carbon Steels Strained at Various Temperatures. Metall Trans A 8A:1689–1695.

85. Terashima T, Tomota Y, Isaka M, et al. (2006) Strength and deformation behavior of bulky cementite synthesized by mechanical milling and plasma-sintering. Scr Mater 54:1925–1929.

86. Meyer L, Weise A, Hahn F (1997) Comparison of Constitutive Flow Curve Relations in Cold and Hot Forming. J Phys IV, Fr 07:C3–13–C3–20.

87. Bonora N, Ruggiero A (2005) Micromechanical modeling of ductile cast iron incorporating damage. Part I: Ferritic ductile cast iron. Int J Solids Struct 42:1401–1424.

88. Ekström M, Jonsson S (2014) High-temperature mechanical- and fatigue properties of cast alloys intended for use in exhaust manifolds. Mater Sci Eng A 616:78–87.

89. Matteis P, Scavino G, Castello A, Firrao D (2014) High temperature fatigue properties of a Si-Mo ductile cast iron. Procedia Mater Sci 3:2154–2159.

90. Herman M (2006) Etude métallurgique et thermomécanique du phénomène de bris lors de traitements thermiques de cylindres de laminoir en acier moyen chrome. PhD thesis. Université de Liège, Belgium.

91. Denis S, Archambault P, Aubry C, et al. (1999) Modeling of phase transformations kinetics and coupling with heat treatment residual stress predictions,. J Phys IV, Fr 09:323–332.

92. Molinari A, et al (2001) Effect of Deep Cryogenic Treatment on the Mechanical Properties of Tool Steels. J Mater Process Technol 118:350–355.

93. Das D, et al (2009) Optimization of the Duration of Cryogenic Processing to maximize Wear Resistance of AISI D2 Steel. Cryogenics (Guildf) 49:176–184.

94. Jelenkowski J, et al (2010) Effect of deep cryogenic treatment on substructure of HS6-5-2 High Speed Steel. J Achiev Mater Manuf Eng 43:80–87.

95. Tchoufang Tchuindjang J (2015) Study of the Crystallization Behavior and the Subsequent Martensitic Transfotrmation in a High Chromium Cast Steel submitted to Different Austenitization Temperatures. Proc. EUROMAT

96. Bala P, Pacyna J (2009) The Kinetics of Phase Transformations during Continuous Heating from As-quenched State in High-Speed Steels. Arch Mater Sci Eng 37:5–12.

97. Bala P (2009) The Kinetics of Phase Transformation during Tempering of Tool Steels with Different Carbon Content. Arch Metall Mater 54:491–498.

98. Taylor, et al (1989) Spinodal Decomposition during Aging of Fe-Ni-C Martensites. Metall Trans A 20:2717–2737.

99. Hase K, et al (2004) Bainite Formation influenced by Large Stress. Mater Sci Technol 20:1499–1505.

100. Bhadeshia HKDH (2001) Transformations, Microstructures and Properties, 2nd ed. IOM Communication Ltd., London

101. Shirzadi AA, Abreu H, Pocock L, et al. (2009) Bainite Orientation in Plastically Deformed Austenite. Int Jrn Mater Res 100:40–45.

102. Yang J., Huang CY, Hsieh WH, Chiou CS (1996) Mechanical Stabilization of Austenite Against Bainitic Reaction in Fe-Mn-Si-C Bainitic Steel. Mater Trans 37:579–584.

103. Liu DS, Wang GD, Liu X., Cui GZ (2009) Mechanical Stabilization of Deformed Austenite During Continuous Cooling Transformation in a C-Mn-Cr-Ni-Mo Plastic Die Steel. Act Met Sin 11:93–99.

104. Jin XJ, Min N, Zheng KY, Hsu TY (2006) The Effect of Austenite Deformation on Bainite Formation in an Alloyed Eutectoid Steel. Mater Sci Eng A 438:170–172.

105. Gong W, Tomota Y, Adachi Y, et al. (2013) Effects of Ausforming Temperature on Bainite Transformation, Microstructure and Variant Selection in Nanobainite Steel. Acta Mater 61:4142–4154.

106. Kalidindi SR (1998) Modeling The Strain Hardening Response of Low SFE FCC Alloys. Int J Plast 14:1265–1277.

107. Kocks UF, Mecking H (2003) Physics and Phenomenology of Strain Hardening: The FCC Case. Prog Mater Sci 48:171–273.

108. Vodopivec V (1975) Dynamic Recovery of Austenite in Low Carbon Steels and its Relationship to the Precipitation of AlN. Jrn Mater Sci 10:1082–1084.

109. Nes E (1995) Recovery Revisited. Acta Mater 43:2189–2207.

110. Kubin L, Hoc T, Devincre B (2009) Dynamic Recovery and its Orientation Dependence in Face-centered Cubic Crystals. Acta Mater 57:2567–2575.

111. Yanagisawa O, Lui TS (1983) Influence of the Structure on the 673 K Embrittlement of Ferritic Spheroidal Graphite Cast Iron. Trans Japan Inst Met 24:858–867.

112. Hung-Mao L, Truan-Sheng L, Li-Hui C (2003) Effect of Silicon Content on Intergranular Embrittlement of Ferritic Spheoridal Graphite Cast Iron Suffered from Cyclic Heating. Mater Trans 44:173–180.

113. Tholence F, Norell M (2001) High Temperature Corrosion of Cast Irons and Cast Steels in Dry Air. Mater Sci Forum 369-372:197–204.

114. Minnebo P, Nilsson K-F, Blagoeva D (2007) Tensile, Compression and Fracture properties of Thick-Walled Ductile Cast Iron Components. J Mater Eng Perform 16:35–45.

115. Carton M, Lecomte-Beckers J (2009) Rapport d'essais réalisés sur de matériaux de coeur.

116. Contrepois Q, Lecomte-Beckers J (2011) Analyses thermo physiques de l'acier haut chrome.

117. Bouffioux C (2002) Caractérisation rationnelle des propriétés à chaud des matériaux métalliques - Comparaison des coefficients de dilatation thermique classique et partiel. Rapport intermédiaire n° 35.

118. Neira Torres I (2011) Identificación de diagramas TTT a partir de diagramas CCT para modelación de transformaciones de fase. Universidad de Concepción

119. Kirkaldy JS, Burchmays B (1990) Modeling of temperature field, transformation behavior hardness and mechanical response of low alloys steel during cooling from the austenite region. J Heat Treat 8:127–136.

120. Röhrig K, Fairhurst W (1979) ZTU-Schaubilder Giesserei.

121. Descrptive sheet. Material No. 1.2379, Cod. X153CrMoV12, Dorrenberg Edelstahl.

122. Neira-Torres I, Gilles G, Tchoufang Tchuindjang J, et al. (2014) Study of residual stresses in bimetallic work rolls. Adv Mater Res 996:580–585.

123. Heinrich A (2003) Modélisation thermomécanique de la coulée continue d'acier en deux dimensions. PhD thesis. Ecole Nationale Supérieure des Mines de Paris.

124. Judlin-Denis S (1987) Modélisation des interactions contrainte-transformation de phase et calcul par éléments finis de la génère des contraintes internes au cours de la trempe des aciers. National Polytechnic Institute of Lorraine, France

125. Coret M (2002) Experimental study of the phase transformation plasticity of 16MND5 steel low carbon steel under multiaxial loading. Int J Plast 18:1707–1727.

126. Neira-Torres I, Gilles G, Tchoufang Tchuindjang J, et al. (2013) Prediction of residual stresses by FE simulations on bimetallic work rolls during cooling. Comput methods Mater Sci 13:84–91.

127. Pernach M, Bzowski K, Pietrzyk M (2014) Numerical modelling of phase transformation in DP steel after hot rolling and laminar cooling. J Multiscale Comput Eng 12:397–410.